UNIVERSITÀ
DEGLI STUDI
FIRENZE

PhD in
Physics and Astrophysics

Cycle XXXII

Coordinator Prof. Raffaello D'Alessandro

# A new experimental apparatus for atom-ion quantum mixtures

Academic Discipline (SSD): Fis/03


*Supervisor:*
Dr. Sias Carlo

*Doctoral Candidate:*
Dr. Detti Amelia

*Supervisor:*
Prof. Fallani Leonardo

*Coordinator:*
Prof. D'Alessandro Raffaello


Years 2016/2019

# Abstract

Hybrid quantum systems represent one of the most promising routes in the progress of experimental quantum physics and in the development of quantum technologies. In a hybrid quantum system two (or more) different quantum systems interact in the same experimental setup. Therefore, these composite systems benefit from both the properties of each single system and from the presence of an interaction term, leading to the emergence of new variables that can be experimentally manipulated.

**A promising hybrid quantum system is the one realized by the combination of an ultracold atomic gas and trapped ions.** Ultracold atoms and trapped ions are two of the most studied physical systems for the implementation of several quantum technologies, like e.g. quantum simulation, quantum computation, and quantum metrology. When trapped together, atoms and ions interact via an interaction potential that scales asymptotically with $R^{-4}$, where $R$ is the inter-particle distance, due to the electrostatic (attractive) force between the ion's electric monopole and the atom's induced dipole. Interestingly, this potential has a typical range on the order of hundreds of nm, i.e. approx. two orders of magnitude longer than the range of atom-atom interactions. Several studies have proposed to use this interaction to realize new quantum simulations, study few-body physics, and control atom-ion chemical reactions.

Elastic collisions between ions and atoms can be exploited to sympathetically cool the ions and try to reach the so-far elusive $s$-wave scattering regime, in which atom-ion collisions can lead to a quantum coherent evolution of the composite system. However, the ultracold atom-ion mixtures realized so far were not brought to the $s$-wave scattering regime because of the so-called "micromotion", a driven motion affecting the dynamics of the ions trapped in Paul traps. Atom-ion collisions in the presence of micromotion cause a coupling of energy from the oscillating field of the Paul trap to the colliding particles, which can be heated up in the collision. In order to realize an atom-ion experiment in which the system could reach the $s$-wave scattering regime, the choice of the atomic species and the ion trapping strategy are crucial.

**We decided to build a new experimental apparatus for the realization of an ultracold atom-ion quantum hybrid system made of a quantum gas of fermionic Lithium and trapped Barium ions**. The choice for the elements ensures that atoms and ions in their electronic ground state will not undergo charge-exchange collisions, i.e. inelastic processes for which an electron is "exchanged" between the two colliding particles. Additionally, the large mass ratio ensures an efficient cooling of the ion in the ultracold gas.

For what regards the ion trapping strategy, in order to remove the limitations set by micromotion, we conceived a new trap. This is formed by the superposition of an electric quadrupole static potential and an optical lattice along the untrapping direction of the electric quadrupole. The ions are moved into this electro-optical trap (EOT) from a standard Paul trap, in which the ions are first trapped after their production through photoionization.

In this thesis, I will describe how this new experimental apparatus for the realization of an ultracold atom-ion quantum hybrid system was conceived, designed and assembled. I will first describe the motivations for investigating atom-ion interactions in the ultracold regime. Then, I will describe the experimental techniques to trap

and cool Barium ions and Lithium atoms, and how we plan to make them interact. The largest part of the thesis will be dedicated to the description of the parts of the experimental setup that I designed and realized, like the Lithium optical setup, the Barium imaging system and the electrical setup of the ion trap, including a compact RF drive based on interdependent resonant circuits that I developed for operating the Paul trap. The last chapter of the thesis is dedicated to this innovative drive.

# Contents

# List of Figures

# Introduction

The investigation of fundamental aspects and applications of quantum mechanics with the experimental realization of individual quantum systems represents a very lively research field. Several quantum systems have been studied over the last decades, and the specific features of each quantum system make them suitable for different applications. In exploiting the properties of a quantum system, the ability to control its evolution is a crucial point. The full control of a quantum system makes it possible, for instance, to prepare the system in a selected quantum state, to ensure a controlled, coherent evolution of the system by engineering its Hamiltonian and to measure with a high level of reproducibility its quantum properties.

Ultracold gases of neutral atoms are an exceptional platform to investigate quantum physics because they realize a coherent many-body system in which the experimental parameters can be precisely controlled. As a result, ultracold gases have been used for several applications, including the quantum simulation of condensed matter models [1] and the investigation of quantum phase transitions [2].

An example of the high grade of control that ultracold gases offer is given by the fact that the interactions can be modeled by using only one parameter, the scattering length, the value of which can be tuned by using Feshbach resonances [3], making it possible to study both weakly and strongly correlated systems [4].

Trapped ions constitute another example of quantum system that is commonly exploited to advance research in quantum physics. Trapped ions represent an exceptional source of single particles that experience extraordinary long coherence times (up to tens of seconds [5]). Because of Coulomb repulsion, trapped ions cooled at sufficiently low temperature arrange themselves in ordered structures, i.e. Coulomb crystals [6].

A high level of control can be exerted on trapped ions by manipulating with laser fields the ions' internal and external degrees of freedom. Trapped ions can be prepared in a selected internal state [5], and their motion can be cooled through laser cooling to the absolute motional ground state [7]. These features make of Coulomb crystals one of the best candidate for several applications of quantum physics – the so-called quantum technologies – like quantum computation [8], simulation [9] and metrology [10].

In recent years, scientists have improved the development of quantum systems by creating hybrid quantum systems composed of two different interacting quantum systems [11]. When these systems are isolated, they undergo evolutions governed by their unperturbed Hamiltonians. When they are made interact with each other, the evolution of both systems is perturbed by the presence of interactions, leading to the emergence of new interesting physical properties. However, realizing an experiment with a hybrid quantum system is extremely challenging because of the complexity in building an experimental apparatus that can be used to control systems with properties

and features that can be very different. Due to the complexity in their experimental realization, only a few hybrid quantum systems have been successfully realized so far, including atoms and ions in optical cavities [12], quantum gases coupled to membranes [13], and atom-ion mixtures [14].

Among them, atom-ion hybrid systems not only inherit the interesting features of their constituents – like the possibility of singly addressing and precisely controlling localized trapped ions, and creating large ensembles of coherent matter with quantum gases – but offer new properties that arise from atom-ion interactions. When trapped together, atoms and ions interact via an interaction potential that scales asymptotically with $R^{-4}$, where $R$ is the inter-particle separation, due to the electrostatic (attractive) force between the ion's electric monopole and the atom's induced dipole. Interestingly, this potential has a typical range on the order of hundreds of nm, i.e. approximately two orders of magnitude longer than the range of atom-atom interactions. Several studies have proposed to use this interaction to realize new quantum simulations [15, 16], study few-body physics [17] and control atom-ion chemical reactions [18].

Ions and neutral atoms can play the role of probe and system at the same time. From the point of view of the atoms, a single ion can act as a single, localized impurity in a many-body system, making it possible to investigate condensed matter models like the Anderson [19] and the Kondo model [20]. From the point of view of an ion, the atoms act as an ultracold bath [21] that sympathetically cools the ions, in which one may encode qubits of information. In this way it would be not necessary to stop a quantum computation process running on the ions to optically cool the Coulomb crystal, which would be continuously cooled by the ultracold gas instead. Moreover, the ion could act as the reaction center for chemical processes in which reactions and molecules are created in a controlled way [22]. For these reasons, quantum atom-ion hybrid systems can be employed to investigate fundamental chemical reactions and they could represent a useful platform to advance quantum chemistry and astrochemistry research [23].

Although much has already been done in the field of atom-ion hybrid systems [14], the problem of lowering the collisional energy between atoms and ions represents the main limitation for the observation of quantum effects in atom-ion interactions. In fact, these quantum features arise mainly in the ultracold regime, in which atom-ion interactions are parametrized by a single parameter: the $s$-wave phase shift or scattering length. The ultracold atom-ion mixtures realized so far were not brought to this $s$-wave scattering regime because of a heating mechanism caused by the so-called "micromotion", a driven motion affecting the dynamics of the ions trapped in radiofrequency traps. Atom-ion collisions in the presence of micromotion cause a coupling of energy from the driving field field of the ion trap to the ions' secular motion [24, 25].

The work reported in this thesis is devoted to the construction of a novel experimental setup for the realization of an ultracold atom-ion quantum hybrid system made of a quantum gas of fermionic Lithium and trapped Barium ions. We plan to overcome current limitations in atom-ion experiments by trapping the ions in a novel trap made of static optical and electric fields that is inherently free of micromotion. Moreover, the choice of fermionic Lithium and Barium as mixture elements, will ensure a strong control over inelastic collisions, like charge-exchange processes or three-bodies recombinations, which can compromise the achievement of the ultracold regime.

In this thesis, I will describe how this new experimental apparatus was conceived, designed and assembled. Several technical problems had to be considered and solved, since the ions experimental setup must be matched with the equally complex setup for producing, cooling and trapping atomic quantum gases.

The thesis is organized as follows:

**Chapter 1: Atom-ion interactions.** This chapter focuses mainly on the interactions between atoms and ions, which are the essential characteristic of atom-ion hybrid systems. First, the atom-ion interactions is described. Then, the choice of $Ba^{+}$-$Li$ as the elements of the mixture is justified by giving an overview of the possible inelastic processes that can be controlled with these elements. Finally, a detailed list of possible applications for ultracold $Ba^{+}$-Li mixtures is given as motivations.

**Chapter 2: Realizing an atom-ion quantum system.** In this chapter the theoretical principles behind the cooling and trapping techniques that will be used for both atoms and ions will be discussed. In particular, the strategy for trapping ions with static fields will be presented. Finally, the experimental apparatus will be shown, and the strategy for mixing together atoms and ions will be provided.

**Chapter 3: Lithium experimental setup.** In this chapter, the experimental setup for trapping and cooling Lithium atoms is described. The different methods for cooling and trapping are based on the generation of several laser frequencies, prepared in an optical setup by splitting, modulating and amplifying laser lights originating from two master lasers locked in frequency. The procedure for realizing both the master lasers and the tapered amplifiers used in the optical setup are reported. Then, the whole optical setup is described, and a model for adiabatically transport the neutral atoms into the ion trap is presented.

**Chapter 4: The $Ba^{+}$ ion trap.** In this chapter the experimental setup for producing and trapping Barium ions is described. The procedure that is planned for trapping Barium ions is discussed: neutral Barium atoms are produced from evaporation in two ovens, photoionized and then trapped first in a linear Paul trap and then moved to our new trap made of static fields. In the first part of the chapter the mechanical features of the ion trap are described. The second part of the chapter is focused on electrical issues: there it is shown the electrical setup for providing high voltages to the DC electrodes and for feeding the ovens with high current for short times. Moreover, an electrical model of the ion trap is given.

**Chapter 5: RF drive.** The Paul trap is a key element in the Ba-Li experiment and it will make it possible to trap linear or 2D ion crystals. In this chapter I will describe the designing and prototyping phases of the RF drive, an electric circuit for feeding with intense RF the Paul trap electrodes that generate the ion trapping potential. The circuit is formed by four interdependent resonant circuits, each of which provides a high-voltage signal to an electrode of a Paul trap. The RF design is conceived both for compensating micromotion and for controlling the shape of the ion crystal. For instance, the presence of a single resonant circuit for each electrode ensures a strong

control on the voltage drop on each electrode, e.g. by applying a DC field through a bias-tee.

# Chapter 1

# Atom-ion interactions

Interactions are the key element in a hybrid system, since they represent the additional term that is not present in the single quantum systems forming the composite system.

This chapter is dedicated to the description of atom-ion interactions, their properties and their importance in the scientific landscape. In the first section [1.1] the atom-ion interaction potential will be described. Section [1.2] will provide an outline of the two-body scattering theory and how, for low scattering energies, it is possible to describe the scattering process by using only one parameter, the scattering length $a_s$ spell in full.

Section [1.3] will give an overview on the state-of-the-art in experimental atom-ion physics. In particular, the main issues that prevent from reaching ultralow temperatures in atom-ion systems will be discussed, and our strategy of using Barium ions and Lithium atoms will be explained.

Finally, Sec. [1.4] will provide an overview of possible experiments that could be realized with an atom-ion system brought to the ultracold regime.

## 1.1 Atom-ion interaction potential

An ion with an intrinsic charge $Ze_0$, with $Z$ integer and $e_0$ the electron's charge, creates an electric field $\vec{E}_{\text{ion}}(\vec{R}) = \frac{1}{4\pi\epsilon_0}\frac{Ze_0\vec{R}}{R^3}$, where $\epsilon_0$ is the vacuum dielectric constant and $\vec{R}$ is the field point. In the presence of an electric field $\vec{E}_{\text{ion}}(\vec{R})$, a neutral atom developes an electric induced dipole $\vec{p} = \alpha_0\vec{E}_{\text{ion}}(\vec{R})$, where $\alpha_0$ is the atomic static polarizability [26]. The interaction potential of the induced dipole moment $\vec{p}$ in the driving field $\vec{E}_{\text{ion}}(\vec{R})$ is given by [27]:

$$V = -\frac{1}{2}\vec{p}\cdot\vec{E}_{\text{ion}} \ , \tag{1.1}$$

the factor 1/2 takes into account that the dipole moment is an induced, not a permanent one.

This potential is the atom-ion interaction potential, usually written in the form [28]:

$$V(\vec{R}) = -\frac{C_4}{2R^4} \ , \tag{1.2}$$

with $C_4 = \alpha_0 Z^2 e_0^2/(4\pi\epsilon_0)^2$.

It is interesting to note that the Van der Waals interactions between two neutral atoms scale asymptotically with $R^{-6}$, because they arise from an interaction between

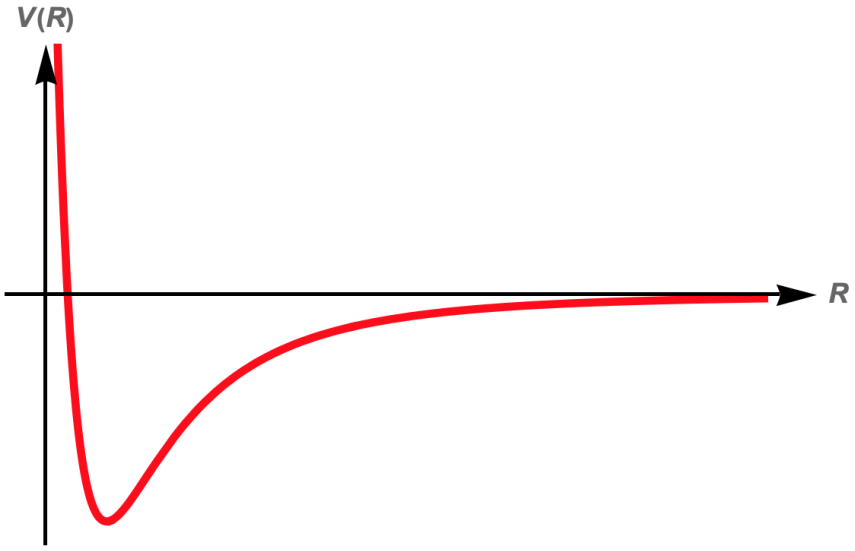


Figure 1.1: Ion atom interaction potential vs. internuclear separation. In this graph the hard-core short-range repulsion has been represented by a term that goes like $R^{-12}$.

two induced dipoles [14]. Because of this longer-range asymptotical scaling, the atom-ion interactions have typically a range that is two orders of magnitude larger than atom-atom interactions: hundreds of nm instead of a few nm. Taking for instance the pair $^{138}$Ba$^{+}$-$^{6}$Li, it has a reduced mass $\mu = m_{\mathrm{Ba}} m_{\mathrm{Li}}/m_{\mathrm{Ba}} + m_{\mathrm{Li}} = 5.75\ u$ with $u$ the atomic mass unit, $m_{\mathrm{Ba}}$ the ion mass and $m_{\mathrm{Li}}$ the neutral mass. The characteristic radius for the $^{138}$Ba$^{+}$-$^{6}$Li interaction potential is $R^{*} = \sqrt{\mu C_4/\hbar^2} = 70$ nm [14] (atomic polarizability for Lithium taken from [29]: $\alpha_0(^2\mathrm{S}_{1/2}) = 164.1125 \pm 0.0005$).

The interaction potential in eq. (1.2) diverges to positive values for $R \to 0$, but this behavior is unphysical since in the short range the real potential has a hard-core repulsive potential, as shown in Fig. (1.1).

## 1.2 A short outline on atom-ion scattering

For obtaining a complete description of the atom-ion scattering process it would be necessary, in principle, to know the exact form of the hard-core repulsive potential. However, in a classical description of the scattering processes, it is sufficient to use the potential of eq. (1.2) to predict some of the main features of atom-ion interactions.

Classically, a collision between two particles in the center-of-mass (COM) frame has energy $E_{\mathrm{col}} = \frac{1}{2}\mu v^2$ and angular momentum $L = \mu v b$, where $v$ is the relative velocity, $b$ is the impact parameter. The possible trajectories after a collision are divided into two different sets on the basis of $b$ being smaller or bigger than a critical impact parameter defined as $b_{\mathrm{c}} = (2C_4/E_{\mathrm{col}})^{1/4}$ [30]. If $b < b_{\mathrm{c}}$, attractive $R^{-4}$ potential makes the particles approach and collide at a short distance, thus strongly deviating their initial trajectories [14]. We will refer to these collisions as *Langevin collisions* [31]. Instead, if $b > b_{\mathrm{c}}$ the free-particle trajectories are only slightly modified by the interaction and the process is classified as *forward scattering*.

Since particles can exchange a considerable amount of momentum only in Langevin collisions, one can assume that Langevin collisions are the ones responsible for most of the physics originating in atom-ion collisions. The total cross section for Langevin collisions is [32]:

$$\sigma_{\text{Lang}} = \pi b_{\text{c}}^2 = \pi \sqrt{\frac{2C_4}{E_{\text{col}}}} \ , \tag{1.3}$$

that scales as $E_{\text{col}}^{-1/2}$. This implies that the collisional rate $\Gamma_{\text{col}} = n_{\text{a}} v \sigma_{\text{Lang}}$, depends only on fundamental properties of the atom-ion system as $C_4$, $\mu$ and the particles density $n_{\text{a}}$ and it is independent by the collisional energy $E_{\text{col}}$, since $v \propto E_{\text{col}}^{1/2}$. This is a special feature of the $R^{-4}$ interaction potential.

### 1.2.1 Wavefunction development in partial-waves

In the limit of low collisional energies, the Langevin formula fails and it is necessary to apply a semi-classical approach to describe the particles dynamics. Because the atom-ion interaction potential of eq. (1.2) is a central potential $V(\vec{R}) = V(R)$, the scattered wave-function in spherical coordinates $(R, \theta, \phi)$ is such that $\Psi(R, \theta, \phi) = \Psi(R, \theta)$ and it is possible to write a partial wave expansion of the atom-ion system wavefunction in the COM frame [33]:

$$\Psi(R, \theta) = \sum_{l=0}^{\infty} Y_l^0(\theta) \frac{u_l(R)}{R} = \sum_{l=0}^{\infty} \left( \frac{2l+1}{4\pi} \right)^{1/2} P_l(\cos\theta) \frac{u_l(R)}{R} \ , \tag{1.4}$$

where $Y_l^m(\theta, \phi)$ are the orthonormalized spherical harmonics [34], $P_l(\cos\theta)$ are the Legendre polynomials and $u_l(R)$ are the solutions of the one-dimensional Schrödinger equation:

$$\left( -\frac{\hbar^2}{2\mu} \frac{\partial^2}{\partial R^2} + \frac{\hbar^2}{2\mu} \frac{l(l+1)}{R^2} - \frac{C_4}{2R^4} \right) u_l(R) = \mathcal{E} u_l(R) \ . \tag{1.5}$$

For the moment we are considering only the $R^{-4}$ term of the potential, and we are not considering the repulsive hard-wall potential dominating at a short interparticle distance. Two terms contribute to the effective potential in eq. (1.5): the interaction potential $V(R)$ and the centrifugal barrier that depends on the angular momentum $\hbar l$. Effective potentials describing the atom-ion interaction for different values of $l$ are plotted in Fig. (1.2). Without considering effects of quantum tunneling through the centrifugal barrier, for a given collisional energy $E_{\text{col}}$ there is a momentum $L = (1/\hbar)\sqrt{2\mu\sqrt{2C_4 E_{\text{col}}}}$ such that for $l > L$, $E_{\text{col}}$ is lower than the centrifugal barrier height and the particles collide with the centrifugal barrier. For $l < L$, the collisional energy is sufficiently high to pass over the centrifugal barrier so that the particles scatter from the repulsive hard wall. These two cases correspond to the classical cases of forward scattering and Langevin collisions, respectively.

The scattered wavefunction of eq. (1.4) can be written in terms of the phase shifts $\delta_l$ acquired by solving the Schrödinger equation for the partial waves:

$$\Psi(R, \theta) = e^{ik\cdot R}\left(1 + \frac{f(\theta)}{R}\right) \quad \text{with} \quad f(\theta) = \frac{1}{k} \sum_{l=0}^{+\infty} (2l+1) e^{i\delta_l} \sin(\delta_l) P_l(\cos\theta) \ , \tag{1.6}$$

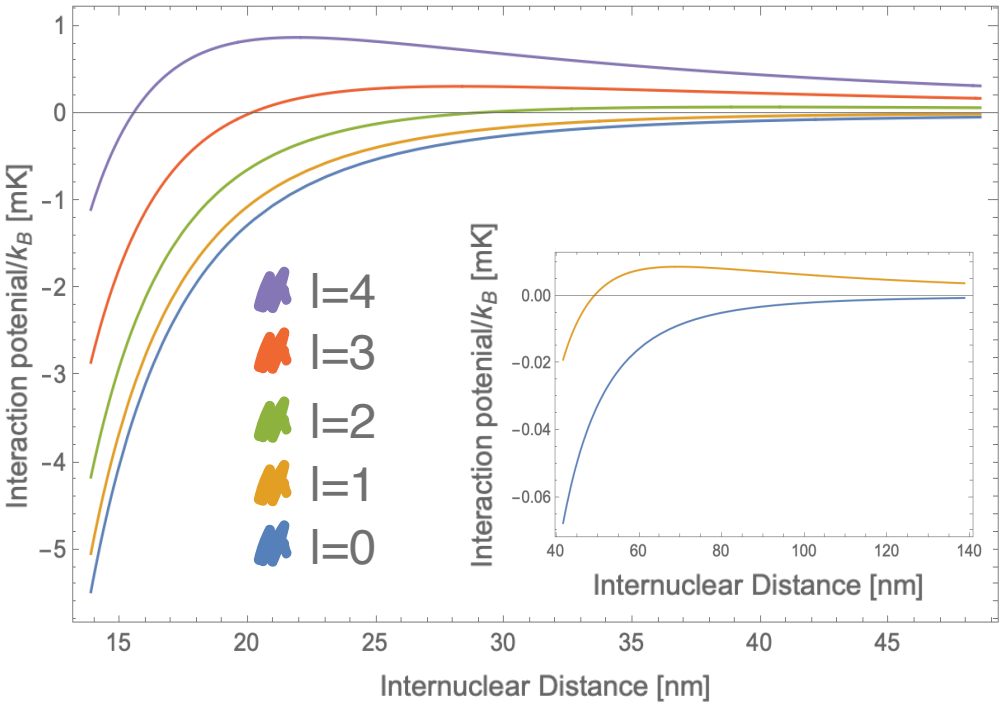


Figure 1.2: Effective interaction potential of eq. (1.5) in which the hard-wall potential has been neglected.

where $k = \sqrt{2\mu E_{\rm col}}/\hbar$ . The scattering cross section can be calculated as the sum of the cross sections from all partial waves [30]:

$$\sigma_{\rm el} = \sum_{l=0}^{+\infty} \sigma_l = \frac{4\pi}{k^2} \sum_{l=0}^{+\infty} (2l+1) \sin^2 \delta_l \ . \tag{1.7}$$

Therefore, in order to determine the total elastic cross section and the scattered wavefunctions, one has to calculate the values of $\delta_l$ for each $l$ by integrating eq. (1.5). For this calculation, we can consider the different contributions for the two cases $l < L$ and $l > L$. If $l < L$, i. e. in case of Langevin collisions, the particles have enough energy to pass over the centrifugal barrier and directly scatter on the repulsive potential. In principle, for these collisions one should add the hard-wall repulsive term in the potential of eq. (1.5) and integrate it. However, this term cannot be precisely calculated, and it is usually derived from experimental measurements related to the molecular potential, such as the energy of a bound state [35]. A possible approximation is to assume that the phase shifts are isotropically distributed between 0 and $2\pi$, so that $\sin^2 \delta_l \simeq 1/2$ in eq. (1.7). With this approximation, which is valid for sufficiently large $L$ [36], each partial wave contributes with $\sigma_{l<L} = 2\pi l/k^2$. The Langevin cross section of eq. (1.3) can be obtained by summing all the $\sigma_{l<L}$ for all $l$s up to $L$.

Instead, if $l > L$ the particles collide with the centrifugal barrier and $\delta_l$ can be calculated by integrating eq. (1.5). The solution of the $l$-dependent integral can be approximated to [36]:

$$\delta_{l>L} \simeq -\frac{\pi \mu^2 C_4}{4\hbar^4} \frac{E_{\rm col}}{l^3} \ , \tag{1.8}$$

and and the cross section contributions can be approximated to $(2l+1)\sin^2\delta_l \simeq 2\delta_l^2$. In this case, summing all the contributions for $l > L$ and $l > L$, we obtain the total elastic cross section:

$$\sigma_{\rm sc} = \pi\left(\frac{\mu C_4^2}{\hbar^2}\right)^{1/3}\left(1+\frac{\pi^2}{16}\right)E_{\rm col}^{-1/3}\ , \tag{1.9}$$

scaling with $E_{\rm col}^{-1/3}$.

In this case the collisional rate depends on the collisional energy and scales as $E_{\rm col}$, differently from the purely classical Langevin treatment. The Langevin classical approximation of eq. (1.3) is typically valid for processes in which the particles needs to approach each other to short distances and the contribution of partial waves with $l > L$ is negligible, e.g. in inelastic processes, see Sec. [1.3]. Otherwise, the elastic cross section is well described by the semiclassical treatment of eq. (1.9) up to low collisional energies [21]. At sufficiently low collisional energy and $L$, the semiclassical approach fails and exact quantum mechanical calculations show a deviation from the semi-classical behavior [36].

### 1.2.2 *s*-wave approximation

When $E_{\rm col}$ is smaller than the height of the $l = 1$ ($p$-wave) collisional barrier, i.e. when $L < 1$, the partial wave with $l = 0$ ($s$-wave) is the only with $l < L$. When this is the case, all the partial waves for $l \geq 1$ provide a small contribution to the scattered wavefunction, and one can use the so-called *s-wave approximation*, for which the total elastic scattering cross section can be written as:

$$\sigma_{\rm el} = \frac{4\pi}{k^2}\sin^2\delta_s = 4\pi a_s^2\ , \tag{1.10}$$

where $\delta_s$ is the phase shift evaluated for $l = 0$ and $a_s$ a scalar named *scattering length*.

When eq. (1.10) is valid, the scattering cross section is independent from the collisional energy and it is described by only one real parameter, i.e. the scattering length $a_s$.

The $s$-wave approximation is well suited for describing the collisional physics in most of ultracold atoms experiments [37], and the success of this field relies also on the possibility of treating atom-atom interactions coherently and to tune them through *Feshbach resonances* [3].

Let's suppose that, in addition to the molecular potential $V_{\rm bg}(R)$ of the two colliding particles, there exists a second molecular potential $V_{\rm c}(R)$ corresponding to a different asymptotic channel, see Fig. (1.3). For large internuclear distances, the background potential $V_{\rm bg}(R)$ asymptotically connects to two free atoms in the ultracold gas. For a collision process, having the very small energy $E_{\rm col}$, this potential represents an energetically *open channel*, since the two particles have enough energy to exit the collision from this channel. The other potential $V_{\rm c}(R)$, instead, represents a *closed channel*, since the particles do not have enough energy to exit the scattering process from it. Nevertheless, the closed channel can support bound molecular states near the threshold of the open channel.

A Feshbach resonance occurs when the bound molecular state in the closed channel energetically approaches the scattering state in the open channel. When this is the case, even weak coupling can lead to strong mixing between the two channels, leading

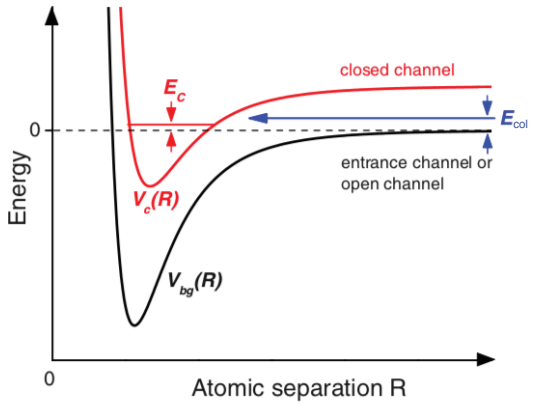


Figure 1.3: Basic two-channels model for a Feshbach resonance. The phenomenon occurs when two atoms colliding at energy $E_{\rm col}$ in the background channel resonantly couple to a molecular bound state with energy $E_c$ supported by the closed channel potential. In the ultracold domain, collisions take place near zero-energy, $E_{\rm col} \to 0$. Resonant coupling can be conveniently realized by magnetically tuning $E_c$ near 0, if the magnetic moments of the closed and open channels differ. Adapted from [3].

to a significant change of the scattering cross section. If the energy gap between $V_{\rm bg}(R)$ and $V_{\rm c}(R)$ can be tuned with an external parameter $B$, e.g. an externally imposed magnetic field (magnetic Feshbach resonance), then the Feshbach resonance can be used to change the scattering length.

In a magnetic Feshbach resonance, the s-wave scattering length $a_s$ can be written as a function of the magnetic field as [38]:

$$a_s(B) = a_{\rm bg}\left(1 - \frac{\Delta_{\rm fr}}{B - B_0}\right) , \tag{1.11}$$

where $a_{\rm bg}$ represents the off-resonant value for the $V_{\rm bg}(R)$ scattering length, $B_0$ denotes the resonance position where the scattering length diverges and $\Delta_{\rm fr}$ is the resonance width.

Magnetic tunable Feshbach resonances have been experimentally observed in most of alkali-metal species [39, 40], including $^6$Li [41, 42]. However, for atom-ion interactions, even if Feshbach resonances were theoretically predicted [43] they have never been experimentally observed for the difficulties encountered in reaching ultracold regimes with atom-ion systems (the next Section is devoted to explain this issue).

Apart from the fundamental interest in observing quantum effects in the charge-induced dipole potential, atom-ion Feshbach resonances would be an important tool in order to reach the maximum grade of control for atom-ion systems. With Feshbach resonances it would be possible to tune the scattering length and to fully control the collisional physics of the atom-ion quantum system.

## 1.3 $Ba^+$-Li: going efficiently to ultracold regimes

In an inelastic collision, the internal state or the chemical composition of the colliding particles is changed after the collision. At low energies endothermic reactions are improbable and energy conservation imposes that the energy difference between

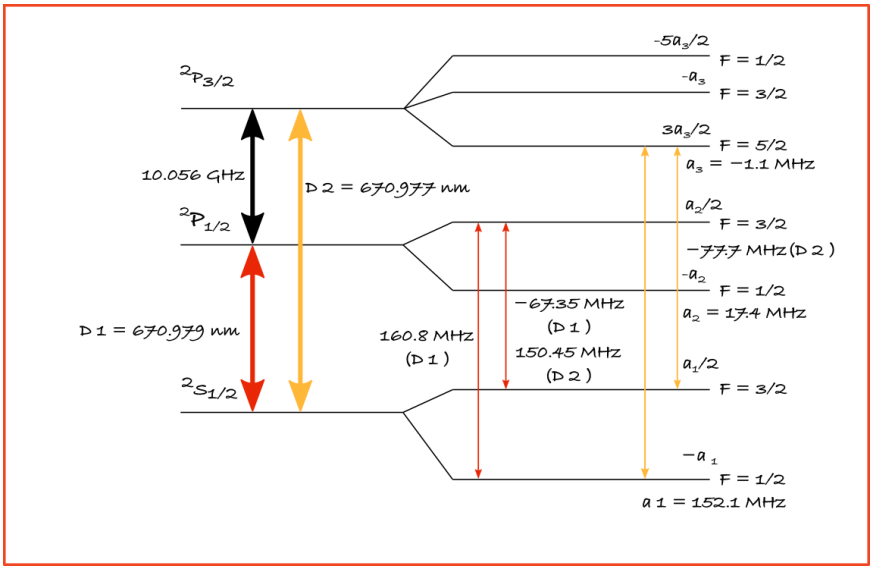


Figure 1.4: $^6$Li energy levels diagram.

the initial and the final particles must be released either by the emission of a photon (*radiative processes*) or by an increase of the kinetic energy (*non-radiative processes*). In atom-ion systems, since in inelastic processes particles must approach each other to short distances, inelastic scattering events follow the Langevin scattering rate behavior [44].

Quantum control of chemical reactions is an important goal in chemistry and physics and for this reason inelastic processes were amply studied in atom-ion systems [18, 45]. However inelastic reactions, especially non-radiative ones, provide a heating mechanism in atom-ion systems [46]. Additionally, in case of chemical reactions, the composition of the atom-ion mixture changes, causing an interruption of the experiment [47].

In order to prevent these inelastic processes in our experiment, we planned to use $^{138}Ba^+$ as the charged particle and fermionic $^6$Li as neutral atom. In this section I will firstly describe the atomic structures of these two species and then I will list the inelastic processes that are typical in atom-ion systems, specifying how they could be prevented by choosing a $^{138}Ba^+$-$^6$Li combination.

### 1.3.1 Li atoms: properties and energy levels

Lithium is an alkali metal with atomic number 3. The energy levels diagram of $^6$Li is sketched in Fig. (1.4). As all the alkali atoms, it has dipole transitions from the ground state $S_{1/2}$ to the excited states $P_{1/2}$ and $P_{3/2}$, which are traditionally named D1 and D2 transitions respectively. D1 and D2 are very close in frequency: their frequency difference is approximately 10 GHz.

$^6$Li is one of the two stable fermionic atoms among the alkali metals, together with $^{40}$K. It has just one $s$-electron in the outer shell ($\vec{S} = 1/2$ and $\vec{L} = 0$) and nuclear angular momentum $\vec{I} = 1$. It follows that the vector $\vec{F} = \vec{I} + \vec{S} + \vec{L}$ has half integer values from which derives its fermionic nature and the rich hyperfine structure shown in Fig. (1.4). Laser cooling in Lithium is particularly convenient since it has accessible transitions in the visible range. But the main interest in using $^6$Li is because of the

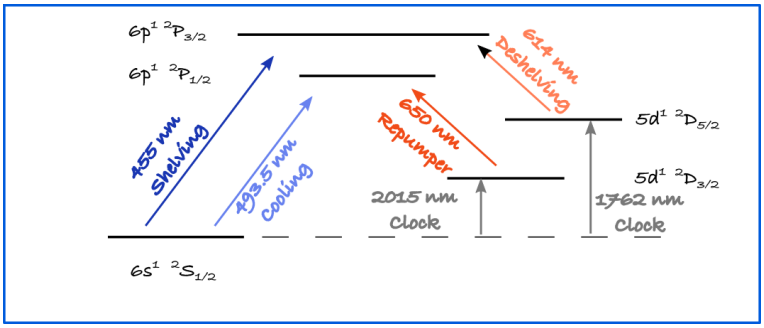


Figure 1.5: $^{138}Ba^{+}$ energy levels diagram.

presence of several broad Feshbach resonances among the two lowest hyperfine levels, one of which located at 834 Gauss [48, 49]. This property makes $^{6}$Li one of the best systems for observing fundamental phenomenons in strongly correlated fermions, like the BEC-BCS crossover and the growth of magnetic phases [50, 51].

### 1.3.2 $Ba^{+}$ ions: properties and energy levels

Neutral Barium is an alkaline earth metal with atomic number 56. It has high chemical reactivity, so it can not be found in nature as a free element and, when exposed to air, it quickly reacts with the molecular oxygen to form Barium oxide. $^{138}$Ba is the most abundant stable isotope in nature with a percentage of about 72 % [52].

The ionized $^{138}Ba^{+}$ has an atomic level structure similar to that of alkali metals: it has the electronic configuration of the xenon with an additional electron in the $6^2S_{1/2}$ state. Since its nuclear spin is null, it does not have a hyperfine structure. The atomic levels of $^{138}Ba^{+}$ are shown in Fig. (1.5). As for Lithium, also in the case of Barium ions the wavelengths for addressing its lower transitions are all in the visible region of the electromagnetic spectrum.

$Ba^{+}$ is one of the first atomic ions that was trapped [53] and nowadays $^{138}Ba^{+}$ ions have been successfully trapped by several groups.

### 1.3.3 Inelastic collisions

In approximately 10 years of experimental atom-ion physics, several inelastic processes were observed and characterized. Here in the following, I provide an overview of the most relevant ones, and explain why a $^{138}Ba^{+}$-$^{6}$Li will be exempt from most of them.

#### Charge-exchange processes

A charge-exchange process is a collision after which the initial atom and ion "exchange" an electron [44, 54]:

$$A^{+} + B \rightarrow A + B^{+} \ .$$

Charge transfer can occur in atom-ion collisions both in radiative and non-radiative processes, characterized with different probabilities that depend on the electronic state of the colliding particles [44]. In principle, the newly formed ion $B^{+}$ can be trapped after its creation, depending on the mass and the final energy of the charged particle. In heteronuclear collisions, non-radiative charge-exchange processes typically release enough energy that the newly formed $B^{+}$ ion escape the trap.

In experiments in which several ions are trapped, the occurrence of a charge-exchange process can be revealed by the presence of a dark ion in the Coulomb crystal [47]. Otherwise, if the new ion $B^+$ escapes from the trap, the process is revealed simply by the loss of the ion $A^+$ from the trap [55]. In both cases the original physical system is modified, and the atom-ion system must be re-loaded.

In the case of $Ba^+$ and Li, charge-exchange collisions of the type $Ba^+ + Li \rightarrow Ba + Li^+$ cannot occur when the atoms are in their electronic ground state, since the $Ba + Li^+$ composite system has an energy 0.2 eV higher than the $Ba^+$+Li one.

### Three body recombinations

A three body recombination is a mechanism for which a diatomic molecule is formed in the presence of a third particle that absorbs a portion of the momentum:

$$A^+ + B + B \rightarrow A^+ + B_2 \ .$$

In this kind of processes the momentum conservation is guaranteed by the presence of the ion during the molecule formation [56]. The reaction is non-radiative and the binding energy of the molecule is transformed into kinetic energy of the colliding particles.

Since the atom-ion interacting potential is long-ranged and attractive, even at low temperature there is a relevant probability for two atoms to interact simultaneously with the same ion as reaction center. This leads to the ion heating up in addition to the loss of the two reactant neutral atoms. In our experimental system, however, three-body recombination reactions ($Ba^+ + Li + Li \rightarrow Ba^+ + Li_2$ but also $Ba^+ + Li + Li \rightarrow LiBa^+$+Li) will be strongly suppressed at sufficiently low temperatures by using a spin polarized gas of $^6$Li, since the Pauli principle does not allow two identical fermions to undergo an $s$-wave collision.

### Collisional quenching

Quenching collisions are inelastic collisions in which one or both particles in the atom-ion pair undergo a relaxation of the internal state [18, 55]:

$$A^+ + B^* \rightarrow A^+ + B \ ,$$

where the superscript $*$ indicates a particle in an excited internal level.

These effects may reduce the lifetime of the ions' excited states, thus affecting processes in which metastable excited states are used like in ion-based clocks [57]. In our case, collisional quenching of the kind $Li^* + Ba^+ \rightarrow Li + Ba^+$, will be avoided by using atoms in the absolute ground state, i. e. $|F = 1/2, m_F = 1/2\rangle$ for $^6$Li, see Fig. (1.4).

A particular type of quenching collisions are *spin-exchange* and *spin-relaxation* processes. These mechanisms can cause a loss of coherence in the system and, in case of non-radiative processes, an increase of the kinetic energy of the particle. The problem of controlling spin-exchange processes is particularly relevant, for instance when a qubit is encoded in an ion's internal state, since quenching reduces the coherence of the qubit itself [58, 59].

In our experimental setup both Zeeman sublevels of the ion's ground state manifold, $|m_J = 1/2\rangle_{\mathrm{Ba}}$ and $|m_j = -1/2\rangle_{\mathrm{Ba}}$, in which we could encode a qubit, are stable

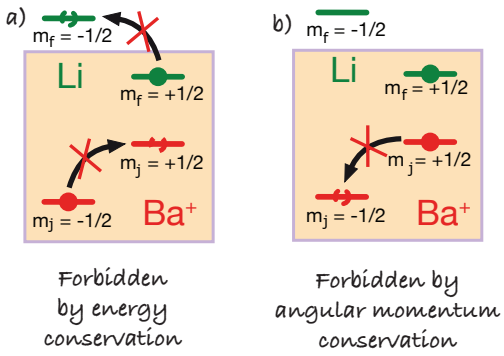


Figure 1.6: Suppression of spin-exchange processes with $Ba^+$ and Li atoms prepared in the absolute ground state. (a) The reaction $|F = 1/2, m_F = 1/2\rangle_{\rm Li}\,|m_J = -1/2\rangle_{\rm Ba} \rightarrow |F = 1/2, m_F = -1/2\rangle_{\rm Li}\,|m_J = 1/2\rangle_{\rm Ba}$ is forbidden because of energy conservation. (b) The reaction $|F = 1/2, m_F = 1/2\rangle_{\rm Li}\,|m_J = 1/2\rangle_{\rm Ba} \rightarrow |F = 1/2, m_F = 1/2\rangle_{\rm Li}\,|m_J = -1/2\rangle_{\rm Ba}$ is forbidden because of angular momentum conservation.

against $s$-wave collisions with an ultracold Fermi gas of $^6$Li in the $|F = 1/2, m_F = 1/2\rangle_{\rm Li}$ state, since (see Fig. 1.6):

1. The reaction

   $$|F = 1/2, m_F = 1/2\rangle_{\rm Li}\,|m_J = 1/2\rangle_{\rm Ba} \rightarrow |F = 1/2, m_F = 1/2\rangle_{\rm Li}\,|m_J = -1/2\rangle_{\rm Ba}$$

   is forbidden because of angular momentum conservation. It can occur only through spin-orbit coupling in a collision with contributions from partial waves with angular momentum $l > 0$ (*spin-relaxation* [59]), which are strongly reduced in the ultracold regime.

2. The reaction

   $$|F = 1/2, m_F = 1/2\rangle_{\rm Li}\,|m_J = -1/2\rangle_{\rm Ba} \rightarrow |F = 1/2, m_F = -1/2\rangle_{\rm Li}\,|m_J = 1/2\rangle_{\rm Ba}$$

   is forbidden because of energy conservation. The process is endothermic: since the Landé $g$-factor has a different sign for the $F = 1/2$ state of $^6$Li and the $J = 1/2$ state for $^{138}Ba^+$, the energy $E_{\rm fin}$ of the $|F = 1/2, m_F = -1/2\rangle_{\rm Li}\,|m_J = 1/2\rangle_{\rm Ba}$ state is larger than the energy $E_{\rm in}$ of the $|F = 1/2, m_F = 1/2\rangle_{\rm Li}\,|m_J = -1/2\rangle_{\rm Ba}$ state. With a magnetic field of only one Gauss the evaluated energy difference is $(E_{\rm fin} - E_{\rm in}) \simeq 200\ \mu{\rm K} \times k_B$, an energy that is 20 times the height of the $p$-wave centrifugal barrier, and therefore much larger than the collisional energy in case of ultracold collisions.

## 1.4 Applications of ion-atom systems

Currently, more than ten experimental groups in the world are currently building or have already reported on experiments with cold atoms and ions [14]. These experiments have so far mainly explored atom-ion collisions in the cold regime by characterizing the effects of elastic and inelastic collisions [22]; only very recently a group

has reported the observation of atom-ion collisions just above the $p$-wave centrifugal barrier [60]. Elastic atom-ion collisions lead to sympathetic cooling of the ions since the atoms are typically much colder [21, 47]. Although sympathetic cooling has been observed by many groups, it has not yet been sufficient to bring atom-ion temperature to the ultracold regime; in the next chapter I will explain the mechanisms causing this limitation. Nevertheless, many groups have instead focussed their investigations in the study of inelastic processes, including chemical reactions like charge-exchange processes [44, 54, 61], molecule formation [55], collisional quenching of excited levels [18], and spin relaxation and spin exchange [59]. Interestingly, sympathetic cooling was successfully used to cool the internal state of a molecular ion to its vibrational ground state [62].

The field of atom-ion hybrid systems is thus very active, and several proposals have been made to use this type of systems to advance various fields of research: from molecular physics [17] to quantum computation [63], to many-body physics [15]. In this section, some of the most interesting applications for experiments with ultracold atom-ion quantum mixtures are listed.

### 1.4.1 Quantum simulation

The use of even small-scale but controllable quantum systems may offer a route to efficiently simulate other quantum systems that could be very hard to describe analytically or numerically on classical computers. This idea dates back to the 1980s and in particular to Richard Feynman, who pointed out that the proper way of simulating quantum physics would be by making use of a quantum machine instead of a classical computer [64].

Both trapped ions and cold atoms, as separate systems, have successfully been employed as quantum simulators. Neutral cold atoms can be prepared in ensembles of many thousands of particles (either bosons or fermions), which can be simultaneously manipulated and be arranged in spatially periodic structures, i.e. optical lattices, for instance to simulate the behavior of electrons in a solid [65]. Trapped ions, instead, form much smaller ensembles of particles that do not experience contact interactions because of Coulomb repulsion. Nevertheless, ion-ion "interactions" can be initiated with the mediation of light fields, which make it possible to simulate models with long range interactions [9].

In an atom-ion system, the presence of a new type of long-range interaction makes it possible to conceive new methods for emulating condensed matter models. Recently, it was suggested to use a one-dimensional crystal of trapped ions to create a quasi-periodic potential for ultracold atoms and induce a band structure [15] or, for instance, to use atom-ion mixtures for simulating bosonic Josephson junctions [16].

The main advantage of using an ion crystal to create a quasi-periodic potential for ultracold atoms instead of an optical lattice, is that the atomic degrees of freedom couple to phonons of the ion lattice, thus emulating a natural thermally excited solid-state system [66]. If we were able to realize systems such as degenerate Fermi gases interacting with localized ions in a crystal, then it would be possible to enable the investigation of models based on localized impurities like the Anderson model [19] and, in the presence of a spin-exchange term, of Kondo physics [20].

#### Quantum chemistry and astro-chemistry

Quantum simulators based on atom-ion hybrid systems can be employed to investigate fundamental chemical reactions and they could represent a useful toy-model for quantum chemistry and astro-chemistry researches.

Ion-neutral interactions have a longer-range character as compared to atom-atom interactions and ionic species can be manipulated and detected at the single particle level. This makes it possible to investigate internal state-controlled chemical reactions with a few particles at a time [18, 22, 45]. Additionally, sympathetic cooling can be an effective method to cool molecular ions to their ground state [62], leading to the possibility of performing molecular spectroscopy.

Ions are ubiquitous in space and are potentially responsible for the formation of increasingly complex interstellar molecules [67, 68]. Typical temperatures of the interstellar clouds are between a few to several Kelvin. Thus, the knowledge gained about cold collisions and especially chemical reactions using cold hybrid ion-atom experiments can be instructive for better understanding chemical transformations of ions in space [23].

### 1.4.2 Quantum computation

An important application for ultracold systems of trapped atoms and ions is quantum computation. Both trapped ions [69, 70] and neutral atoms [71, 72] have been identified as good candidates for implementing a quantum computer, since they are closed quantum systems that have a very long decoherence time and in which entanglement can be realized with external fields such as lasers. Trapped ions were defined as one of the most promising physical systems for implementing quantum computation [73], even if scaling current machines to a large number of qubits is a tough technological issue [74].

Ultracold atoms in a trapped ion quantum computer could act as a coolant that is transparent to the wavelengths used for manipulating the ions, and that could continuously cool a trapped ion quantum computer, which in principle could operate without stopping the operation for cooling the particles. Additionally, ions have been proposed as a tool to create entanglement on demand in an array of atoms loaded in an optical lattice [63], and to measure the atoms at the single particle level [75].

### 1.4.3 Metrology

In recent years, optical clocks were demonstrated to be the most stable and accurate clocks in the world [76]. Several atoms [77] and ions [78, 79] have been investigated as optical clock candidates.

Atom-ion systems can provide a novel platform to study some of the open problems in ion-based clocks. For instance, studying atom-ion interactions at both quantum and classical level could help in improving the estimate of the frequency shift due to collisions with background particles in ion-based clocks. The longer-ranged interaction potential with neutral particles makes the ions more sensitive to collisions with particles of the background gas. However, at the moment, the estimate of background collisional shift is only based on theoretical calculations [80] and precision measurements have been so far realized only in atom-based clocks [81].

Moreover, in ion-based clocks the particles are trapped using radio-frequency fields and their dynamics is affected by micromotion, see Sec. [2.2]. The Doppler shift caused by micromotion is currently one of the largest contributions to the overall uncertainty in state-of-the-art ion-based clocks [82].

The effects of atom-ion collisions in the presence of micromotion are currently the best method to measure micromotion in RF traps [83]. Therefore, atom-ion interactions could be used to improve the performances of ion-based optical clocks by providing a more accurate measurement of the micromotion affecting the ion.

# Chapter 2

# Realizing an atom-ion quantum system

In the previous chapter I showed the basics of atom-ion interaction and why it can represent a new "knob" in the atomic physics toolbox for advancing different fields like quantum simulation and quantum computation. In particular, I showed how the atom-ion pair we chose for our experiment, i.e. $Ba^+$ and Li, is protected by energy and momentum conservation from inelastic scattering processes like charge-exchange collisions. In this chapter I will provide more details about our $Ba^+$-Li machine, and our strategy to reach the *s*-wave regime with this mixture.

## 2.1 Cooling Lithium

In atomic physics, the manipulation of atoms is managed in the most part using interactions between atoms and electromagnetic fields. By tuning the electromagnetic field parameters, like the intensity and the frequency, it is possible to engineer the atomic interaction hamiltonian and to exert a high level of control over the atoms motion.

Lasers constitute an exceptional tool in order to manipulate atoms: they can produce a coherent electromagnetic wave with a narrow frequency spectrum. When the mean atomic orbital dimension, typically on the order of the Bohr radius $a_0$, is much smaller than the electromagnetic wavelength $\lambda_l$, then it is possible to work in *electric dipole approximation*. Let's consider a hydrogen-like atom, i.e. an atom with only one electron in the outer shell. Then the Hamiltonian of an atom in the presence of an electromagnetic field $\vec{E}(t)$ is:

$$H_{\text{atom}} = H_0 + V_{\text{AL}} \ , \tag{2.1}$$

where $H_0$ is the unperturbed atomic hamiltonian and $V_{\text{AL}} = -\vec{d}\cdot\vec{E}(t)$, with $d = -e_0\vec{r}$ the atomic *electric dipole* and $r$ the electron position, is the electric dipole interaction hamiltonian between the laser and the atom.

In our application it is reasonable to work in the the following approximations:

1. The laser wavelength $\lambda_l$ is much bigger than the length-scale of the atomic wavefunction. In this way it is possible to treat the atom as localized and to treat the atomic position operator $\hat{\vec{R}}_{\text{a}}$ as a classical variable $\vec{R}_{\text{a}}$, by approximating it

to its mean value. In this approximation the electric field perceived by the atom will be:

$$\vec{E}(\vec{R}_{\rm a},t) = E_0\vec{\varepsilon}(\vec{R}_{\rm a})\cos\left(\omega_{\rm l}t + \xi(\vec{R}_{\rm a})\right) , \tag{2.2}$$

where $\vec{\varepsilon}(\vec{R}_{\rm a})$ is the laser electric field polarization, $\omega_{\rm l}$ is its angular frequency, $E_0$ its amplitude and $\xi(\vec{R})$ its phase.

2. If the laser's angular frequency $\omega_{\rm l}$ is such that $\omega_{\rm l} \simeq \omega_0$, where $\hbar\omega_0 = E_e - E_g$ is the energy gap between the atom ground state $|g\rangle$ of energy $E_g$ and one of its excited atomic levels $|e\rangle$ of energy $E_e$, then the hamiltonian contribution due to other excited states can be neglected and the atom can be treated as a two level system. The difference between the angular frequencies of the laser and of the atomic transition is called detuning: $\delta = \omega_{\rm l} - \omega_0$.

3. I will consider the atom stationary during the atom-light interaction. This assumption is correct if the typical timescales of the internal atomic degrees of freedom are much shorter than the evolution timescales of the external dynamics of the atom. This condition is verified if $\omega_{\rm recoil} \ll \Gamma$, where $\Gamma$ is the linewidth of the atomic transition $|g\rangle \rightarrow |e\rangle$ and $\omega_{\rm recoil} = \frac{\hbar k_l^2}{2M_{\rm atom}}$ is the recoil frequency associated with a laser with $k_{\rm l} = \frac{2\pi}{\lambda_{\rm l}}$ and an atom of mass $M_{\rm atom}$.

With all these approximations it is possible to calculate the mean atomic force that the laser exerts on the atom [84]:

$$\vec{F}_{\rm al} = -\frac{\hbar}{2}(\vec{\nabla}_{\vec{R}_{\rm a}}\Omega)U_{\rm st} + \frac{\hbar\Omega}{2}(\vec{\nabla}_{\vec{R}_{\rm a}}\xi(\vec{R}_{\rm a}))V_{\rm st} , \tag{2.3}$$

where

$$U_{\rm st} = \Omega\frac{\delta}{\frac{\Gamma^2}{4} + \delta^2 + \frac{|\Omega|^2}{4}} , \tag{2.4}$$

$$V_{\rm st} = \Omega\frac{\frac{\Gamma}{2}}{\frac{\Gamma^2}{4} + \delta^2 + \frac{|\Omega|^2}{4}} , \tag{2.5}$$

and $\Omega = \frac{e_0\vec{\mu}_{eg}\cdot\vec{\varepsilon}}{\hbar}$ is the Rabi frequency and $\vec{\mu}_{eq}$ is the dipole moment of the transition.

The first term of eq. (2.3) is called reactive force or *optical dipole force* and it arises from the non-absorptive interaction between light and atoms. The second term of eq. (2.3) is called dissipative force or *radiation pressure force*, associated with the transfer of momentum from light to atoms in a resonant scattering process [85].

### 2.1.1 The Zeeman Slower

The Zeeman Slower (ZS) is a first application of the radiation pressure force of eq. (2.3) in our experiment. The Lithium gas is created for evaporation from a solid sample in an oven at high temperature $T_{\rm Li,Oven} \simeq 650$ K for creating an adequate vapor pressure [48]. In the oven, the particles at temperature $T$ follow a Maxwell-Boltzmann distribution:

$$f_{\rm MB}(v_x,v_y,v_z) = \left(\frac{m_{\rm Li}}{2\pi k_B T}\right)^{3/2} e^{-\frac{m_{\rm Li}(v_x^2+v_y^2+v_z^2)}{2k_B T}} , \tag{2.6}$$

and their mean velocity in a certain direction, e.g. $z$-axis, is $\bar{v} \simeq 800$ m/s at $T_{\rm Li,Oven}$.

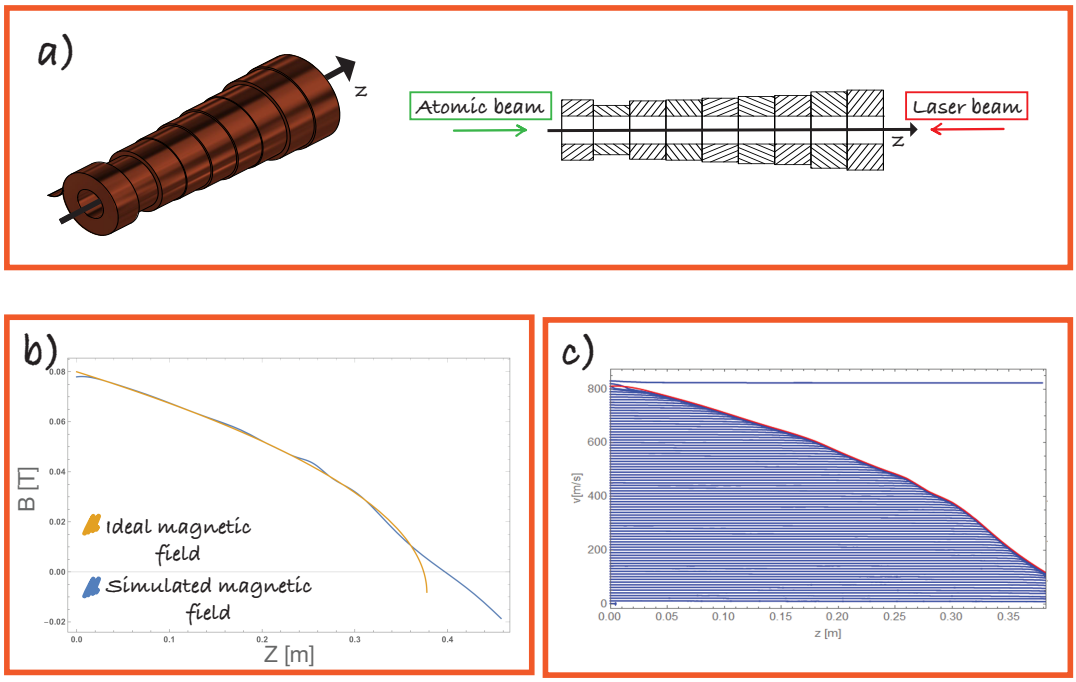


Figure 2.1: (a) Rendering of a ZS solenoid and scheme of the ZS working principle. The atoms are evaporated in an oven at $T_{\mathrm{Li,Oven}}$ and an array of nozzles (not shown) creates a first velocity selection in the directions perpendicular to the ZS symmetry axis. A proper magnetic field is generated by the solenoid. The laser beam, counter-propagating with respect to the atomic beam, decelerates the atoms along the $z$ direction. (b) Magnetic field along the ZS optical axis. In blue the theoretical magnetic field of eq. (2.9) with $\ddot{z} = \ddot{z}_{\max} = \frac{\hbar k_l \Gamma}{2m_{\mathrm{Li}}}$, where $\Gamma$ is the natural linewidth of the used atomic transition and $v_{\max} \simeq 830$ m/s. The simulated magnetic field generated by the ZS solenoid in figure (a). (c) Velocity trajectories along the $z$-axis for the simulated magnetic field in picture (b). Each blue line corresponds to a particle with a different initial velocity. Particles with velocities higher than about 800 m/s are not decelerated.

The Zeeman Slower (ZS) is an experimental apparatus to longitudinally cool a beam of atoms from hundreds of Celsius to a few Kelvin [86]. Typically, a first velocity selection is done using some micro-tubes called nozzles which select the atoms with small speed components $v_x$,$v_y$ in the directions perpendicular to the ZS optical axis $z$. The nozzle velocity selection leaves unchanged the velocity distribution along the $z$-axis. The idea of the Zeeman slower is to slow an atomic beam in one direction by exerting radiation pressure on the atoms over a large distance by compensating the reduced Doppler shift of the slowed atoms with an additional magnetic field. Then the Zeeman slower is composed by two elements: a special solenoid that creates a tailored magnetic field $B(z)$ and a laser with angular frequency $\omega_{\mathrm{l}}$, propagating along the $z$-axis (see Fig. (2.1)).

The shape of the required magnetic field can be found imposing the condition of maximum decelerating force acting on the atoms. From eq. (2.5), we know that the

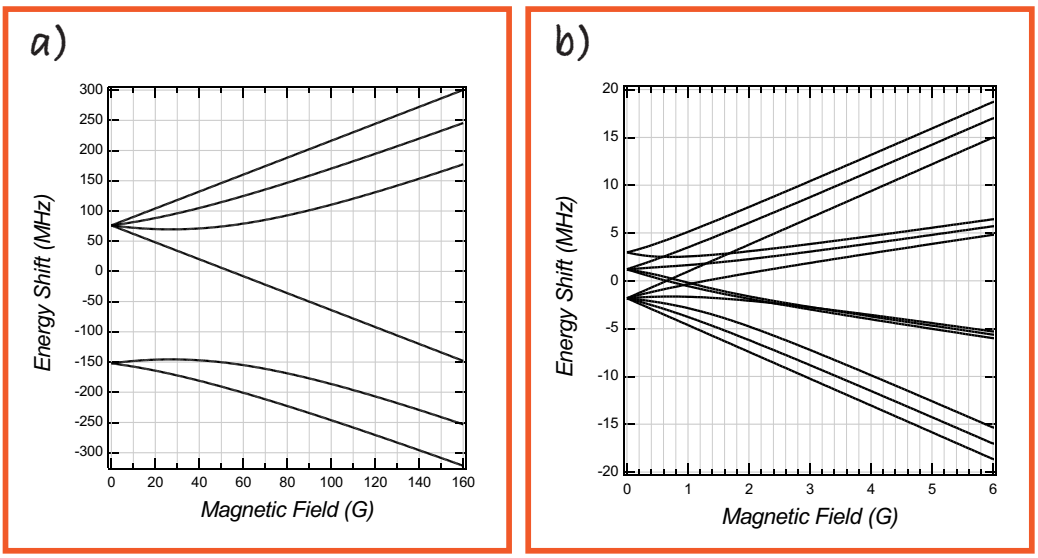


Figure 2.2: a)Magnetic-field dependence of the $2^2S_{1/2}$ ground state of $^6$Li. (b) Magnetic-field dependence of the $2^2P_{3/2}$ excited state of $^6$Li. Adapted from [48].

dissipative force has a maximum when the effective detuning $\Delta_{\text{eff}}$ is zero, with:

$$\Delta_{\text{eff}} = \omega_{\text{l}} - \omega_0 + k_{\text{l}} v - \frac{\Delta E_{\text{hs}}(B)}{\hbar} \ , \tag{2.7}$$

where $\Delta_{\text{hs}}E(B)$ is the hyperfine splitting of the cooling transition, dependent on the magnetic field, $v$ is the atom speed, and $k_{\text{l}}v$ is the Doppler shift.

For $^6$Li atoms, as shown in Fig. (2.2), both the ground state and the excited state hyperfine levels enter the high field regime, also called Paschen-Back regime, for magnetic fields larger than 100 Gauss for the ground state and larger than 3 Gauss for the excited one. In the Paschen-Back regime, the hyperfine splitting among these states can be written as $\Delta E_{\text{hs}}(B) = \Delta\mu \cdot B$, with $\Delta\mu$ a constant dependent on the Zeeman sub-levels selected for the transition.

Working in the condition for zero effective detuning, i.e. putting $\Delta_{\text{eff}} = 0$ in eq. (2.7), we obtain the expression for the magnetic field:

$$B = \frac{\hbar}{\Delta\mu}(\delta + k_l v) \ , \tag{2.8}$$

which, with the help of the kinematic formula at constant deceleration $\ddot{z}$, $v^2(z) = v_{\text{max}}^2 - 2\ddot{z}z$, gives us an expression of the form [87]:

$$B(z) = \frac{\hbar}{\Delta\mu}(\delta + k_l \sqrt{v_{\text{max}}^2 - 2\ddot{z}z}) \ , \tag{2.9}$$

where $v_{\text{max}}$ represents the maximum velocity which is slowed down by the slower. In Fig. (2.1 b) is represented the ideal parabolic magnetic field behavior of eq. (2.9). Atoms with a speed larger than $v_{\text{max}}$ will never be resonant with the laser radiation and will be lost. The atoms with $v_z \leq v_{\text{max}}$, instead, will be resonant with the laser beam in one point along the $z$-axis and, starting from there, they will be decelerated. In Fig. (2.1 c) I show an example of atoms trajectories in a ZS, calculated numerically with Wolfram Mathematica.

### 2.1.2 Optical molasses

By combining two counter-propagating, red detuned plane waves, it is possible to create a viscous force for cooling atoms [88]. The dissipative force term in eq. (2.3) can also be written, for an atom of velocity $\vec{v}$, as:

$$\vec{F}_{\mathrm{D}} = \frac{\hbar\vec{k}\Gamma}{2}\frac{s}{1+s+\frac{4(\delta-\vec{k_l}\cdot\vec{v})^2}{\Gamma^2}} \ , \tag{2.10}$$

where the parameter $s$ is defined as $s = \frac{2|\Omega|^2}{\Gamma^2} = \frac{I}{I_{\mathrm{sat}}}$ with $I_{\mathrm{sat}}$ is the *saturation intensity*.

For the same atom with velocity $\vec{v}$ illuminated by two counter-propagating laser beams at the same angular frequency $\omega_{\mathrm{l}}$, the total dissipative force at which it is subjected is:

$$\vec{F}_{\mathrm{tot}} = \frac{\hbar\vec{k}\Gamma}{2}\left(\frac{s}{1+s+\frac{4(\delta-\vec{k_{\mathrm{l}}}\cdot\vec{v})^2}{\Gamma^2}} - \frac{s}{1+s+\frac{4(\delta+\vec{k_{\mathrm{l}}}\cdot\vec{v})^2}{\Gamma^2}}\right) . \tag{2.11}$$

Working with small intensities $s \ll 1$, and expanding the eq. (2.11) for small velocities $|\vec{k_{\mathrm{l}}}\cdot\vec{v}| << \Gamma, \delta$, the total force takes the form of a viscous force:

$$\vec{F}_{\mathrm{tot}} = -\alpha_{\mathrm{mol}}\vec{v} + o(v^3) \ , \tag{2.12}$$

where

$$\alpha_{\mathrm{mol}} = -8\hbar k_{\mathrm{l}}^2 s\frac{\frac{\delta}{\Gamma}}{1+\frac{4\delta^2}{\Gamma^2}} \ , \tag{2.13}$$

is the damping factor.

However, there is a limit in how much an optical molasses can cool an atomic sample. This limit is due to the fact that, while the interaction with photons cools the atoms as a viscous force, the random recoil of the atom, due to the spontaneous emission, makes the atoms acquire a random momentum $\hbar k_{\mathrm{l}}$ and induces a heating mechanism. The limit is reached when the cooling rate is comparable to that of the spontaneous emission and the atom performs a random walk of step size $\hbar k_{\mathrm{l}}$ in momentum space. The limit temperature for an optical molasses coincides with the equilibrium between these two opposing effects, corresponding to :

$$T = \frac{\hbar\Gamma}{4k_B}\frac{1+(\frac{2\delta}{\Gamma})^2}{\frac{2|\delta|}{\Gamma}} \ , \tag{2.14}$$

which for $|\delta| = \frac{\Gamma}{2}$ has its minimum:

$$T_D = \frac{\hbar\Gamma}{2k_B} \ . \tag{2.15}$$

This limit temperature is usually called *Doppler temperature*, and in the case of $^6$Li it's on the order of 140 $\mu$K.

Mechanisms that can be used to cool an atom to a temperature lower than the Doppler cooling limit are called *sub-doppler cooling*. An example of sub-doppler cooling is the Sisyphus cooling, which can be achieved in an optical molasses in which the two counter-propagating laser beams have orthogonal polarization [89, 90].

### 2.1.3 The magneto-optical trap

Since the force in a molasses is just a viscous one, atoms cannot be trapped in it and after some time spent in the molasses they will escape from it. In order to confine the atoms one can superimpose in each spatial direction a magnetic field gradient to two counter propagating beams with opposite circular polarizations [91]. This configuration forms the so-called *Magneto-Optical trap* (MOT) and it is the most convenient method to create relatively large clouds formed by $10^8$–$10^9$ particles at cold temperatures [92].

In the one-dimensional case, the MOT configuration consists of two counter propagating red detuned laser beams with opposite circular polarization, right-handed $\sigma^+$ and left-handed $\sigma^-$, with the addition of an inhomogeneous magnetic field. The field magnitude is zero in the center of the trap and increases linearly along the direction of propagation of the beams, e.g.

$$\vec{B}(z) = \tilde{b}\vec{z}\,, \tag{2.16}$$

where $\tilde{b}$ is the magnetic field gradient. For simplicity, I will consider a scheme for an atom with ground state with total angular momentum $F = 0$ and an excited one with $F' = 1$ moving in one direction, see Fig. (2.3). The atomic levels will be affected by Zeeman shifts, the amplitude of which depends on the atoms position along $z$. As a consequence, the hyperfine energy levels of the atom will be shifted by an amount $\Delta E = \mu'\tilde{b}z$, with $\mu' = \mu_B g_{F'} m_{F'}$, $\mu_b = \frac{e_0\hbar}{2m_e}$ the Bohr magneton, $g_{F'}$ the hyperfine Landé factor and $m_{F'}$ is the projection of $F'$ on the quantization axis. As shown in Fig. (2.3), the effect of the Zeeman shift is to make resonant to the red-detuned lasers only the atoms that are moving away from the trap center, as if there were a restoring force towards the center of the trap.

By inserting the Zeeman shift in eq. (2.11) and expanding it for small $|v|$ and $z$ in $s \ll 1$ approximation, the total force can be written as [85]:

$$F_{\text{tot}} = -m_{Li}\omega_{\text{MOT}}^2 z - \alpha_{\text{mol}} v + o(z^3, v^3)\,, \tag{2.17}$$

where the parameter $\alpha_{\text{mol}}$ is defined in eq. (2.13) and:

$$\omega_{\text{MOT}}^2 = \frac{g_{F'}\mu_B\tilde{b}}{\hbar k_l m_{\text{Li}}}\alpha_{\text{mol}}\,. \tag{2.18}$$

In the case of red detuning $\delta < 0$, eq. (2.17) describes a damped harmonic oscillator motion. Furthermore, by tuning the slope of the MOT magnetic field it is possible to choose the trap radius of capture. For a fixed radius of capture $r_{\text{cap}}$, the value for the magnetic field gradient is found by imposing a resonance condition between the beam and an atom at rest at a distance $r_{\text{cap}}$ from the MOT center:

$$\tilde{b} = \frac{\hbar|\delta|}{\mu' r_{\text{cap}}}\,. \tag{2.19}$$

For a fixed radius of capture $r_{\text{cap}}$ and, consequently, for a fixed magnetic field gradient $\tilde{b}$, it is possible to demonstrate that only atoms with velocity $|v| \leq v_{\text{cap}}$ can be trapped [84]:

$$v_{\text{cap}} = \frac{\hbar^2 k_l^2}{\mu'\tilde{b}}\frac{\Gamma}{2m_{\text{Li}}}\frac{s}{1+s}\,. \tag{2.20}$$

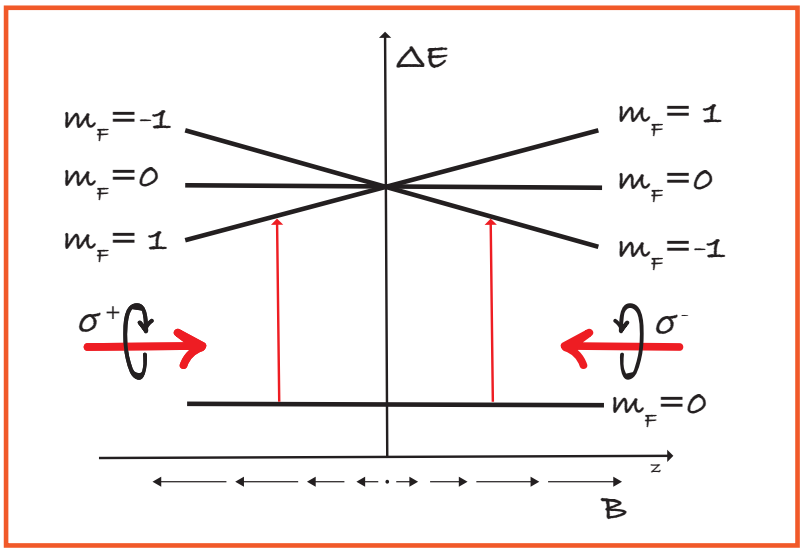


Figure 2.3: Principle of the MOT. The atoms perceive a restoring force towards the center of the trap in addition to the viscous force of a standard optical molasses. This restoring force is due to the fact that the beams circular polarization makes the atoms scatter photons from the counter propagating laser beam.

Typically the $^6Li$ MOT is implemented by using the D2 transition because it has no dark states. For instance, if we set a magnetic field gradient $\tilde{b} \simeq 25$ Gauss/cm and MOT beam intensities such that $s = 2$, then the capture velocity is around 250 m/s.

Nevertheless, it is necessary to use two laser frequencies in order to avoid dark states: the cooling laser near resonant to the $^2S_{1/2}\ F = 3/2 \rightarrow\ ^2P_{3/2}\ F' = 5/2$ transition and a repumper light acting on the $^2S_{1/2}\ F = 1/2 \rightarrow\ ^2P_{3/2}\ F' = 3/2$ transition, which depopulates the state $^2S_{1/2}\ F = 1/2$ on which atoms may decay from the excited state of the cooling transition, see Fig. (1.4). However, when the D2 line transition is used, the sub-Doppler cooling is not efficient and a temperature below the Doppler one cannot be reached. This is due to the small energy separation of the levels of the excited state, which doesn't allow to have any closed transition. The optical pumping scheme is so inefficient and consequently a typical value of the temperature in a lithium MOT is of the order of 1–2 mK, one order of magnitude larger than the Doppler limit [87].

### 2.1.4 Compressed MOT and grey molasses

In order to reduce the temperature and the size of the cloud it is possible to create a so-called *compressed MOT* stage (CMOT). In the CMOT the repumper intensity is reduced with respect to the optimal MOT operation, typically around 1–2% of the initial value. At the same time the gradient of the MOT magnetic field is increased. After a short period of time, all the atoms spend most of the time into the $^2S_{1/2}\ F = 1/2$ state and so the scattering of photons from the cooling beams is reduced. In this way also the heating effect is reduced. The CMOT stage optimizes the compression and the cooling of a cloud that is first loaded into a MOT, but it works for a limited amount of time, since eventually the atoms will escape from the trap because the

poor interaction with light significantly increases the rate of loss of atoms. In other experiments with $^6$Li temperatures on the order of 300 $\mu$K were observed at the end of a CMOT phase [87].

After a CMOT phase, atoms are typically transferred into a trapping potential, e.g. magnetic or optic, that does not use light scattering for its operation. Before doing so, it is common to perform a short stage of optical molasses without magnetic field, optimized to lower as much as possible the atoms temperature by using laser cooling [84].

In a standard optical molasses the main problem that prevents to reach the Doppler temperature limit is that the atoms are trapped in states that do not prevent their mutual interaction. The fact that trapped atoms emit a lot of spontaneous photons that can be reabsorbed by other atoms can lead to a repulsive force and a heating effect on the sample. On the other hand, atoms in a dark state do not interact with light at all and cooling them using interactions with light will be impossible. The solution is to use a weakly interacting state with light, a so-called gray state for which the light interaction is present but the probability of absorbing a scattered photon is significantly lower. This cooling technique is called *gray molasses* [93, 94].

For $^6$Li atoms the gray-molasses cooling was experimentally proved using the D1 transition [95]. This method is based on the combined effect of a standard gray molasses, working on the D1 ($2S_{1/2} \rightarrow 2P_{1/2}$) transition, and velocity-selective coherent population trapping [96] in a $\Lambda$-type three-level system. Following the experimental procedure described in [95] it is possible to obtain a sample of about $7 \times 10^5$ atoms at temperature of about 40 $\mu$K, far below the Doppler temperature.

### 2.1.5 Evaporative cooling

After having cooled and compressed the atomic sample using CMOT and gray-molasses, the atoms can be confined in a magnetic or optical trap, and all near-resonant laser fields are turned off. In the following, I will discuss the principle of operation of an optical dipole trap, since this is the trapping potential that we are going to use in our experiment.

*Optical dipole traps* rely on the electric dipole interaction with far-detuned light and they have trap depths typically in the range of the millikelvin. In these traps the atoms are spatially confined by the optical dipole force of eq. (2.3), which can be written as [27]:

$$\vec{F}_{\mathrm{dip}}(\vec{r}) = \vec{\nabla} U_{\mathrm{dip}}(\vec{r}) \ , \tag{2.21}$$

where

$$U_{\mathrm{dip}}(\vec{r}) = \frac{\hbar\delta}{2} \log\left(1 + \frac{\frac{\Omega^2}{2}}{\delta^2 + \frac{\Gamma^2}{4}}\right) . \tag{2.22}$$

In far-detuning approximation, i.e. when $\delta \gg \Gamma, |\Omega|$, the dipole potential is directly proportional to the laser intensity $I$

$$U_{\mathrm{dip}}(\vec{r}) = -\frac{1}{2\epsilon_0 c}\mathrm{Re}(\alpha_{\mathrm{p}})I = \frac{\hbar\Omega^2}{4\delta} \ , \tag{2.23}$$

where $\alpha_{\mathrm{p}}$ is the so-called *atomic polarizability* [27]. It follows that for red-detuned laser beams the atoms will be attracted to a maximum of the laser intensity $I(\vec{r})$, instead for blue-detuned lasers they will be attracted to the minimum intensity. As a

result, a single gaussian beam works as a trap for the atoms only if it is red detuned with respect to the main transitions.

The temperature of the atoms in a dipole trap can be efficiently reduced by performing the so-called evaporative cooling. Evaporative cooling, originally proved with magnetically trapped hydrogen [97], relies on the selective removal of high-energetic particles from the trap and subsequent thermalization of the remaining particles through elastic collisions [92]. At low collisional energies, elastic collisions can be parametrized with only one single parameter, the scattering length $a_s$, and the cross section takes the form of eq. (1.10).

The evaporative cooling technique allows to reach the fermionic degeneracy for the atoms [98]. The evaporative cooling timescale is inversely proportional to the collisional rate $\Gamma_{\mathrm{col}}$. The collisional rate is proportional to the cross-section $\sigma_{\mathrm{el}}$, see Sec. [1.2]. At zero magnetic field the collisional rate is not sufficiently high to perform an efficient evaporative cooling for $^6$Li in reasonable times. Feshbach resonances must be used in order to enhance the scattering cross-section and to implement an efficient evaporative cooling [48, 99].

## 2.2 The Paul trap

The Paul trap is a standard experimental method to trap ions, widely used in the atomic physics community in experiments with atomic ions, molecular ions, and even mesoscopic objects [100]. A Paul trap can have trap depths on the orders of thousands of Kelvin and, for this reasons, charged particles can be trapped almost indefinitely in time. The Paul trap is the easiest method to trap a charged particle, and in all the atom-ion experiments reported so far the ion was trapped in a Paul trap.

### 2.2.1 Paul trap working principle

The Earnshaw theorem states that it is not possible to maintain in stationary equilibrium charged particles by using an arrangement of purely static electric fields [101]. A possible way out is to use oscillating fields, e.g. radiofrequencies (RF), in addition to static DC fields to create a confining potential. This is the principle of the RF trap (or Paul trap).

Let's consider an electric potential created by the combination of an RF and a DC quadrupole potential:

$$\begin{aligned}\Phi_{\mathrm{tot}}(\vec{r},t) &= \Phi_{\mathrm{RF}}(\vec{r},t) + \Phi_{\mathrm{DC}}(\vec{r}) \\ &= \Phi_{\mathrm{RF}}(\alpha x^2 + \beta y^2 + \gamma z^2)\cos(\omega_{\mathrm{RF}} t) + \Phi_{\mathrm{DC}}(\alpha' x^2 + \beta' y^2 + \gamma' z^2)\ ,\end{aligned} \tag{2.24}$$

where $\omega_{\mathrm{RF}}$ is the RF frequency and the sets of real coefficients $(\alpha,\beta,\gamma)$ and $(\alpha',\beta',\gamma')$ must satisfy the Laplace equations $\nabla^2\Phi_{\mathrm{RF}}(\vec{r},t)=0$ and $\nabla^2\Phi_{\mathrm{DC}}(\vec{r})=0$ [103].

Of the possible sets of values for the parameters $(\alpha,\beta,\gamma)$ and $(\alpha',\beta',\gamma')$, let's consider the case of $\alpha=-\beta$, $\gamma=0$ and $\alpha'+\beta'=-\gamma'$. This configuration is the one of the so-called linear Paul trap (see Fig. (2.4)) in which the radiofrequency is provided by linear rods parallel to the z-axis, so that in principle there is at the center of the trap no RF field along $z$. The DC fields are provided by additional electrodes (called *endcaps*) that can be placed, for instance, along $z$. The full potential of eq. (2.24) can

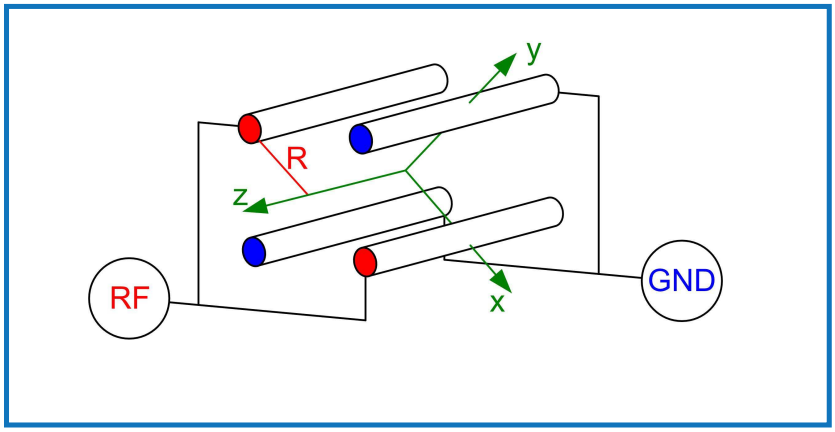


Figure 2.4: Schematic configuration of the trap electrodes. Four parallel rods define an electric field with a dominating quadrupole term in the centre of the trap. Two opposing rods are on an oscillating electric potential (RF) the other two on ground (GND). The distance from the centre of the trap to the surface of an electrode is R. Adapted from [102].

be written as [103]:

$$\Phi_{\text{tot}}(\vec{r},t) = \frac{\phi_{\text{RF}}}{2}\frac{\kappa_{\text{RF}}}{R_{\text{RF}}^2}(x^2-y^2)\cos(\omega_{\text{RF}}t) + \frac{\phi_{\text{DC}}}{2}\frac{\kappa_{\text{DC}}}{R_{\text{DC}}^2}(2z^2-x^2-y^2)\ , \tag{2.25}$$

where $\phi_{\text{RF}}$ is the RF amplitude, $\phi_{\text{DC}}$ is the potential applied on the endcaps, $R_{\text{RF}}$ and $R_{\text{DC}}$ are respectively the distances of the RF and DC electrodes from the trap center, and $\kappa_{\text{RF}}$ and $\kappa_{\text{DC}}$ are trap geometrical factors.

A classical electrode configuration of a linear Paul trap consists in setting two opposite electrodes on an RF-voltage and the other two electrodes on ground. The simplicity of this configuration arises because only one RF signal is needed. However, another configuration might be preferable: with respect to Fig. (2.4), the electrodes connected to ground can instead be connected to another RF-potential, equal in frequency and amplitude but with a phase shift of $\pi$ relative to the first RF-potential. The electric potential of eq. (2.25) remains unchanged if we redefine the RF amplitude $\phi_{\text{RF}}$ as peak-to-peak voltage, with an overall gain of a factor of two in the potential depth [104].

### 2.2.2 Kinematics of ions in a Paul trap

For an ion with positive charge $e_0$, the electric force acting on it is $\vec{F}_{\text{ion}} = -e_0\vec{\nabla}\Phi_{\text{tot}}(\vec{r},t)$. In the specific case of the potential of eq. (2.25), the equation of motion for an ion with mass $m_{Ba}$ reduces to a system of differential equations [7]:

$$\frac{d^2x}{d\tau^2} - (a - 2q\cos(2\tau))x = 0\ , \tag{2.26}$$

$$\frac{d^2y}{d\tau^2} - (a + 2q\cos(2\tau))y = 0\ , \tag{2.27}$$

$$\frac{d^2z}{d\tau^2} + 2az = 0\ , \tag{2.28}$$

where $\tau = \frac{1}{2}\omega_{\mathrm{RF}}t$ and the parameters $a$ and $q$ are defined as:

$$a = \frac{4e_0\phi_{\mathrm{DC}}\kappa_{\mathrm{DC}}}{m_{Ba}\omega_{\mathrm{RF}}^2 R_{\mathrm{DC}}^2} \ , \tag{2.29}$$

$$q = \frac{2e_0\phi_{\mathrm{RF}}\kappa_{\mathrm{RF}}}{m_{Ba}\omega_{\mathrm{RF}}^2 R_{\mathrm{RF}}^2} \ . \tag{2.30}$$

Eq.s (2.26), and (2.27) have the canonical form of Mathieu equations, which can be solved via the Floquet theorem [7]. This yields the following general solutions for the coordinates to the lowest order in the adiabatic approximation $a, q \ll \omega_{RF}$:

$$x(t) = [C_x \cos(\Omega_t t) + S_x \sin(\Omega_t t)](1 - \frac{q}{2}\cos(\omega_{\mathrm{RF}}t)) \ , \tag{2.31}$$

$$y(t) = [C_y \cos(\Omega_t t) + S_y \sin(\Omega_t t)](1 + \frac{q}{2}\cos(\omega_{\mathrm{RF}}t)) \ , \tag{2.32}$$

$$z(t) = [C_z \cos(\omega_z t) + S_z \sin(\omega_z t)] \ , \tag{2.33}$$

with the constants of integration denoted by $C_j$ and $S_j$, $j = \{x, y, z\}$. Along the $z$-direction the ion motion is purely harmonic, with angular frequency $\omega_z = \sqrt{2a}$, since there is no radio-frequency field in this direction. In the transverse $xy$-plane, instead, the ion motion shows two components: the first term is the so-called *secular motion* with a slow frequency of $\Omega_t = \frac{\omega_{\mathrm{RF}}}{2}\sqrt{a + \frac{q^2}{2}}$ and the second term, that is a fast oscillating component called *micromotion*, at RF field frequency $\omega_{\mathrm{RF}}$.

### The stability zones

Mathieu equations have two types of solution [103]:

1. *Stable motion*: the particles oscillate in the $x$-$y$ plane with limited amplitude.
2. *Unstable motion*: the amplitude grows exponentially in $x$, $y$ or in both directions. The particles will be lost.

Whether stability exists depends only on the parameters $a$ and $q$ and not on the initial parameters of the ion motion, e.g. its initial velocity and position. Therefore, it is possible to delineate an area in the $a$-$q$ space for which the ions experience a stable motion or, vice versa, get accelerated out of the trap. The stable region that contains the origin $(a, q) = (0, 0)$ is often called the *lowest stability region* and it is typically the region in which most of the experimental Paul traps work.

As it is shown in eq.s (2.29) and (2.30), the parameters $a$ and $q$ depend on the trap geometry, on the RF and DC voltages that are applied on the electrodes, and on the ion mass. Once the ion is set (in our case atomic mass is 138) and the design of the electrodes is decided, it is possible to biunivocally map the $a$-$q$ stability diagram in an equivalent graph with $\phi_{\mathrm{DC}}$ and $\phi_{\mathrm{RF}}$ as independent variables, this graph for our trap is shown in Fig. (4.3).

### Trajectory of an ion

An example of the dynamics of the ion moving following the eq.s (2.31,2.32, 2.33) is shown in Fig. (2.5). The ion motion is characterized by the "slow" secular motion at frequency $\Omega_t$ and its micromotion at $\omega_{\mathrm{RF}}$. In many applications the role of micromotion can be ignored and only the ion secular motion is taken into consideration. In this

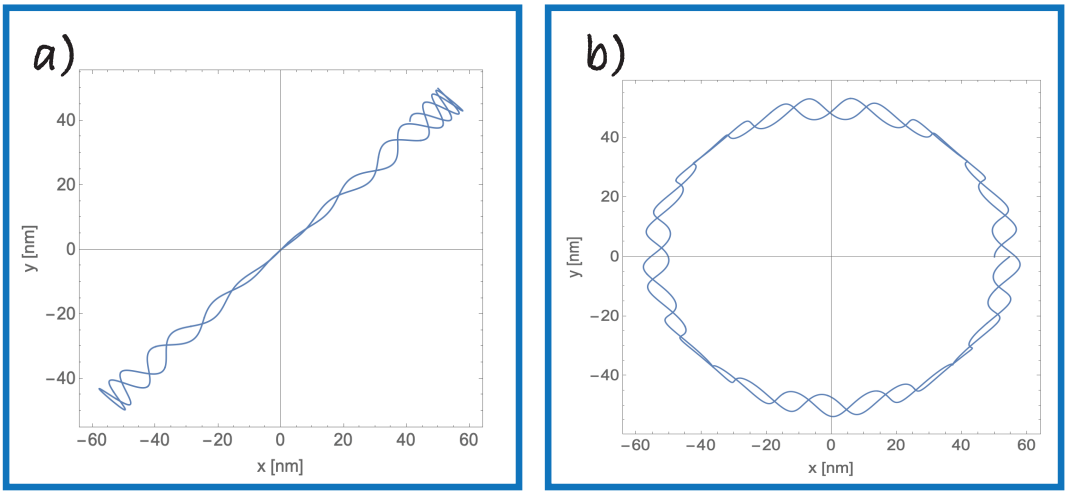


Figure 2.5: Example of trajectories in a Paul trap for an ion of mass $m_{Ba}$. The trap parameters used in these plot are: $\omega_{\mathrm{RF}} = 2\pi \times 3.5$ MHz, $\kappa_{\mathrm{RF}} = \kappa_{\mathrm{DC}} = 1$, $R_{\mathrm{RF}} = R_{\mathrm{DC}} = 2.0$ mm, $\phi_{\mathrm{RF}} = 200$ V, and $\phi_{DC} = 4.5$ V. These values generate $a$ and $q$ parameters similar of those of our experimental trap. (a) Trajectory for an ion starting with zero initial velocity at position $\vec{r} = (50, 50, 0)$ nm. (b) Trajectory of an ion starting with initial velocity $\vec{v}(t = 0) = (0, 0.08, 0)$ m/s at position $\vec{r} = (50, 0, 0)$ nm.

case the ion is considered as moving in a harmonic potential with angular frequency $\Omega_t$ [7]. However, in the most general case, micromotion has to be considered for a complete treatment of the ion motion.

The derivation of the eq.s (2.31)-(2.33) for the ion motion is purely classical. In this case, there is no lower limit to the kinetic energy of a trapped ion: it can, in principle, be cooled down to zero motion.

However, micromotion is an intrinsic and ineradicable effect of the trapping process with an RF electric field: a quantum mechanical analysis of the ions' motion shows that the dispersion of the wave-packet leads to a minimum micromotion amplitude. The minimum energy associated with this motion corresponds to [22]:

$$E_{\mathrm{min},j} = \frac{\hbar\Omega_t}{4} \tag{2.34}$$

with $j = \{x, y\}$ is called *micromotion quantum limit*.

Other additional contributions to the micromotion are called *excess micromotion* and they are [105]:

1. *In-phase excess micromotion*: it occurs when the center of the pseudopotential and of the RF quadrupole field do not coincide. Let's suppose that in the centre of the trap there is an electric field $\vec{\varepsilon}_{\mathrm{emm}} = (\varepsilon_{\mathrm{emm}}, 0, 0)$; this field displaces the ion equilibrium position from the centre of the trap. This leads to an increase of the average ion kinetic energy equal to $E_{\mathrm{emm}} = \frac{e_0^2 q^2 \varepsilon_{\mathrm{emm}}^2}{16 m_{Ba} \omega_{\mathrm{RF}}^2 (a + \frac{q^2}{2})^2}$. For our trap values, for instance, it is sufficient that $\varepsilon_{\mathrm{emm}} \simeq \pm 0.2$ V/m to obtain an in-phase excess micromotion equal to the micromotion quantum limit of eq. (2.34).

2. *Axial micromotion*: If the electrodes of the linear Paul trap are not exactly symmetric, then $\gamma \neq 0$ in eq. (2.24). This adds a contribution of the RF field in

the $z$-direction, leading to a correction to the micromotion quantum limit, which becomes: $E_{\min,z} = \frac{\hbar e_0 \phi_{\mathrm{RF}} \gamma}{4 m_{Ba}} \sqrt{\frac{1}{2}(1 + \frac{2 m_{Ba} \omega_{\mathrm{RF}}^2}{e_0} \frac{\phi_{\mathrm{DC}} \gamma'}{\phi_{\mathrm{RF}}^2 \gamma^2})}$. In our trap configuration $\gamma \simeq 0$ m$^{-2}$ from simulation (see Tab. (4.2)): a factor $\gamma$ of approx. $3.3 \times 10^5$ m$^{-2}$ is necessary to have a contribution from the axial micromotion $E_{\min,z}$ equal to that of radial micromotion of eq. (2.34).

3. *Out-of-phase excess micromotion*: Excess micromotion can also be caused by a phase difference $\varphi_{\mathrm{emm}}$ between the RF electrodes that are supposed to be in phase. A phase mismatch may originate from differences in impedance of the electrodes and their electric connections to the RF source, or from length differences in the wiring between the radio-frequency electrodes and the RF sources. The immediate effect of this phase difference is to make time-dependent the position of the zero-field line. At the first order of approximation in $\varphi_{\mathrm{emm}}$ this phenomenon gives an average energy contribution of $E_{\mathrm{pmm},i} = \frac{1}{64} m_{Ba} (q R_{\mathrm{RF}} \varphi_{\mathrm{emm}} \Omega_t)^2$. In our trap geometry, explained in detail in Chapter 4, it is necessary a phase difference $\varphi_{\mathrm{emm}} \simeq 0.013°$ to obtain an $E_{\mathrm{pmm},i}$ value equal to the quantum limit of eq. (2.34).

Excess micromotion can be prevented or minimized toward the micromotion quantum limit. To prevent excess micromotion, in particular axial and out-of-phase micromotion, it is sufficient to take particular care in designing and assembling the Paul trap [106]. For instance, it is important to ensure a symmetrical arrangement of both the electrodes and the wiring in their proximity in order to prevent contributions to the micromotion.

Micromotion can be detected with several experimental methods, for example by detecting the ion position with a high numerical aperture objective [83], or by observing the ion spectral composition of the absorbed excitation lasers [105], or by exerting a parametric excitation of the secular ion motion [107] or, in an atom-ion hybrid system, by monitoring atom losses [108]. Once the micromotion is characterized it can be minimized by applying extra DC or RF fields: for this reason, in the trap design it is important to include additional electrodes and/or bias tee for adding compensating fields.

## 2.3 Atom-ion collisions in the presence of micromotion

Thermodynamics principles affirm that two separate, interacting objects in thermal contact tend to the same temperature, i.e. to the thermodynamic equilibrium. This concept is exploited in atomic physics, e.g. in sympathetic cooling, in which two different atomic species are made interact to each other [109].

However, an ion trapped in a Paul trap with a quantum gas do not reach a thermodynamic equilibrium [21, 110]. This evidence strongly differs from what observed in atomic mixtures, and it is due to the presence of the RF field in the atom-ion mixture.

Let's consider a particle confined in a one-dimensional static trap of angular frequency $\omega_{\mathrm{h.a.}}$ having position $\bar{x}$ and velocity $v$ at time $t'$. Let's suppose that at the same time $t'$ the particle collides instantaneously with a much colder particle of the same mass. After a billiard-ball collision the velocity of the particle can be assumed to be zero: $v(t') = 0$. Then, the trapped particle undergoes a new trajectory

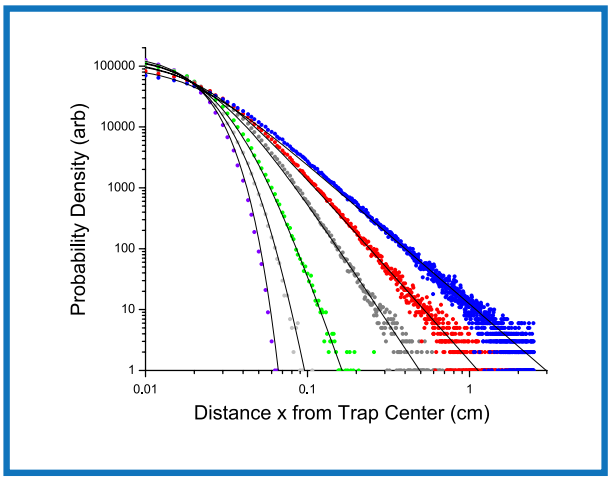


Figure 2.6: $^{136}Ba^{+}$ ion cooled by six different buffer gases at 300 K with mass $m_B = 4, 40, 84, 136, 170$ and 200 amu from left to right, corresponding to the noble gases He, Ar, Kr, Xe and to two hypothetical heavier gases. Note the evolution from Gaussian to power law (straight line) as the mass increases. The solid lines are Tsallis functions of eq. (2.35) with fixed $\sigma_{ai} = 0.0815$ cm and decreasing $n_{ai}$ from $n_{ai} \geq 60$ for He to $n_{ai} = 1.15$ for the buffer gas with the element with $m_B = 200$. Adapted from [112].

$r(t) = \bar{x}\cos(\omega_{h.a.}t)$ and the collision will always reduce the total energy of the atom confined in the trap.

Let's consider now the same example, but with an ion confined in a Paul trap. The condition $v(t') = 0$ can be realized by imposing $v_{sec} = -v_{mm}$, where $v_{sec}$ is the secular velocity and $v_{mm}$ is the instantaneous micromotion related velocity. Therefore, the ion would begin a trajectory in the secular potential with an initial velocity $v_{mm}$, which can correspond to a larger energy [111].

Apart from this intuitive description, the dynamics of an ion in a Paul trap and immersed in a buffer gas has been studied by different groups [44, 110, 112]. By considering the case in which trapped ions interact with a buffer gas at finite temperature via hard-core collisions, it was shown that the ions should develop non-Gaussian distributions with power-law tails that fits well with a Tsallis distribution. The Tsallis function is:

$$T_{Tsallis}(x_p/\sigma_{ai}, n_{ai}) = \frac{T_0}{[1 + (x_p/\sigma_{ai})^2/n_{ai}]^{n_{ai}}} , \tag{2.35}$$

where $x_p$ is the distance of the ion from the trap center, $T_0$ is the normalization parameter and $\sigma_{ai}$ and $n_{ai}$ parameters of the distribution depending on the atom-ion mass ratio [112]. For $n_{ai} \to +\infty$, $T_{Tsallis}$ reduces to a Gaussian, while for small $n_{ai}$ it has power-law tails of the form $(x_p/\sigma_{ai})^{-2n_{ai}}$. In Fig. (2.6) it is shown the probability density of finding an ion at a given distance from the trap center after a Monte-Carlo simulation with $10^6$ trials for ensemble that reproduce 500–50000 collisions each, calculated in Ref [112].

Following the results of Ref. [112], an analytical model that predicts the steady-state distribution of the kinetic energy of a single ion immersed in a neutral buffer gas was developed in Ref. [111]. By defining $\tilde{m}$ as the ratio between the neutral atom mass and that of the ion, it is possible to define a critical mass ratio $\tilde{m}_c$, the value of which

depends on the trap parameters, for which if $\tilde{m} \ll \tilde{m}_c$ the ion is efficiently cooled, while if $\tilde{m} \geq \tilde{m}_c$ the ion heats up until it becomes too energetic to be trapped, regardless of the temperature of the buffer gas. Ref. [32] showed that for very elongated Paul traps $\tilde{m}_c = 2.17$.

Also in the best possible scenario in which the neutral buffer is a degenerate quantum gas, the ion is optically cooled to its motional ground state and the micromotion is well compensated, it is possible to still have a strong heating mechanism due to the RF [24]. This phenomenon is related with the $1/R^4$ long-range nature of the atom-ion interaction: as the atom approaches the ion, it "pulls" the ion out of the trap center and the collision occurs at the center of mass of the two particles, which do not coincide with the Paul trap center [25]. The heating mechanism can be mitigated if $\tilde{m} \ll \tilde{m}_c$, since the center of mass in the atom-ion collision is closer to the RF trap center. Therefore, the best candidates for reaching the $s$-wave regime are mixtures with a strong mass imbalance, as $Yb^+$-Li [25] and $Ba^+$-Li.

## 2.4 The Electro-Optical trap (EOT)

An atom-ion quantum system in which the ion is trapped in a Paul trap is, even in the most favourable conditions, an energetically open system. The coupling with the RF field makes it particularly challenging to reach ultra-low temperatures and the $s$-wave regime in atom-ion collisions.

In order to avoid RF coupling of energy in the atom-ion system, the simplest method is to eliminate the presence of the RF field itself. A possible approach is to use an optical dipolar trap, see Sec. [2.1.5], which provides a conservative and static potential.

In recent years, three-dimensional optical trapping of ions in optical tweezers and optical lattices has been demonstrated [113, 114]. However, optical dipolar traps are typically much weaker than a Paul trap, and laser cooling is challenging since the light used for the trap may shift the energy levels of the cooling transition. As a result, even if there has been an improvement over the years of orders of magnitude in the ions' lifetime in an optical trap, this is still limited to a few seconds [115].

### 2.4.1 Working principle of the EOT

The Earnshaw theorem states that it's not possible to trap ions using static electric potential in all the three spatial dimensions. However, the problem can be circumvented by superimposing to an electrical quadrupole static potential a trapping potential of different nature, e.g. an optical potential, along the untrapping direction of the electrical quadrupole.

This is the trap that we chose for our experiment: an electro-optical trap (EOT) formed by a static electric quadrupole and an optical lattice.

The idea is to use an electric quadrupole that provides a trapping potential in two directions, and an optical lattice that confines the particles in the third direction, where the electric potential is anti-trapping. If the optical lattice is deep enough to counteract the untrapping potential of the electrical quadrupole, then the ions will be trapped in all three dimensions with a static potential and they will not experience any micromotion.

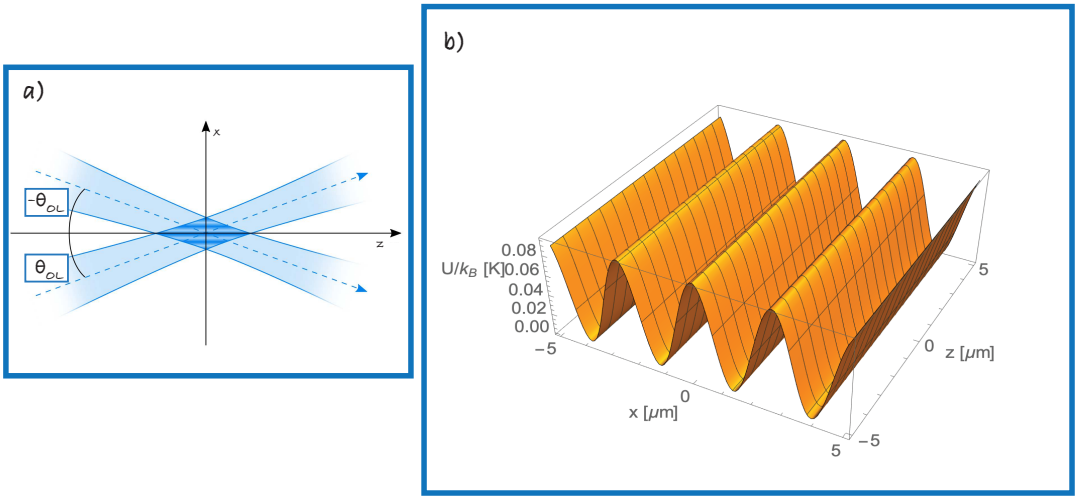


Figure 2.7: (a) Sketch of two focused gaussian beams that cross at angle $2\theta_{\mathrm{OL}}$ and give rise to an interference pattern along the x axis. Adapted from [116]. (b) Optical lattice potential rescaled by the Boltzmann's constant $k_B$ in plane $y = 0$.

The optical lattice is created by the interference of two laser beams. If two laser beams of wavelength $\lambda_M$ cross each other at an angle $2\theta_{\mathrm{OL}}$ as shown in Fig. (2.7 a), the optical lattice originating from the interference will have a lattice constant:

$$d_{\mathrm{OL}} = \frac{\lambda_M}{2\sin(\theta_{\mathrm{OL}})} \ . \tag{2.36}$$

The generic expression of the electric field of a circular gaussian beam with waist $w_0$ in the origin of the reference frame, traveling along the z direction, can be written as [117]:

$$\vec{E}(x,y,z) = \vec{\varepsilon} E_0 \frac{w_0}{w(z)} e^{-(x^2+y^2)/w(z)^2} e^{-ikz} e^{-ik(x^2+y^2)/2R(z)} e^{i\zeta(z)} e^{i\phi_g} \ , \tag{2.37}$$

where $\vec{\varepsilon}$ is the unitary polarization vector, $E_0$ is the field amplitude, $k = 2\pi/\lambda$ is the wave vector, $\phi_g$ is a generic phase, $z_R = \frac{\pi w_0^2}{\lambda}$ is the Rayleigh length, $\zeta(z) = \arctan(z/z_R)$ is the so-called Gouy phase, and $R(z)$ and $w(z)$ are, respectively, the radius of curvature and the radius of the beam:

$$R(z) = z\left(1 + \frac{z_R^2}{z^2}\right) \ , \tag{2.38}$$

$$w(z) = w_0 \sqrt{\left(1 + \left(\frac{z}{z_R}\right)^2\right)} \ . \tag{2.39}$$

In the paraxial approximation, $z \ll z_R$, eq. (2.37) can be approximated to:

$$\vec{E}(x,y,z) = \vec{\varepsilon} E_0 (1 - \frac{z^2}{2z_R^2}) e^{-(x^2+y^2)/w_0} e^{-ikz} e^{iz/z_R} e^{i\phi_g} \ . \tag{2.40}$$

In order to obtain the total intensity profile of the optical lattice it is sufficient to rotate the coordinates around the $y$-axis of an angle $\theta_{\mathrm{OL}}$ for the first beam $\vec{E}_1$ and of

an angle $-\theta_{OL}$ for the second beam $\vec{E_2}$:

$$I(x,y,z,\theta_{OL}) = \frac{1}{2}c\varepsilon_0|\vec{E_1}+\vec{E_2}|^2 \ , \tag{2.41}$$

where $c$ is the speed of light. Under the assumption that the two beams have the same intensity and polarization, the intensity profile is (see Fig. (2.7 b):

$$\begin{aligned} I(x,y,z,\theta_{OL}) = I_0 \exp\left(-2\frac{y^2}{w_0^2}\right)\exp\left(-2\frac{\cos^2(\theta_{\rm OL})x^2+\sin^2(\theta_{\rm OL})z^2}{w_0^2}\right) \\ \left[\left(2\cosh\left(\frac{2\sin(2\theta_{\rm OL})xz}{w_0^2}\right)+2\cos\left(2\sin(\theta_{\rm OL})(k-1/z_R)x\right)\right)\times \right. \\ \left.\left(1-\frac{\cos^2(\theta_{\rm OL})z^2+\sin^2(\theta_{\rm OL})x^2}{z_R^2}\right)-\frac{\sin(2\theta_{\rm OL})xz}{2z_R^2}\sinh\left(\frac{2\sin(2\theta_{\rm OL})xz}{w_0^2}\right)\right] \end{aligned} \tag{2.42}$$

where

$$I_0 = \frac{2P_c}{\pi w_0^2} \tag{2.43}$$

and $P_c$ the power of each laser beam.

The full potential created in the electro-optical trap is the combination of the field of eq. (2.42) and an electric quadrupole:

$$\phi_{\rm EOT} = {\rm Re}(\alpha_p)I(x,y,z,\theta_{OL}) + \frac{\kappa_{\rm EOT}e_0\phi_{EOT}}{2R_{\rm EOT}^2}(2x^2-y^2-z^2) \ , \tag{2.44}$$

where atomic polarizability is a function of the wavelength $\lambda_{\rm M}$ of the interfering beams: $\alpha_{\rm p} = \alpha_{\rm p}(\lambda_{\rm M})$. The intensity profile of eq. (2.42) is directly proportional to $P_{\rm c}$ and so the optical potential of eq. (2.44). In order to enhance as much as possible the trap depth it is convenient to create the optical lattice using an optical resonating cavity [117]. The optical resonating cavity used in our experimental setup is a bow-tie cavity, described in Sec. [4.2.2].

### 2.4.2 The magic wavelength

There are several aspects that we considered in choosing the laser frequency for the optical potential in the EOT. If one wants to trap more than one ion, the electrostatic repulsion between the ions sets the energy scale for the dipolar potential, which, therefore, must be as deep as possible. In selecting the laser wavelength to generate the EOT potential, an opportune laser frequency corresponding to a high value of the atomic polarizability should be chosen. Moreover, in order to reduce the heating mechanism of off-resonant scattering from the trapping beams, it is convenient to select a blue-detuned laser with respect to the $6^2S_{1/2} \rightarrow 6^2P_{1/2}$ transition of $Ba^+$, since the ions will arrange in the minima of light. Furthermore, in order to cool the ions both during the trap loading processes and when the EOT is on, the trapping laser frequency should be a "magic wavelength" for the $Ba^+$ cooling transition. A magic wavelength is a laser wavelength that causes the same energy shift for ac Stark effect for two atomic levels of interest. If we use for the optical lattice a magic wavelength for the cooling transition, the detuning of the cooling laser will be the same with or without the optical lattice and it will be possible to cool the ions in the EOT. A wavelength with all these features is $\lambda_{\rm M} = 451.762$ nm with an atomic polarizability of ${\rm Re}(\alpha_{\rm p}) = -4460$ a.u [118].

For the neutral Lithium in the ground state $S_{1/2}$ the atomic polarizability is approx. $-133$ a.u. [119]: the optical lattice created with lasers at $\lambda_M$ is blue-detuned for the Lithium too. Consequently it would be possible to trap either the Barium ions and the Lithium neutral atoms in the same light minima of the optical lattice at $\lambda_M$.

In terms of geometry, the simplest way to realize a 1D optical potential is to retro-reflect a laser beam with a mirror, i.e. to choose $\theta_{OL} = \frac{\pi}{2}$. However, in this configuration, the distance between two neighbour minima of the EOT potential is $\lambda_M/2 \simeq 226$ nm (see eq. (2.36)). This value is particularly small, and it would make it very challenging to load the ions in only one minimum of the potential. By choosing an angle $\theta_{OL}$ smaller than $\frac{\pi}{2}$ it is possible to increase the lattice constant; e.g. for $\theta_{OL} \simeq 5°$ we obtain $d \simeq 2.6$ $\mu$m, a value that is one order larger than in the counter-propagating geometry.

## 2.5 The $Ba^+$-Li experiment

Realizing a hybrid quantum system requires the separate realization of the two composing quantum systems, which must then be confined in the same physical location. For this reason the experimental implementation of these kind of systems is, in general, more complex than realizing a single quantum system.

The strategy we have decided to adopt consists of creating quantum gases and trapped ions first in two separate vacuum chambers, and only in a second time to make them interact in one place. This allows us to separate the complexity in the realization of the two quantum systems by taking them one at a time.

In this chapter we have described the techniques that we plan to use for trapping and cooling both neutral atoms and ions. In the next two chapters I will present the strategy for the experimental implementation of the methods, and provide all the details on the parts of the experimental apparatus that have been realized in this thesis. The purpose of this section is to provide an overview of the experimental apparatus that is currently under development and to introduce the general strategy we intend pursue for realizing an ultracold atom-ion mixture.

Fig. (2.8) shows a schematic rendering of the experimental apparatus of the Ba-Li experiment. The vacuum system is formed by two chambers connected through a valve. The Lithium chamber, described in Chapter 3, will be used to create quantum gases of Lithium atoms, starting from hot vapours originating from an oven, then cooled in a Zeeman slower. The Zeeman slower ends at the Lithium chamber, where the atoms will be accumulated in a MOT. Then, following a CMOT and a gray molasses phase, we will transfer the atoms into an optical potential for some evaporative cooling. Finally, the atoms will be transported into the chamber with the ion trap by moving the optical potential. The Barium chamber, described in Chapter 4, will host the ovens for the Barium, a Paul trap, an electro-optical trap with a bow-tie cavity to enhance the depth of the optical potential, and a high numerical aperture objective for the detection of the atom-ion mixture. The role of the Paul trap is to trap the hot ions produced by photoionization of hot Barium atoms originating from the ovens. The ions will be then transferred into the EOT before the atoms enter into the ion trap and start interacting with the ions.

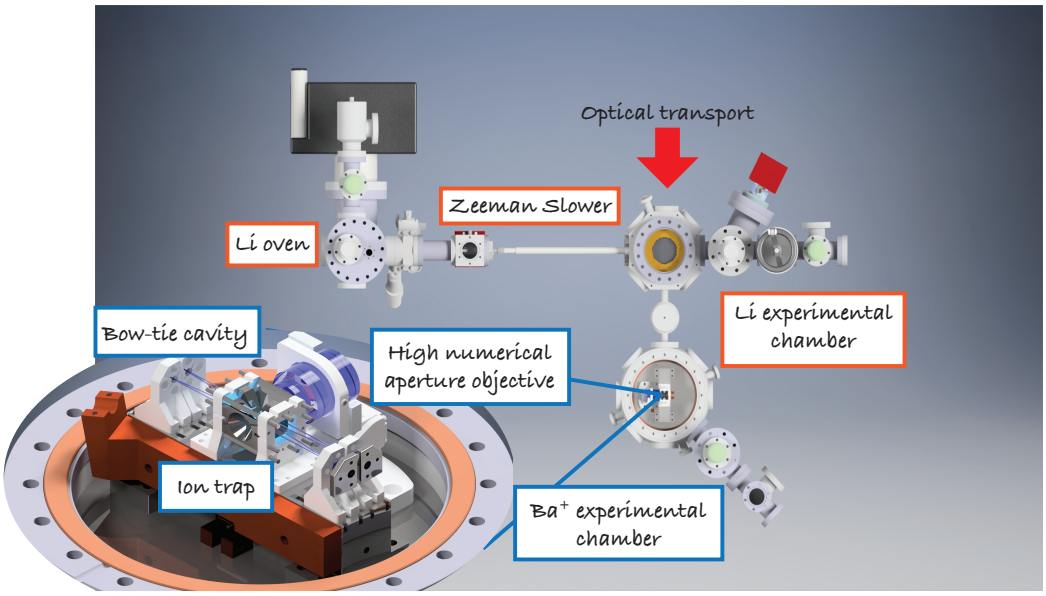


Figure 2.8: Rendering of the Ba-Li experimental setup. The procedure we have planned for the experiment is made of several steps. Barium neutral atoms are produced from an oven below the ion trap; after photoionization, hot $Ba^+$ ions are trapped in a Paul trap and optically cooled. The Paul trap is then switched off and the ions are captured in the EOT. In parallel, Lithium atoms form a hot vapour in an oven, then they pass through a Zeeman slower for a first deceleration process. When they arrive in the Lithium vacuum chamber, the atoms are trapped and further cooled in a MOT, before being trapped in an optical trap in which they are evaporatively cooled. Finally, the ultracold Lithium gas is transported from the Lithium experimental chamber to the Barium one, by using a red-detuned laser beam, the focus of which is displaced. Once in the centre of the ion trap, the Lithium gas can interact with the Barium ions, and atom-ion interactions arise.

# Chapter 3

# Lithium experimental setup

The procedures that allows to cool and trap Lithium atoms were described in Sec. [2.1]. A number of laser frequencies are necessary to carry out these operations, they are listed in Tab. (3.1).

All these frequencies can be generated by using only two laser sources, one at frequency $\omega_{L,D1} \simeq \omega_{D1}$ and the other at frequency $\omega_{L,D2} \simeq \omega_{D2}$, where $\omega_{D1}$ and $\omega_{D2}$ are the frequencies of the D1 and the D2 transitions, respectively. Then, these two laser beams will be split, amplified and shifted in frequency by some *acousto-optic modulators* (AOM) in an optical circuit, in order to obtain all the desired light frequencies and powers.

In this Chapter I will describe how the Lithium optical circuit was designed and partially realized, and the plan for the vacuum chamber in which we will trap and cool quantum gases of fermionic Lithium.

## 3.1 Laser sources for D1 and D2

Lasers diodes are inexpensive lasers composed by a semiconductor gain medium enclosed in a Fabry-Pérot cavity. Lasers diodes emitting on a single transversal mode can be easily found in the market, with output powers typically ranging from a few to hundreds of mW, and frequency in the near infrared or in the blue/red portion of the visible spectrum. However, the mirrors of the Fabry Perot cavity in a diode laser are right at the surfaces of the active medium (with a relative distance of 100s of $\mu$m), and the free spectral range of the laser cavity is so large that the linewidth of bare diode lasers is typically hundreds of times larger than the typically linewidth of atomic transitions. A common strategy to realize inexpensive laser sources with a narrower linewidth is to use laser diodes as an active medium inside an external cavity.

### 3.1.1 The ECDL configuration

The configuration in which laser diodes are used as an active medium inside an external cavity is called extended cavity diode lasers (ECDL) and is widely used in optical spectroscopy of atoms, ions and molecules [120]. Typically, one can use the back mirror of the diode as the high reflectivity mirror of the laser cavity, and a second partially reflective element placed at a few cm distance from the diode laser as the output coupler of the laser.

Commercial laser diodes have typically the two surfaces coated in order to reflect the emitted light back in the active medium and consequently induce the stimulated emission. These laser diodes are Fabry-Pérot (FP) diodes and they have an internal cavity. If a FP coated laser diode is placed in an external cavity configuration (*external cavity diode laser* - ECDL), then the spectrum of the internal FP cavity is added to the contribution of the external cavity.

In order to avoid that the external cavity response may be affected by that of the internal cavity, in our laboratory we have used only diode lasers with *anti-reflection* (AR) coating on the front facet (in this case the diode lasers are also called gain chips), in which the internal cavity is not present and all the emitted light is transmitted by the front facet. These diodes need the external cavity injection to emit coherent light for stimulated emission.

In order to select an optical mode of the external cavity as the emission laser mode, the ECDL setup may be realized by using the diode as a gain medium enclosed in an external cavity composed by an element providing retro-reflection to the gain medium, like a mirror, and frequency-selector elements, e.g. an interference filter or a diffraction grating. In this way an external optical feedback is given to the diode and the emission spectrum is modified by the stimulated emission at the selected frequency.

Moreover, in order to lock the laser frequency to an external frequency reference, it is necessary to modify the laser emission by changing external laser parameters such as:

1. *the diode temperature*: the correction bandwidth is typically not enough broad for granting alone an efficient lock, because the temperature variations are slow due to the laser thermal capacitance,

2. *the diode forward current*: the correction bandwidth is typically wide from hundreds of MHz to GHz, but the emission range is in general limited at hundreds of MHz because of jumps to other modes of the external cavity,

3. *the external cavity length* varied actively for instance with a piezo-electric stage: in this last case we can observe a wider emission range than that of the fast current corrections, but small correction bandwidth limited at frequencies on the order of a few of kHz.

### Modified Littrow ECDL

One possible ECDL configuration (see Fig. (3.1) a) employs interference-filters or etalon to perform the wavelength selection and a partially reflecting mirror, named *output-coupler* (OC), to provide the feedback into the diode [121]. The main advantage of this design is the decoupling between the wavelength selection and the optical-feedback operations, but it has a few drawbacks like the temperature sensitivity of the optical interference filter and the generally lower output power which is due to the non-negligible transmission losses of the filter, even at the peak wavelength.

For these reasons the most common configuration of ECDL is the Littrow type (see Fig. (3.1) (b)), where the first order of diffraction of a grating is back reflected to the laser diode, while the laser output is the grating's zero order refracted light [122]. In order to achieve more tunability, the grating tilting has to maintain the tracking between the grating selected frequency and the external cavity resonance. In the

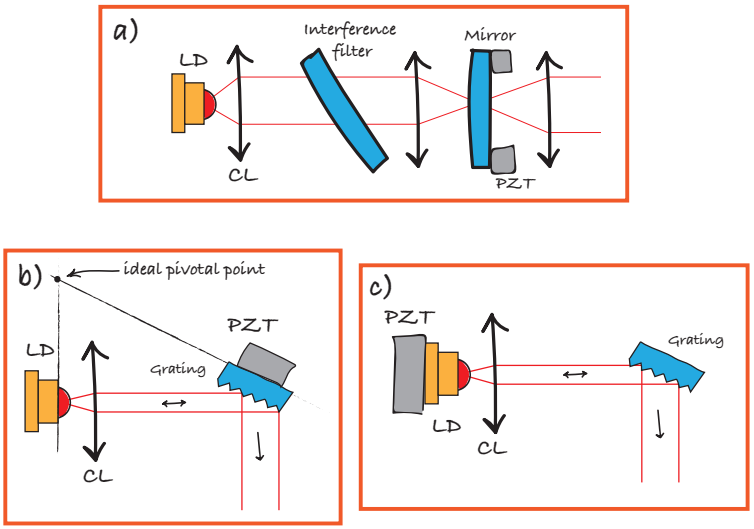


Figure 3.1: Possible configuration for ECDL laser. With LD is indicated the laser diode, with PZT the piezo-electric translator and with CL the laser collimating lens. (a) Etalon configuration. (b) Littrow configuration. (c) Modified Littrow configuration.

Littrow design, the ideal pivotal point for the grating should lie on the LD emission plane [123, 124]. However, this design is sensitive to misalignment due to mechanical and thermal stresses and, consequently, several designs have been developed with improved damping and isolation from the external environment [125, 126] and with a careful choice of the grating pivotal point [124, 127].

The laser design used for D1 and D2 master laser is an ECDL in a modified Littrow configuration [128], illustrated in Fig. (3.1) (c). This alternative design combines the advantages of the interference filter models with the high output power typical of the Littrow designs. The main feature of the new design is the decoupling of the fine-tuning of the wavelength via small changes of the external cavity length from the coarse-tuning of the wavelength and the alignment of the optical feedback achieved by manually tilting the grating. This is realized by positioning a piezo transducer behind a tube containing the laser diode and the collimating lens, while the diffraction grating is tilted with a standard mirror mount. The main advantage is that the lasers do not suffer of mechanical hysteresis that often affect conventional Littrow lasers, a result of the contradicting demands for a rigid construction and fine tunability of the opto-mechanical components.

### Finding injection conditions

The AR coated gain chip begins to laser when its collimated output beam is perfectly superimposed to the grating's first diffracted order, this condition is called *injection*. When the laser is mounted and electrically connected it remains to find the injection condition.

The first thing to do is to move the collimating lens inside its holder to collimate the output beam of the diode. This operation is in general not trivial since the gain chip optical mode is not gaussian and it is therefore sometimes complicated to assess

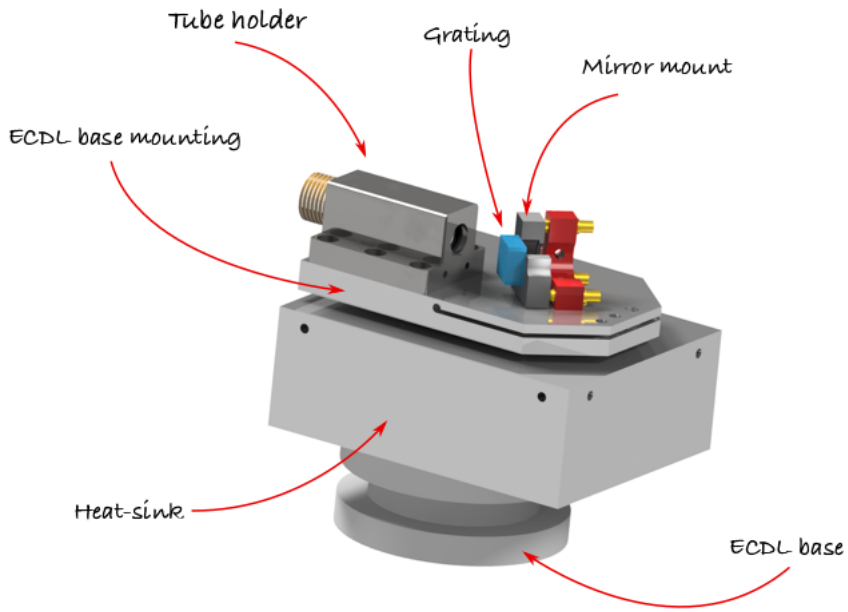


Figure 3.2: Rendering of our experimental ECDL. The tube holder contains both the gain chip and the collimating lens.

by eye when the emission is collimated. If necessary, multiple measurements with a camera at different distances from the gain chip may help finding the best collimation.

When the laser is collimated, then the injection condition has to be found by moving the micrometric screws of the grating holder, see Fig. (3.2). When the first diffracted order of the grating overlaps the diode output then the injection condition is reached. In order to find this condition, the laser forward current should be set to a value slightly larger than the threshold value declared by the gain chip provider. The signature of the injection is a sudden increase in the output intensity, appreciable with naked eye in case of 670 nm diodes. Finding the injection of an ECDL can be a time consuming operation, since there are in general two degrees of freedom (vertical and horizontal tilting of the grating) and since the injection is not reached after optimizing a measurable variable, but it's rather a condition that is either there or not. In order to reduce the time needed to inject a laser, I found it convenient to realize a small disk of black paper with a very small hole (usually realized with a needle) placed at its center, and put this disk at the center of the collimating tube output. By aligning the grating so that the small portion of light passing through the hole is back reflected, one is able to place the grating at an angle that is usually very close to the one for which the laser is injected.

Data of light power versus forward current are measured for not-injected diode without the external cavity, see Fig. (3.3) (a). Then, when the injection condition is reached new data are taken, see Fig. (3.3) (b). Below the threshold value the laser behavior is similar to when there is no feedback, above the threshold the linear slope of the current-vs-power curve suddenly increases. The data of light power versus forward current before and after the injection are useful to characterize the diode response and

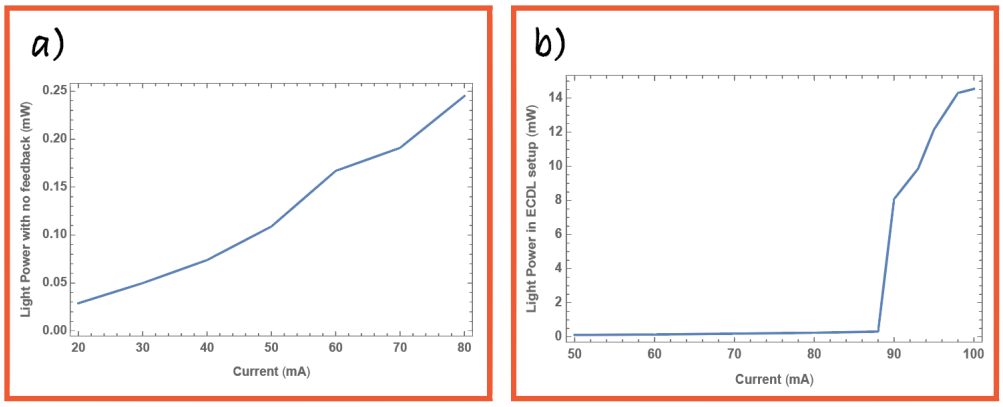


Figure 3.3: (a) *P-I* characteristic measured below the declared laser threshold and without optical feedback. (b) Light power in ECDL setup versus forward current.

to be able to diagnose any problem that may occur to the diode. For example, when a diode is aged or near failure one can usually observes an increase of the threshold value.

### 3.1.2 The Gain Chip

The laser diodes used for the experimental setup are gain chips EYP-RWE-0670-00703-1000-SOT02-0000 sold by Eagleyard Photonics [129]. The wavelength emission of these gain chips has a tuning range from 665 nm up to 675 nm. They are designed to work in an ECDL configuration, and their main application is the Lithium spectroscopy at 671 nm, so they are in principle perfect for our setup. For these gain chips I have used the Thorlabs $C330TMD-B$ lens as collimating lens, and holographic Thorlabs grating GH25-18U for the optical feedback.

#### Technical requirements

The Eagleyard 670 nm laser diode has a cathode-ground configuration as shown in Fig. (3.4). The declared threshold current for stimulated emission is about 70 mA but experimentally we found this value ranging from 60 mA to 90 mA depending on the chip. The maximum forward current in recommended operational conditions is 140 mA and its absolute maximum rating is 160 mA.

For the current supply and temperature control of the diodes we use a combined unit provided by a startup company based at LENS: ppqSense (model QubeCL). Our QubeCLs are formed by three modules: current drivers (CD), temperature controllers (TC) and Phase-Locked-Loop (PLL) modules.

We use the CD and TC modules for both master lasers and we plan to use a PLL module to lock the D1 source on the D2, see Sec. [3.3]. Fig. (3.5) describes the electrical configuration for our laser setup.

The CD module is not directly connected to the gain chip, but the CD output is connected to a protection board, placed as close as possible to the gain chip and connected to it. The role of this board is to prevent possible causes of breakage like ground shocks or misconnections of the gain chip anode/cathode. The protection board is substantially composed by a Schottky diode, a Zener diode, and two transient

| **Reference Transition** | **Function** | **Detuning from the reference transition** |
|---|---|---|
| D2 | D2 MOT cooling | $-3.4\Gamma_{D2} = -20$ MHz [95] |
| D2 | D2 MOT repumper | +211 MHz |
| D1 | D1 MOT cooling | $5.4\Gamma_{D1} = +31.7$ MHz |
| D1 | D1 MOT repumper | +207 MHz [95] |
| D2 | Zeeman Slower cooling | −127 MHz |
| D2 | Zeeman Slower repumper | +104 MHz |
| D2 | Imaging at 0 G | 0 MHz |
| D2 | Imaging at 1000 G | 920 MHz |

Table 3.1: List of the laser detunings from D1 and D2 frequencies that are needed to efficiently trap and cool the $^6$Li atoms.

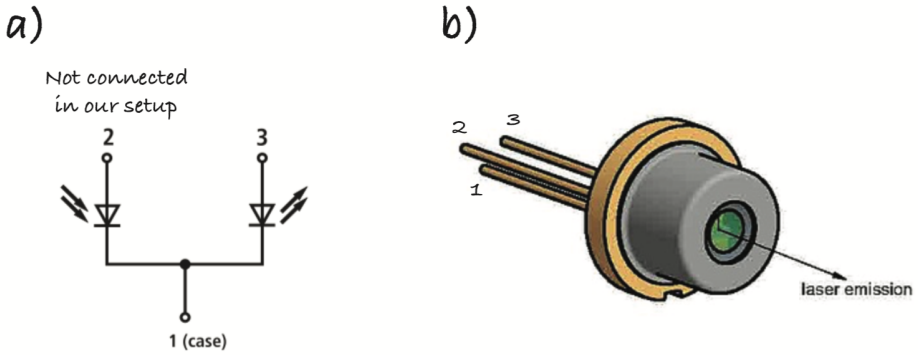


Figure 3.4: (a) Electrical schematic of the gain chip. The package pin-out is: (1) Laser Diode Cathode, Monitor Diode Cathode, Case (2) Photodiode Anode (3) Laser Diode Anode. In our experimental setup the pin (2) is not connected. (b) Rendering of the package of the gain chip EYP-RWE-0670-00703-1000-SOT02-0000 and the pin-out correspondent to the schematic (a). The gain chip package is SOT02, for the complete data-sheet see [129].

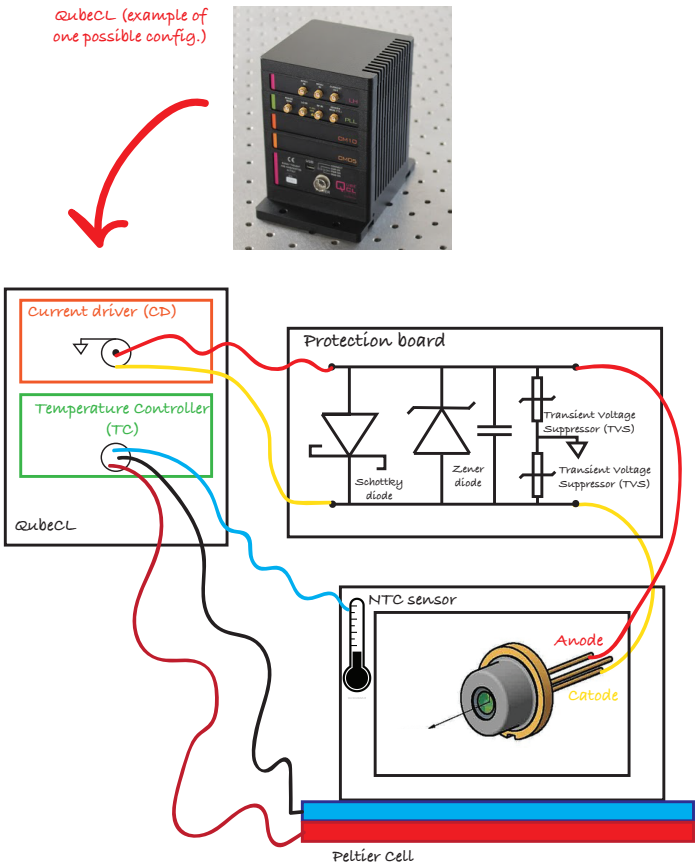


Figure 3.5: Conceptual schematic of the electric connections for feeding the laser diode and for stabilizing its temperature. The protection board is installed as near as possible to the gain chip to better protect it from possible ground shocks.

voltage suppressor (TVS). Additionally a capacitor in parallel to the gain chip is used as low-pass filter (theoretically limited to 3 MHz) to protect the chip from possible spikes of current.

In the datasheet of every gain chip sold by Eagleyard it is possible to find the emission spectrum of the laser diode, a graph showing the junction voltage $U$ versus the forward current $I$, and one showing the light power $P$ vs $I$. All these data are measured by Eagleyard without injection, i.e. with the diode not mounted in an ECDL setup.

In Fig. (3.6) (a) is reported an example of a so called $P$-$U$-$I$ graph. The $U$-$I$ behavior has been tested by using the QubeCL software to ensure consistency with the test protocol sheet. The $P$-$I$ behavior was tested by using a power meter, see Fig. (3.3) (a). These tests were particularly useful to assess a possible failure of a gain chip. Also the light power without injection has been measured with a power-meter, see Fig. 3.6 (a).

### 3.1.3 The premature death of 671 nm gain chips

In the assembly of the Lithium optical setup, I have first mounted and injected the two master lasers for the D1 and the D2 lines of Li. However, after a few days of normal

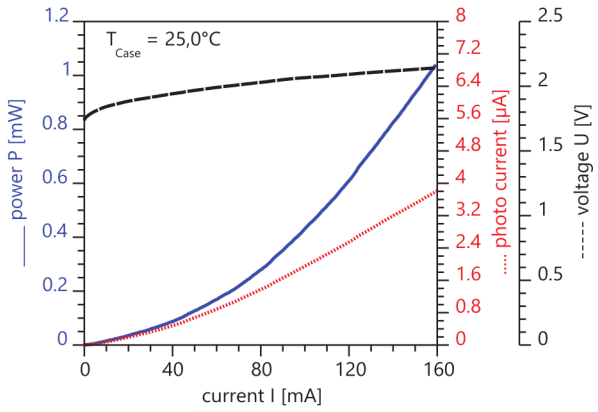


Figure 3.6: *P-U-I* characteristics are measured below threshold without feedback from an external cavity resonator. Laser parameters are not applicable in this setup. The blue line is the light power, the red line is the diode photocurrent if used as photodiode (not our case), while the black dashed line is the voltage drop across the gain chip. Adapted from [129].

operation, the first operating laser lost its injection, and eventually failed. After the first failure, other chips were tested, and their lifetime ranged from a few days to a month; in all cases the first signal of an upcoming failure was the loss of the injection, which was either never found again or found first at higher currents before the laser was failing after running for a few hours at a higher current. The output power of the gain chips with no feedback after this event was lower than the value measured at the beginning of the diode operation, see Fig. (3.7) (a).

The damaged chips were sent back to Eagleyard to analyze the possible causes of failure. Eagleyard provided to us a return merchandise authorization (RMA) final report, see Fig. 3.7 (b), which showed two types of damage between the diode surface and the AR coating:

1. The critical optical damage (COD), that might be caused by back reflection of the setup,

2. The spalling, that might be caused by current peaks of the electrical equipment (current driver).

We have thoroughly investigated our ECDLs in order to find the problem that have caused these repeated damages.

### Electrical issue

We started our investigation from the QubeCL power supply. It was tested in stationary conditions using a low resistance as load, and we observed a very low noise in current, as expected from data-sheet [130]. We observed a $2 \times 10^{-4}$ relative stability at 100 mA (this data could be lower since we were limited by the resolution of the instrument). We subjected the QubeCL system to a stress test in transient conditions: not only by turning on and off the forward current by software but also abruptly turning off the DC power supply of the QubeCL. It resulted that the QubeCL was able to turn off the forward current smoothly, running an exponential decrease of the

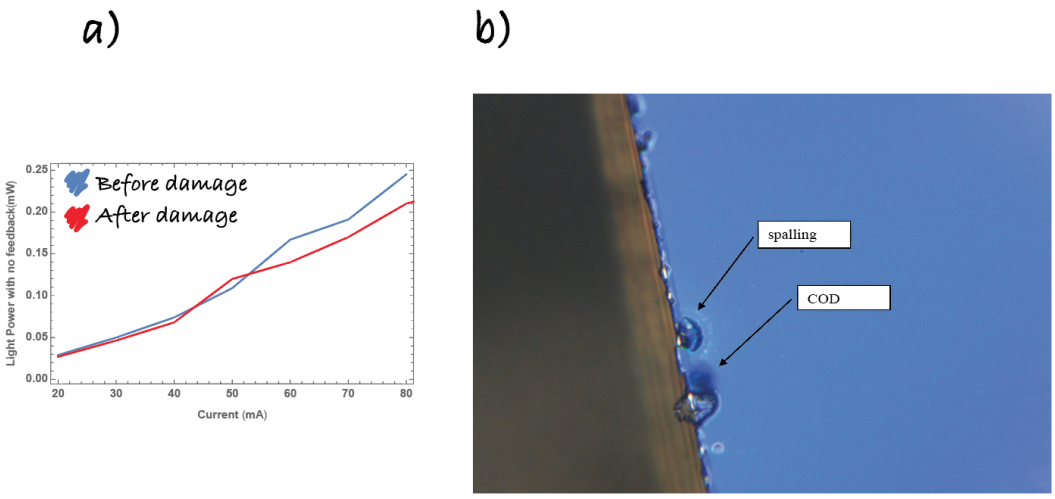


Figure 3.7: (a) Light power versus forward current. These data are relative to the gain chip S/n:AG-07373, previously tested by Eagleyard. (b) Picture adapted from the RMA final report of the gain chip with S/n:AG-08415, one item from the first batch of diodes we have acquired. According to the report the diode shows a COD (critical optical damage) and a spalling.

current with a fixed time-constant and not showing significant current peaks during the transient.

### Optical issue

The critical optical damage could be due to a too intense stationary electro-magnetic wave, which could damage the gain chip AR coating. The value of the maximum optical feedback for the gain chip is not given in Eagleyard data-sheet, but only that of the maximum light power output in an ECDL setup is present, equal to 20 mW. This value was not communicated even after specific request [131].

In order to reduce the optical feedback intensity as far as possible, we tried to inject the gain chip with three holographic Thorlabs gratings with different reflectivities in the first diffraction mode: the GH25-18V that provides a measured back reflected light of approximately 28%, the GH25-18U (reflected light of $\simeq$ 8%) and the GH25-24U (reflected light of $\simeq$ 5%). With the latter I was not able to inject the laser, so we decided to mount the GH25-18U grating.

We measured that the reflectivity of the Thorlabs C330TMD-B collimating lenses are about 0.8%, a value comparable with what declared by the manufacturer and much smaller than the grating reflectivity. Regarding the optical behavior of the gain chips we discovered after some interactions with Eagleyard [131] that the recommended operating temperature is 15° C, while all the graphs in the data-sheet were taken at 25° C, see Fig. (3.6). This temperature value was then corrected by Eagleyard [131].

Eagleyard also informed us that the gain chip could have 24 hours of "krunning behavior" during which it is not recommended to perform measurements, so we decided to never turn the diodes off. We have also discovered that other colleagues were given a similar advice of never turning off the device for amplification stages from Toptica

at 671 nm, a company that uses the same active media we use [132]. It is important to note that in our setup this is the only wavelength for which we experienced several diode failures (7 in total).

#### How to solve the problems with 671 nm laser diodes

At the time of writing of this thesis, we are still investigating the possible causes of the laser diode failure. Without the information about the maximum optical feedback sustainable for the diode, which we would have expected to receive from Eagleyard, we have decided to concentrate our attention on the electrical issues. Mounting the grating that provides the smallest optical feedback we should be sure that there are no optical problems; therefore, it is possible that electrical problems may induce an optical failure by creating an excess of optical feedback, for instance with a sudden discharge through the diode.

For what regards the electrical issue, as previously said, we have investigated the QubeCL behavior both in stationary and in stress conditions using a resistive load in place of the laser diode – for example disconnecting the power supply and observing the power off transient – and we did not observe anything that could be harmful to the diode. However, we observed some coupled signal between the protection board and the external current supply, for example the discharge signals of the laboratory's fluorescent lights. These signals should not be dangerous for the laser diode: they last a few microseconds and have a maximum amplitude of approximately 100 nA, with the QubeCL case properly connected to the same laser ground. This coupling is due to the fact that the current cable in between the protection board and the diode is not shielded. In order to limit this coupling we reduced the bandwidth of the protection board to 100 kHz.

Our debugging strategy that we will apply in the immediate future is the following: in order to understand if the QubeCL is somehow involved in the failure of the diodes in a way not yet understood, we will exclude it from the setup of the D2 master laser. We have substituted the QubeCL with a laser driver by Thorlabs (PRO8000 LD and TEC Controller). The idea is to change a single experimental variable at a time in order to isolate the failure source. If we experience another failure with this new setup, we could exclude the QubeCL and continue the investigation focusing on other elements. Otherwise we could deepen the QubeCL debbuging for understanding the failure causes. We have mounted a new Eagleyard diode powered by a Thorlabs driver for a month now and it continues to work properly. The longest lasting diode with the QubeCL setup survived for about a month and a half but most diodes did not survive for more than two weeks.

If the QubeCL should prove to be the failure cause we will try to understand the physical reasons why this happens, in collaboration with the ppqSense startup which has proved to be not only available to provide technical assistance but also to help us with their experience in the field of lasers.

## 3.2 D2 lock-in on the transfer cavity

The emission of the ECDL in a single mode of the external cavity is yet not sufficient for using it in the experiment, since slow fluctuations due to noise or thermal stability

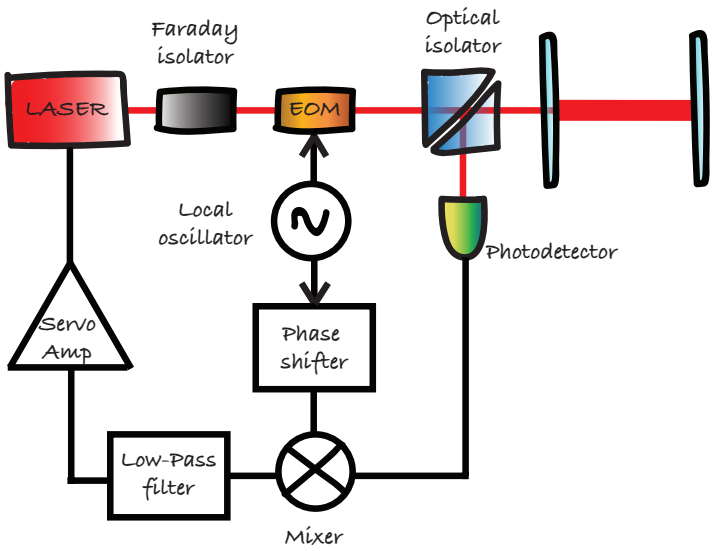


Figure 3.8: The basic layout for locking a cavity laser. Red lines represents optical path, black lines represents electric signal paths. The signal going to the laser controls its forward current and, consequently, its frequency [133].

will affect the stability of the laser frequency. It is then necessary to stabilize the laser frequency, e.g. by comparing it to a given, fixed frequency with a stable reference.

A stable frequency reference could be found by exploiting a passive stable resonator or a spectroscopy signal. In the laboratory, it was recently purchased a stable Ultra Low Expansion (ULE) cavity that is resonant at two wavelengths: 1762 nm (the $S_{1/2} \rightarrow D_{5/2}$ clock transition in $Ba^+$) and 903.4 nm (corresponding to twice the magic wavelength in $Ba^+$). The finesse of the 10-cm-long ULE cavity at 903.4 nm is approx. 3000, so a laser source at 903 nm can be locked to a cavity mode of width 500 kHz. The laser at 903.4 nm has been realized in the laboratory as a primary source for producing the light at 451.7 nm that will be used for the ions' EOT. The lock-in strategy for the D2 laser is to use a transfer cavity to lock it by using the 903.4 nm light as reference after the 903.4 nm will be locked using the ULE.

For the frequency lock-in of the laser at $\omega_{D2,L} = 2\pi \times (446.8)$ THz we will use the Pound-Drevell-Hall laser frequency stabilization technique [133]. With this method, the laser's frequency is measured with an optical resonator cavity, and this measurement is fed back to the laser to suppress frequency fluctuations. The measurement is made using a form of nulled lock-in detection, which decouples the frequency measurement from the laser's intensity.

The experimental setup to realize the Pound-Drever-Hall lock-in is sketched in Fig. (3.8). The main elements for the Pound-Drever-Hall stabilization are a stable resonating cavity, a device to modulate the laser frequency, e.g. an *electro-optic modulator* (EOM), and a photodiode to reveal the error signal from back reflection of the transfer cavity.

For the transfer cavity we consider a cavity of length 10 cm formed by two curved mirrors with radius of curvature 1000 mm. In order to obtain a cavity linewidth comparable to the Lithium D2 natural linewidth the finesse must be 250. A similar cavity

was successfully built in the $Ba^+$ optical setup [116] to transfer a Rb spectroscopy reference to the lasers for cooling and manipulating $Ba^+$ ions.

All the material required for the D2 lock is present in the lab and ready to be mounted. The delay caused by the gain chip failures prevented from being able to lock the D2 laser.

### 3.2.1 Selecting the reference laser frequency

To lock the D2 source at the desired frequency we have to find the correct cavity length that makes it possible to ensure a resonance of both the reference laser and the laser at $\omega_{D2}$.

In a Fabry-Perot cavity a wavelength is resonant when it is an integer multiple of twice the cavity length. In our strategy, the cavity length is stabilized by adjusting the position of one of the mirrors in order keep the cavity resonant with the reference laser.

Therefore, the frequencies at which a second laser can be locked are determined by the cavity length. As a consequence, we must ensure that one of the cavity resonances at approx. 671nm is sufficiently close to the angular frequency $\omega_{D2,L}$. If the cavity length is $n$ times $\lambda_S$, where $\lambda_S = c/\nu_S$ is the stable wavelength, one can change the length of the cavity $L$ of $\Delta L$ by shifting the reference frequency of $\Delta\nu_S = \frac{c\Delta L}{\lambda_S L}$.

The cavity length can be changed only in steps of $\lambda_S/2$. The number of steps that must be made before the resonant modes around 671 nm cover an entire FSR centered on $\nu_{D2,L} = \omega_{D2,L}/2\pi$ depends on the ratio between the frequencies of the reference laser and the 671 nm laser:

$$\frac{\Delta L}{L} = m\frac{\nu_{D2,L}}{\nu_S} \ , \tag{3.1}$$

where $m$ is an integer number. In Fig. 3.9 (a) it can be seen that, using $\lambda_S = 903.4$ nm as a reference laser, 25 steps around the 10 cm of the transfer cavity are sufficient to cover up an entire FSR centered in $\nu_{D2,L}$. At $\lambda_S$ the difference in cavity length between two adjacent resonances is: $\Delta L_{\text{step}} = \frac{\lambda_S}{2} \simeq 451.7$ nm. As a consequence, $25\Delta L_{\text{step}}$ correspond to an excursion of the piezo-translator of about 11 $\mu$m. Using as reference wavelength the $\lambda_{Rb} = 780.2$ nm from the Rubidium spectroscopy, we observe that the same excursion in cavity length is not sufficient to cover the entire FSR around the D2 frequency, because the excursion depend on eq. (3.1), see Fig. (3.9) (b).

The piezo-electric stack translator that will be mounted in the transfer cavity is the HPSt 500/10–5/7, sold by Piezosystem Jena, that could have an excursion of maximum 12 $\mu$m if a voltage from $-100$ V to 500 V is applied. However, it is not recommended to use negative voltages because in this configuration the piezo-translator will experience a larger hysteresis.

The maximum excursion of the cavity length can be considerably reduced if we consider possible frequency shifts provided by *acousto-optic modulator* (AOM). In Fig. 3.9 (c) it is shown, as an example, that with only $\Delta L = 5\lambda_S$ for the translator and using AOMs at 80 MHz or at 200 MHZ, the entire FSR is covered.

### 3.2.2 The electro-optic modulators

In order to modulate the laser light we use electro-optic modulators. These devices are based on the electro-optical phenomenon experienced by certain materials that

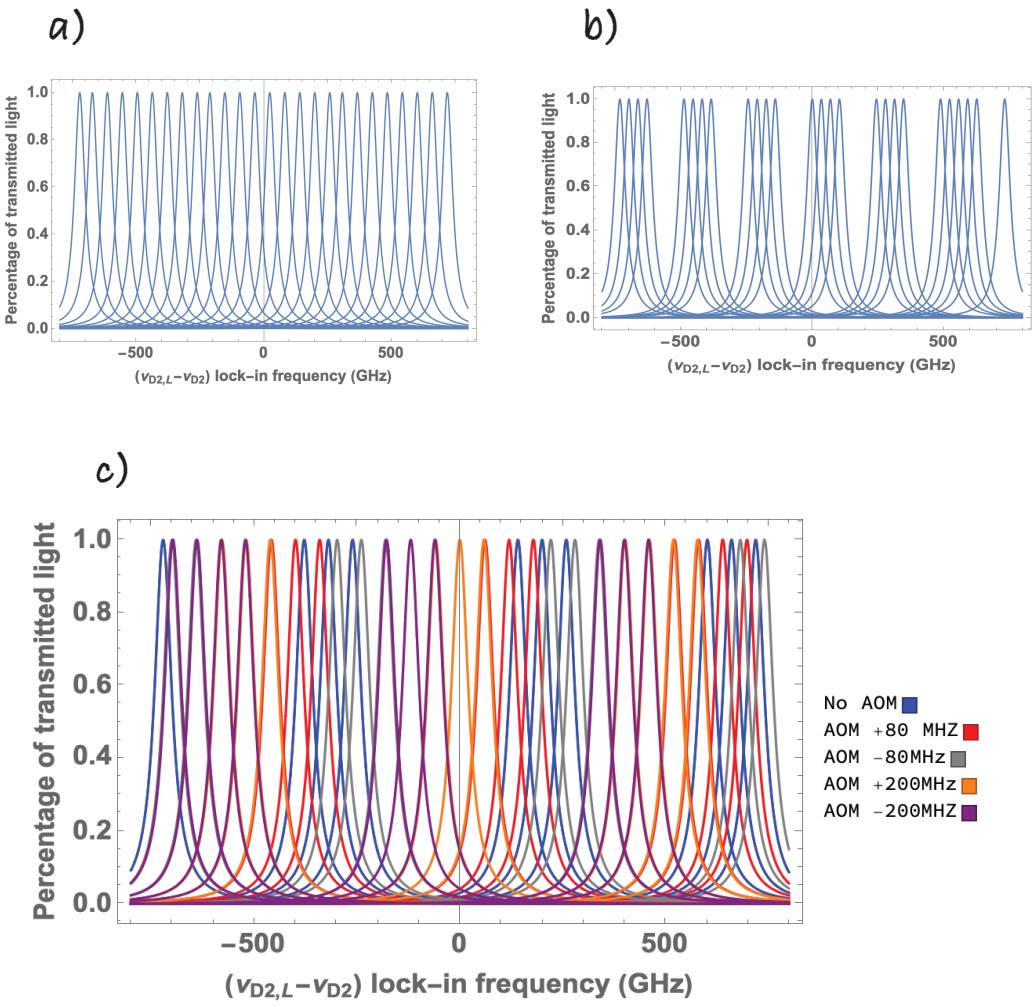


Figure 3.9: (a) Plot of the resonant modes at 671 nm for 25 adjacent resonant modes at $\lambda_S$. The FSR is homogeneously covered. (b) Plot of the resonant modes at 671 nm for 25 adjacent resonant modes at 780 nm. The FSR is not homogeneously covered, and the transfer cavity strategy for locking the Lithium spectroscopy lasers may fail. (c) If an AOM at 80 MHz or one at 200 MHz is used, the entire FSR can be homogeneously covered by extending the cavity for only 10 adjacent resonant modes at $\lambda_S$.

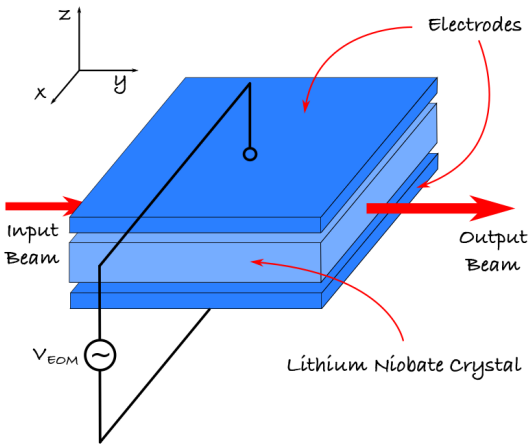


Figure 3.10: Scheme of a transverse modulator used in the electro-optical modulator.

are birefringent, i.e. they have two different refractive indices (ordinary and extra-ordinary), with one of the two refractive indices being dependent on the local electric field. In our experiment we used Lithium Niobate crystals with extraordinary optical axis ($z$-axis) that belongs to one of the surfaces of the crystal.

Let's suppose to have a laser beam with a wave vector $\vec{k_0}$ parallel to $y$-axis and linear polarization parallel to the $z$-axis. We imagine to generate a constant electric field $E$, parallel to $z$, by placing the crystal as a dielectric in an ideal capacitor with flat and parallel faces. It is possible to demonstrate that the laser's phase shift acquired in passing through the crystal is [117]:

$$\phi = \phi_0 - \pi \frac{V}{V_\pi} \ , \tag{3.2}$$

where $\phi_0$ is the phase shift in the absence of an electric field, $V$ is the voltage potential applied at the terminal of the capacitor and $V_\pi$ is called half-wave voltage and depends on the material and on the geometrical properties of the crystal. In our case $V_\pi \simeq$ 187.2V [117]. We use a crystal of Lithium Niobate of dimensions $(2 \times 2 \times 20)$ mm. The capacitor is realized using two copper plates that cover the $xy$-faces of the crystal, as shown in Fig. (3.10).

In order to modulate in frequency the laser, it is necessary to apply a radiofrequency $\omega_{RF}$ of amplitude $V_{\text{EOM}}$. In this way the time-dependent phase shift is:

$$\phi = \phi_0 - \pi \frac{V_{\text{EOM}} \sin \omega_{RF} t}{V_\pi} \ , \tag{3.3}$$

resulting in a modulation of the laser frequency.

### EOM electrical schematic

We want to modulate the EOM by feeding it with as low power as possible and reaching potentials of the order of $V_\pi$. In order to have a signal more monochromatic as possible, it is advisable not to actively amplify the input signal in order to have as low injected noise in the circuit as possible.

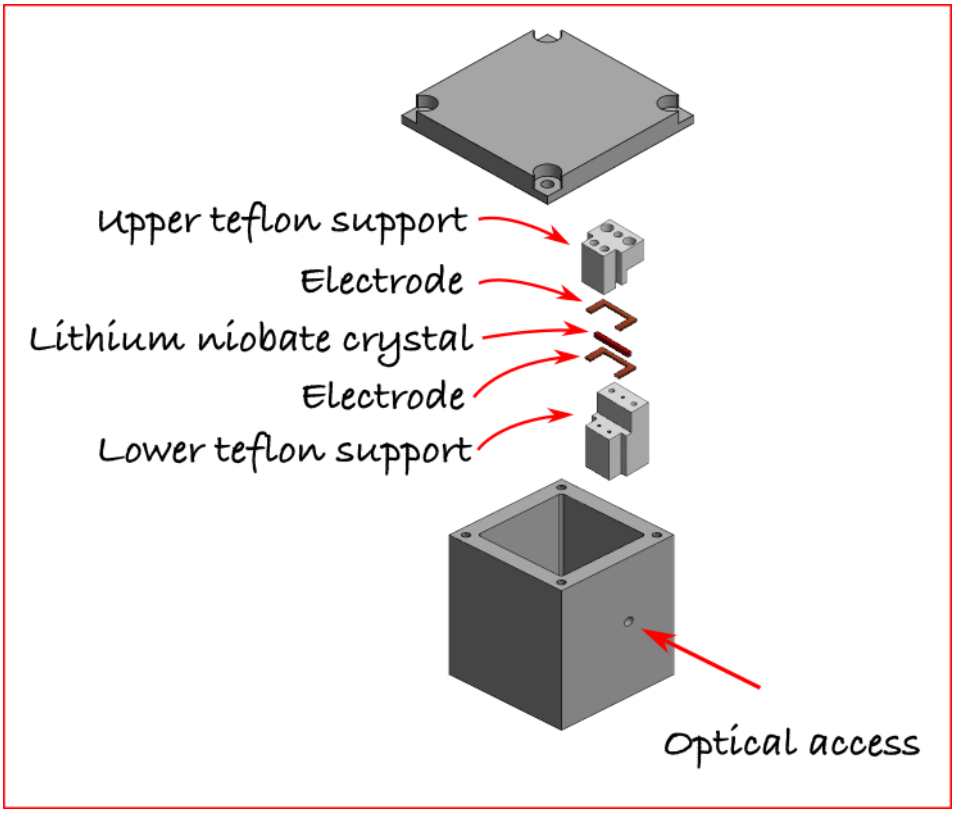


Figure 3.11: Exploded rendering of the mechanical parts that compose the EOM. The transformer, wound in air, is not shown.

Therefore, I designed an electrical schematic for feeding the EOM based on a resonant RLC series circuit. In this way the voltage amplitude at the EOM capacitor will be enhanced by the Q-factor of the resonant circuit and at the same time the circuit will act as a pass-band filter centered on the resonant frequency.

The measured capacity of the EOM capacitance load is about 7 pF, measured with a vector network analyzer (VNA). The inductance that is needed to make the RLC series circuit resonate at 20 MHz is about 9 $\mu$H, which – wound in air – occupies approximatively a cylindrical volume with a diameter of 25 mm and height of about 50 mm. These dimensions are comparable to the ones of conventional optical elements in an optical circuit. The typical $Q$-factor of the resonant circuits is approximately 50, and we are able to reach a signal of amplitude $V_\pi$ with an input signal of amplitude 3.75 V.

### EOM mechanical design

In Fig. (3.11) are shown the mechanical parts that constitute the EOM. The main issue in realizing this device is that the Lithium Niobate crystal is a fragile material and it is critical to press it between two flat metal plates without breaking it.

The solution, much less technically sophisticated and expensive, is to press the crystal between two flat electrodes, made in copper, which is not only a good conductor but also a soft material. The electric contact is made by applying pressure as evenly as possible over the entire facets of the crystal. The upper and lower supports, made

in teflon, ensure the presence of a "soft" material that reduces the stress on the crystal and therefore reduces the probability of breaking it. The electrodes have a U-shape in order to facilitate the soldering of the inductance on it.

Commercial solutions usually solve this issue by gold plating the crystal's facets and doing the electrical connection with wire bonding but we do not have such machinery available at LENS. An alternative could be to solder the wire on the gold plated facet, but this would be critical in many aspects, since soldering gold and copper requires special techniques.

## 3.3 D1 lock-in on D2

We have two master lasers, one for the spectroscopy of the D1 line, and one for the D2 line of Lithium. Sec. [3.2] described how to lock the D2 laser to an actively stabilized cavity by using the Pound-Drever-Hall technique. The D1 master laser can be locked by referring its frequency to the D2 master laser.

This can be done by using the technique called offset lock [134]. Following this technique, the D2 laser beam is superimposed to the D1 laser beam and, by making the two beams interfere, a beatnote originates from this interference. The beat note has a frequency $\omega_{L,D2} - \omega_{L,D1} = 2\pi \times 9.9938$ GHz that can be detected by a fast photodiode, i.e. by a photodiode with a sufficiently large bandwidth (Hamamatsu G4176-03). The D1 locking in frequency can be assured by imposing the frequency of the beatnote remains constant in time.

In order to lock the D1 frequency, then one has to realize an electronic circuit that locks the microwave beating signal. A possible solution is to use a phase-locked-loop (PLL) chip that can be easily integrated in the laser current and temperature-controller supply.

### 3.3.1 Electrical setup

Our fast photodiode is able to detect the beat note frequency between the D1 and D2 laser. It needs to work counter-polarized with about 7 V. Working with approx. 10 GHz is very demanding because the signal could experience reflections along the circuital lines and it needs special coaxial cables to be transmitted without losses. For these reasons, the photodiode output is down-converted in a radiofrequency signal of the order of 100 MHz by beating the photodiode signal and a stable 10.25 GHz signal (Sage Millimeter SOD-10304117-SF-S1 oscillator by Sematron) on a mixer. To minimize the path of the 10 GHz signal the photodiode will be directly connected to a bias-tee for its counter-polarization and to the amplifier.

The output of the mixer is in the radiofrequency range and could be connected to the input of the PLL module with an SMA cable. Fig. (3.12) describes the electrical setup for the D1 frequency lock-in.

The PLL module provided by QubeCL can adjust the laser forward current to keep constant the frequency of the beat note. It has on board a PLL chip that generates an error function proportional to the phase shift between a reference signal – generated in our setup by a DDS at 80 MHz – and the down-converted signal from the photodiode. This error signal is sent to a Proportional-Integral-Derivative (PID) control circuit, which acts on the laser forward current in order to vary the laser frequency. It is

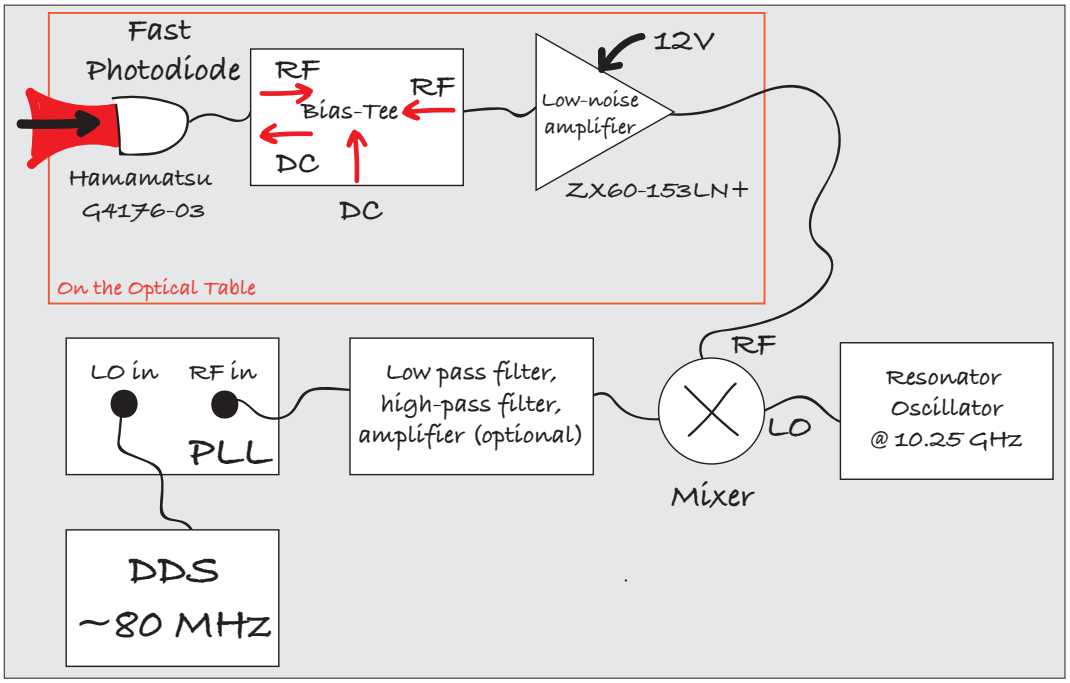


Figure 3.12: Scheme of the electrical setup for the D1 frequency lock-in. The parts enclosed in the orange box are directly connected to each other and are mounted on the optical table.

sufficient to know the frequency response of the diode to current variations and to set the correct parameters for the feedback loop by using the software provided.

## 3.4 The Lithium optical setup

The Ba-Li experimental setup is organized in three optical tables: one hosts the vacuum chambers for Barium and Lithium, one hosts the light sources to cool and trap Barium ions, the third one is dedicated to the light sources for cooling and trapping Lithium atoms.

In this section I will describe the optical setup of this third table. On top of the table we have placed three breadboards on which we have placed different parts of the optical circuit. The optical connections between the breadboards are realized with optical fibers, so if in the future it is necessary to make room in the lab for other parts of equipment, each breadboard can be moved independently without affecting the alignment of the whole circuit. For the moment, in order to provide an extra dumping of low frequency noise we have placed small pieces of neoprene between the breadboards and the optical table.

In Sec. [3.4.1] I will describe the optical setup of the first breadboard that hosts the two master lasers and a first *tapered amplifier* laser (TA) that amplifies the lasers' light. Sec. [3.4.2] provides a description of our home made tapered amplifiers. In Sec. [3.4.3] I will describe the second breadboard: here the laser light is further amplified to provide enough cooling and repumping light for the magneto-optical trap and the Zeeman slower. Finally, Sec. [3.4.4] describes the the third breadboard, in which we

produce the cooling and repumping light for the imaging of Lithium atoms at zero and high magnetic field.

### 3.4.1 The first $Li$ optical breadboard

Fig. (3.13) shows the optical setup of the first breadboard. The two ECDL lasers, described in Sec. [3.1], are mounted near the two opposite long sides of the breadboard. Just after the optical isolator, the D2 laser beam is split into four: a beam with most of the power is sent to the TA, one beam is sent to a beamsplitter for the offset lock with the second master laser, the last two beams are sent, through two optical fibers, to the transfer cavity and a wavemeter.

The laser beam that is sent to the transfer cavity is first modulated by using an EOM. The optical circuit of the D1 laser is similar to the D2 circuit; in this case, though, the laser is locked to the D2 by offset lock, therefore we take only two small portions of the laser light with a beam sampler for the offset lock and for the wavemeter.

The D1 and D2 main laser beams are both $s$-polarized at the laser outputs. One half-wave plate modifies the D2 linear polarization to superimpose the two beams on a polarizing beamsplitter (PBS). At the output of this PBS the D1 light is $p$-polarized and the D2 is $s$-polarized.

Because the MOT and the gray-molasses are realized at different times, see Sec. [2.1], the D1 and the D2 lights can be sent selectively at the input of the first TA. The switch from the first frequency to the second must be done fast, in a time of 10 $\mu$s as magnitude order, for not breaking the TA at high currents. In other setup this switching is realized by turning on and off two AOMs which select the correct frequency [87].

However, in our setup AOMs can not be used because too much laser power is dispersed on them and the threshold injection power for the TA would not be reached. Moreover, the input of the TA must be $s$-polarized.

Then, we will use a Pockels cell (from Leysop ltd.), which guarantees both the fast switch between the two frequencies and the correct polarization selection. When the Pockels cell is turned on, it acts as a half-wave plate. It is only a transparent medium if it is off. Therefore, when the Pockels cell is off the D2 light injects the TA and the D1 is deviated, when the Pockels cell is on the opposite situation occurs.

### 3.4.2 Light power amplification on the first TA

Master lasers for Lithium atoms need to be amplified to be used for all the cooling and trapping operations. For instance, the magneto-optical trap needs large laser powers: we need waists on the order of 1.5 cm and peak intensity of approximately 7 $I_s$, with $I_s$ the saturation intensity for the D2 ($I_s = 2.54$ mW/cm$^2$) [95]. A relatively cheap and practical method to amplify laser light is to employ tapered amplifiers. To amplify the 671 nm master lasers the Eagleyard EYP-TPA-0670-00500-2003-CMT02-0000 tapered amplifier is used [129].

The TA electrical configuration is similar to that described for the ECDL in Fig. (3.5). The only differences are that the QubeCL must provide a rather higher current (our TA's maximum current is 1 A), and that the TA is anode ground, a configuration for which QubeCL has better noise performances.

The GaAs semiconductor amplifier is mounted in an homemade setup sketched in in Fig. (3.14). The TA chip has a CMT02 package that allows to fix it to a brass

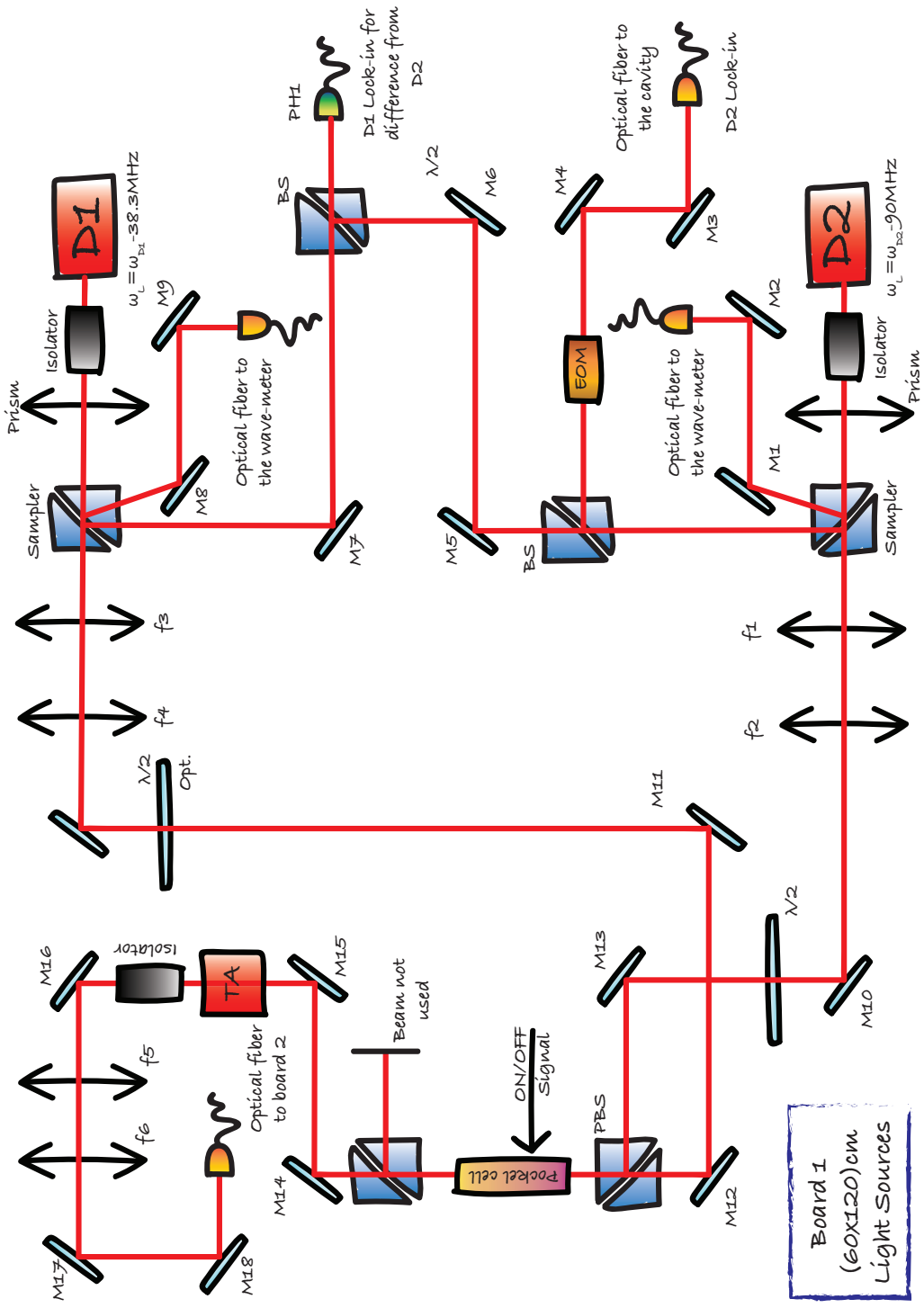


Figure 3.13: Optical Setup for the first breadboard of the Lithium laser lights optical table.

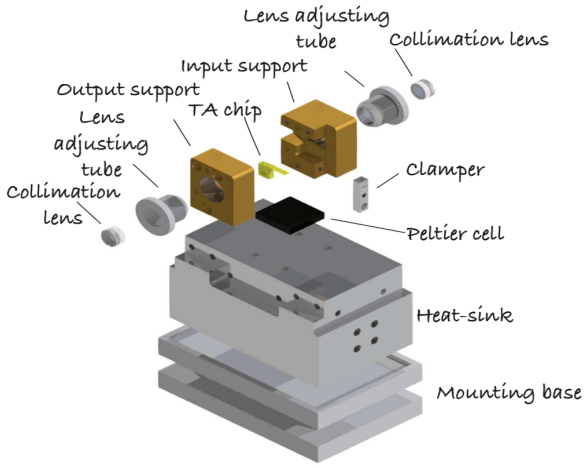


Figure 3.14: Exploded view of the tapered amplifier mounting. Adapted from [116].

base by means of a screw. In the brass base there is a terminal to ensure the ground connection. The anode terminal of the chip is connected to the power supply by means of a clamper. In the TA brass base there are two lens adjusting tubes with micrometer thread that host two high numerical-aperture lenses. This two lenses are: the input lens, which focuses the input laser on the TA chip, and the output lens which collimates the TA output beam. The collimating lenses used for this setup are Thorlabs C230 TMD-B, with a focal of 4.51 mm. The optical axes of the two lens adjusting tubes and the TA chip coincide.

Positioning correctly these two lenses is quite critical because the TA active medium is particularly small – the input aperture is 3 $\mu$m wide and the output aperture 190 $\mu$m wide – and a high numerical aperture caused a reduction of the depth of field. For this reason the lens adjusting tubes are externally micrometric threaded.

In general the TA may have thermal dissipation problems, for this reason the TA mounting is equipped with a water cooling system, whose operation is described in the next section.

An easy procedure for injecting a TA is to feed it with low current (around 100 mA) and then superimpose the input beam with the fluorescence emitted by the TA backward from the input facet. Once the first signal of amplification is present, the current of the TA can be gradually increased in steps, while the input beam alignment must be optimized at each step. The light power amplification occurs at a certain current value, typically at approx. 300 mA, with a behavior shown in Fig. (3.15).

### Water cooling TA system

The maximum TA recommended operational temperature condition is 40°C from datasheet [129]. However, in the exchange of information with Eagleyard about the gain chips failure (see Sec. [3.1]), we have learned that also TAs at 671nm should rather work at around 15°C.

This temperature condition is quite demanding considering that the temperature in the lab is approx. 23°C and that the TA runs at relatively high currents. When the TA is running at operational current, we found it necessary to water cool the device.

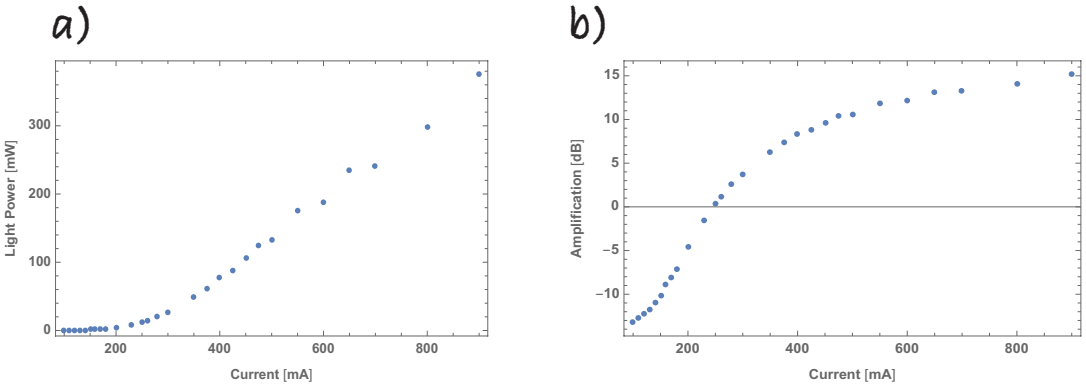


Figure 3.15: (a) Light power of the TA versus forward current, measured with an injection input power of 11.5 mW. (b) Amplification of the light power with respect to the input power. At high forward currents it is possible to reach amplifications higher than the 10 dB declared by Eagleyard Photonics.

Using eight compression fittings with outer thread, water can flow inside four through holes in the TA heatsink, see Fig. (3.15). We use a water cooling system for PC hardware by Phobya: the water is collected in a reservoir, then a pump creates a water flow in the tube passing through the heatsink holes. A special NTC temperature sensor installed inside a hydraulic fitting is used to control that the water temperature remains constant. Since this NTC is sold without a datasheet, I have calibrated it by measuring its resistance at some different temperatures, using a chiller. Once I have found the parameters of the Steinart-Hart equation that describes the NTC behavior [135], I have connected the electrical terminals of the NTC to an Arduino Uno to periodically measure the temperature of the water in the TA.

### 3.4.3 Optical Setup - Breadboard 2

The optical setup designed for the second optical breadboard of the Lithium laser table is shown in Fig. (3.16). In this board are produced the laser beam for the MOT and for the Zeeman Slower and there are present three TA units identical to the one described in the previous section. Every TA has a declared typical amplification of 10 dB (though we measured a higher amplification, see Fig. (3.15)), with an input ranging between 10 mW and 50 mW. This technical requirement explains why we have planned to mount two TAs in sequence, one at the end of the first breadboard and one at the beginning of the second one: the D1 and D2 light injecting the TA on the first breadboard are about 11.5 mW and they are just enough to inject a TA before the optical fiber, but not after.

With the first TA in the second board it is possible to reach the maximum TA output power in operational condition of about 500 mW. The laser is then divided in several branches, in order to produce the frequencies needed for the Lithium gas production (see Table (3.1)).

For both D2 and D1 lines, we need to produce light resonant with both a cooling transition ($|F = 3/2\rangle \rightarrow |F' = 5/2\rangle$ for the D2 line and $|F = 3/2\rangle \rightarrow |F' = 3/2\rangle$ for the D1 line) and a repumper transition ($|F = 1/2\rangle \rightarrow |F' = 3/2\rangle$ for the D2 line and $|F = 1/2\rangle \rightarrow |F' = 3/2\rangle$ for the D1 line). The shifts between repumper and cooling are sufficiently small that they can be realized with double passed AOMs.

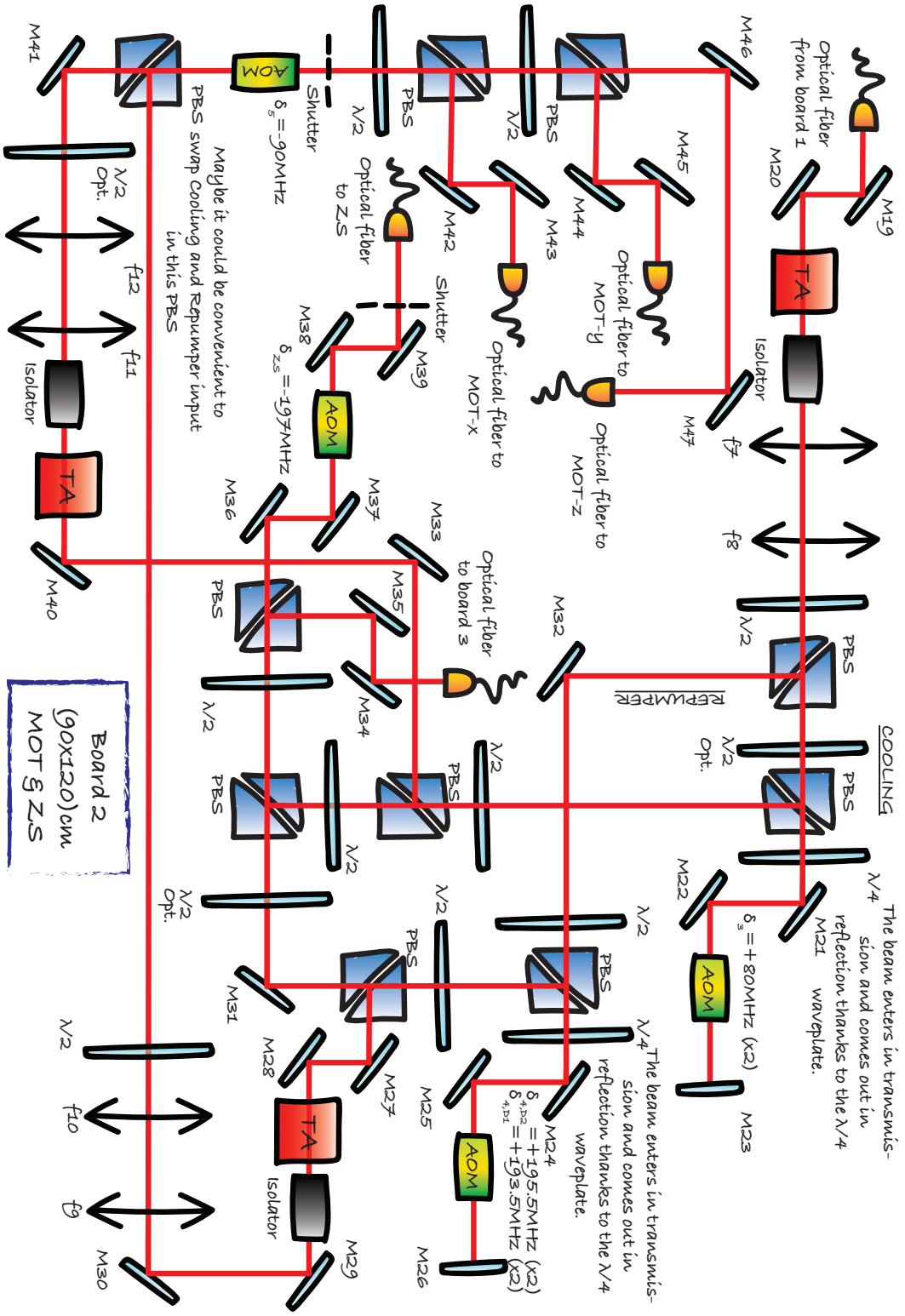


Figure 3.16: Optical Setup for the second breadboard of the Lithium laser lights optical table.

The repumper and the cooling light are created in two separate optical paths, amplified, and then superimposed again using a PBS, see Fig. (3.16). The frequency difference between the cooling and repumper beams correspond to the shift between the cooling and repumper transitions for D1 and D2 respectively. For D1, an additional shift of $0.2\Gamma_{D1}$ is added to the shift between the cooling and repumper transitions, as suggested in Ref. [95]. After recombination, cooling and repumper beams do not interfere because they have perpendicular linear polarization, independent of each other.

At the moment of writing, the second breadboard is not yet implemented, because of the problems we encountered with the laser sources (see Sec. [3.1]).

### 3.4.4 Optical Setup - Breadboard 3

The third breadboard is dedicated to the realization of the laser beams for the absorption imaging of Lithium atoms. The imaging will be carried out only employing the D2 transition. Two imaging beams have been planned: the one in which the atoms experience a high magnetic field, approximately 1000 G, and one at zero magnetic field. The imaging at high magnetic field is necessary in order to observe the atoms while they experience a Feshbach resonance without turning off the magnetic field.

The required frequencies for imaging are different in the two conditions because of the Zeeman effect: at zero field we use the exact D2 frequency $\omega_{D2}/2\pi$, while at high magnetic fields the laser must be shifted of approx. 920 MHz [48].

The optical setup shown in Fig. (3.17) has a scalable number of optical fiber outputs for both the imaging configurations. This is because we may need to perform imaging of the atoms in different locations and directions.

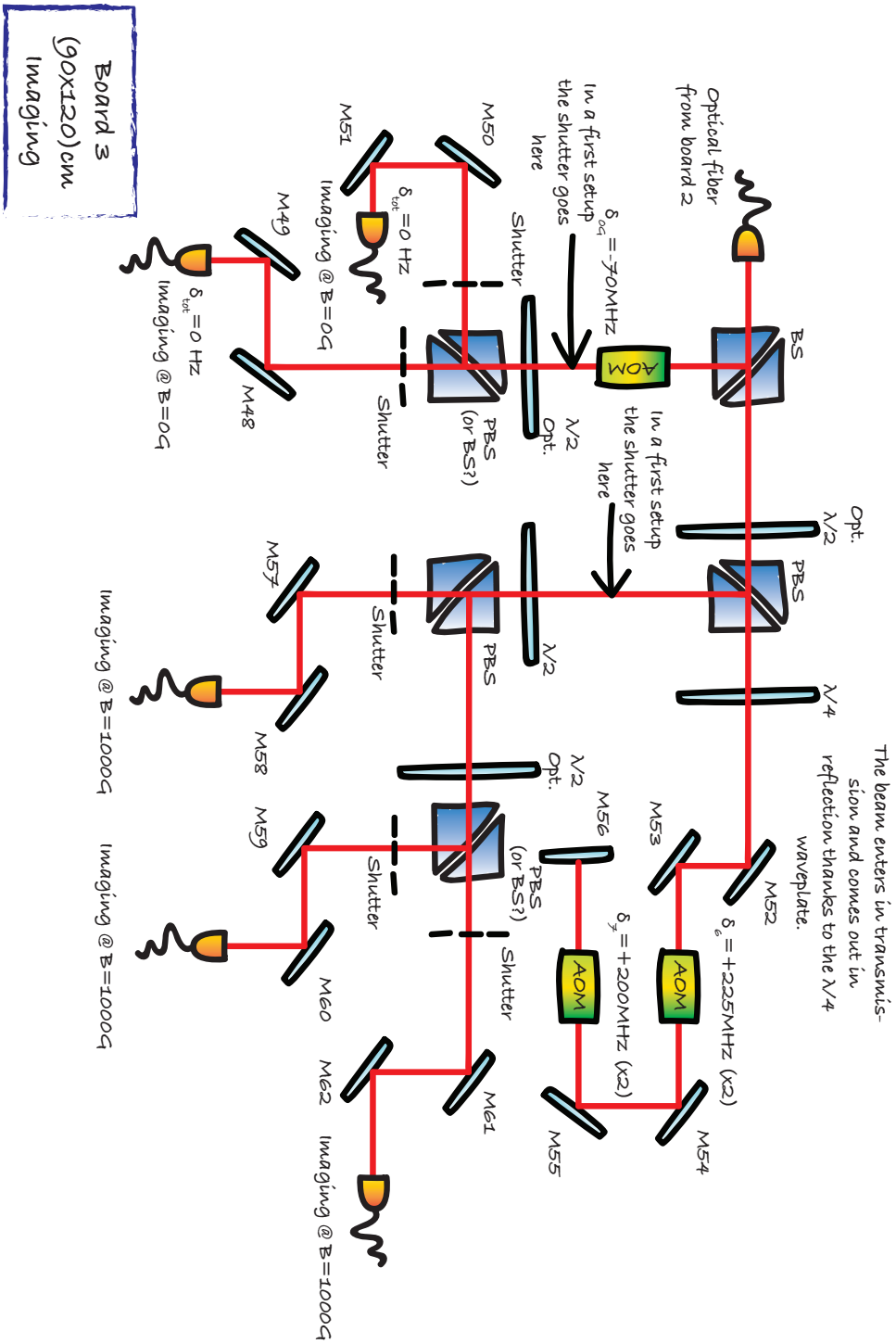


Figure 3.17: Optical Setup for the third breadboard of the Lithium laser lights optical table.

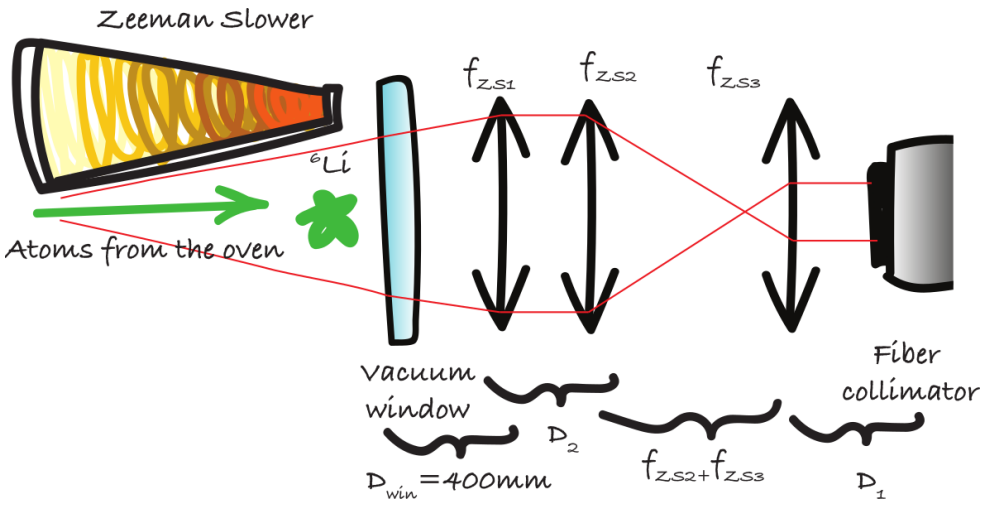


Figure 3.18: Sketch of the optical setup for the ZS laser beam, to be mounted in the experimental table. The vacuum window is made in UV silica and its thickness is 8 mm.

## 3.5 Optical Setup in the experimental table

Sec. [2.1] described the methods for cooling and trapping Lithium atoms. In this Section I will describe how we plan to implement these methods by using the laser lights produced in the Lithium laser table described in the previous sections of this chapter.

I will treat: the optical setup for the Zeeman slower, the MOT, the imaging, the optical trap, and the transport for moving the Lithium atoms from the Lithium experimental chamber to the ion trap.

These optical setups involve one or more laser beams passing into the vacuum chamber through a window: in Sec. [3.5.6] I will give an overview of this Lithium experimental chamber.

### 3.5.1 Optical Setup for the Zeeman Slower

As explained in Sec. 2.1.1, in a Zeeman Slower a laser beam has to counter-propagate with respect to the atoms flux in order to slow down the atomic beam. Far away from the focus the profile for a gaussian beam can be written as linear in function of $z$. The optimal shape for the Zeeman Slower beam, estimated with a simulation [136], is:

$$w_{\mathrm{FAR}}(z) = -\frac{w_{ZS}}{2L_{ZS}}z + q_{ZS} \ , \tag{3.4}$$

where $w_{ZS} = \beta_{ZS} R_{\mathrm{MOT}}$, $R_{MOT} \simeq 5.1$ mm is the estimated capture range of the MOT, $\beta_{ZS} \simeq 1.41$ is a parameter obtained by a simulation of the kinetics of the Lithium atoms (see Sec. 2.1.1). The $q_{ZS}$ is a parameter found by imposing that in correspondence of the centre of the MOT the waist of the Zeeman slower beam has to be $w_{ZS}$, $L_{ZS}$ is the length of the Zeeman slower.

The optical path designed to obtain a good approximation of the beam profile of eq. (3.4) with standard optical elements is shown in Fig. (3.18). In order to simulate

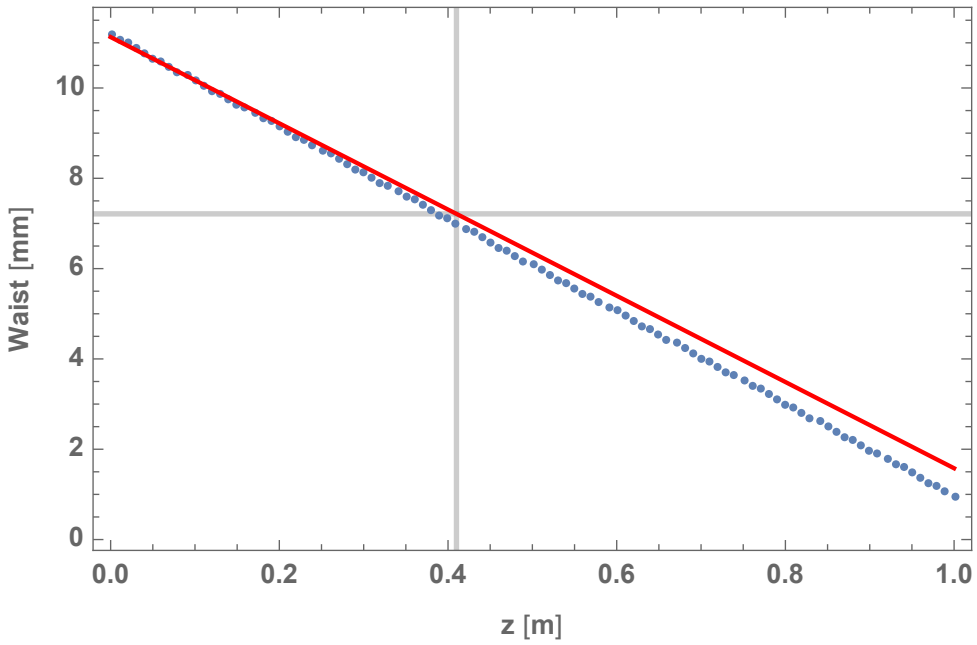


Figure 3.19: Beam waist of the Zeeman slower laser beam along the Zeeman slower axis. The origin of the optical axis is placed in correspondence of the internal surface of the ZS dedicated vacuum window. Gray lines indicate the MOT centre position along the z-axis and the desired waist of the ZS beam in this point, respectively. In red the ideal laser profile is reported, see eq. (3.4), blue points represent the estimated laser profile with the optical setup of Fig. (3.18).

the beam profile I propagated the laser beam profile through the optical path using the ABCD matrix methods [137].

The ZS laser beam is brought to the experimental table with an optical fiber; its output is collimated by using a fiber collimator (60FC-4-A11-02 fiber collimator by Schäfter and Kirchhoff). The beam must then be increased in size by placing a telescope with the first lens focal of 50 mm and the second of 125 mm. We considered a 10 mm distance between the collimator and the first lens of the telescope. Finally, a lens with focal length 1500 m (placed in the simulation at a distance of 10 mm from the objective) creates a focussing beam that resembles closely the ideal beam profile (see Fig. (3.19)).

### 3.5.2 Optical Setup for MOT and imaging

For the operation of a MOT (see Sec [2.1.3]), three pairs of counter-propagating, $\sigma^+$-$\sigma^-$ polarized laser beams must be implemented. For the parameters of the laser beams I followed the experimental setup of Ref. [95], in which the MOT beams have waist of about 1.5 cm and the peak intensity has to be $7I_S$, where 2.54 mW/cm$^2$.

The MOT beams are brought to the experimental table through three separate optical fibers, one for each spatial direction. At their output, the fibers will be connected to a fiber collimator (60FC-4-A11-02 fiber collimator by Schäfter and Kirchhoff), and the beam expanded to the desired waist of approx. 15.8 mm by using a telescope composed by one lens of focal length $-50$ mm and the second of 400 mm. In order to obtain the desired peak intensity with this waist a laser power of 70 mW is necessary.

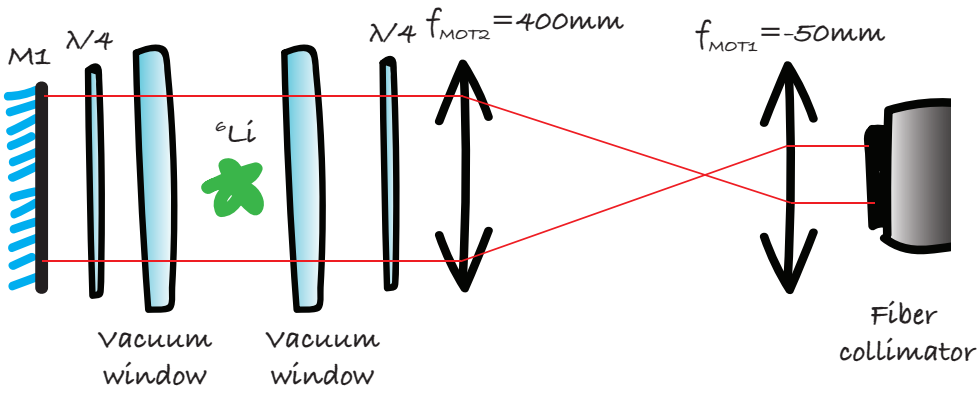


Figure 3.20: Sketch of the optical setup for the MOT-$x$ and MOT-$y$.

The optical setup is shown in Fig. (3.20). The laser beam exits from the fiber collimator with a linear polarization, the polarization is made circular with a quarter-wave plate, then the laser propagates inside the vacuum chamber, just outside another quarter-wave plate makes the polarization linear again, and finally the laser is counter-propagated back in the vacuum chamber by a mirror.

### 3.5.3 Optical Setup for MOT $z$-direction

The optical scheme of Fig. (3.20) does not apply for the $z$-direction since this is the direction that we chose for our imaging. This choice originates from the fact that we have placed re-entrant viewport in the vacuum chamber and we are able to perform imaging with a better resolution with respect to the horizontal plane (see Sec. [3.5.6]). As a consequence, in the $z$-direction the MOT beam has to be superimposed to the imaging one.

The MOT beam and the imaging one will not to be used at the same time, thus a possible solution to the problem could be to use a mirror mounted on a rotating stepper motor to deviate the imaging beam inside the vacuum chamber when the MOT beam is turned off. However, this solution presents some problems: the main one is that the speed of the switching from the MOT to the imaging beam is limited by the bandwidth of the stepping motor.

Therefore, I decided not to use this option, but rather to exploit polarization for separating the two beams. The sketch of this optical circuit is shown in Fig. (3.21). The MOT beam and the imaging laser are superimposed by using two PBSs, one above the vacuum chamber, in which enters the imaging beam from the fiber collimator, one below the chamber, in which enters the MOT beam. This configuration is selected because the lower vacuum window gives an optimal optical access to the atoms, allowing to dispose the heavy and bulky camera directly on the optical table and not in the upper optical breadboards that provide limited space and may be subject to mechanical vibrations.

The collimated imaging beam enters in the first PBS and it is reflected by it in the vacuum chamber. A quarter waveplate changes the imaging beam polarization to circular before entering the vacuum chamber. The imaging is done in absorption, but we can consider for simplicity the image of the atoms' shadow as a point light source. This "light source" is collimated by a high-numerical aperture objective of effective focal length $f_{ob}$, changed in polarization by a quarter waveplate, separated

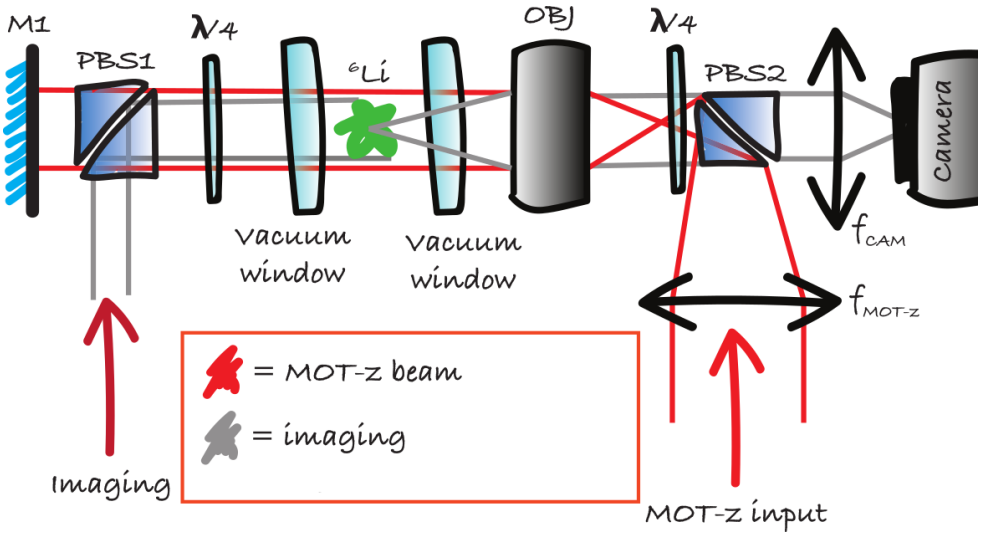


Figure 3.21: Sketch of the optical setup for the MOT-$z$ and for the Lithium imaging. For simplicity of treatment, we consider the atoms as a point light source.

from the MOT beam by a second PBS, and then refocussed on a camera (iXon Ultra 888 camera by Andor) with a lens of focal length $f_{\text{cam}}$. The magnification of this imaging will be $f_{\text{cam}}/f_{\text{ob}}$.

The MOT beam enters in the second PBS, but it is not collimated, because of the presence of the objective along its path. Before entering in PBS, the beam must be shaped in order to obtain after the telescope a collimated beam of waist of approx. 15 mm, see Fig. (3.21).

We are currently collaborating with Sill Optics for the design and the production of the objective for Lithium imaging. We are asking for a numerical aperture of 0.5, to be able to have the maximum resolution allowed by the lower vacuum windows. Since the depth of field is inversely proportional to the numerical aperture, we would like to have the possibility to reduce it on demand in order to image relative big atomic clouds. Referring to Fig. (3.21), by inserting a telescope between PBS 2 and the lens of focal $f_{\text{cam}}$ it will be possible to select the numerical aperture of the whole optical system by acting with an iris in the imaginary image plane placed between the two lenses of the telescope [138].

### 3.5.4 Outlines about the Lithium FP cavity

The last part of the cooling procedure for producing Lithium quantum gases is to use the evaporative cooling technique, see Sec. [2.1.5]. In order to perform evaporative cooling, the atoms will be first transferred from the MOT to a deep optical trap. The optical trap could be made up of a single beam [139] or a crossed beam configuration [140]; however, in this case extreme powerful lasers ($> 100$ W) must be used. Instead, we have chosen to increase the depth of the optical trap by using a Fabry-Perot (FP) resonator. The Fabry-Perot resonator will be placed inside the vacuum chamber and it is currently under construction, a rendering is presented in Fig (3.22).

The FP resonator is designed to work at $\lambda_S = 903.4$ nm, a wavelength for which we can stabilize a laser by using the ULE cavity, see Sec. [3.2]. The cavity will have

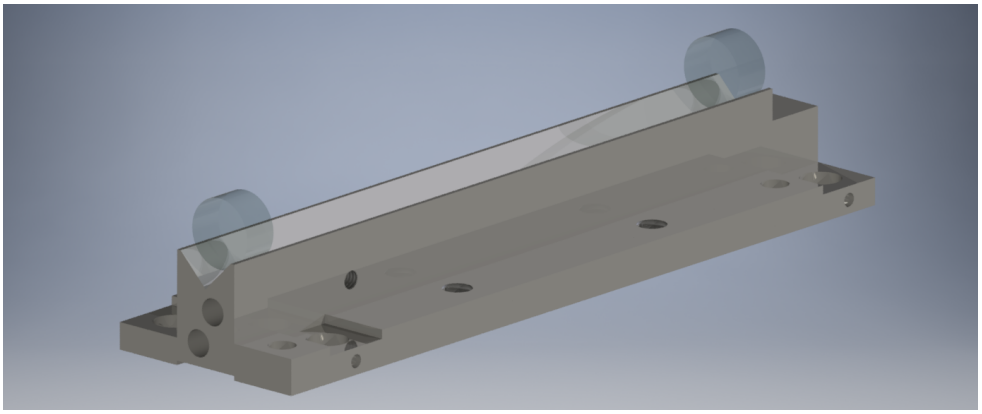

Figure 3.22: FP Lithium cavity rendering. Resonator mirrors will be held in place by a V-shaped holder mounted in vacuum chamber. One of the two mirror will be permanent, while the other will be able to move thanks to a piezo-electric translator. The monolithic cavity will be fixed at the inferior vacuum flange in the Lithium experimental chamber.

a length of about $L_{Li} = 68$ mm, tunable by moving one of the mirrors with a piezo-electric translator, and an expected finesse of $\mathcal{F}_{Li} = 17500$, for $\lambda_S$.

We plan to use a $\lambda_S$ laser with an input power of $P_{\text{in},Li} = 100$ mW and to have a waist at the centre of the cavity of $w_{Li} = 116$ $\mu$m. With these numbers, the maximum trap depth would be approx. 26.5 mK, a value that is much larger than the temperature that can be reached with the gray molasses (30 $\mu$K [95]). Therefore, we believe that with these characteristics we will be able to confine in the resonator a relatively large portion of the atoms in the MOT. Finally, we note that at the maximum expected trap depth, the trap frequency associated with a single lattice site in the resonator is approx. 9 MHz, a value comparable to the natural linewidth of the D1 and D2 lines in Lithium. Therefore, the possibility of a single laser sideband cooling could be explored [141].

At $\lambda_S$, the Lithium polarizability for the level $P_{1/2}$ differs only of the 16% from the $S_{1/2}$ one, while the polarizability of the $P_{3/2}$ differs from the $S_{1/2}$ one of approx. 9% for sublevels $m_J = \pm 1/2$ and of 44% for sublevels $m_J = \pm 3/2$ [119]. Therefore, it would be possible to perform laser cooling on the atoms while they will be trapped in the lattice by slightly modifying the D1 and D2 laser frequencies.

### 3.5.5 Adiabatic displacement of the atoms

Once a sufficiently cold gas is formed, this will have to be displaced to the Barium vacuum chamber where the ion trap is. This translation will be operated by first moving the atoms from the resonator trap to a single beam optical dipolar trap realized with a tightly focussed laser at $\lambda_{\text{OT}} = 1064$ nm. Then, after turning off the resonator trap, we will transport the atoms in the second chamber by moving the focus of the intense $\lambda_{\text{OT}}$ laser beam [142, 143].

#### Transition from the resonator trap to single beam trap

The $\lambda_{\text{OT}}$ laser dedicated to the optical transport has a power $P_{\text{OT}} = 5$ W. At a fixed power, the waist of the laser determines the depth, the frequency, and the radius of

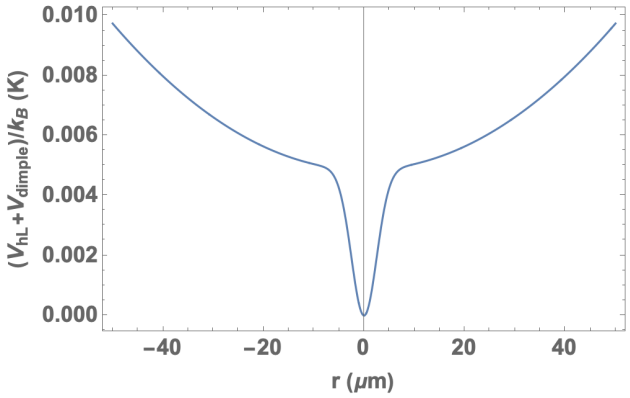


Figure 3.23: Plot of the potential $V_{hL} + V_{\text{dimple}}$, calculated for $\omega_{LR} = 2\pi\nu_{L,||}(S_{1/2})$, $P_{\text{OT}} = 5$ W and a waist of 5 $\mu$m for the optical transport laser beam.

.

the optical dipole trap. Our goal is to transfer as many atoms as possible from the resonator to the dipole trap. To this end, I have modeled the trap swap in order to find the optimal value for the beam waist.

I model the transport procedure in 1D for simplicity, this is reasonable because the angle between the optical axis of the resonator and the transport direction is relatively small, approx. 17.20°. I assume that $N_{\text{atoms}} = 10^6$ atoms are trapped in an harmonic potential at frequency $\omega_{LR}$ with temperature $T_{D1} \simeq 30$ $\mu$K, the typical temperature of the D1 gray-molasses [95]. I assume also that the atoms have energies that follow a Maxwell-Boltzmann distribution. Supposing that in the initial conditions the atoms have only potential energy, from the Maxwell-Boltzmann distribution it is possible to obtain a probability distributions of the positions in the harmonic trap. Under this hypothesis I basically assume that the size of the cloud in the resonator is the largest possible.

I consider the potential of the resonator a harmonic potential $V_{hL} = \frac{1}{2} m_{Li} \omega_{LR} r^2$ as approximation of one lattice site in its minimum of potential, and the potential $V_{\text{dimple}}$ of the dipole trap creates a dimple on top of it (see Fig. (3.23)). For Lithium in $^2S_{1/2}$ state, the estimated trap frequency perpendicular to the resonator optical axis is approx $\omega_{LR} = 10$ kHz.

I now consider to suddenly turn on the dipole trap, i.e. in a timescale faster than the atoms' dynamics in the resonator. At the instant in which the potential $V_{\text{dimple}}$ is turned on, the particle in position $r$ assumes energy $V_{hL}(r) + V_{\text{dimple}}(r)$. Under these assumptions, I am considering "the worst case scenario", since I basically maximize the energy transferred to the atoms by the fact of suddenly turning on the dipolar trap. I now assume that the particles in the combined trap formed by the two optical potentials will thermalize, and I assume that the temperature is the mean energy of one particle divided by the Boltzmann's constant $k_B$. When the lattice potential is turned off, I assume that only the atoms with energy lower than $|V_{\text{dimple}}(r)|$ will remain trapped. Integrating the new Maxwell-Boltzmann distribution from 0 to $|V_{\text{dimple}}(r)|$ I make an estimate of the percent of atoms that remain trapped in the dimple.

Fig. ( 3.24) shows the ratio of atoms transferred from the resonator to the optical dipole trap as a function of the dipole beam waist and power. Interestingly, this value

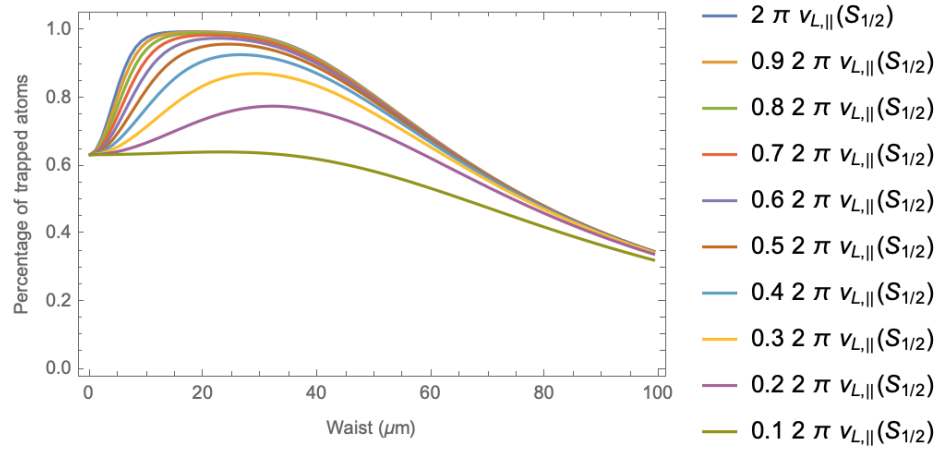


Figure 3.24: Number of estimated atoms survived at the optical transport procedure as a function of the waist of the transport laser beam. The graph is evaluated for different trap frequency in the resonator where $\nu_{L,||} = \frac{\omega_{LR}}{2\pi}$ for the $S_{1/2}$ Lithium ground state.

.

approaches unity in a wide range of parameters. We opted to work with a waist for $\lambda_{\mathrm{OT}}$ of approx. 25 $\mu$m.

### Optical transport experimental setup

The displacement of the focus of a single dipole trap can be realized by moving one or more lenses [144].

In principle, in order to translate the atoms of a distance $\Delta z$ it should be sufficient to move the last lens focussing a collimated beam on the atoms of the same distance $\Delta z$. However, we have to move the atoms of a considerable distance ($D_{\mathrm{Li}} = 30$ cm), and low-noise translators' price increases proportionally to their range. Therefore, we have opted for an optical setup made in total of five lenses, in which the waist of the laser is constant during the displacement of the first lens, and the focus location after the last lens is moved $M_{\mathrm{OT}}^2$ times $\delta_{\mathrm{OT}}$, where $M_{\mathrm{OT}}$ is the magnification of the setup and $\delta_{\mathrm{OT}}$ is the excursion of the translator, see Fig. (3.25).

The optical setup to translate the laser focus is instead constituted by three lenses $f_{\mathrm{OT1}}, f_{\mathrm{OT2}}, f_{\mathrm{OT3}}$ [142, 143]. The lens that is moved is $f_{\mathrm{OT1}}$ and its focal is equal at that of the second, $f_{\mathrm{OT1}} = f_{\mathrm{OT2}}$. The distance between the first two lenses is $f_{\mathrm{OT1}} + f_{\mathrm{OT2}} + \delta_{\mathrm{OT}}$, and in the starting condition $\delta_{\mathrm{OT}} = 0$ (the center of the optical trap is at the center of the Lithium vacuum chamber). The distance between the second and the third lens is fixed at $f_{\mathrm{OT2}} + f_{\mathrm{OT3}}$, so these two lenses constitute a telescope with magnification $M_{\mathrm{OT}} = f_{\mathrm{OT3}}/f_{\mathrm{OT2}}$.

The lenses $f_{\mathrm{OT4}}$ and $f_{\mathrm{OT5}}$ only constitute a telescope for increasing the waist of the laser, which is brought to the experimental table with an optical fiber (60FC-4-A11-03 optical collimator by Schäfter and Kirchoff). In the scheme reported in Fig. (3.25), choosing $f_{\mathrm{OT1}} = 200$ mm, with an input waist of 7 mm it is possible to obtain the desired waist of approx. 25 $\mu$m on the atoms.

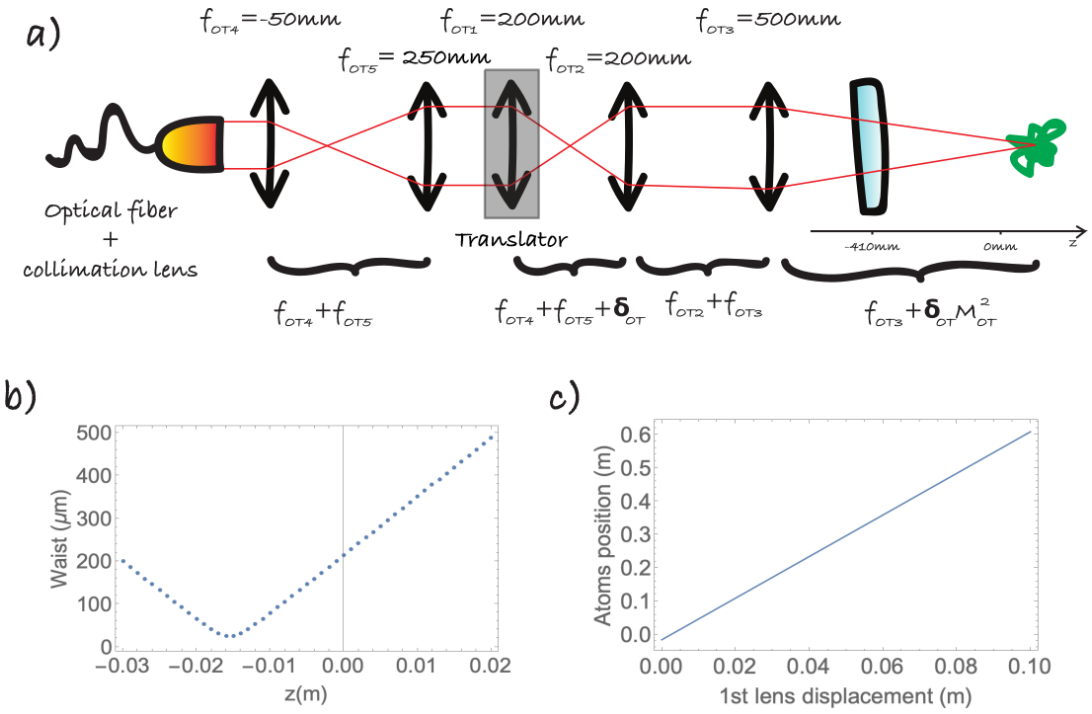


Figure 3.25: (a) Schematic sketch of the complete optical setup for the atom transport. After the fiber collimator we expect a waist of 1.4 mm, so we plan to use a $1:5$ telescope in order to produce a sufficiently large beam. (b) Laser beam profile at $\delta_{\mathrm{OT}} = 0$ near the centre of the Lithium experimental chamber. The waist of the laser is about 25 $\mu$m as desired and remains constant during the transport. (c) Position of the laser focus as a function of $\delta_{\mathrm{OT}}$.

**Adiabatic displacement of the atoms**

The lens $f_{\mathrm{OT1}}$ is placed on a computer-controlled air bearing translator (Aerothech ABL1000-050-E2-CMS1-PL2-TAS) that makes it possible to linear displace the lens for up to 10 cm. Ideally, we want to move the trap adiabatically in order to minimize heating [145]. To this end, if we assume that the probability to transfer one atom from a level $n$ of the dipole potential to a more excited state is much smaller than one, the best acceleration profile for adiabatic transport is a sawtooth one [142]: the translator is constantly accelerated from $t = 0$ to $t = \frac{T_{\mathrm{OT}}}{2}$ and constantly decelerated from $t = \frac{T_{\mathrm{OT}}}{2}$ to $t = T_{\mathrm{OT}}$. With this acceleration profile, the jerk, i.e. the rate of change of acceleration, is kept constant during the transport procedure.

If we approximate the dipole potential to a harmonic potential near the centre of the trap and suppose to apply an acceleration to the lens translator with a sawtooth profile, the transport is adiabatic if [146]:

$$T_{\mathrm{OT}} \gg \sqrt{\frac{D_{\mathrm{Li}}}{a_{\mathrm{OT}}}} \frac{1}{\Omega_{\mathrm{OT}}} \ , \tag{3.5}$$

where $a_{\mathrm{OT}}$ is the ground state radius for the harmonic potential with trap frequency $\Omega_{\mathrm{OT}}$ that approximates the optical transport dipole potential.

For the optical setup of Fig. 3.25 this adiabatic condition is $T_{\mathrm{OT}} \gg 5$ s for a waist of 25 $\mu$m.

### 3.5.6 Overview of the Lithium experimental chamber

Atom-light interactions are the keystone of an experiment of atomic physics, since they are used to cool and trap the atoms and thus exert a strong level of control over their dynamics.

In the design of the Lithium experimental chamber we had to consider the presence of a large number of laser beams, each with its specific features of shape and power, that must interact with the atoms.

As already explained in Sec. [2.5], Lithium atoms are prepared in an oven and then first slowed down in the Zeeman Slower. Then they arrives in the Lithium vacuum chamber where they interact with different lasers for different cooling and trapping stages.

In Fig. (3.26), the different laser paths are shown. In order to trap and cool the atoms the vacuum chamber must ensure optical access to the laser beams for the ZS, the 3D-MOT, the FP resonator, and for the imaging.

There are several constraints that we had to consider in designing the chamber. First, the chamber is connected in vacuum to other two bulky parts: the Zeeman slower and the Barium vacuum chamber; these elements take out space that could be used for placing optical elements close to the chamber. Second, the viewport for the Zeeman slower beam must be kept at a high temperature in order to avoid the coating of the viewport with the Lithium atoms from the Zeeman slower. Third, the positioning of the MOT beams.

The MOT needs laser beams in three directions. In the $z$-direction the MOT beam path is superimposed to the imaging one, as explained in Sec. [3.5.3].

The imaging light enters from the upper viewport while the MOT beam enters from the lower one. In this way the camera can be mounted on the optical table, as well as the objective. To realize the MOT also a magnetic field with the profile

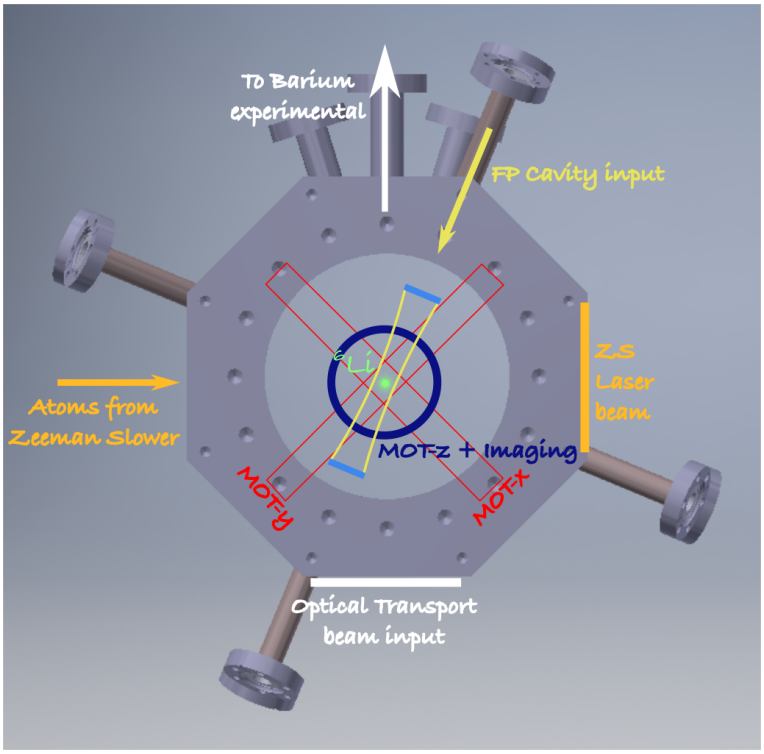


Figure 3.26: Rendering of the Lithium experimental chamber with a schematic map of the spatial position of all the laser beams for trapping and cooling Lithium atoms.

of eq. (2.16) is needed. This magnetic field will be realized using a pair of coils in anti-Helmoltz configuration by Behncke Elektromaschinenbau, already delivered in lab, that will be mounted over and under the Lithium vacuum chamber.

As explained in Sec. [3.5.4], the evaporative cooling will be realized after trapping the atoms in an optical lattice generated by the Fabry-Perot resonator mounted inside the vacuum chamber. The $\lambda_S$ laser input enters from a small CF16 viewport, while another CF16 flange will be equipped with the feedthroughs that are needed to bring the electric signal to the cavity piezo. In order to realize an efficient evaporative cooling we plan to use Feshbach resonances to speed up the pace of atomic thermalization [3]. For this purpose we will switch to Helmoltz configuration the MOT coils. However, in order to execute measures on which a higher precision on scattering length is required, we will have to transport the Lithium atoms into the Barium vacuum chamber, where are present other coils by Oswald Company able to develop high magnetic fields (approx. 1000 G) without curvature.

In order to transfer the atoms in the Barium chamber after the evaporative cooling, we will use a single beam dipolar trap at $\lambda_{\mathrm{OT}}$. By moving the focus of the $\lambda_{\mathrm{OT}}$ laser we will adiabatically move the atoms from the Lithium chamber to the Barium ones through a path of approx. 30 cm.

# Chapter 4

# The $Ba^+$ ion trap

In this chapter I will give a brief overview of the structure of the Barium experimental chamber. This vacuum chamber, differently from the Lithium one, contains many mechanical parts that are needed to trap Barium ions. This chapter is divided in two parts: first, I will describe the mechanical parts composing the chamber, then I will describe the electrical components that are needed to create the potentials that confine the ions.

The process of assembling and running an ion trap from zero is composed by several activities of design, simulation and realization. In our laboratory, this work was shared between myself and Elia Perego, who recently completed his Ph.D. [116]. While we both contributed in all the decisional processes related to the design, Elia took charge mainly of the $Ba^+$ laser system, the parts related to the mechanics of the electrodes, and the simulation of the electric fields generated by them, while I took charge of most of the electronic problems related to the trap operation, e.g. feeding the electrodes with high voltage RF and DC signals, in addition to taking care of the imaging system. In this chapter, I will provide a description of the ion trap design and operation. In the first part, I will provide an overview of the geometry of the trap and its general properties, referring to Elia's thesis for more details. In the second part I will focus mostly on the electronic devices that I designed for operating the trap, with exception for the RF drive, which will be discussed in detail in Chapter 5.

## 4.1 Paul Trap design

Our Paul trap has been designed to fulfill some general criteria. First, we wanted to have the possibility to have a linear Paul trap, similar to what described in Sec. [2.2]. With a linear Paul trap several ions can be trapped with minimum micromotion at the same time. This feature is essential to be able to observe atom-ion interactions at low temperatures with an RF field on and with many particles at the same time (see [2.3]). This option represents a feasible "plan b" in case we are not able to efficiently trap ions in the EOT for any reason.

Second, in order to ensure an efficient transition from the Paul trap to the EOT with minimal ion losses, it is essential that that the ion crystal in the Paul trap resembles as much as possible the 2D structure that the Coulomb crystal would take in the EOT. To this end it is needed an effective potential, created by RF and static electric fields, in which the trap frequencies in two directions are equal, i.e. $\Omega_z = \Omega_y$ (see Fig. (4.1)), and the third is much larger than the other two.

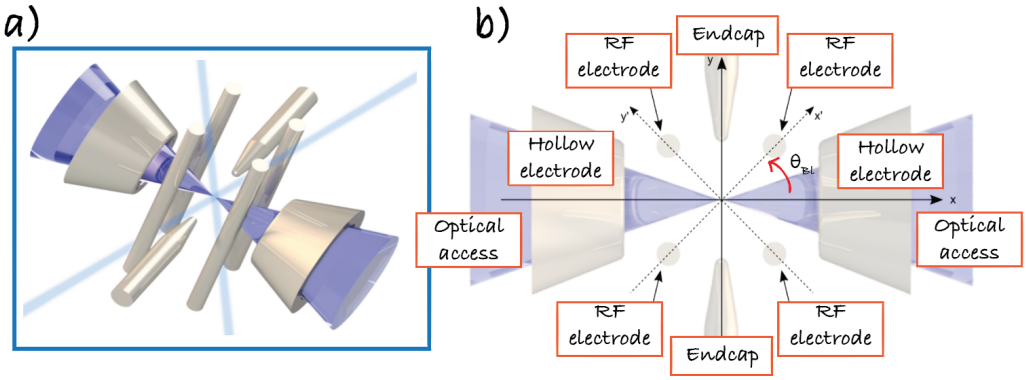


Figure 4.1: Archetypical configuration from which our ion trap is inspired, it is an efficient solution to the integration of a linear Paul trap in an electro-optical one with a special attention in providing a wide optical access to detect the 2D ions crystals. The optical access is obtained by hollowing the EOT electrodes and it is represented by the blue cones. Note that the RF electrodes are rotated of an angle $\theta_{\mathrm{Bl}} = 45°$ with respect to the endcaps' frame. Adapted from [116].

In designing the Paul trap, the necessity to insert the EOT electrodes and its laser beams had to be taken into consideration. Two intense counter-propagating laser beams will provide the optical potential for confining the ions in one direction, say the $x$-direction. Then, at least two electrodes will trap ions in the remaining other two directions, the $z$-$y$ plane.

To fulfill in a satisfying way all these requirements, our experimental Paul trap has been designed following a model design as in Fig. (4.1). The four RF electrodes are placed at the vertices of a square to create a linear geometric place of effective potential minima along the $z$-axis.

In a linear Paul trap, the static trapping potential along the $z$-direction, which is not provided by the RF electrodes, is created typically by using positive charged tips collinear to $z$-axis itself [147] or by using segmented linear electrodes [104]. With this electrodes configuration, trapped ions form a linear crystal along the $z$-axis. However, we are interested in swapping the ions from the Paul trap to an EOT, in which the ions are expected to form a 2D crystal in the y-z plane. Therefore, we have decided to opt for a configuration in which the DC potential is created with two negatively-charged electrodes along the $y$-axis. In this way, we are able to continuously change the shape of the ion crystal from linear to a disk in the $y$-$z$ plane.

### 4.1.1 Mechanical description

The ion trap concept shown in Fig. (4.1) was the starting point for the design of our experimental ion trap. The RF electrodes have a blade shape with a tip having a hyperbolic profile to better reproduce an ideal electric quadrupole, see Fig (4.2) (a) and (b). Because of their shape, the RF electrodes will be in the following indicated also as blades. In order not to occlude completely the optical access along the vertical direction, the DC electrodes pair along the $y$-axis was substituted with four electrodes (see Fig. (4.2) (c) and (d)). In order to reproduce the same potential created by a

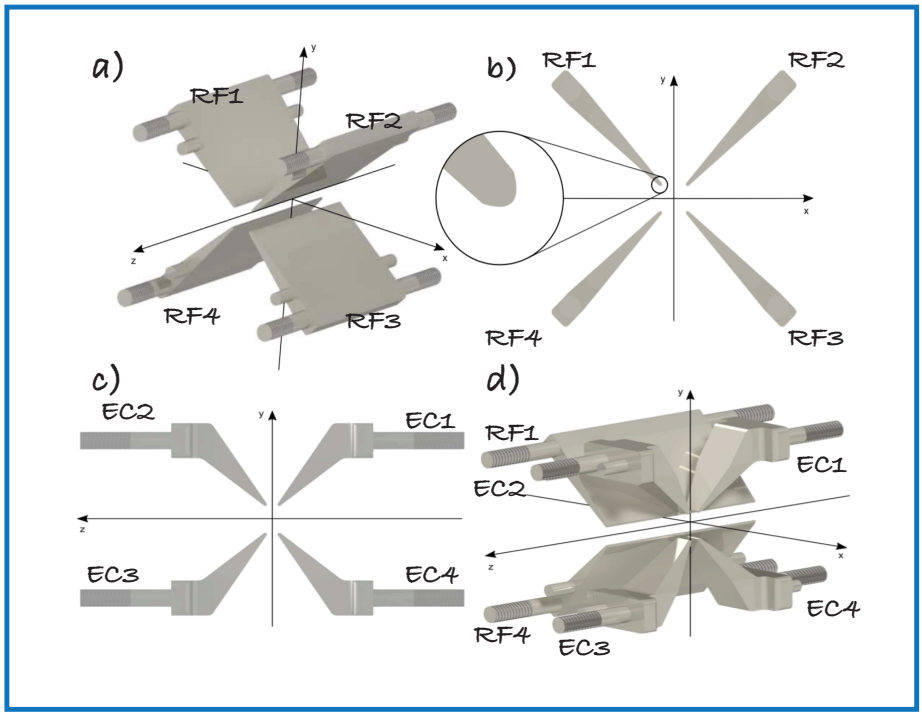


Figure 4.2: (a) Rendering of the four blade electrodes arrangement. They are equipped with four pins in order to ensure their spatial positioning. (b) Section of the four blades with a zoom on one of their tip, which is characterized by a hyperbolic profile. The distance between two near RF blades is 2.1 mm. (c) Section of the endcap (EC) electrodes. (d) General view of the endcaps with the blade electrodes, two blades have been removed for a better insight. Figures adapted from [116].

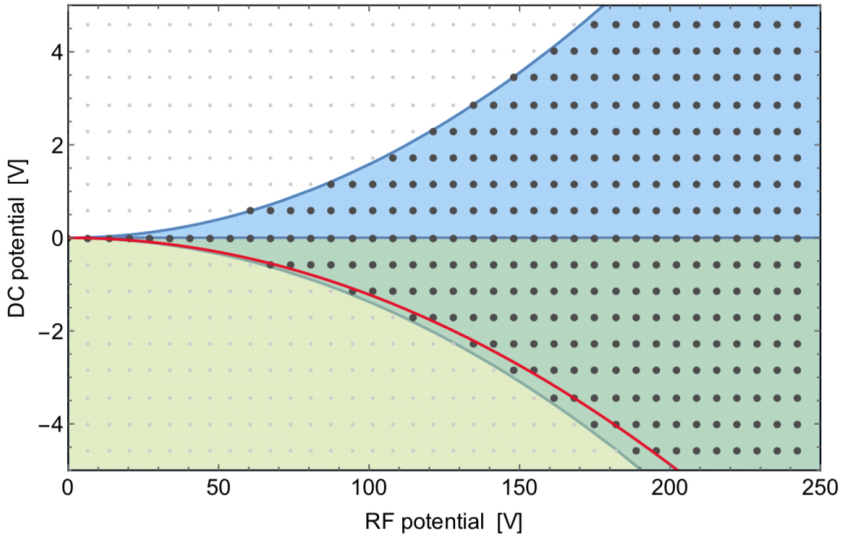


Figure 4.3: Stability diagram for our experimental Paul trap at low potentials range. The black thick dots represent $\{q, a\}$ pairs for which the Paul trap (described by a system of coupled Mathieu equations) is stable, whereas the small gray dots indicate instability pairs. The blue curves, calculated with the multiple-scale perturbation theory, enclose a stability region which is wider than the numerically estimated one, yet well describing the stability behavior for small values of $q$. The green area is the stability region of the corresponding uncoupled system. The red curve indicates the pairs of RF and DC voltages for which the trapping frequencies along the $y$ and $z$ directions are equal. Figures adapted from [116].

pair of tips aligned along the $y$-axis , the distance between each pair of DC electrodes must be small compared to the distance between the two pairs [116].

### 4.1.2 Stability diagram of the Paul trap

In Sec. [2.2] it is shown how the kinetic of an ion in a Paul trap can be entirely modeled by the Mathieu equations (2.26-2.28). The geometry of the electrodes forming the trap determines $\kappa_{RF}$ and $\kappa_{DC}$, i.e. the proportionality factors in Mathieu parameters $a$ and $q$, see eq.s (2.29,2.30). The $a$ and $q$ parameters, that depend respectively on the amplitude of the RF voltage and on the DC voltage of the endcaps, determine if the centre of the trap is a stable or unstable equilibrium point [103].

In designing the ion trap, the electric fields for running the Paul trap were simulated, and a stability diagram for our trap geometry was calculated [116]. As a reference, Fig. (4.3) shows the scales of the voltages that must be applied to our electrodes: a crystal can be obtained by using DC voltages in the range $[0, -4.5V]$ for a RF field of 200 V amplitude. In particular, for sufficiently large negative DC fields, the crystal can be tuned from a linear shape to a 2D symmetric shape (red line in Fig. (4.3)).

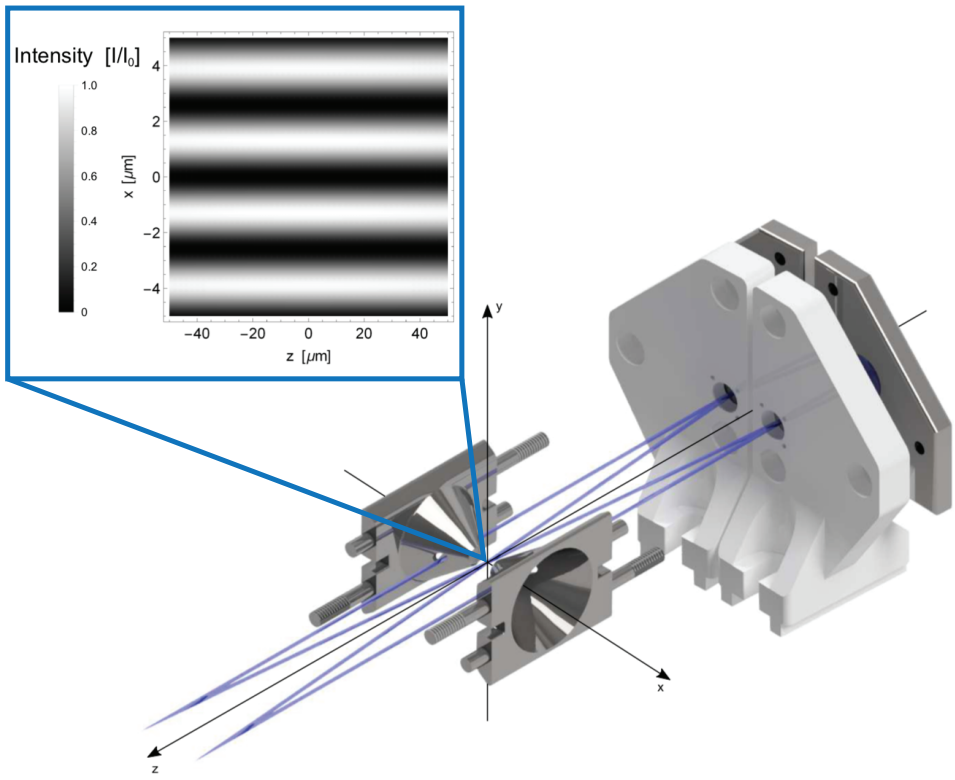


Figure 4.4: Rendering of the cone electrodes and of two of four mirrors that consitutes the bow-tie cavity for the EOT. In blue the optical path of the bow-tie cavity laser beams. In the box panel the intensity profiles of the interference between two focused gaussian beams forming a crossing angle $2\theta_{\mathrm{OL}} = 10°$. Figures adapted from [116].

## 4.2 Electro-optical trap design

The electro-optical trap consists of a quadrupole electrostatic potential confining the ions in two directions and an optical lattice superimposed in the untrapping direction of the quadrupole potential. Our experimental EOT has a design inspired by the scheme of Fig. (4.1). The quadrupole potential is provided by two electrodes that have an hollow shape that makes it possible to have optical access for the imaging. The optical trap is generated by two intersecting laser beams that form an optical lattice. In order to create a deep optical potential, the laser beam power is enhanced by including in the setup a bow-tie cavity. Fig. (4.4) represents the EOT experimental setup, described in detail in this Section.

### 4.2.1 EOT electrodes: mechanical description

In our experimental EOT, the electrodes have a conic hollow shape in order to maximize the exploitable numerical aperture for an objective with the optical axis along the $x$-direction. Moreover, the conic shape maintains the same rotational symmetry around an axis as that of a simple tip. Fig. (4.4) shows the cone electrodes: two holes are placed on the sides of each cone electrode and the laser beam resonating in the bow-tie cavity passes through these holes. Numerical simulations of the fields guar-

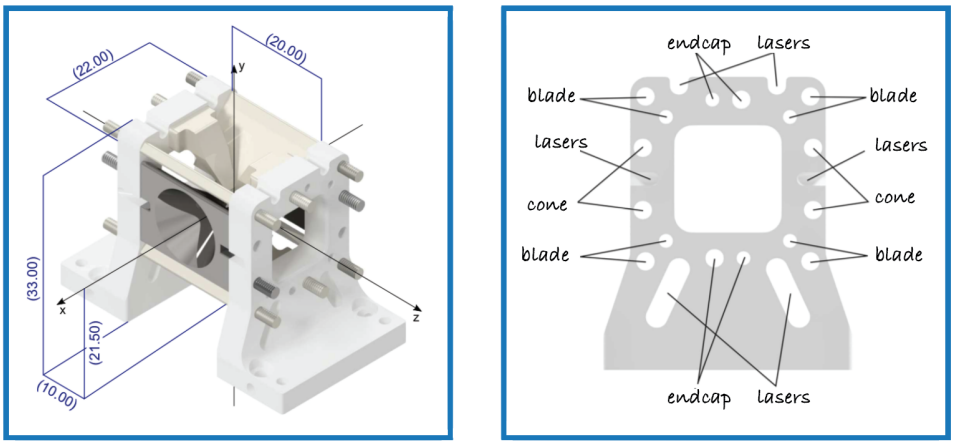


Figure 4.5: a) Rendering of our experimental ion trap design, some relevant ideal distances between electrodes are reported in mm. (b) Section of one lateral support for the ion trap electrodes. In the design some holes have been provided for extra-optical access for laser beams. Figures adapted from [116].

antee that the holes for the passage of the laser beams do not modify the quadrupole potential generated by the cones [116].

### Lateral Supports

All the electrodes must be precisely placed near the ideal trap center. Fig. (4.5) (a) provides some of the dimensions of the trap, more details about the exact dimensions of each electrode can be found in Elia Perego's thesis [116].

In order to ensure a precise positioning of all ten electrodes, the electrodes are mounted on the two lateral supports represented in Fig. (4.5) (b). Each electrode is provided with two dowels, some of which provided with a M2 thread at the end of the tip, so that the electrical connections are ensured by using cable toes tightened to the same nuts used to tighten the electrodes.

### Materials

As conductor material for the realization of the electrodes, a titanium alloy has been chosen because of its ease in processing and for its low thermal expansion coefficient compared to other metals. As isolator material it has been used the patented Shapal Hi-M Soft [148], a special aluminum nitride ceramic that has the property to be a good electric isolator but also a good thermal conductor. Moreover, like titanium, it has a very low thermal expansion coefficient of 4.8 $\mu$m/mK. This property makes Shapal an excellent material to construct electrodes holders, ensuring the electrode positions remain constant and thus ensuring a stable alignment between the optical and the electrical potential. For the same reasons also the bow-tie cavity mirror holders are made in Shapal ceramic while the base on which both the mirrors and the ion trap are mounted is realized in titanium alloy.

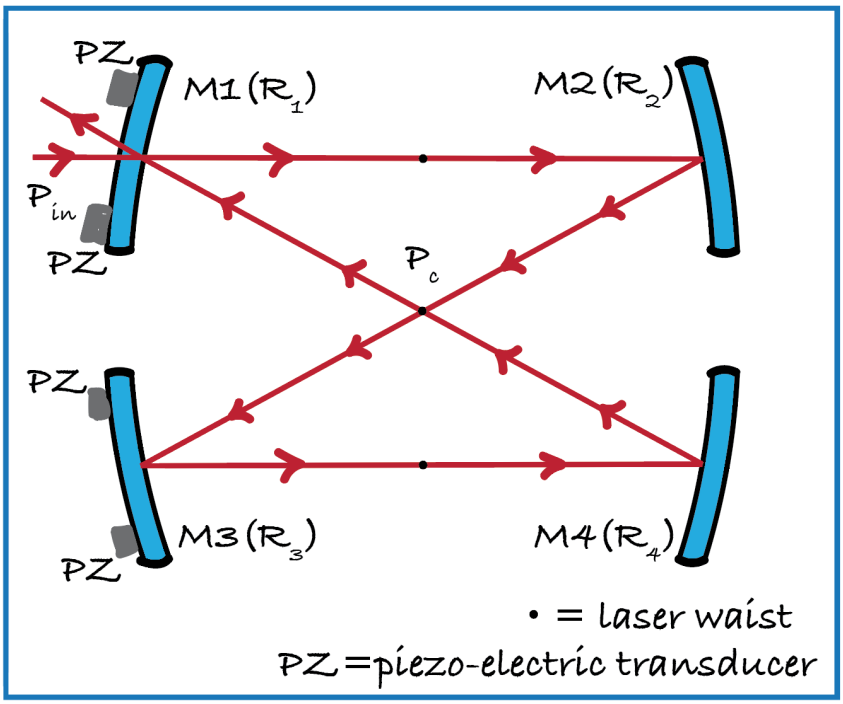


Figure 4.6: Scheme of four-mirror bow-tie cavity resonator.

### 4.2.2 The bow-tie cavity

In order to increase the lifetime and the number of ions that can be trapped in the EOT, it is important to realize the deepest possible optical potential. To this end, we have decided to pursue the strategy of using an optical resonator to increase the intensity of the interfering optical fields. Specifically, we have decided to use the interference between the two crossed arms of a bow-tie cavity, see of Fig. (4.6).

In a traveling-wave resonator like a bow-tie cavity, an optical mode travels in one direction along a closed path – the total length of which is $2l_c$ – and repeats this path without reversing the wave-vector [117]. The resonant frequencies of the modes may be obtained by equating the round-trip phase shift to $2\pi$. It results that the resonance frequencies are $\nu_0 = n \times \mathrm{FSR}$, where

$$\mathrm{FSR} = \frac{c}{2l_c} \tag{4.1}$$

is the frequency spacing between two adjacent resonator modes (the cavity *free spectral range*, FSR) and $n$ an integer.

An important parameter for an optical resonator is the *finesse* $\mathcal{F}$, a parameter that depends only from the mirrors' reflectivity and that is proportional to the number of round trips a photon does before leaving the cavity [117]:

$$\mathcal{F} = \frac{\pi L_p}{l_c} = \frac{\pi c t_c}{l_c} , \tag{4.2}$$

where $L_p$ is the mean optical path of a photon in the resonator and $t_c$ is the photon lifetime in cavity. With the free spectral range and the finesse, it is possible to calculate

the full width half maximum of a resonator mode:

$$\delta\nu = \frac{\mathrm{FSR}}{\mathcal{F}} \ . \tag{4.3}$$

The intra-cavity power is also proportional to the finesse, and it is equal to:

$$P_\mathrm{c} = \frac{\mathcal{F} P_\mathrm{in}}{\pi} \ . \tag{4.4}$$

By exploiting this factor, we can increase the power of light participating to the formation of the optical lattice of the EOT. Notably, this type of optical trapping has been successfully realized for neutral atoms [149].

The bow-tie cavity of our experimental setup is designed to create a one-dimensional blue-detuned optical lattice to confine ions in $z$-$y$ parallel planes, see Fig. (4.4). The bow-tie cavity is formed by four curved mirrors, supported by ceramic holders, that make the laser beam circulate in the optical path shown in Fig. (4.4).

All the four mirrors have the same radius of 100 mm. This choice ensures that each arm of the bow-tie cavity has its own focus. The two focuses of the intersecting arms are superimposed to generate the optical lattice. The intersecting angle between the two laser beams that form the optical lattice is $2\theta_{OL} = 10°$. The small amplitude of $\theta_{OL}$ facilitates the possibility of confining atoms and ions in a single minimum of the optical potential because the lattice constant is much larger than in the case of a lattice made by counter-propagating laser beams.

The laser light at $\lambda_\mathrm{M} = 451.7$ nm is generated in a second harmonic generation cavity (SHG cavity) from a laser at 903.4 nm. The lattice constant is given by equation (2.36) and for $\lambda_\mathrm{M}$ is about 2.5 $\mu$m. The light at 903.4 nm originates from an ECDL and then it is amplified by a TA that guarantees an emission power up to 3 W. The detailed experimental setup is described in [116]. The duplicated light is sent to the experimental table with an optical fiber. Considering all the possible losses, i.e. cavity coupling, doubling efficiency, fiber coupling, AOM efficiencies etc., we estimate to be able to couple in the bow-tie cavity approximately 250 mW of light at $\lambda_\mathrm{M} = 451.7$ nm.

A bow-tie cavity has four arms with a gaussian laser beam each: the waists of horizontal beam branches are about 200 $\mu$m, while the waists of the intersecting beams are about 40 $\mu$m.

With ultracold neutral atoms, trapping techniques that exploit a deep optical potential generated by a bow-tie resonator cavity were yet experimentally tested [149]. Moreover, a large literature exist about controlling the coupling between ions and electromagnetic fields in optical cavity [12, 150–152]. In our experiment the cavity is designed essentially to obtain a deep trapping potential for the EOT and experiments to investigate the ion-cavity coupling are not planned in the immediate future. However, in order to not preclude such opportunity the cavity mirrors (by FIVENINEoptics) have a coating designed to work at three wavelength: $\lambda_\mathrm{M} = 451.7$ nm, $2\lambda_\mathrm{M} = 903.4$ nm and at 493.5 nm, i.e. the $^{138}$Ba cooling transition.

Every mirror holder has three micrometric screws to align the cavity and two of the four mirrors have piezoelectric translators to lock the cavity: the cavity resonance at $2\lambda_\mathrm{M}$ will be used to lock the cavity length. The resonance at 493.5 nm was used to measure the cavity finesse $\mathcal{F}$, value that does not differ so much from the finesse at $\lambda_\mathrm{M}$. The esteemed finesse value is $\mathcal{F} \simeq 1700$ and it was obtained by measuring

the photon lifetime in cavity $t_c$, i.e. by turning off the cavity at resonance and then observing the decay of the cavity intensity profile in time.

Using eq. (4.4) to evaluate the EOT potential of eq. (2.44) with our experimental value for $P_c$ and $\mathcal{F}$ we can estimate a trap depth of 300 mK.

## 4.3 Other elements in trapping process

We have so far rapidly discussed the elements of the Paul trap and of the electro-optical trap. In this chapter we focus on the ions production, which is based on photoionization of hot neutral Ba atoms produced in two separate ovens.

### 4.3.1 The ovens

The ion trap is equipped with two ovens to produce hot vapours of neutral Barium atoms. Referring to Fig. (4.7), the oven are the grey tubes labelled with number (5). Micro-spheres of metallic Barium were pressed inside these tubes in an inert atmosphere of Argon gas to avoid Barium oxidation. Then, the ovens were carefully inserted in two holes in a copper heat-sink (1). The friction between the ovens and the heat sink ensures that the ovens hold without the necessity of fixing them in other ways. The inclination of the heat-sink holes applies a first velocity selection on the Barium atoms and ensures that their trajectories pass through the trap center. The tubes are both thermally and electrically connected to the copper-heat sink that has two functions: ensuring the connection to ground and rapidly cooling the Barium sample when the ovens are turned off.

The oven tubes are realized in stainless steel 316L, a metal with low electric conductivity that facilitates the heating for Joule effect. The tubes have a total length of 10 mm, an outer diameter of about 1.5 mm and an inner diameter of 1.2 mm. The tubes are crimped to a copper wire with a diameter of 1 mm covered by Kapton coating, a patented polyamide film. This thin wire brings current to the tubes, which flows through them towards ground: a ground pin is then connected to the copper heatsink. The lowest part of the ovens is expected to reach a temperature of about 500 K, only estimated with simulations [116] and not measured, while the upper sides of the tubes are in direct contact with the copper heat-sink that can be considered at room temperature: in the ovens there is a temperature gradient that facilitates the production of a collimated atomic beam. Because of this thermal gradient the ovens were filled with Barium only in their lowest parts, those that would reach high temperatures. Moreover, thanks to the thermal connection with the heat-sink the oven is rapidly cooled down when the current is turned off.

The barium atomic beam experiences a first velocity selection by two small holes placed in a ceramic plate at room temperature, (11) in Fig. (4.7). Before reaching the trap center, the atomic beam pass through a cylindrical hollow (13) that protects the electrodes from possible sputtering of atoms, and through a hole on the titanium baseplate. The diameter of this hole is different for each oven: the one indicated with (15) in Fig (4.7) has a diameter of 0.4 mm and the one indicated with (16) a diameter of 1.2 mm. The atomic beam passing from the smallest hole should reach the trap center without sputtering the electrodes, while the larger one is thought for applying a coarser velocity selection of the Barium atoms, and a minimal sputtering of the electrodes surface may occur when the oven is run.

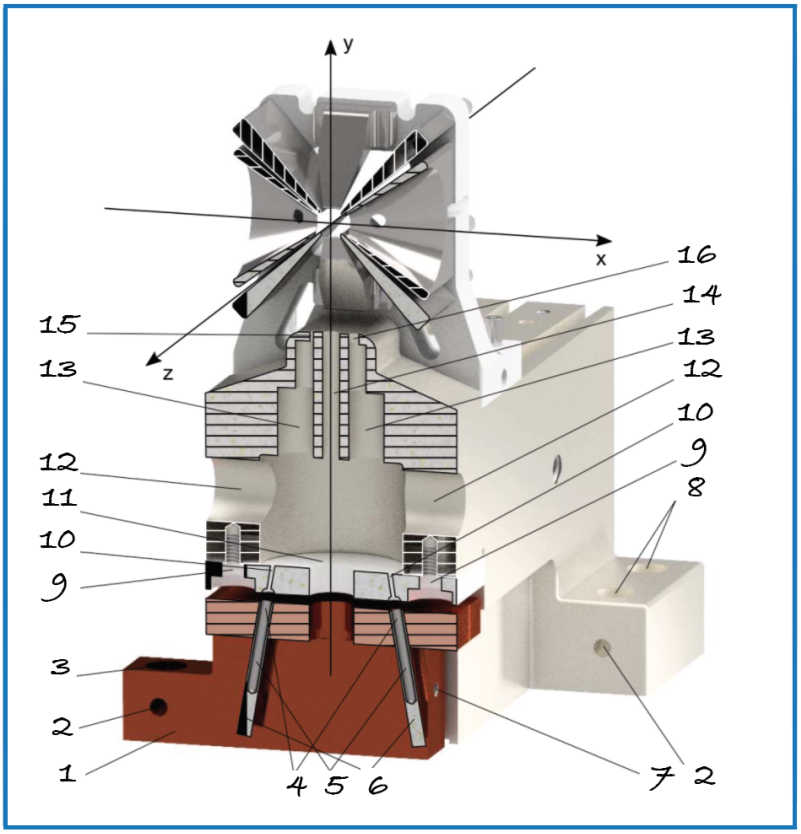


Figure 4.7: Section of our experimental ion trap in a vertical plane passing through the trap center. The numbered elements of the trap are: (1) copper heat-sink,(2) venting holes,(3) screw passing hole for fixing the heat-sink on the flange, (4) cold upper part of the (5) tubes with Barium, (6) tube stripes for the electric connection, (7) threaded hole for the ground-connecting the heat-sink, (8) screw passing holes for fixing the base on the flange, (9) pipes and (10) screw passing holes of the cold ceramic, (11) skimmer, (12) inspection viewports of the (13) cylindrical oven chamber, (14) anti-sputter wall for protecting the vertical optical access, (15) and (16) output holes. Adapted from [116].

At the moment of designing the ovens, several simulations were executed to estimate their performance [116]. In order to reach a temperature of 500 K for the ovens it is necessary to provide them with a current of 100 A for 200 ms. This value will be experimentally adjusted during the trap loading optimization phase, and from some preliminary runs it would be sufficient to let the current on for about 100 ms to see a change of pressure in the vacuum pump.

From electrostatic simulations also the oven electric resistance has been estimated: $R_{\text{oven}} \simeq 5.9$ m$\Omega$. This value, despite the fact that the design of the oven is conceived to maximize the resistance, is quite small. In realizing the electrical setup for the ovens, described in Sec. [4.6], this value has to be compared with the resistance of the other components of the circuit. The electrical setup is designed in order to ensure that most fraction of the dissipated power for Joule effect will be dissipated in the oven and not on the copper cables and in their junctions and eyelet lugs. This not only for having an efficient electrical setup but, in particular, to avoid the heating up of the cables and the trap environment in general. We have estimated that the total resistance of the oven setup should be smaller than 10 m$\Omega$: in Sec. [4.6] the precautions for reducing as much as possible the total resistance of the circuit are described.

### 4.3.2 Ionization process

Barium neutral atoms are produced for evaporation from a solid sample by using the ovens described in the previous section. Then, the atoms are ionized near the centre of the trap and captured in the Paul trap. A typical method to ionize neutral atoms is to use an *electron gun* [153]. However, this method present strong drawbacks as massive charging up of trap surfaces, due to the electron impact on them, and the creation of impurity ions, i.e. ions of different isotopes, because the ionization process is not isotope selective.

For these reasons, we have decided to adopt the photo-ionization method in our experimental setup. This technique has already been tested for loading Barium ions in Paul traps [154] and it is isotope-selective.

Our photoionization scheme relies on a first excitation of neutral Barium atoms from the ground state $6s^2\ {}^1S_0$ to the level $5d6p\ {}^3D_1$ by absorbing a photon at 413 nm, then the atoms are ionized by absorbing a second photon at the same wavelength. This photoionization scheme is not the most efficient because the transition between the level $6s^2\ {}^1S_0$ and $5d6p\ {}^3D_1$ is an intercombination line for neutral Barium with a transition line width of about 240 kHz [155]. Moreover from $5d6p\ {}^3D_1$ the Barium atom can decay in other metastable levels that are dark for 413 nm light [155].

In order to improve the efficiency and increase the production rate, a second resonant two-photon scheme can be adopted. This scheme involves the radiation at 553.7 nm to drive the transition from the level $6s^2\ {}^1S_1$ to the level $6s6p\ {}^1P_1$ of the neutral Barium and then the absorption of a photon at 413 nm for the effective photoionization transition [156]. The ionization rate with this second method is expected to increase by a factor 40 with respect to the previous laser waists and the same laser powers, but has the disadvantage of adding a second laser source. However, we decided to opt for the photoionization method that requires only one laser source at 413 nm because realizing a laser at 553.7 nm is technically challenging while buying it is very expensive and we believe that the selected photoionization method would not compromise the experiment performances.

Our 413 nm is focussed at the centre of the trap, and it has a light power of about 10 mW. As a reference, in a similar experiment on $Ba^+$ ions, ion loading rate on the order of one ion per second was observed for a laser of 4 mW and a waist of 440 $\mu$m [154].

## 4.4 $Ba^+$-Li imaging

A fundamental part of the experiment is constituted by the high numerical-aperture (NA) objective, since it will provide a high resolution imaging of the quantum hybrid system. In this experiment the objective is designed to work in vacuum, very close to the centre of the ion trap and, in order to focus at the same time the fluorescence of the ions at 493 nm and of the neutral atoms at 671 nm in the same image plane, it has to be achromatic and fulfill different optical requirements for the atoms and the ions. We expect the ions to arrange in crystal-like configurations that range from linear to two-dimensional crystals. The typical reciprocal distance between the ions is approximately 10 $\mu$m, and they can occupy an area of radius up to $\simeq$ 100 $\mu$m. The imaging system has to be able to detect the ions in a large crystal, and a sub-micron resolution could allow us to measure the temperature and the micromotion of the ions from their spatial delocalization [157]. Moreover, we plan to eventually trap the neutral atoms in an optical lattice with lattice constant 532 nm. Therefore, the resolution of the objective should ensure a single site resolution imaging [158].

The choice of installing the objective directly in the vacuum chamber is not very common [159]. It was adopted because it gives us the possibility to collect light from a very large portion of solid angle and to collimate the light rays before they pass through the vacuum window. The collimation in vacuum solves most of the problems related to aberrations because the vacuum window is substantially a plate with plane parallel faces, which does not create aberrations on a collimated beam but it does on light rays originating from a point source. However, the objective has to be ultra-high vacuum (UHV) compatible, and doublets cannot be used since the glue is not UHV compatible. As a result, the realization of an achromatic objective working at the Li and $Ba^+$ wavelength is particularly challenging. Additionally, a high numerical aperture objective must be precisely positioned in space, and we opted to use a 5-axis translator (three directions and two angles) in vacuum.

The objective has an original design that fulfills all the requirements. My master thesis work consisted in the design of this objective, by implementing a program based on simulated-annealing algorithm to minimize a particular test function which takes into account all the relevant aberrations. The final results of the objective is shown in Fig. (4.8): it is achromatic and diffracted limited with a NA $\simeq$ 0.5 [160]. In the next two subsections I will describe briefly the tests made on the two objectives we have commissioned to a specialized company (Sill Optics) and delivered during my second PhD year. I will explain first the theoretical relations between the numerical aperture NA and the diffraction limit of the objective, then I will show how it is really diffracted limited and how it is possible to quantify its field depth. Finally, I will illustrate how the most performing objective was mounted on the five-axis translator and how the imaging system in its final position was tested.

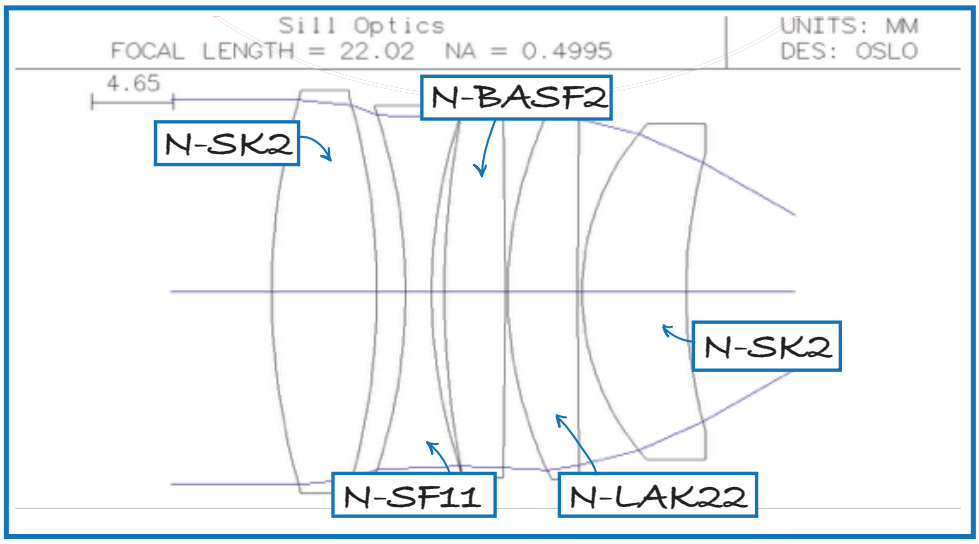


Figure 4.8: Final design of the high NA objective. Of every lens is indicated the glass material used to fabricate them. The poor image quality is due to low-resolution graphics of OSLO, the ray tracing program used for the objective design.

### 4.4.1 Diffraction theory

Let's consider a collimated beam that enters on a circular aperture of radius $a_{\mathrm{cb}}$: the planar infinite wavefront is cut by the diaphragm. Let's also consider a thin lens of focal length $f$ having the optical axis coincident with that of the aperture stop and placed after it. If we measure the light intensity on a plane at a distance $f$ from the thin lens, the intensity profile will be the Airy function, which in the far-field approximation reads [137]:

$$I(X) = I_0\left(\frac{2J_1(X)}{X}\right)^2 , \tag{4.5}$$

where $I_0$ is the maximum intensity of the pattern at the Airy disk center, $J_1(X)$ is the Bessel function of the first kind of order one and $X = ka_{\mathrm{cb}}\sin(\theta_{\mathrm{obs}})$ with $k$ the wavenumber, and $\theta_{\mathrm{obs}}$ the observation angle, the latter defined as the angle between the axis of the circular aperture and the line between the aperture center and the observation point (see Fig. (4.9) (a)). This resulting image is a collection of concentric circles with variable intensities, like the ones represented in Fig. (4.9 (b)).

The brightest disk at the centre is called Airy disk and its radius can be evaluated using the equation:

$$R_{\mathrm{Airy}} = 0.61\frac{\lambda}{2\mathrm{NA}} . \tag{4.6}$$

The numerical aperture NA is defined as:

$$\mathrm{NA} = n\frac{a_{\mathrm{cb}}}{f} = \frac{n}{2(F\#)} , \tag{4.7}$$

where $n$ is the refractive index of the lens and $(F\#)$ is the so called *f-number*. The Airy Disk sets the scale of the physical limit in the resolution of an imaging system.

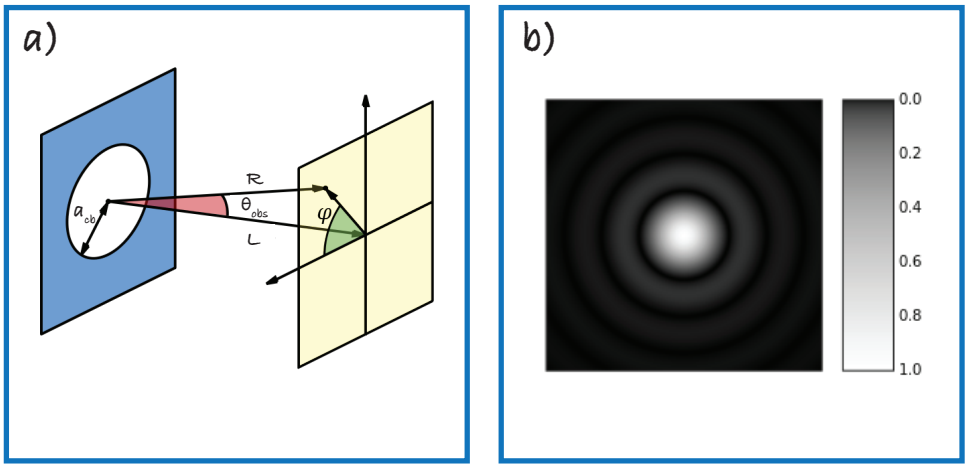


Figure 4.9: (a)Schematic representation of the aperture stop, in blue, and of the image plane in yellow. The angle in red is the observation angle $\theta_{obs}$ and the one in green is the angle that identifies the image point in the image plane. (b) Reproduction of the Airy function in 2D, the grey scale is adapted to enhance the external disks.

If we attempt to image atoms or ions, which can be approximated to point sources, at best we will see them as their correspondent Airy Disk, unless one has additional information, e.g. the spacing between particles like in optical lattices [158]. Systems that focus all the rays inside the Airy Disk are said diffracted limited. Theoretically, our objective should have a resolution limit of about 600 nm for the fluorescence wavelength of the Barium ions and of approximately 820 nm for the fluorescence wavelength of the Lithium atoms.

### 4.4.2 Testing the objective depth of field

We have decided to produce two identical objectives since it cost little more than purchasing a single one; in this way we could implement in the experiment the best one of the two. In order to test the objectives we used an experimental setup constituted by a target, the objective collecting and collimating the light from the target, and a lens of focal $f = 500$ mm that focuses the collimated light from the objective onto a CCD camera. The target, shown in Fig. (4.11) (a), is a glass opaque slide with nanometric slits (courtesy of Christian Gross) backlit with a laser of the proper wavelength: 493 nm or 671 nm in our case. The magnitude was measured by moving the target on a calibrated translator with respect to a direction perpendicular to the optical axis of the system. By comparing the shift of the real target to that of its image it is possible to measure the magnification. The estimated magnification of the setup is $22.67 \pm 0.45$, compatible to the expected magnification of 22.8, simulated with a ray-tracing software.

Knowing the magnification of the optical setup and the theoretical resolution limit of the system, it is possible to measure the depth of focus of the objective. To this end, we moved the target along the direction of the objective's optical axes and found a set of positions for which some points have an image with a diameter comparable to the resolution limit times the expected magnification. In this interval of positions the objective can be considered at focus and this interval corresponds to the depth of

field. The measured depth of field is approximately 5–10 $\mu$m for both wavelengths at which the objective must work. In Fig. (4.10) I show the measured depth of field for the objective that we decided to mount in the vacuum chamber.

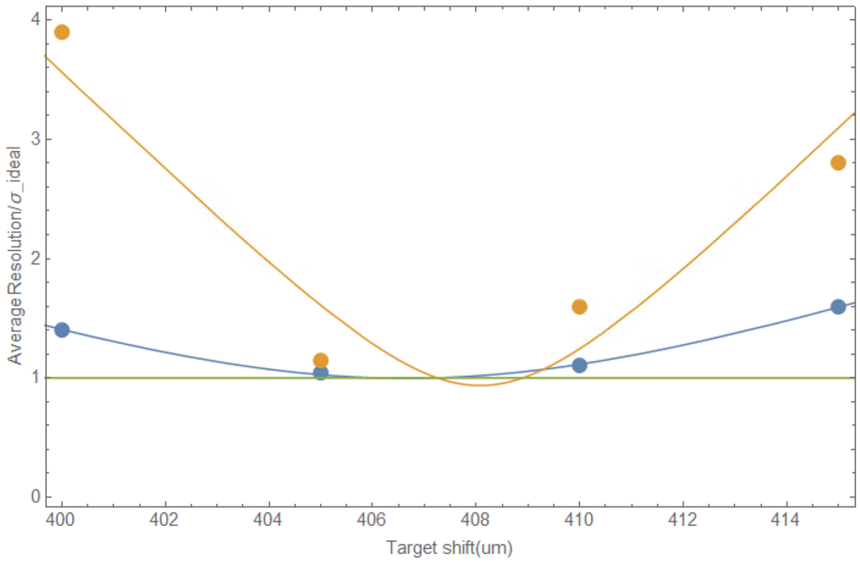


Figure 4.10: Measure of the depth of field for the objective mounted in the vacuum chamber at 493 nm and 671 nm. The green line represents the resolution limit. In blue the data taken at 493 nm for some diffracted limited slits, in orange the data for 671 nm, the data are fitted with eq. (2.39). The points images' dimensions are reported in diffraction limit units.

From this test we concluded that both objectives are resolution limited and behave up to specs for achromaticity and lateral displacements. However, we chose to discard one of the two objectives because it presented a ghost image and a more significant diffraction pattern, probably related to the ghost image problem.

### 4.4.3 Installation of the high NA objective in vacuum

The UHV compatible translator by SmarAct, holds the objective with the possibility to move it in the three spatial directions and to rotate it with respect to the two directions perpendicular to the optical axis. The translation along the optical axis is constantly monitored by an encoder that quantifies the translation in $\mu$m. For the other degrees of freedom, the translator is not provided of such encoder, so its displacement is affected by hysteresis.

To prove the correct functioning of the translator and characterize the hysteresis, we have used as target a micrometric needle in tungsten that I have realized, using an electrolytic erosion technique [161]. The tips have been measured with a micrometric ruler using a microscope and their tighter parts are about 10 $\mu$m thick. With the upper flange removed, we have positioned the needle tip in the place where approximately there would be the centre of the trap and where the ions will be detected. By irradiating the needle from the side with a laser at 493 nm and using an imaging setup similar to that described in the previous section, we have obtained the image of the tip, shown in Fig. (4.11) (b).

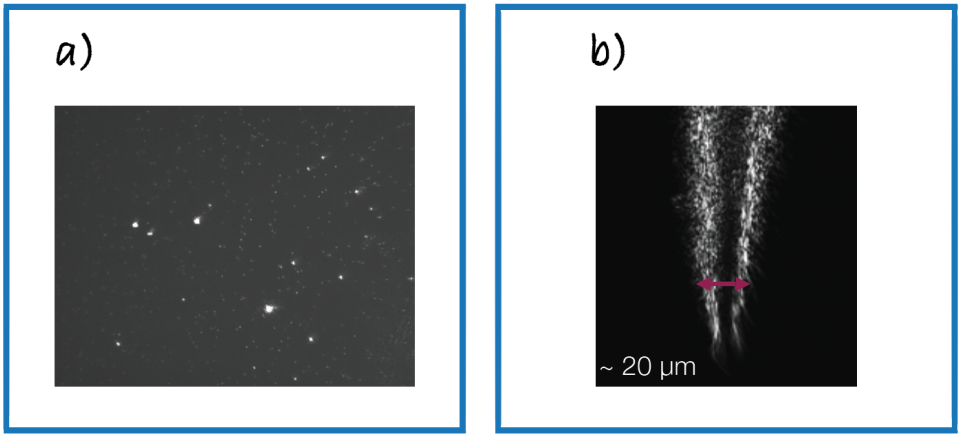


Figure 4.11: Images of some target used to test the objective and calibrate the 5-axis translator. In picture (a) the image of a glass opaque slide with same nanometric slits backlit with a laser of the proper wavelength (493 nm or 671 nm). In picture (b) a micrometric tip of a tungsten needle realized with electrolytic erosion technique [161].

We used the needle image to measure the minimum displacement of the translator: we fit the intensity profile of the needle in a certain position and then, moving the objective of the minimum translator step, we acquired a new image and fit it again. In this way it was possible to determine that one step of the translator along the horizontal direction corresponds to about 4 $\mu$m, and to about 0.13 $\mu$m in the vertical direction. Then, in order to quantify the hysteresis, we moved the translator back and forth, taking more images when the translator was in the same nominal position. By extrapolating the shift between the various fits of the needle, it is possible to determine that the hysteresis in the horizontal direction is $0.70 \pm 0.02$ $\mu$m and that in the vertical direction is $0.022 \pm 0.003$ $\mu$m. The uncertainty due the hysteresis phenomenon is consequently characterized at most as the diffraction limit of the objective and therefore it should not represent an issue for the imaging.

## 4.5 The Barium vacuum chamber

In the previous sections of this chapter I have described all the mechanical parts inside the Barium experimental chamber. All these components are mounted on the lower vacuum flange of the chamber. The positioning of all the elements is shown in Fig. (4.12), in which is presented a rendering of the lower vacuum flange. In this Section I will give some information about the assembling procedure of the vacuum flange.

### 4.5.1 Barium chamber assembling

Before the final assembling, the trap elements were cleaned using isopropanol and blowed dry with nitrogen. This procedure is a slight modification of the technique used in similar experiments [162] in which the components are first cleaned with a degreasing detergent, then acetone and finally methanol, before blowing the parts with nitrogen to dry them up. The reason why we have decided to modify this procedure

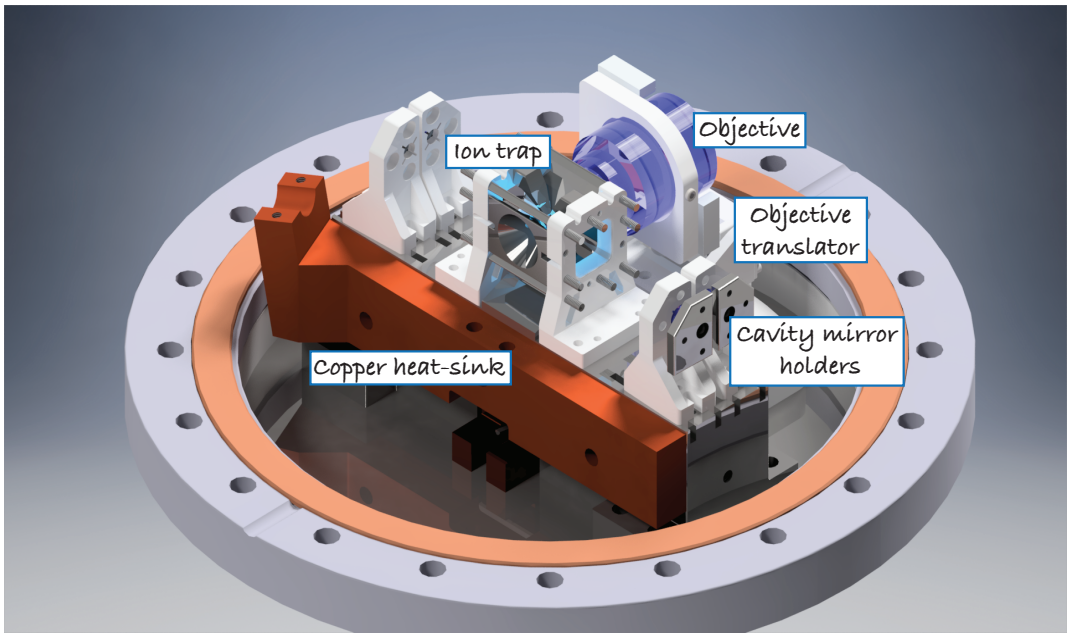


Figure 4.12: Rendering of the interior vacuum flange of the Barium experimental chamber in which is mounted the ion trap with its bow-tie cavity for the EOT and the vacuum-compatible high NA objective just near the trap itself.

is that titanium alloys are subjected to *Stress Corrosion Cracking* (SCC) by effect of methanol [163].

After assemblying, we ensured that all the electrical connections between the electrical feedthroughs in the lower vacuum flange and the trap electrodes were not faulty. The connections were realized by using copper wires coated in Kapton furnished by Allectra, a company specialized in vacuum products. I removed the kapton coating at the endings of the wires by using a scalpel to scrape off the insulating material with the help of a microscope. More layers of Kapton film form the coating, and it is necessary to remove all of them in order to ensure a good electrical connection of the wires. For each wire, I crimped an eyelet lug to screw the wire to the threaded dowel of one of the electrodes, while I crimped the other end of the wire on a hollow connector provided by Allectra, which was then inserted on the flange feedthrough. The trap is completely symmetric with respect to a vertical plane passing to its centre, so we tried not to break the symmetry of the configuration with the electrical connections, while avoiding the obstruction of the optical access to the center of the trap. In order to verify that the symmetry of the physical circuit was respected as much as possible we measured the trap capacitances with a Vector Network Analyzer (VNA), see Sec. [4.7]. The network analyzer was connected to the external side of the feedthroughs in the lower flange and calibrated to measure the impedance at the feedthrough. In order to minimize the wire capacitances, we took care to make the wires as short as possible, and in keeping them far apart. Fig. (4.13) shows a picture of the lower flange with the ion trap and the wire connections.

As already mentioned, Barium is a reactive element, and it can oxidize in minutes if left at open air. Therefore, we had to fill the ovens in an inert atmosphere. We have used two different disposable glove-boxes in PVC (Sigma Aldrich atmosbag): a small

one to fill the ovens and a larger one covering the entire vacuum chamber to install the oven in place and close the vacuum chamber. To do so, we accessed the vacuum chamber by removing the upper flange. In order to ensure an inert atmosphere in the glovebox, we continuously filled it with Argon from a gas bottle, while from a second aperture we pumped the air in the glove box out by using a membrane vacuum pump. The transition from one glove box to the second one was done by placing the oven structure in a hermetic sealed jar. Moreover, in order to ensure that the Barium in the oven was not oxidizing, we placed some of the Barium in an open jar, which was periodically checked during the operation until the vacuum chamber was closed. The overall operation took approximately 4 hours, mainly caused by the remote position of the ovens and by the necessity of working in the very uncomfortable environment of a glovebox.

### 4.5.2 The Bake-Out

Before assembling the vacuum system, all the components in the vacuum chamber, like flanges, the chamber itself, vacuum tubes, screws etc., were pre-baked at relative high temperatures ($T_{\text{pre-baking}} \simeq 400°\text{C}$ at maximum) for about two weeks. Other components like the objective, the objective translator, the trap itself and the copper wires, were not brought to such high temperatures, in order to avoid either damage to the materials (e.g. the coating of the lenses in the objective) or mechanical problems in the assembly of the ion trap due to hysteresis on the materials. Bake-out is an artificial acceleration of the natural process of outgassing; therefore, during the pre-baking phase the stainless steal part of the vacuum chamber lost for sublimation or evaporation most part of the volatile impurities trapped, absorbed or dissolved over the objects surfaces. This acceleration is due to the enhancement of the mean squared velocity of the volatile compounds caused by the heating. The main part of the impurities trapped in steel are $H_2$ and $H_2O$ molecules.

After this pre-baking the vacuum chamber was assembled and closed by using a blind flange as the lower flange. A preliminary vacuum was realized in this condition to test that all the necessary parts were correctly assembled and nothing was damaged during the baking. We decided not to add the lower vacuum flange with the ion trap during this stage to remove a degree of complexity in the first attempt in the realization of a UHV environment. We were able to place the chamber at a fraction of $10^{-9}$ mbar with a turbo pump and a gauge for measuring the pressure.

After this preliminary vacuum test the lower flange with the ion trap was placed in place of the blind one. Once the vacuum chamber was completely assembled, it was heated using thermo-regulated bands. In order to make heat propagation uniform, the vacuum chamber was completely covered with multiple layers of aluminum sheets, held together by copper wires. A turbo pump (Agilent Twis 84) was pumping the system while the bake-out was running at a temperature $T_{\text{Bake-out}} \simeq 95°\text{C}$, sufficiently low to not damage the sensitive parts in the chamber. With the turbo pump on we reached a pressure of some $10^{-9}$ mbar. Aside an ionic-getter pump (SAES Next Torr 500D) was activated: during the activation the getter material is heated to approximately 500°C to clean the getter from impurities pumped out by the turbo pump. When the activation was completed, we waited the ionic pump to reach the room temperature and then we turned it on while the valve that connects the vacuum chamber to the turbo pump was closed.

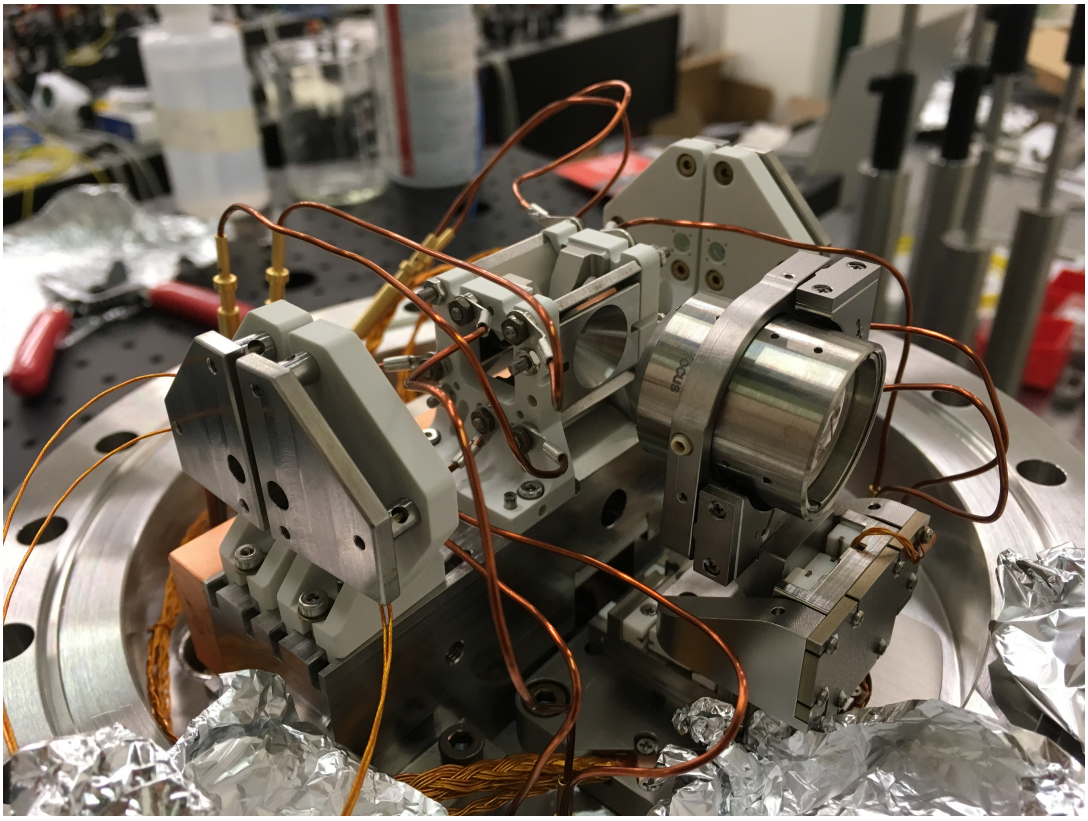

Figure 4.13: A picture of the Barium interior trap before the chamber was closed. In addition to the trap and the objective, the electrical connections provided by the copper cables can also be seen.

After this first attempts to realize the UHV we obtained a pressure of approximately $10^{-10}$ mbar while we expect pressures of the order of $10^{-11}$ mbar. These pressures were measured by looking at the residual current in the ionic pump. After a leak test with helium flux we discovered a small leak in one of the flanges, leak that was not discovered with the only turbo pump on. Consequently we substituted the flange and its gasket and run a new bake-out. However we still found a residual current in the ionic pump: using a residual gas analyzer (RGA 100 SRS) we discovered an unexpected water residual, probably due to the wire's kapton cover out-gassing. We repeated the bake-out at a higher temperature $T_{\text{Bake-out},2} \simeq 110°\text{C}$ and we managed to reach an acceptable UHV of approx. $5 \times 10^{-11}$ mbar.

## 4.6 Electrical setup for the ovens

In many ion trapping experiments, the ovens are heaten up by running through them moderate currents (typically a few Ampére [147]) for some time until one or more ions are loaded in the trap. The oven then slowly cools down while the vacuum pump lowers the pressure in the chamber. In our experiment, we are interested in studying atom-ion collisions, which may lead to ion losses or the creation of dark ions in the trap [18]. Therefore, we have opted for ovens that can create hot vapours for a very short time (hundreds of ms). In order to create hot vapours in this timescale we need to provide to the ovens brief shots of current on the order of hundreds of Ampére and which last hundreds of ms, see Sec. [4.3]. Feeding the ovens with a high current is a delicate operation and it has to exist a safety system that prevents from evaporating all the Barium by exhausting the ovens or even melting the oven connections.

Our lab is furnished with an original experiment control software, called Yggdrasil, that manages all the analog and digital signals towards the experiment and their timing [164]. By using Yggdrasil, we can turn on the ovens employing a digital signal of the appropriate duration.

The scheme of the electric setup for the Barium ovens is sketched in Fig. (4.14). Through a decoupling circuit, the digital control signal drives the gate of a power MOSFET and connects the oven power supply circuit for the entire duration of the command. The MOSFET driver circuit acts substantially like as a switch for the ovens. When a signal arrives from the command channel, the current can flow from the MOSFET source to its drain and up to 100A are provided by a high current power supply.

In this section, I describe the electric circuit that I designed for feeding the ovens with large currents and protecting them from possible faults of the control software.

### 4.6.1 Precautions for the high amperage

Electrostatic simulations done with Comsol Multiphysics by Elia Perego during the trap design [116] show that the ovens can be treated as a resistive load of 5.9 m$\Omega$ each and that in order to heat them up to 500 K it is necessary to provide a current of 100 A for about approximately 200 ms. Considering the high currents involved, one needs to take a number of precautions in realizing the circuit.

It is important to select copper wires with an appropriate section: the resistance of a conductor is inversely proportional to its area, so a larger wire's section implies a smaller resistance and hence the risk of overheating. For our electrical setup, I have

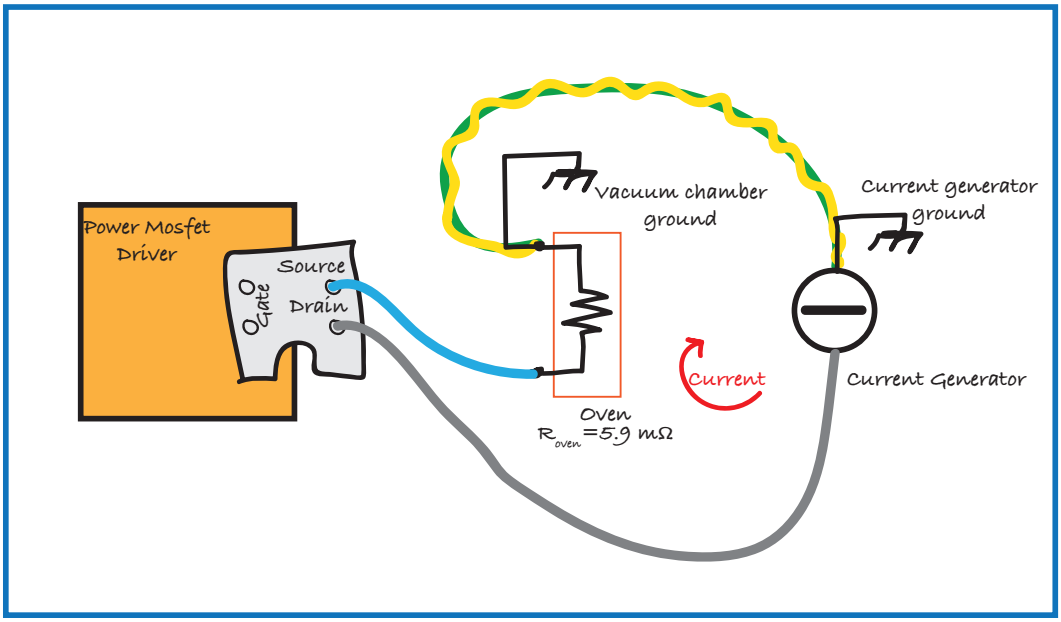


Figure 4.14: Sketch of the electrical setup for each of the two Barium ovens. The current power supply is a Delta SM30-220

used braided copper wires with a section of 35 mm$^2$, the maximum cross-section for a wire that can be crimped in a 8 mm diameter eyelet lug. This limit in the eyelet lugs diameter is due to the need to screw them onto the MOSFET terminals.

In general, connections are the most delicate part to make in a circuit for high current: they typically presents holes and screws, with unavoidable consequent bottlenecks regarding the passage of current. In these points it is difficult to determine the resistance of the connection, and one may incur in the risk of creating local overheating. To avoid this, I decided to realize connections with large contact surfaces and use materials with excellent conductivity. Consequently, the other endings of the wires are connected to the chamber feedthroughs by means of a homemade power terminal block, realized in bulky copper to reduce the resistance of the connection.

Another element that must be considered when designing circuits with high currents is the *induced electromotive force* on all the conducting materials in the laboratory caused by the mutual inductance coefficient. Even when the mutual inductance coefficient is relatively small, the induced electromotive force can be relevant, since this is proportional to the growth rate of the current, which in our case passes from 0 A to 100 A in a few ms. Therefore, we have realized the shortest possible cables and reduced as much as possible the area enclosed by the circuit by intertwining the cables going from the MOSFET to the vacuum chamber and back.

### 4.6.2 The power MOSFET driver

The current of the oven is switched on and off by a power MOSFET (IXFN180N15P N-Channel power MOSFET), which can accept up to 150 A at its source and up to 150 V as the maximum voltage between drain and source. A homemade power MOSFET driver manages the MOSFET status by using a 5V digital signal from the control system of the experiment as input. For simplicity of assembly and construction – the

PCB was printed in the electronic workshop – the circuit consists solely of through-hole components.

The MOSFET driver circuit is composed by three functional blocks as illustrated in Fig. (4.15):

1. The power supply circuit, that takes voltage from the 50Hz power line, generates a DC signal of 15 V by using a transformer and a diode bridge.

2. The control circuit, which passively turns off the current flowing in the ovens after a preselected time $t_{\text{safety}} \simeq 300$ ms, even if the digital command signal is still on. The control circuit prevents damages originating from possible errors in the management of the ovens, which could result in a melting of the ovens or a permanently damage of the trap. The time constant $t_{\text{safety}}$ can be tuned around 300 ms, by using a trimmer .

3. The MOSFET managing circuit with an optocoupler which decouples the digital command signal from the input signal on the power MOSFET gate. The decoupling protect both the digital signal output and the MOSFET gate.

## 4.7 Ion trap electrical model

The Ba-Li ion trap is a complex system of electrodes, designed to implement both a Paul trap and an EOT. Several simulations were performed during the designing phase to ensure the creation of potentials to trap ions, and learn at what voltages the electrodes must be placed.

To this end, it is necessary to simulate the ion trap from an electric point of view and create an equivalent electric circuit modeling the trap. In these section I will describe how I realized this model by using a finite elements software (Comsol Multiphysics). Realizing a correct electrical model of the trap is essential to design the appropriate power supply circuit for the trap.

### 4.7.1 Comsol Multiphysics platform

Comsol Multiphysics is a general-purpose simulation software for modeling designs, devices, and processes in all fields of engineering, manufacturing, and scientific research. It allows to simulate a variety of physical and chemical phenomena both in stationary conditions and in time transients, e.g. electromagnetic and acoustic processes, fluid flows, heat transfer, chemical reactions.

The design of our trap was conceived using Inventor software, a professional-grade 3D CAD software. Comsol Multiphysics is compatible with Inventor and it is possible to import the Inventor's trap assembly in the platform. When solid figures are imported, Comsol meshes the surfaces in a number of tetrahedrons: it is possible to manually impose the level of precision in this "discretization" of surfaces in planar elements. To each solid is assigned a material and every material is characterized by its own electric properties like the conductivity and the relative dielectric constant. For the domain of the simulation we have selected a cube with 1 m side: a volume much larger than the vacuum chamber. Nevertheless, I did not consider the vacuum chamber in the simulation in order not to make it computationally too heavy.

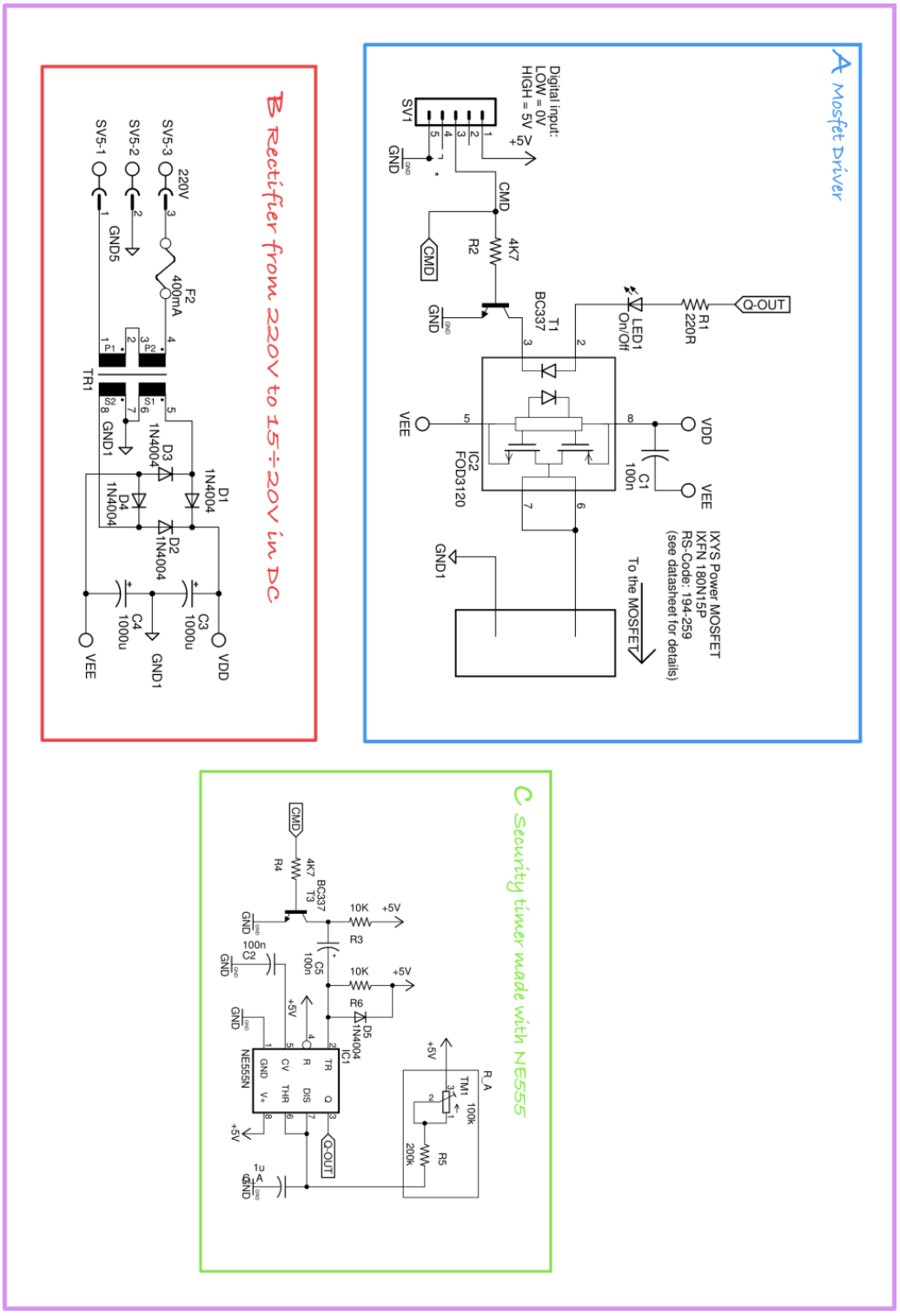


Figure 4.15: MOSFET driver circuit schematic for the Barium ovens

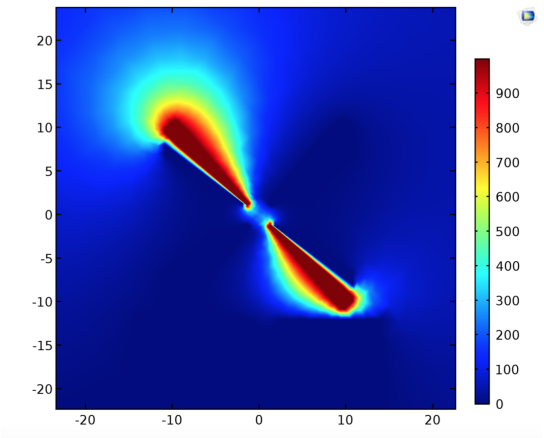


Figure 4.16: Simulated voltage potential generated by charging the RF electrodes of the Paul trap. The electrodes RF1 and RF3 are at the same potential of 1000 V, while the voltage potential of electrodes RF2 and RF4 is set to ground. The simulation allows to predict the voltage in all the domains points: near the centre of the trap the electrostatic potential can be approximated to an electric quadrupole potential. However the potential distribution around the two electrodes is not symmetric with respect to the horizontal plane passing through the trap axis, this is due to the presence of the Titanium base – not shown in picture but present in the simulation – on which the trap is mounted.

When all the physical properties of the system are defined, the electrostatic package of Comsol Multiphysics is invoked. Starting from user defined boundary conditions, e.g. the voltage potential value for the solids' surfaces, the Comsol platform runs a finite element simulation to evaluate the voltage potential in all the preselected domain. Fig. (4.16) is an example of a Comsol Multiphysics simulation. When the voltage potential is numerically determined, all the other electrostatic physical quantities can be extrapolated from it. It is possible, for instance, to determine the charge distributed in all the solid surfaces by integrating the charge density related to the simulated voltage potential distribution.

### 4.7.2 Simulation of the capacitances of the ion trap

The mechanical trap design is shown in Fig. (4.5). Using Comsol Multiphysics, I have estimated the capacitances between all possible pairs of electrodes. To do so, I considered one RF electrode at a time and I set it at a constant potential $V \in [100, 1000]$ V. Then, I set all the other electrodes to ground. By running a stationary study with Comsol, it is possible to obtain the voltage spatial distribution. Then, by integrating the superficial charge distribution on the single electrodes, I computed the total charge in each of them.

A charge $+Q$ is distributed on the RF electrode set to a nonzero voltage. Neglecting electrical losses, each electrode at ground has a charge $-Q_i$, with $i$ being the index of the electrode, such that $\sum_i Q_i = Q$. As a result, it is possible to extract the capacitance $C_i = Q_i/V$ between the $i$-th electrode and the RF electrode set at potential $V$. For each RF electrode I was able to extract all the capacitances $C_i$, which

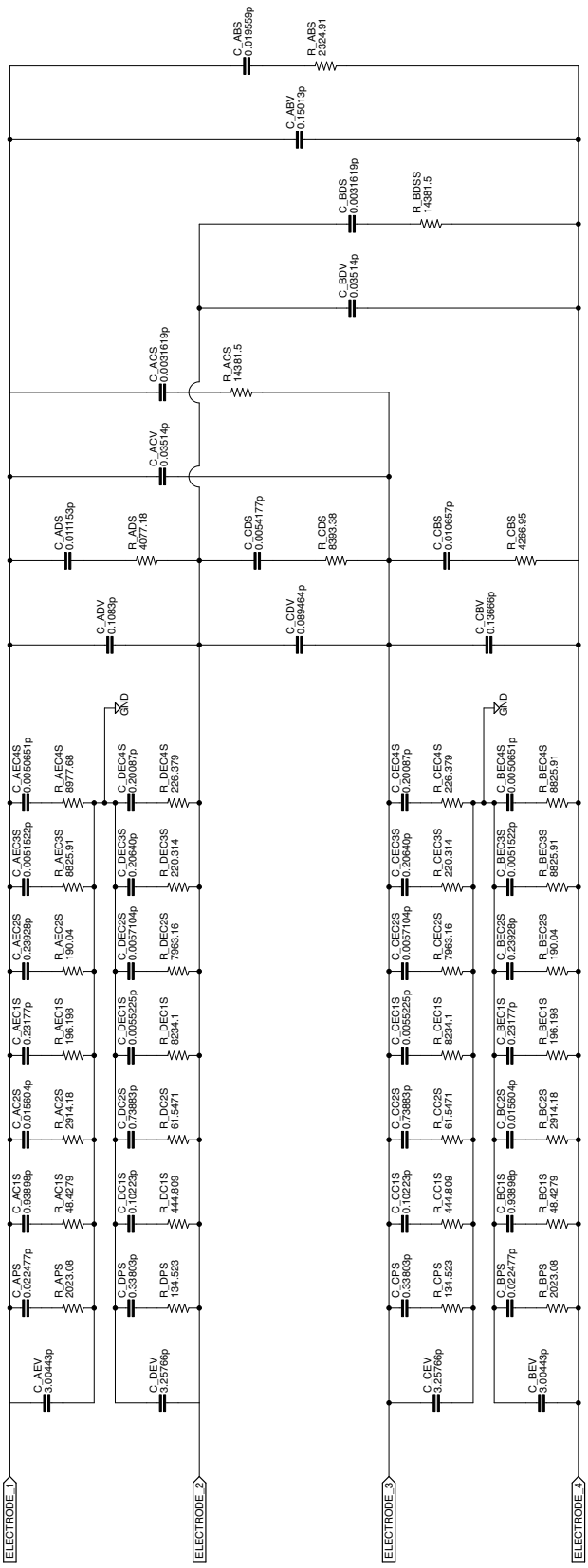


Figure 4.17: Electrical model for the trap in which we considered all the capacitances and the ESRs between each RF electrode and all the other DC and RF electrodes. This values are estimated with Comsol Multiphysics at $\Omega_T = 2\pi \times 3.5$ MHz (see text for procedure).

must be considered in parallel in the evaluation of the equivalent circuit modeling the trap.

Additionally, each electrode has two or more dowels that hold it in between two holders made in Shapal hi-M soft. Therefore, each capacitance $C_i$ is the result of the parallel of two capacitances: the capacitance $C_i^v$ between the electrode $i$ and the electrode at potential $V$ on the portion of the electrodes that is into the vacuum, and the capacitance $C_i^s$ between the dowels of the electrodes that are inside the Shapal holders. With Comsol, $C_i^v$ is computed integrating the charge density only over the surfaces of the electrode in vacuum. $C_i^v$ is basically what expected from an ideal capacitor, since there are no losses in the vacuum. The capacitance $C_i^s$, instead, is computed integrating the charge density only over the dowels of the $i$-th electrode inserted in the Shapal holders. The dowels inserted in the Shapal do not represent an ideal capacitor, since the ceramic has a nonzero dispersion. The dispersion can be quantified by calculating the *equivalent series resistance* (ESR):

$$ESR_i = \mathrm{DF}\ X_i\ , \tag{4.8}$$

where DF is the dissipation factor of the dielectric element (in our case, Shapal), and $X_i = 1/\Omega_T C_i^s$ is the reactance of the capacitance through the Shapal holders.

As shown in Fig. (4.5), the trap is symmetric with respect to the vertical plane passing through the trap axis, while the symmetry with respect to the horizontal plane passing through the trap axis is broken by the presence of the Titanium base on which the trap is mounted. Therefore, one can identify two different "sets" of capacitances, one for the upper electrodes (RF1 and RF4) and one for the lower electrodes (RF2 and RF3). The symmetry with respect to the horizontal plane passing through the centre of the trap, instead, is broken by the presence of the trap base.

The equivalent circuit of the trap is presented in Fig. (4.17). If we don't consider the capacitances between the RF blades, the equivalent capacitances $C_{E1}$, $C_{E4}$ between the electrodes RF1, RF4 and ground are:

$$C_{E1} = C_{E4} = 4.46\ \mathrm{pF}, \tag{4.9}$$

with an ESR $R_{E1} = R_{E4} = 3.33\ \Omega$ calculated for $\Omega_T = 3.5$ MHz. The equivalent capacitances $C_{E2}$, $C_E3$ between the electrodes RF2, RF3 and ground are:

$$C_{E2} = C_{E3} = 4.86\ \mathrm{pF}, \tag{4.10}$$

with an ESR $R_{E2} = R_{E3} = 3.08\ \Omega$. For calculating the ESRs we considered a RF frequency $\Omega_T = 3.5$ MHz.

### 4.7.3 Measurement of the capacitances on the real trap

Once the manufacturer had produced the electrodes and the trap was assembled, I used a Vector Network Analyzer to measure the capacitances of the real trap and compared their value to the simulated ones. With the VNA one can perform two different measurements of the capacitance: an absolute measurement, i.e. the capacitance referred to ground, or a relative measurement, i.e. the capacitance referred to a second terminal of the VNA.

In absolute capacitance measurements, the VNA is calibrated by using one calibrated short circuit, one open circuit and a 50 Ω termination. The possible perturbation caused by a home made co-axial cable connected to the vacuum feedthrough

| **Name** | $C$ **[pF]** |
|---|---|
| $C_{E1}$ | 10.7 |
| $C_{E2}$ | 10.8 |
| $C_{E3}$ | 10.1 |
| $C_{E4}$ | 10.6 |

Table 4.1: Absolute values of the capacitance between each RF electrode and ground measured using a VNA. For our configuration, with electric permittivity set to 1, the needed embedded electrical length was 171 mm. The absolute error on all the capacitances is $\pm 0.1$ pF.

was taken into account by performing a second calibration with the home made cable connected to a known capacitance. Table (4.1) lists the measured values of the capacitances between each RF electrode and ground.

There is approximately a factor 2 of difference between the simulated and the measured values of the capacitances. A possible reason for the underestimation of $C_{E1}$ and $C_{E2}$ made in the simulation, is that the simulation does not take into account the capacitances of the not-coaxial, copper wires that connect the pins in the vacuum flange to the threaded dowels of the electrodes, estimated of $\sim 3$ pF each. Experimentally, I noticed that the measurements are significantly affected by the positioning and bending of the copper wires. In order to minimize the wires' effects, we first placed them in order to ensure that the optical access was not obstructed by the wires, and then we modified them in order to make the capacitances of the four electrodes as equal as possible.

## 4.8 High Voltage Amplifier for DC electrodes

The ion trap electrodes constitute a capacitative load for any power supply circuit. The RF electrodes are fed by an RF drive, that will be described in detail in Chapter 5. However, the trap is constituted not only by the four RF electrodes but also by the other six electrodes that will be fed with DC signals. Of these DC electrodes, four are the endcaps providing the axial confinement in the Paul trap, while the two conic electrodes will be used to generate the static quadrupole potential for the EOT.

Considering the relatively small size of the optical potential in the EOT, in order to trap relatively large crystals we need to provide a strong confinement with the DC quadrupole. By simulating the fields created by the DC electrodes, we could find that in order to create a trapping potential on the order of $2\pi \times 500$ kHz we need to provide voltages up to $\sim 250$ V to the DC electrodes.

Providing a high voltage DC potential is considerably easier than realizing four identical high voltage RF signals. We have adopted a commercial solution to power these electrodes that consist in using a High-Voltage (HV) operational amplifiers designed for capacitative loads.

### 4.8.1 Electrical Setup for the HV Amplifiers

To preserve the possibility of controlling the value of the DC signals at any time, we want some circuitry that could be driven by an analog signal generated by the lab control system. To this end, I have selected the PA97DR, a high voltage MOSFET operational amplifier, sold by Apex Microtechnology, designed as a low cost solution for driving continuous output currents up to 10 mA and pulse currents up to 15 mA into capacitive loads. This amplifier is able to provide voltage signals up to ±450 V, a value that is sufficient for our application.

The PA97DR are rail-to-rail op-amps, so two linear high voltage power supplies (Heinzinger PNC), one for the positive voltage and one for the negative one, feed them with ±450 V. The lab control system sends in input to the amplifiers a ±10 V analog signal. The op-amps are mounted in their evaluation board in an inverting configuration. The total gain of the circuit is $G_{\mathrm{HV}} \simeq 40$.

If $R_{\mathrm{F}}$ is the feedback resistance and $R_{\mathrm{in}}$ is the input resistance mounted at the negative input of each op-amp, the gain is given by the ratio $G_{\mathrm{HV}} = \frac{R_{\mathrm{F}}}{R_{\mathrm{in}}}$. I selected the values for the resistances after a gross estimate of the feedback resistance dissipated power. I considered as a constraint a maximum dissipation of 1 W on $R_{\mathrm{F}}$, which means that in order to not overheat the circuit $R_{\mathrm{F}}$ has to be higher than 160 kΩ. I chose $R_{\mathrm{F}} = 195$ kΩ: in this way the feedback current is approximately 2 mA, a value that can be easily sustained by the operational amplifier. Once $R_{\mathrm{F}}$ is set, $R_{\mathrm{in}}$ is set in order to have the desired gain, i.e. I set $R_{\mathrm{in}} = 5$ kΩ. Moreover, in order to reduce the dissipated power, $R_{\mathrm{F}}$ is constituted by five resistors in series: mounting equal resistors their value is 39 kΩ and each resistor will dissipate at most 160 mW. Therefore, we can safely use 1/4 W resistor for the feedback.

### 4.8.2 Noise perfomances

We characterized the noise of the HV amplifying circuit by considering a bandwidth of 1 MHz. We measured the mean noise density with a spectrum analyzer, and we found the mean noise to be approximately 120 nv/$\sqrt{\mathrm{Hz}}$. The noise spectrum is shown in Fig. (4.18). The noise characterization of the PA97DR allowed us to decide how to filter the amplifier output, by finding the optimal compromise between the bandwidth of the circuit and the noise injected in the trap electrodes. On the one hand, the noise in the DC signals may lead to heating of the trapped ions. On the other hand, a relatively high bandwidth for the DC signals is crucial in the fast switch between the Paul and the electro-optical trap, see Sec. [4.9]. A 5 $\mu$s transient corresponds to a frequency of about 200 kHz, with a related noise of 24 mV: this is the compromise we opted for, since it matches all the requirements of our experiment.

This filter was implemented by mounting a capacitor $C_{\mathrm{F}} = 5.6$ pF as feedback capacitance. The op-amp bandwidth is consequently limited to $f_{\mathrm{C}} = \frac{1}{2\pi R_{\mathrm{F}} C_{\mathrm{F}}} \simeq 150$ kHz.

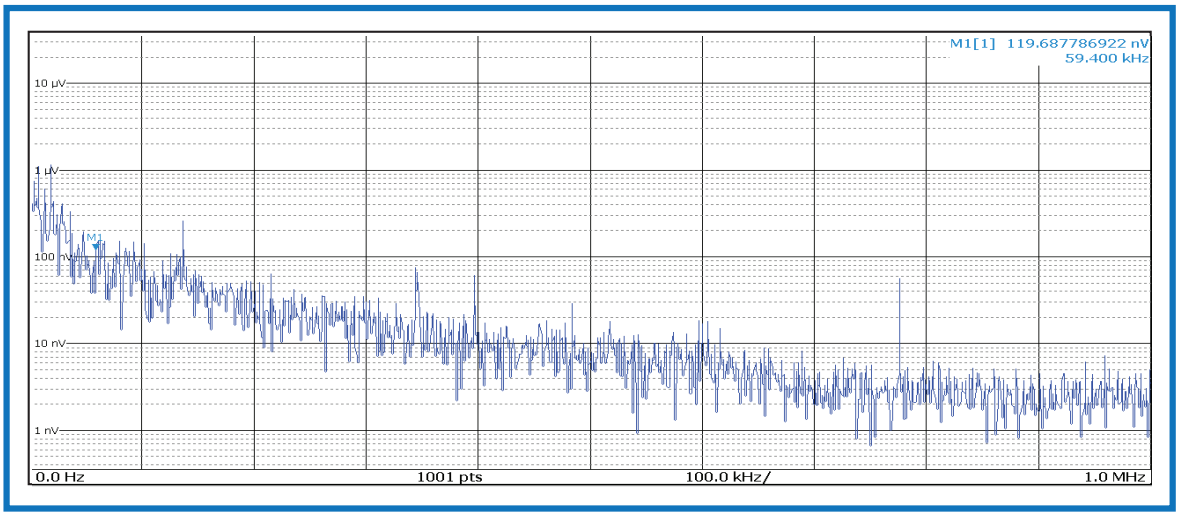


Figure 4.18: Noise density of the PA97DR amplifier measured with a Spectrum Analyzer. The set resolution bandwidth was 1 Hz so the noise spectrum coincides with the noise density.

## 4.9 Transition from the Paul trap to the EOT

In order to minimize the loss of particles, the transition between Paul trap and EOT must be optimized. Although it's impossible to simulate it perfectly since we have no knowledge of the possible patch potentials that may modify the trap, we can only speculate over the optimal timescale for the process.

Let's suppose that the Paul trap shutdown is instantaneous, then the ion will keep the same velocity at the moment of the shutdown. If also the EOT turns on instantaneously, then the kinetic energy of the ion would not be altered during the transition from one trap to the other. However, in practice the transition process is not instantaneous. Even if we turn on the EOT while we turn off the RF field, the transient time will be finite.

When the trap is switched off the electric quadrupole potential continues to oscillates at an $\omega_{\mathrm{RF}}$ frequency, but the amplitude decays exponentially. The exponential behavior is due to the fact that the trap is a capacitative load and is fed by a resonating circuit, as I will describe in Chapter 5.

Calculating analytically the full dynamics of the ion in an exponentially decreasing RF is challenging; therefore, I will consider the worst case scenario, that is to consider the phase of the RF "frozen" at the moment in which the trap is turned off, while the RF amplitude decays exponentially to zero. If the transient time is sufficiently short this is a good approximation of the real case. The electric field generated by our Paul trap is described, near the trap center, by the equation:

$$\begin{aligned} E_x(x,t) &= -\alpha\Phi_{\mathrm{RF}}\cos(\omega_{\mathrm{RF}}t)x - \alpha'\Phi_{\mathrm{DC}}x \\ E_y(y,t) &= -\beta\Phi_{\mathrm{RF}}\cos(\omega_{\mathrm{RF}}t)y - \beta'\Phi_{\mathrm{DC}}y \\ E_z(z,t) &= -\gamma\Phi_{\mathrm{RF}}\cos(\omega_{\mathrm{RF}}t)z - \gamma'\Phi_{\mathrm{DC}}z \end{aligned} \tag{4.11}$$

where the parameters values are reported in table (4.2).

| | | | |
|---|---|---|---|
| $\boldsymbol{\alpha}$ | $2.6\ 10^5\ \mathrm{m}^{-2}$ | $\boldsymbol{\alpha}'$ | $-3.0\ 10^5\ \mathrm{m}^{-2}$ |
| $\boldsymbol{\beta}$ | $-2.6\ 10^5\ \mathrm{m}^{-2}$ | $\boldsymbol{\beta}'$ | $3.5\ 10^5\ \mathrm{m}^{-2}$ |
| $\boldsymbol{\gamma}$ | $0.0\ \mathrm{m}^{-2}$ | $\boldsymbol{\gamma}'$ | $-4.6\ 10^4\ \mathrm{m}^{-2}$ |

Table 4.2: In table are reported the parameters for our experimental ion trap. The parameters refer to eq. (4.11).

Let's suppose that at $t = 0$ the electric field points outwards in the $y$-axis with amplitude $E_{\mathrm{off}}(t)$. Let's also suppose that the ion is placed at 0.1 $\mu$m from the center of the trap in $y$ direction, this value corresponds to the mean displacement of an ion at Doppler temperature from the trap center, in which we consider a trap of frequency $2\pi \times 300$ kHz.

Also supposing that the field experienced by the ion varies only in function of time, as $\vec{E}_{\mathrm{off}} e^{-t/\tau_{\mathrm{RF}}}$, it is possible to evaluate the work done by the electric field on the ion for the turning-off transient $\tau_{RF}$:

$$\mathcal{L} = \int F_{\mathrm{ion}}\, ds = \int_0^{\tau_{\mathrm{RF}}} F_{\mathrm{ion}} \frac{ds}{dt}\, dt = \frac{(eE_{\mathrm{off}})^2}{m_{\mathrm{Ba}}} \tau_{\mathrm{RF}} \int_0^{\tau_{\mathrm{RF}}} e^{-t/\tau_{\mathrm{RF}}} (1 - e^{-t/\tau_{\mathrm{RF}}})\, dt\ , \quad (4.12)$$

where $F_{\mathrm{ion}} = eE_{\mathrm{off}}$.

I select as working condition $\Phi_{\mathrm{RF}} = 100$ V and $\Phi_{\mathrm{DC}} = -1.0$ V, values inside the experimental ion trap stability zone, see Fig. (4.3). Assuming that $\tau_{\mathrm{RF}} \simeq 7\mu$s, i.e. to be able to turn off the Paul Trap in the same transient time in which the EOT is powered on, the estimated electric field work is about $7 \times 10^{-24}$ J. The Barium ion estimated heating up is $\Delta T_{\mathrm{Ba}} = \frac{2\mathcal{L}}{3k_B} \simeq 0.5$ K, if we consider three degrees of freedom in Barium motion. This value has the same order of magnitude of the expected depth of the EOT. However, the estimate provided by eq. (4.12) is an overestimation of the heating of the particles for two reasons: first, we considered a static electric field with the highest possible absolute value; second, we did not consider the dissipation by the cooling light, which is going to occur during the whole trap swapping process since the trapping light in the EOT is at the magic wavelength for the cooling transition of $Ba^+$.

# Chapter 5

# RF drive

The Paul trap is a key element in the Ba-Li experiment: it is not only the first step in trapping hot ions just after photoionization, but it constitutes a "reference trap" that can be used to explore possible inelastic processes in our mixture, for molecular compounds that can be formed collisionally [47].

In Chapter 4, I have presented our ion trap and I showed the equivalent circuit that represents it. In this Chapter I will describe the design and realization of the RF drive, an electric circuit that is used to feed the Paul trap with an intense RF signal. The RF drive project is one of the main projects that I led during my Ph.D., and it aims at addressing some of the specific problems in the realization of our atom-ion mixture, like providing an excellent micromotion compensation and having the possibility of quickly turning on and off the RF in order to facilitate the transfer of the ions to/from the EOT.

In the first Sec. [5.1], I will give an overview on the RLC circuit theory, the electrical theory at the base of the RF drive working principle. In Sec. [5.2] I will present some of the solutions reported in literature to provide RF to Paul traps, and I will explain the innovations that we included in our drive. The Sec. [5.3] is focused onto the description of the design process while Sec. [5.4] and Sec. [5.5] provide details on the main issues encountered in the experimental realization and characterization of the drive. Finally, in Sec. [5.6] I will describe how the RF drive has been mounted below the Barium experimental vacuum chamber and some preliminary attempts to use it in searching ions.

## 5.1 Resonant RLC circuit theory

The main challenge in designing a compact RF drive relies on the difficulty of amplifying the RF signal on a capacitive load without having a large amount of dissipated power. To accomplish this goal, we want to use a RLC resonating circuit with a high $Q$-factor such that the required pre-amplification is reduced and the noise minimized, since a resonating circuit works as a narrow band-pass filter. An RLC circuit is an electrical circuit consisting of a resistor $R$, an inductor $L$, and a capacitor $C$, connected in series or in parallel. For our application it is sufficient to focus on the series configuration. The resonance frequency is defined as the frequency at which the impedance of the circuit is at its minimum. Equivalently, it can be defined as the frequency at which the impedance is purely real (that is, purely resistive). We can define a number of parameters in the circuit: the resonant frequency $\omega_R = \frac{1}{\sqrt{LC}}$, the

| **Quantity** | **At resonance** $\omega = \omega_R$ | **At** $\boldsymbol{\omega = \omega_0}$ **which maximizes** $\lvert V_C \rvert$ |
|---|---|---|
| **Frequency** | $\omega_R = \frac{1}{\sqrt{LC}}$ | $\omega_0 = \omega_R S^2$ |
| **Impedance** | $Z_{\mathrm{TOT}} = R$ | $Z_{\mathrm{TOT}} = R + i(\omega_0 L - \frac{1}{\omega_0 C})$ |
| **Current** | $I = \frac{V_s}{R}$ | $\lvert I \rvert = \frac{\lvert V_s \rvert}{\sqrt{R^2 + (\omega_0 L - \frac{1}{\omega_0 C})^2}}$ |
| **Potential at capacitor** | $\lvert V_C \rvert = Q \lvert V_s \rvert$ | $\lvert V_C \rvert = \frac{Q \lvert V_s \rvert}{S}$ |

Table 5.1: RLC series circuit electrical quantities at the resonance frequency $\omega_R$ and at the frequency $\omega_0$ for which the voltage potential at the capacitor terminal $|V_C|$ is maximized.

quality factor of the circuit $Q = \frac{1}{R}\sqrt{\frac{L}{C}}$, the so-called damping factor $\delta = \frac{R}{L}$, and the characteristic time constant $\tau = RC$, where $\tau\omega_R = Q^{-1}$. It is possible to evaluate the voltage $V_C$ across the capacitor as a function of the frequency $\omega/2\pi$ and the voltage $V_s$ source powering the circuit.

An important consideration is that the condition of maximum voltage at the capacitor does not coincide with the position of the resonance of the current $I$ in the circuit. Table (5.1) lists the values of the main parameters of the circuit at resonance, $\omega = \omega_R$ and at the frequency $\omega = \omega_0$ for which the voltage at the capacitor terminals is at its maximum. In Table (5.1), the scale parameter $S$ is defined as $S = \sqrt{1 - \frac{1}{2Q^2}}$. It is possible to note that, when the $Q$ factor grows, $S$ tends to the unitarity and $\omega_0$ and $\omega_R$ converge to the same value.

### 5.1.1 Discussion about matching condition

In order to maximize the quality factor of the circuit, we have also to pay attention to the impedance matching between the primary circuit (i.e. the RF source, having typically 50 Ω impedance) and the secondary circuit (i.e. the RLC resonant circuit). Intuitively, impedance matching might seem necessary to improve the $Q$ factor of a resonating circuit. However, the more the transmitted power is, the larger is the heat dissipated by the resonant circuit, including the electrodes: a condition that is in general undesirable. In order to maximize $Q$ while keeping the dissipated power on the electrodes low, we need to carefully analyze the impedance matching between the RF source and the drive circuitry.

Referring to Fig. [5.1], two different situations can exist. In the situation (a) the source resistance $R_{\mathrm{S}}$ is bigger than the load resistance $R_{\mathrm{L}}$, in the situation (b) the

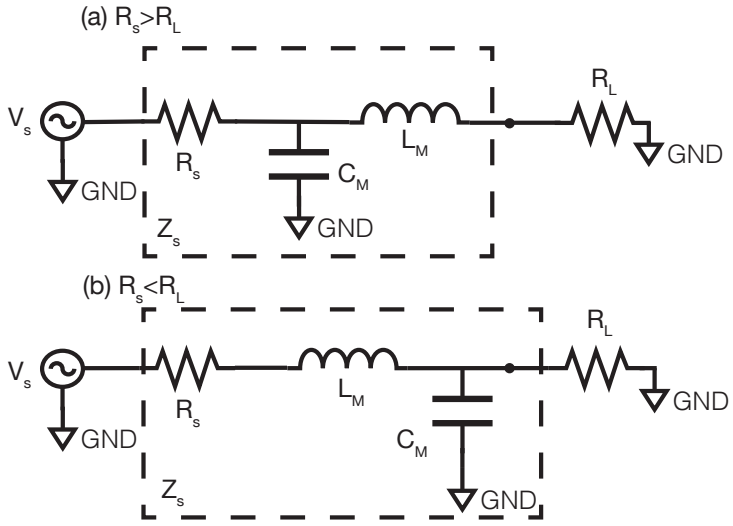


Figure 5.1: Representation of two possible matching condition between the voltage source and the load. In case (a), $R_S > R_L$, the matching is reached using a shunt capacitor $C_M$ and a series inductor $L_M$. In case (b), $R_S > R_L$, the matching is always obtained by introducing a shunt capacitor $C_M$ and a series inductor $L_M$ but they are exchanged in place respect the case (a).

viceversa is taken into consideration. In both circuits (a) and (b) the matching can be reached by using only reactive components, i.e. a shunt capacitor $C_M$ and a series inductance $L_M$ placed as in Fig. [5.1]. At resonance $\omega_R$ the RLC series circuit is equivalent to a completely resistive load $R_L$ as that of Fig. [5.1]. Table [5.2] reports the equations for selecting $C_M$ and $L_M$ values in order to obtain the matching.

In absence of matching condition (*mismatch*), the quality factor of the RLC circuit fed by a real voltage source with internal resistance $R_S$ is $Q = \frac{1}{R_S+R_L}\sqrt{\frac{L}{C}}$. However, if one of the matching filters illustrated in Fig. [5.1] is added, the quality factor becomes $Q' = \frac{1}{2R_L}\sqrt{\frac{L}{C}}$. This is due to the fact that both the matching filters act on the source resistance value to make it equivalent to $R_L$ at $\omega_R$. The positions in the circuit in which the two impedances are equivalent are indicated with a dot in Fig. [5.1]. Interestingly, impedance matching increases the quality factor only if $R_S < R_L$.

Considering that commercial RF sources, like *direct digital synthesizers* (DDS), have typically an internal resistance of 50 Ω, a question that I had to address while designing the drive is whether to work with impedance matching or not.

## 5.2 Ion trap drive circuits

The first step in approaching the design of the RF drive was a search in the literature about possible solutions reported by other groups.

In general, feeding the electrodes of a Paul trap with a "monochromatic" RF signal that is as least noisy as possible is needed in order to reduce the heating rate of ions in the trap [165]. The reduction of the heating rate is a constant challenge in ion

| **Case $R_S > R_L$** | **Case $R_L > R_S$** |
|---|---|
| $L_M = \frac{1}{\omega_R}\sqrt{R_L(R_S - R_L)}$ | $L_M = \frac{1}{\omega_R}\sqrt{R_S(R_L - R_S)}$ |
| $C_M = \frac{1}{\omega_R}\sqrt{\frac{1}{R_S}(\frac{1}{R_L} - \frac{1}{R_S})}$ | $C_M = \frac{1}{\omega_R}\sqrt{\frac{1}{R_L}(\frac{1}{R_S} - \frac{1}{R_L})}$ |

Table 5.2: Equations for calculating the values of $C_M$ and $L_M$ that guarantee the matching condition in the two cases depicted in Fig [5.1].

trapping, and several aspects have been pointed as critical [166]: the distance between the ions and the electrodes, the RF noise, and the RF frequency. Additionally, it was noted that the heating rate can be reduced by performing an active stabilization of the RF amplitude [167].

In the case of atom-ion experiments, there is another aspect that must be considered: micromotion compensation. In fact, an excellent compensation of the micromotion is needed in order to reduce the heating mechanism originating from atom-ion collisions in the presence of a strong RF field. To this end, it is fundamental to provide DC signals to the electrodes for moving the ions in all possible spatial direction. Moreover, in our specific case we are interested in transferring the ions from the Paul trap to the EOT. Therefore, we must be able to turn off and on the RF signal fast enough in order to ensure that the ions do not get lost in the transfer between the traps.

In this section I show the pros and cons of the main methods for providing intense RF to ion Paul traps: the helical resonators (Sec. [5.2.1]), and the compact resonators mounted on *printed circuit board* (PCB), see Sec. [5.2.2]. During the designing phase, the main goal has to be the realization of a drive able to trap ions with the least possible heating rate, defined as the mean value of the time derivative of the ion quantum energy [165]. To search for a solution which minimizes all the possible heating factors is fundamental to obtain cold trapped ions and to be able to observe cold atom-ion collisions also in the Paul trap configuration. The main causes of ion heating in a Paul trap are listed below [166]:

1. The heating rate is proportional to $\omega_{RF}^{-1}$ or, in some experimental case, to $\omega_{RF}^{-2}$. Compatibly with the trap stability is better to work with small RF frequencies for the flipping quadrupole potential.

2. Some measurements shows that the heating rate has a behavior that seems to go like $D_{trap}^{-4}$, where $D_{trap}$ is the trap dimension scale. The reasons of this behavior are probably due to the fact that with a large trap the presence of *patch charges* on the electrodes surfaces are less relevant in the ions dynamic. However, this contribution to the heating does not depend in any way on the drive and it has already been taken into consideration: our trap, with a $D_{trap} \simeq 2$ mm, can be considered relative big with respect to the common ion trap.

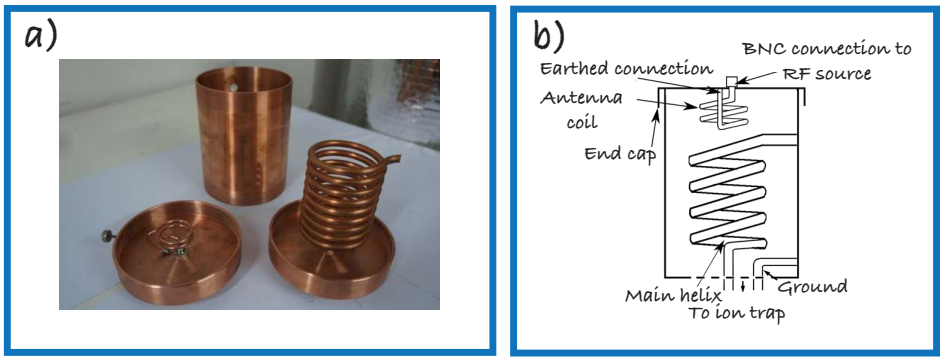


Figure 5.2: (a) Picture of an example of helical resonator, adapted from [171]. To have an idea of typical dimension of a helical resonator, the shield diameter is 107 mm. The antenna coil has 2 turns and the main helical coil has 9 turns. (b) Scheme of a helical resonator, adapted from [168].

3. The heating rate is directly proportional to $S_{\mathrm{E}}(\omega)$, the noise spectral density of electric field fluctuations. For this reason it is important to have an RF signal generated with the least noise as possible to feed the Paul trap.

4. It is also observed an empirical dependence of the ion heating on the voltage amplitude $\Phi_{\mathrm{RF}}$ at the RF electrodes. This is reasonable because, enhancing $\Phi_{\mathrm{RF}}$, also $S_{\mathrm{E}}(\omega)$ enhances probably due to the electrodes heating.

### 5.2.1 The helical resonators

A common solution for efficiently feed a Paul trap with RF is to use a so-called *helical resonator* [168–171]. A helical resonators is a special transformer in which the primary winding, called *antenna*, is constituted by a few turning of thin wire and the second winding is constituted by a bulky helicoidal solenoid with a large inductance, called the *main helix* in Fig. [5.2].

Typically the RF source for an helical resonator is a standard commercial voltage source with an internal resistance of 50 Ω. The little antenna in the primary winding is designed to guarantee the matching between the secondary circuit load and the RF source. The matching is ensured by a proper choice of the mechanical features of the antenna, e.g. the number of windings, the wire diameter, the helicoidal pitch. The mechanical features of the main helix are designed to enhance as much as possible the quality factor of the resonant circuit and to make it resonate at the desired frequency. The behavior of the helical resonator can be predicted with analytical formulas [168], but also simulated with finite elements software [169].

The helical resonators allows to obtain quality factors $Q \simeq 500$–$1000$ and thousands of volts on the RF electrodes with a few volts input. They are typically made resonant at frequencies in a range from 10 MHz up to about 20 MHz and, thanks to the high quality factor, are characterized by excellent noise performances because the resonance acts as a very narrow bandpass filter.

However, a large quality factor constitutes the main drawback for mounting a helical resonator in our experimental setup. In fact, one of the requirements for our experiment is to have a short shutting down transient in order to facilitate the

transition from the Paul trap to the EOT (see Sec. [4.9]). In a simple RLC series circuit the transient time scale is $\tau_{RLC} = \frac{2Q}{\omega_{RF}}$. For an helical resonator with $Q = 1000$ and resonating frequency of 3.5 MHz, the transient time scale corresponds to $\tau \simeq 90$ $\mu$s to compare with the required transient of about 5 $\mu$s of our setup.

Another issue that made us abandon the idea of using a helical resonator is that it is considerably bulky and it has to be installed near the vacuum chamber: with respect to typical ion trapping experiments we have the necessity of more optical access to the vacuum chamber since we need to implement also all the laser beams for manipulating the atoms. In addition, the bulky structure of the main helix is easily subjected to mechanical vibration which can lead to fluctuations in the helical resonator mechanical and electrical features which in turn can cause $S_E(\omega)$ enhancement.

### 5.2.2 PCB based resonators

In place of helical resonators, several groups use active amplification and commercial electronic components to feed the RF electrodes [172–174]. These electric circuits are mounted in a PCB, which can also have a very small size [174]. To obtain the desired high voltages at the RF electrodes, the circuit is typically made by a pre-amplification stage followed by a low quality factor RLC circuit [172, 173]. The RLC circuit is used as bandpass filter and its inductance value is chosen to resonate at the desired frequency, given the trap load capacitance.

In this type of circuit, the amplification gain can require a large power dissipation on the active components. In some circuits it is necessary to provide a water cooling system to maintain constant the temperature of the components [102]. However, a great electrical power is not needed in principle to obtain a large voltage drop across a capacitance, since a capacitance is a reactive component and, at least ideally, does not absorb power.

Therefore, it is in principle possible to realize a compact, low power RF drive that does not suffer from overheating, which could create transients in the operation of the drive or the necessity of implementing water cooling of the components. This is our strategy for our RF drive, for which we want a quality factor that is sufficiently large in order not to require high power in the pre-amplification stage, but small enough to facilitate the transition to the EOT.

## 5.3 Design of a low-power, compact RF drive

The main challenge in designing a compact RF drive relies on the difficulty of amplifying the RF signal on a capacitive load without having a large amount of dissipated power. To accomplish this goal, we decided to use a resonating circuit with a moderate high Q-factor such that the required pre-amplification is reduced and the noise minimized.

The design of the RF drive must fulfill a number of requirements, some of which originate from the specific characteristic of our experimental setup:

1. The RF drive has to resonate at a relative small frequency in the RF domain. The RF frequency $\omega_{\mathrm{RF}}$ is chosen small for minimizing the heating rate [105]. In order to create resonance an RLC circuit is used. The desired quality factor of the circuit has to be $Q \simeq 50$, in order to ensure that the turning off time is $< 10$ $\mu$s.

2. In order to enhance the voltage drop on the electrodes without modifying the fixed $Q$ factor, the drive should have a pre-amplification of the input signal with a gain $G_{\mathrm{RF}}$. With an input signal of about 1 V peak-to-peak amplitude at the resonant frequency, the expected peak-to-peak amplitude on the electrodes will be $\Phi_{\mathrm{RF}} = G_{\mathrm{RF}} Q V_{\mathrm{in}} \simeq 250$ V if $G_{\mathrm{RF}} \simeq 5$.

3. The RF drive should be compact enough to be placed under the Barium vacuum chamber, so it can be directly connected to the feedthroughs. Considering the size and the height of the chamber, the size of the driver should be approximately 100 mm × 70 mm × 50 mm. Placing the RF drive as near as possible to the electrodes, is fundamental because in an RLC circuit the point of connection between the inductance (on the board) and the capacitance (the electrodes) is a high-impedance point.

4. The drive should have the option of providing a separate DC offset on each electrode. Having four DC offsets will ensure the possibility of providing an excellent micromotion compensation even in the presence of possible mechanical misalignments of the electrodes, for which DC offsets on the blade electrodes may displace the ions also along the trap axis [105, 175]. In order to have one DC offset per electrode, the RF drive should have an independent RF output per electrode.

5. The four RF signals must have the same amplitude and the correct phase. If these two conditions are not respected, the electric potential can experience fluctuations or modulations, causing an increase of the micromotion and of the ion heating rate [105].

### 5.3.1 Four meshes circuit

The fundamental element of the RF drive is an RLC circuit resonating at the frequency $\omega_{\mathrm{RF}} = \sqrt{1/L_{\mathrm{eq}} C_{\mathrm{eq}}}$, where $L_{\mathrm{eq}}$ and $C_{\mathrm{eq}}$ are the equivalent inductance and capacitance of the whole circuit, respectively. The quality factor of this circuit is:

$$Q = \frac{1}{R_{\mathrm{eq}}} \sqrt{\frac{L_{\mathrm{eq}}}{C_{\mathrm{eq}}}} \,, \tag{5.1}$$

with $R_{\mathrm{eq}}$ being the equivalent series resistance. If we imagine to feed this circuit with a signal of frequency $\omega_{\mathrm{RF}}$ and amplitude $V_0/2$, for instance through a transformer, the voltage drop at the capacitor of the RLC circuit is $QV_0/2 \sin(\omega_{\mathrm{RF}} t)$. The circuit is designed such that the capacitive load $C_{\mathrm{eq}}$ is mainly due to the capacitance of the RF electrode. Its value is considered to be a fixed quantity, since it depends on the Paul trap geometry, i.e. the electrode's shape, size and the distance from the other electrically conductive parts. The equivalent inductance $L_{\mathrm{eq}}$, instead, is a free parameter that can be tuned in order to find the best compromize between a large quality factor $Q$ and a relatively large resonant frequency $\omega_{\mathrm{RF}}$. Additionally, and independently from the resonant frequency, the quality factor is increased by reducing the total resistance $R_{\mathrm{eq}}$, which should be ideally kept as low as possible.

One electrode of a Paul trap can be modeled as a capacitive load. However, it is reasonable to associate to it also an equivalent series resistance (ESR), which may originate e.g. from the dielectric losses of the electrode's insulating support. Ideally,

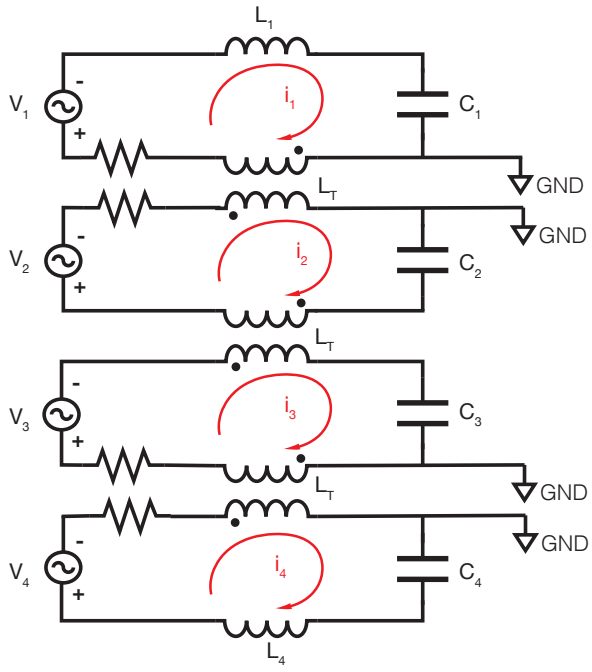


Figure 5.3: Schematic of the RF drive, representing the conceptual idea behind the design. Four resonant RLC circuits feed four capacitors - representing total capacitance of the ion trap plus the drive circuit - at iso-frequency $\omega_{\mathrm{RF}}$. Adapted from [176].

capacitance and resistance should be the same for each electrode; in practice, this is never exactly true due to possible asymmetries in the trap assembly (see Sec. [4.7]) or to mechanical imperfections. This makes it practically very hard to realize four independent RLC circuits having the same resonant frequency. Our strategy to ensure the presence of a common resonant frequency is to place $1:1$ transformers that connect the four resonant circuits. The whole circuit can be considered as a single resonator and we avoid problems of frequency splitting that could arise in coupling independent resonators. The working principle of the RF drive is schematized in Fig. (5.3).

The circuit in Fig. (5.3) is analytically solvable. The meshes equations of the four circuits in Fig. (5.3) are:

$$\begin{cases} V_1(t) = R_1 i_1(t) + \dfrac{Q_1(t)}{C_1} + (L_1 + L_t)\dfrac{di_1(t)}{dt} + L_t \dfrac{di_2(t)}{dt} \\ V_2(t) = R_2 i_2(t) + \dfrac{Q_2(t)}{C_2} + 2L_t \dfrac{di_2(t)}{dt} + L_t \dfrac{di_1(t)}{dt} + L_t \dfrac{di_3(t)}{dt} \\ V_3(t) = R_3 i_3(t) + \dfrac{Q_3(t)}{C_3} + 2L_t \dfrac{di_3(t)}{dt} + L_t \dfrac{di_2(t)}{dt} + L_t \dfrac{di_4(t)}{dt} \\ V_4(t) = R_4 i_4(t) + \dfrac{Q_4(t)}{C_4} + (L_2 + L_t)\dfrac{di_4(t)}{dt} + L_t \dfrac{di_3(t)}{dt} \end{cases} \tag{5.2}$$

where we assumed that the $1:1$ transformers are ideal (mutual induction coefficient $k = 1$).

Eq.s (5.2) are analytically solvable with $Q_j$ the charge on the capacitors $C_j$, $j = 1, \ldots 4$. In complex field let's suppose $V_j(t) = V_j e^{i\omega t}$ and search solutions in the form

$i_j(t) = i_j e^{i\omega t}$. The solutions for the system (5.2) are:

$$\begin{cases} i_1 = -\dfrac{i\omega(a^2cV_1 + a^2fV - 1 - cdfV_1 + a^3V_2 - adfV_2 - a^3V_4 - a^2fV_3)}{a^4 - a^2bc - a^2bf - a^2df + bcdf}, \\ i_2 = -\dfrac{i\omega(a^3V_1 - adfV_1 + a^2bV_2 - bdfV_2 - a^2bV_4 - abfV_3)}{a^4 - a^2bc - a^2bf - a^2df + bcdf}, \\ i_3 = -\dfrac{i\omega(-a^2fV_1 - abfV_2 + a^3V_4 - abcV_4 + a^2fV_3 - bcfV_3)}{a^4 - a^2bc - a^2bf - a^2df + bcdf}, \\ i_4 = \dfrac{i\omega(a^3V_1 + a^2bV_2 - a^2bV_4 - a^2dV_4 + bcdV_4 - a^3V_3 + abcV_3)}{a^4 - a^2bc - a^2bf - a^2df + bcdf}, \end{cases} \tag{5.3}$$

where we have defined the following parameters:

$$\begin{aligned} a &= L_t\omega^2, \\ b &= -(L_1 + L_t)\omega^2 + \frac{1}{C_1} + i\omega R_1 , \\ c &= -2L_t\omega^2 + \frac{1}{C_2} + i\omega R_2 , \\ d &= -2L_t\omega^2 + \frac{1}{C_3} + i\omega R_3 , \\ f &= -(L_2 + L_t)\omega^2 + \frac{1}{C_4} + i\omega R_4 . \end{aligned}$$

The four meshes circuit follows eq. (5.3), so it is possible to study its behavior by varying the component values. Fig. (5.4) shows the dependence of the current phases and amplitudes from the components values. If we assume that the equivalent inductance and the equivalent capacitance are the same in all the RLC circuits, there is only one common resonance frequency $\omega_{\mathrm{RF}}$ and proper phase on the signal of each electrode. If, instead, the electrical components are different, all the meshes still resonate at a common frequency, but other resonances appear in addition to the main one. As a consequence, even if the optimal working condition for the circuit in Fig. (5.3) is the one where all the meshes are characterized by the same $L_{\mathrm{eq}}$ and $C_{\mathrm{eq}}$, the inter-dependence of the meshes make the iso-frequency feature robust against small variations of the electrical components, permitting to drive all the RF electrodes at resonance at the same time.

We have already mentioned how, from the geometry of the trap, we can assume that the electrode RF 1 has the same capacitance of RF 4 but different from the capacitance of the pair of electrodes RF 2 and RF 3. Therefore, the most reachable grade of circuit symmetry is offered by the configuration in which all the transformers are ideal ($k = 1$) and identical and $L_1 = L_2$. In this case $i_1 = i_4$, $i_2 = i_3$ but, as we can see from Fig. (5.4), the $i_1$ amplitude differs from that of $i_2$. The iso-amplitude signal problem due to horizontal plane symmetry break can be solved by inserting balancing capacitors between RF electrodes in phase.

### 5.3.2 Block Diagram of the RF drive

We have designed an RF drive based on the strategy represented in Fig. (5.3). The scheme is divided in five main "blocks" (see Fig. (5.5)). The block **A** represents the part of the circuit that is placed inside an ultra-high vacuum chamber, i.e. the

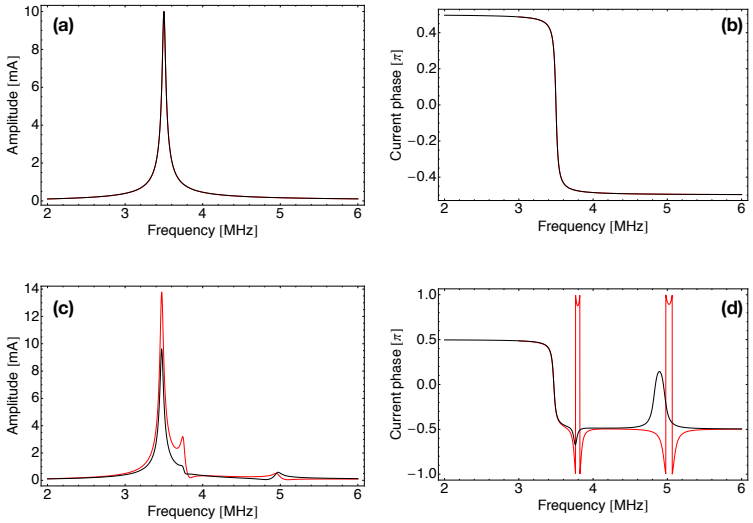


Figure 5.4: Simulated amplitude and phase of the current circulating in the circuit as a function of the frequency. Plots (a) and (b) show the current's amplitude and phase in the four resonant circuits in which all the capacitances are equal to $C_{\rm eq} = 5.6$ pF, all the resistances are set to 100 Ω, and $L1 = L2 = L_{\rm eq}/2$, $L_{\rm T} = L_{\rm eq}/4$, $L_{\rm eq} = 370$ $\mu$H, with $L_{\rm T}$ being the transformers' mutual inductances. Plots (c) and (d) show amplitude and phase of the current $i_1$ (red line) and $i_2$ (black line) in a circuit in which the electric components have the same values as in the plots (a), (b), except for $C_1 = 1.1\ C_{\rm eq}$ and $C_2 = 0.9\ C_{\rm eq}$. Adapted from [176].

capacitances and the ESRs of the Paul trap electrodes, which we simulated with a finite element software (see Sec. [4.7]). The block **B** represents the portion of the secondary circuits that is placed outside the vacuum chamber: the blocks **A** and **B** constitute the four interdependent RLC circuits described in Fig. (5.3). The inductances in block **B** are designed to resonate at approximately $\omega_{\rm RF} = 2\pi \times 3.5$ MHz. This frequency was chosen in order to maximize the quality factor for a given value of $C_{\rm eq}$, and $R_{\rm eq}$ while keeping the RF frequency reasonably large in order to ensure a successful trapping of the ion. Additionally, 3.5 MHz lies in the range of frequencies for which the RF trap should not interfere with the Lithium quantum gas.

Block **C** is formed by four 1 : 4 transformers that are used to connect the primary and the secondary circuits, i.e. to feed the resonant lines with RF signal. The purpose of these step-up transformers is to increase by a factor $a_{\rm T} = 4$ the voltage amplitude from the primary to the secondary circuit, thereby enhancing the total amplification factor.

Conceptually, the RF sources of Fig. 5.3 are realized by the blocks **D** and **E**. Block **E** is constituted by four independent Direct Digital Synthesis (DDS) chips that are set at a frequency $\omega_{\rm RF}/2\pi$ and have tunable amplitudes and phases. In our realization, the block **E** is not placed on the RF drive board but it is embedded in the control system of the experiment [164]. The DDSs are connected to four amplifiers (block **D** — Analog Devices AD8392) characterized by an output impedance of $R_S = 0.2$ Ω at $\omega_{\rm RF} = 2\pi \times 3.5$ MHz. The amplifiers' input impedance is matched to the 50 Ω output of the DDSs. The op-amps are set for a feedback gain of $G_{\rm RF} \simeq 5$. This choice

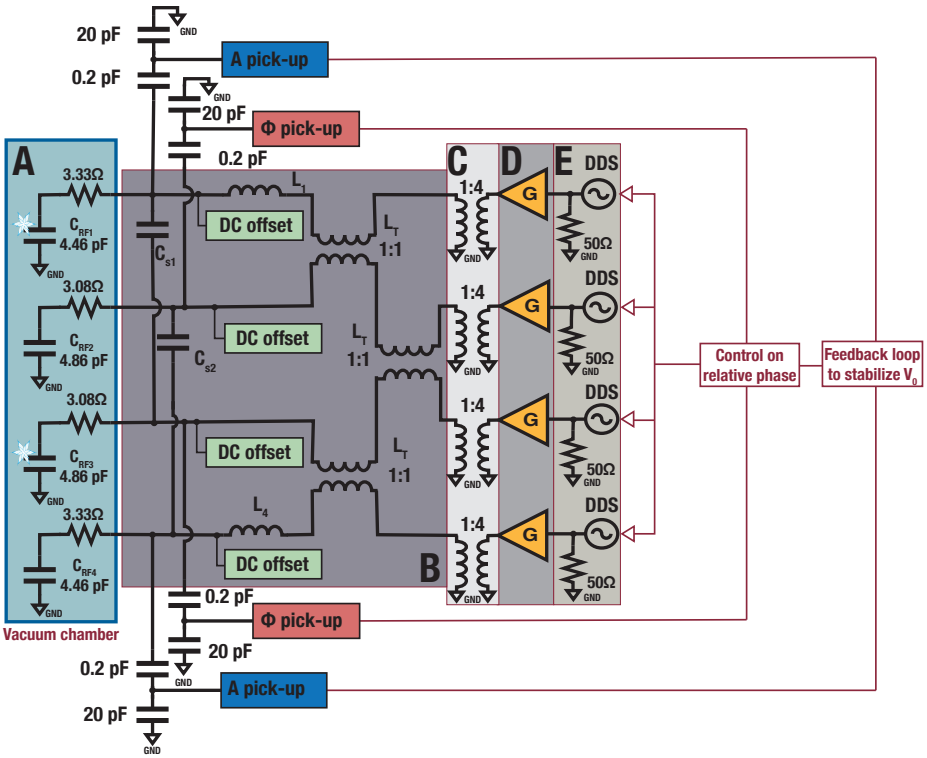


Figure 5.5: Simplified block diagram of the complete RF drive. **A** Electrodes of a Paul trap, considered as a series of a capacitance and a resistance. The values in figure are obtained by simulating with COMSOL Multiphysics the Paul trap for which this RF drive was designed, see Sec. [4.7]. Electrodes marked with a star are out of phase with respect to the other two. **B** Iso-frequency resonant lines with pick-ups for phase and amplitude stabilization, balancing capacitors $C_{S1}$ and $C_{S2}$ and DC offset inputs. **C** $1:4$ step-up transformers that inductively couple the resonant circuits to the RF sources. **D** Low-impedance op-amps for pre-amplification of the input signals. **E** Four independent DDS sources providing the RF signals with tunable amplitude and phase. Adapted from [176].

ensures an increase of the signal enhancement at resonance, since the real part of the impedance of the circuit is reduced.

Since the capacitance and the ESR of the electrodes are in general not identical, we have placed two balancing capacitors $C_{S1}$ and $C_{S2}$ that connect the in-phase lines of the drive in order to ensure that the RF signals of the secondary circuits have all the same amplitude. Moreover, we have equipped the RF drive with phase and amplitude pick-ups that can be used to perform active stabilization of the RF signal, with the goal of counter-acting possible effects — like thermal fluctuations of the different elements of the drive — that may affect the long-term stability of the trap frequency $\omega_r$ [167].

The active stabilization of the RF potential requires a faithful sampling of the voltage drop at the electrodes. This needs to be done in a section of the circuit that is at a high impedance load. To this end, we implemented little-invasive probes with $1:100$ capacitive dividers realized with the 0.2 pF and 20 pF capacitors as the last elements of the circuit outside the vacuum (see Fig. (5.5) and the complete drive schematic in Appendix A). We chose the value of the capacitors in order to extract approximately 1% of the signal without affecting the resonance, since the impedance of the capacitive dividers is much larger than the lines' impedance. The capacitive dividers are realized by placing commercial SMD capacitors as close as possible to the lines in order to suppress the capacitive effects of the additional lines. The prototyping phases for the pick-up development will be described in Sec. [5.5.2].

The capacitive dividers work as phase pick-ups ($\phi$-pick-ups) that carry information on the resonance frequency $\omega_{\mathrm{RF}}$ and the relative phase between the signals on the RF electrodes. The amplitude pick-ups (A-pick-ups) are realized by placing a rectifier, not shown in Fig. (5.5), after the capacitive divider to generate a signal linearly dependent on the RF amplitude $V_0/2$ [167]. The board has one A-pick-up and one $\phi$-pick-up for both pairs of electrodes at $V_0/2\sin(\omega_{\mathrm{RF}}\,t)$ and at $V_0/2\sin(\omega_{\mathrm{RF}}\,t+\pi)$. The pick-ups signals can be used to actively stabilize both the trap frequency and the relative phase between the electrodes.

## 5.4 Technical issues in RF Drive

In the previous Sec. [5.3] I described the working principle and the circuit topology of the RF drive. In this section I describe some of the technical issues that were addressed for both defining the schematic of the drive and its realization.

In Sec. [5.4.1] I will discuss the realization of the inductors and transformers by using ferromagnetic cores. Ferromagnetic cores were necessary in order to have a compact circuit.

Ferromagnetic cores can enhance a solenoid inductance of a factor $\mu_r$, the real part of the cores' relative magnetic permeability, but they cause an increase of the circuit's resistance through the complex term of the permeability $\mu_i$.

In Sec. [5.4.2] I will discuss the problem of impedance matching, and explain why we eventually chose to use a mismatched circuit and the possible drawbacks of this choice. Finally, in Sec. [5.4.3] I will discuss possible problems related to the cross-talk between the lines and how these effects can be minimized by choosing the right circuit topology.

### 5.4.1 Choosing ferrite magnetic cores

A possible strategy for realizing a sufficiently large inductance – e.g. on the order of a few 100s $\mu$H — without implementing a bulky helical resonator is to build inductors by winding a conducting wire on a ferrite core. Ferrite cores are characterized by a frequency-dependent magnetic permeability that depends on the material, the size and the shape of the core. While the reactive term of the impedance is proportional to the real part of the magnetic permeability, its imaginary part provides a resistive term, physically caused by the eddy currents induced in the core. In general, the resistive and reactive parts are linked by the dispersion factor $DF$, a specific characteristic of the core material. The presence of the inductors' resistive term affects the overall resistance $R_{\rm eq}$ of the RLC lines, which then reads:

$$R_{\rm eq} = R_0 + \omega_{\rm RF} L_{\rm eq} DF, \tag{5.4}$$

where $R_0$ is the component of $R_{\rm eq}$ that does not depend on the drive frequency, originating for example from the wires' resistance. Other possible frequency-dependent terms of the resistance, for instance due to the skin effect on the wires, have for the moment been neglected. The quality factor of eq. (5.1) can then be re-written in the form:

$$Q = \frac{1}{R_0 \omega_{\rm RF} C_{\rm eq} + DF} \ . \tag{5.5}$$

In the low resistance regime ($R_0 \omega_{\rm RF} C_{\rm eq} \ll DF$), the real limitation to the $Q$-factor is the dispersion factor $DF$: in order to keep a high value of $Q$ it is crucial to choose a ferrite material with the lowest possible losses.

If we consider the circuit described in the block diagram of Fig. (5.5), the overall $Q$-factor for the circuit is:

$$Q = \frac{1}{(R_0 + a_T^2 R_S)\omega_{RF} C_{\rm eq} + DF} \ . \tag{5.6}$$

The magnetic cores used for the inductors of the RF drive are toroidal Ni-Zn ferrite cores (material: DN5H from the company DMEGC – from an intensive search this material resulted the one having the lowest $DF$ in the market), which are characterized by a low dispersion factor around $\omega_{\rm RF}$ and $\mu_r \simeq 30$. In order to estimate the cores' dispersion factor, we have realized a number of resonant circuits formed by a single inductor and a conventional capacitor resonating at approximately $\omega_{\rm RF}$. With these circuits, we have measured the resistance at resonance as a function of the impedance of the inductor. The results are plotted in Fig. 5.6. A dispersion factor $DF = (8.0 \pm 0.2) \times 10^{-3}$ is obtained from a linear fit to the data. By substituting this value in Eq. (5.6), we can estimate $Q \simeq 115$, and a resonance frequency of $\omega_{\rm RF} = 2\pi \times 3.5$ MHz. We notice that the dispersion factor $DF$ is the largest term in the denominator of Eq. (5.6), and therefore the dispersion of the core represents the strongest limitation to the $Q$ factor of this RF drive.

### 5.4.2 Considerations about impedance matching

The RF drive is equipped with a preamplifier circuit placed between the RF source and the resonant lines. Therefore, we can match the impedance of the DDSs, typically 50 $\Omega$, with the op-amp input, but without matching it to the op-amp output. For this

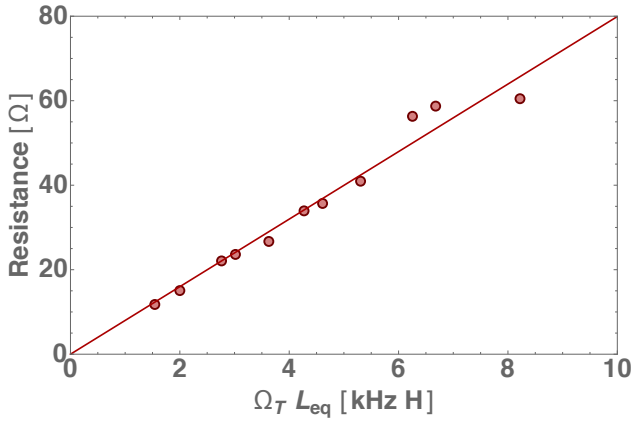


Figure 5.6: Calibration of the dispersion factor $DF$ for DN5H toroidal ferrite cores of height 6 mm, internal radius 10 mm and external radius 18 mm. The copper wire used had a diameter of 0.2 mm. Each point in the plot corresponds to the resistance at resonance of an RLC circuit formed by a ceramic capacitor and a homemade inductor. The values of resistance, inductance and resonant frequency are obtained with a vector network analyzer. The dependence of the total resistance as a function of $L_{\mathrm{eq}}$ and $\omega_{\mathrm{RF}}$ is extracted. The value $DF = 0.0080 \pm 0.0002$ is extracted from the linear fit to the data. Adapted from [176].

purpose, I chose to use the low-impedance AD8293 op-amp, which ensures a small value of $R_{\mathrm{S}}$.

In Sec. [5.4.2] we discussed about the methods to match the impedances of the load and the RF source by using reactive components. However, I decided to realize a drive in which the impedances are not matched in order to maximize the $Q$-factor: $R_{\mathrm{L}} \gg R_{\mathrm{S}}$ and the source resistance is added to the overall resistance of the resonant line and the $Q$-factor can be expressed as in eq. (5.6).

However, the absence of power matching is correlated with some drawbacks, which have to be taken into consideration during the designing phase. First, the electrical power transfer is depressed by a strong unbalance between the source resistance $R_{\mathrm{S}}$ and the load $R_{\mathrm{L}}$: the power is largely dissipated on the source internal resistance, i.e. the op-amp is subjected to heating due to the Joule effect. For this reason we have put in contact to the AD8392 a home made metal heatsink that thermally connects the AD8392 upper part with the RF Drive metal box.

Second, a mismatched circuit could experience signal reflections in the resonant lines. These reflections were not observed in our realization of the drive. Moreover, if present, these reflections would have manifested themselves as a voltage offset at the trap terminals, and we would have been able to correct for them by using the DC offsets that are present in each RLC line of the drive.

### 5.4.3 Cross-talk effect on the board

RF signals are particularly suitable for propagation in media by means of electromagnetic radiation, which is why they are used in radio communications. Every RLC line of the four RF drive interdependent circuits can act both as an emitter and as an antenna.

In our application, however, we want to make sure that these effects are minimized since they could create interference between the operation of each RF line in a way that is little predictable. When the 1 : 1 transformers in block **B** of Fig. (5.5) are disassembled, the four RF lines resonate at different frequencies due to small differences between them. In this case, we observed all the four independent resonance peaks in each single line.

This effect of cross-talk between the lines is caused by the proximity between the RF lines in the PCB. The signals of electrode pairs that are fed with RF with the same phase interfere constructively, while out-of-phase signals interfere destructively.

The cross-talk cannot be eliminated in our design: the spatial constraints on the board dimensions make impossible to shield each resonant line from the others. However the cross-talk can be made non-problematic by adopting some precautions.

The electrodes' geometry (see Sec. [4.7]) is symmetric with respect to the vertical plane passing through the trap center. The RF drive schematic is designed to preserve this kind of symmetry, and the geometry of the circuital lines in the PCB is symmetric with respect to the vertical plane passing by the center of the board. The symmetry assures the iso-amplitude of the RF signals even in presence of cross-talks because every lines will be affected by the same cross-talk quantity.

## 5.5 Prototyping the RF drive

At the end of the designing phase, I realized the complete RF drive schematic. I first simulated the schematic by using LTspice, a freeware computer software implementing a SPICE (*Simulation Program with Integrated Circuit Emphasis*) electronic circuit simulator. The simulations in time and frequency domains confirmed the circuit correct functioning: especially confirming the various inductance values, evaluated by using the model of Sec. [5.3.1].

When the RF drive schematic was completed, I created the PCB using Eagle, a PCB design software, and the project was sent to print. The prototyping phase consisted in mounting the electronic parts on the PCB and in testing its functioning and its performances.

In Sec. [5.5.1] I describe how to assemble the circuit in a way that facilitates the debugging process. In Sec. [5.5.2] I discuss the problems related to the realization of the pick-ups, and describe some of the models that we tested before finding the optimal one. In Sec. [5.5.3] the pick-up calibration results are provided while in Sec. [5.5.4] the tests on the completed RF drive are presented.

### 5.5.1 Assemblying and debugging the circuit

In principle with the PCB and all the inductances and transformers at hand, all the electronic components of the board can be mounted and the circuit performances can be tested. In practice, this is not the most efficient method to assemble a prototype, because it precludes the possibility of debugging independently the different parts composing the board. I adopted a strategy for assembling the board that consisted in mounting each circuital blocks one at a time and in verifying that they properly worked before assembling the next block. Referring to Fig. (5.5), the procedure I used is the following:

1. The first circuital parts I mounted are the external RLC lines of electrodes RF1 and RF4 in block **B** without the balancing capacitors $C_{S1}$ and $C_{S2}$. The electrodes capacitative loads in block **A** were temporarily substituted by ceramic 5.6 pF capacitor. Before continuing in the assembly, I made sure that the two circuits resonated at a similar frequency, adjusting accordingly the inductances by removing or adding windings.

2. I installed the two RLC lines of electrodes RF2 and RF 3 in block **B** without the central 1 : 1 transformer. I used jumpers on the PCB to bypass this transformer. In this way I had two independent circuits constituted by two resonant lines each. As in step 1. of the procedure, I verified that the resonant frequencies of the two circuits are as equal as possible.

3. I mounted the last central 1 : 1 transformer in block **B** and verified the iso-frequency condition between all the resonant lines.

4. I mounted the balancing capacitors $C_{S1}$ and $C_{S2}$ in block **B** and verified the iso-amplitude condition at the electrodes terminals.

5. I mounted the 1 : 4 transformers in block **C** and I verified that the conditions of iso-resonance holds.

6. I mounted the pre-amplification stadium in block **D** by using the standard mounting method for the op-amps: first I mounted the ±5 V dual alimentation circuit and then the op-amp with its feedback loop. The main part of the resonant circuit was now complete.

7. I measured the voltages at the capacitors that simulate the loads of the trap with some external probes and an oscilloscope. This measurement is not indicative of the $Q$-factor because the oscilloscope probes disturb the line. However, this measurement allowed me to check the basic features of the circuit, like the presence of a common resonance and of the proper phase relations between the different lines.

8. I mounted the pick-up circuits and calibrated them using the measurements with the oscilloscope probes (see Sec. [5.5.3]).

Following this procedure it is possible to mount the RF drive and to proceed to determine its performances, described in Sec. [5.5.4].

### 5.5.2 Design of the pick-up

The pick-ups are an important element in the RF drive circuit, since they make it possible to find the resonant frequency, to quantify voltage amplitudes at the electrodes and to generate an error signal for actively stabilizing the RF signal. In order to perform all of these operations, it would be necessary to pick-up the signal right on the electrodes. This operation is particularly delicate because in this point the lines are at high impedance.

In a high impedance point in a circuit (a node), a relatively small current corresponds to a relatively high voltage. Therefore, high impedance circuits are low current and potentially high voltage, whereas low impedance circuits are the opposite (low

voltage and potentially high current). If we considered an RLC series circuit constitutes by a resistance $R_{\text{eq}}$, a capacitor $C_{\text{eq}}$ and an inductor $L_{\text{eq}}$, with a quality factor described by eq. (5.1), the equivalent impedance in the point between the capacitor and the inductor is $|Z_{\text{pick-up}}| = R_{\text{eq}}Q^2\sqrt{1+\frac{1}{Q^2}}$. Supposing to have $R_{\text{eq}} \simeq 100\ \Omega$ and $Q \simeq 50$, then the absolute value of the equivalent impedance in this circuital point is about 250 k$\Omega$. As a result, the measurement of the voltage drop across the capacitance made with an oscilloscope closed on 1 M$\Omega$ is not a faithful measurement since the oscilloscope resistance is comparable to $|Z_{\text{pick-up}}|$, thus forming a voltage divider, and the measurement would be underestimated by around 20%.

In principle, an oscilloscope with a 10 M$\Omega$ impedance should be sufficient to realize a trustful measurement. However, a typical voltage probe has also a capacitance of about 10 pF in parallel to the 10 M$\Omega$ resistance. This probe capacitor is higher than the estimated trap capacitances and significantly alters the resonance conditions. Therefore it is necessary to find an alternative solution for the pick-ups.

We separately tested inductive probes based on parallel lines placed at a side or below the RF output lines in the PCB, but we observed a strong cross talk between each pick-up and all the four RF lines.

Therefore, we opted for using little-invasive probes with 1 : 100 capacitive dividers realized with the 0.2 pF and 20 pF capacitors. The complete schematic of the pick-ups [167] is shown in Appendix A.

With respect to inductive probes, the capacitive divider has the advantage that the circuit can still be treated with a lumped element model, while an inductive probe requires the theory of distributed elements for its description.

In a first PCB version these pick-up circuits were placed in a board zone very close to the vacuum feedthroughs, but in this place they suffered from cross-talks and, even if their response was quite linear, their behaviors were different from one another. A second version of the PCB solved this problem by spatially disposing the pick-up electronic components in areas farther away possible from the feedthroughs, but still in the last part of the RF lines before the vacuum.

### 5.5.3 Calibration of the pick-up circuits

We tested the response of the pick-ups at resonance. Fig. (5.7) shows the response of the two A-pick-ups as a function of the amplitude of the primary RF source. The data show a very good linear response. Additionally, we measured the bandwidth of the A-pick-ups, finding it equal to 6 Hz. This corresponds to the maximum bandwidth for a stabilization loop that can correct slow amplitude variations. If needed, this bandwidth can be changed by modifying the components of the rectifiers. This can be done at the cost of increasing the ripple amplitude on the pick-up signal — currently approximately 15 mV for $V_0 = 200\ V$.

Additionally, we used the $\phi$-pick-ups to measure the relative phase between the RF signals used to feed neighbour electrodes. For maximizing the frequency of the secular potential, this phase should be $\pi$. Fig. (5.8) shows the output signals of the two $\phi$-pick-ups when phase, frequency and amplitude of the DDSs are set correctly. The sinusoidal signals of frequency $\omega_{\text{RF}}$ have a phase difference $\phi/\pi = 0.99435 \pm 0.00004$, measured from the fit. This differs only slightly from the ideal value $\phi/\pi = 1$; however, by treating this difference of the relative phase with the same approach of Ref.[105] it emerges that this phase mismatch does not provide a contribution to the micromotion,

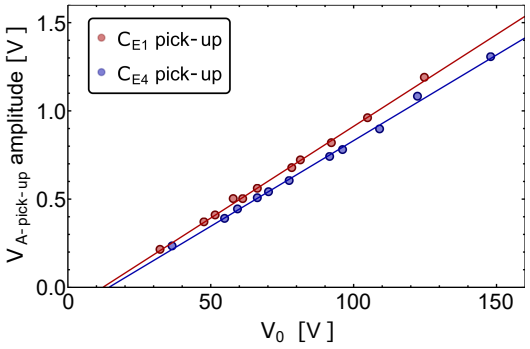


Figure 5.7: Linearity test for the two A-pick-ups sensing the signals reaching $C_{E1}$ and $C_{E4}$. The measurement is performed by changing the amplitude of the RF signal, $V_0/2$. Experimental data are plotted together with their linear fits, which lead to the slopes $(10.4 \pm 0.2) \cdot 10^{-3}$ and $(9.7 \pm 0.2) \cdot 10^{-3}$ for the pick-ups placed close to $C_{E1}$ and $C_{E4}$, respectively. The difference between the two curves are due to small mismatches in the values of the electric components forming the capacitive dividers and the rectifiers. The linear fitting functions have a non-zero offset caused by the non-linear behaviour at low RF amplitudes of the diodes that are part of the rectifiers. Adapted from [176].

as a phase mismatch affecting signals fed to opposite electrodes would. We note that the amplitude of the two A-pick-ups and the two $\phi$-pick-ups are different, possibly because of small differences in the components forming the capacitive dividers. These differences can be easily calibrated by using external probes.

### 5.5.4 Performances of the RF drive

The operation of the board was first characterized by substituting the electrodes with 5.6 pF ceramic capacitors. This choice allowed us to directly monitor the RF signal with external probes, if needed.

Fig. (5.9) shows the amplitude of the RF signal in the secondary circuit as a function of the frequency of the primary RF source. The circuit has several resonances,

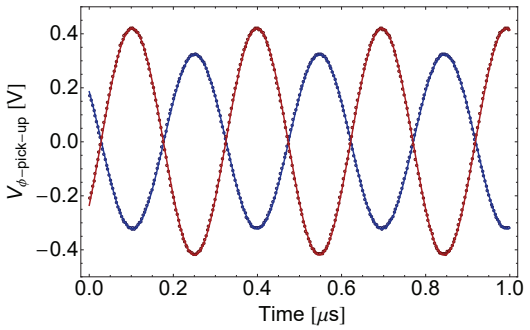


Figure 5.8: Phase of the signal outputs. The data show the outputs of the $\phi$-pick-ups probing the signals at the capacitors $C_{E2}$ (red) and $C_{E3}$ (blue). Measurements are taken with the DDSs frequencies set to $\omega_{\mathrm{RF}}$. When the phase of the input signals are set correctly, the outputs of the two $\phi$-pick-ups are sinusoidal signals that are out of phase. The sinusoidal fit to the data gives a phase difference $\phi/\pi = 0.99435 \pm 0.00004$.

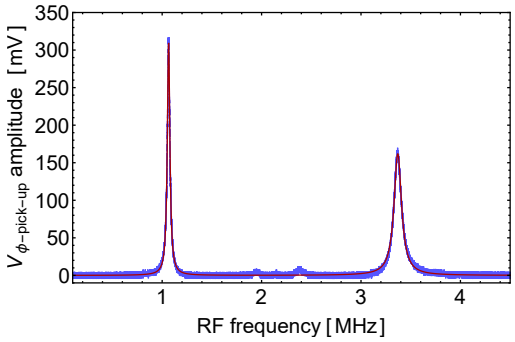


Figure 5.9: Plot of the drive response tested with 5.6 pF ceramic capacitors emulating the trap electrodes. The frequency of the input RF signals is swept to observe the main resonances of the circuit. The peak-to-peak amplitude of the RF signal reaching $C_{E2}$ is detected via the $\phi$-pick-up output and fitted with a Lorentzian curve (red) to extract the linewidth. Among all the resonances, the one at 3.37 MHz is the only one for which the RF signals of the four secondary circuits have the right phase relation.

including the one at $\omega_{\mathrm{RF}} = 2\pi \times 3.37$ MHz that we had initially targeted as the working resonance, and that we expected from the simulation to be at approximately $2\pi \times 3.5$ MHz. The resonance at $\omega_{\mathrm{RF}}$ has a full width at half maximum of $2\pi \times 91$ kHz, which we extracted from a Lorentzian fit. The resulting quality factor is $Q = 57$, which is lower than what expected from Eq. (5.6). We attribute this discrepancy to the non-ideal behavior of the transformers that have a mutual inductance coefficient smaller than 1. Other effects that may reduce the quality factor of the circuit are possible cross-talks between the transformers that are closely placed on the board. We notice that the value of the quality factor could be increased e.g. by changing the inductors of the board, at the price of lowering the resonant frequency $\omega_{\mathrm{RF}}$. The relatively small quality factor ensures a fast operation of the drive: we measure a falling time at resonance of 7.7 $\mu$s, corresponding to a time constant $\tau = 3.5\,\mu$s.

In addition to the resonance at $\omega_{\mathrm{RF}}$, other resonances arise at different frequencies, see Fig. (5.9). We attribute the presence of these resonances to the small unbalancing between the four resonant circuits, the components of which are not perfectly equal. This speculation was confirmed by simulating the circuit with the commercial software LTSpice, in which a small variation of one of the components of the circuit results in the appearance of new resonances. Of all the additional resonances, we further investigated the strongest one at about 1.06 MHz. This resonance corresponds to the creation of four RF signals having all the same phase. This condition clarifies the appearance of this resonance at a frequency considerably smaller than $\omega_{\mathrm{RF}}$: since the equivalent inductances associated to the 1:1 transformers in the block **B** of Fig. (5.5) depend on the direction of the currents, a resonance with all the RF signals in phase is characterized by values of $L_{\mathrm{eq}}$ that differ with respect to the ones associated with the resonance at $\omega_{\mathrm{RF}}$, resulting in a strong difference in both the frequency and the quality factor of the resonance.

At resonance, we are able to produce signals of peak-to-peak amplitude up to $V_0 = 200$ V with an input RF of peak-to-peak amplitude 1 V. We checked the stability of the drive by running it for 24 hours at the maximum output without active stabilization. We found no appreciable changes of the resonant frequency, but we noticed a small

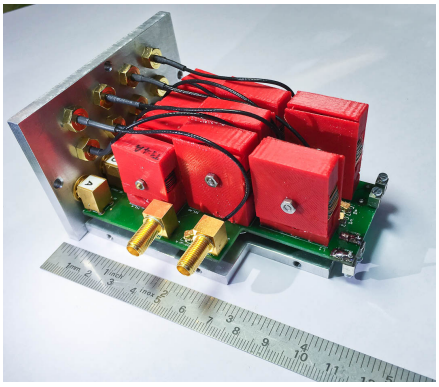

Figure 5.10: Picture of the RF drive implemented on a 4-layer PCB. The blocks **B**, **C** and **D** of Fig. 5.5 are implemented on the board. The home made inductors are incapsulated in small plastic cases (in red) in order to avoid capacitative couplings with the PCB conducting planes.

variation of the phase of the RF signal. These small instabilities, possibly due to thermal effects on the ferrite core, can be actively corrected by probing the signals with the $\phi$-pick-ups. The total power consumption of the board is due to the op-amps and is $\sim 2$ W. This value, which is calculated for the sum of all four resonant circuits, currently limits the maximum reachable peak-to-peak voltage, since a higher power could lead to a failure of the op-amps. We note that the power consumption is nominally higher than other compact drive implementations in literature. However, the power consumption in these drives is kept low by realizing smaller gains [174], by running at lower frequencies [172], or by working at temperatures for which a cryostat is needed [173].

## 5.6 Installing the RF Drive

We have realized the RF drive on a 4-layers PCB of size 100 mm×70 mm, see Fig. (5.10).

The RF drive is enclosed in a metal box held with columns of adjustable height, see Fig. (5.11). At its top end the RF drive is equipped with terminals which allow to connect the resonant lines to the feedthroughs of the ion trap.

We tested the RF drive when connected to the linear Paul trap with the open chamber, i.e. in open air. We measured a resonance at $\omega_{\mathrm{RF}} = 2\pi \times 3.23$ MHz, with a full width at half maximum of $2\pi \times 75$ kHz, resulting in a quality factor $Q = 67$. This small variation from the values found in the test with the ceramic capacitors used as load originates from the fact that, in its actual implementation, we found the electrodes to have a capacitance of approximately 10 pF, slightly larger than what initially simulated. When the UHV is realized, the drive resonance frequency becomes $\omega_{\mathrm{RF}} = 2\pi \times 3.19$ MHz, because the ion trap capacitance is slightly modified by replacing the air with the vacuum as a dielectric.

The resonance frequency does not follow the expected $1/\sqrt{C_{\mathrm{eq}}}$ scaling due to the presence of a 37 pF offset capacitance, which we attribute to parasitic capacitances between the wire windings around the ferrite cores.

The sinusoidal $i$-th RF input signal from the DDSs is characterized by an amplitude $V_i$ and a phase $\phi_i$. The signal amplitude $\Phi_{\mathrm{RF}}$ at the RF electrodes depends on all

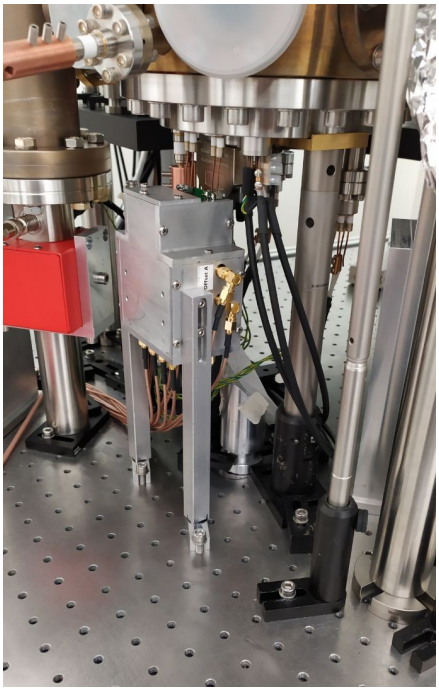

Figure 5.11: Picture of the RF drive box installed under the Barium experimental vacuum chamber. In the box inferior panel there are the four RF signal inputs from the DDSs and the four pick-up outputs. On the lateral panels there are the four DC offset SMA input.

these eight parameters: $\Phi_{\mathrm{RF}} = \Phi_{\mathrm{RF}}(V_1, \phi_1, V_2, \phi_2, V_3, \phi_3, V_4, \phi_4)$. If all the resonant lines were identical, in theory all the derivative $\frac{\partial \Phi_{\mathrm{RF}}}{\partial V_i}$ would be equal, and so $\frac{\partial \Phi_{\mathrm{RF}}}{\partial \phi_i}$ for all $i$. In the real case, however, the differences between lines and the non identical realization of the transformers makes these derivatives all different to each others.

In order to maximize the RF drive voltage output in function of the DDSs input, it is convenient to slightly unbalance the input amplitudes, increasing the inputs with larger derivative $\frac{\partial \Phi_{\mathrm{RF}}}{\partial V_i}$ with respect to the others, while keeping the current sufficiently low in order not to go over the maximum dissipation of the op-amp. It is important to note that all these parameters can be used to maximize the voltage drop on the capacitances, while keeping the right phase of the signals, a condition that is ensured by the transformers in the RLC lines. The input phases $\phi_i$ can be optimized to precisely regulate the phases of the outputs of the drive.

# Conclusions and Outlook

The work of this thesis was carried out with the aim of realizing a new experimental apparatus for the realization of a quantum mixture of ultracold trapped Barium ions and degenerate neutral Lithium atoms. In order to obtain a coherent and well controllable quantum evolution for the atom-ion mixture, we want to reach the so far unexplored ultracold regime, i.e. to reach atom-ion collisional energies for which the $s$-wave approximation is valid. This ambitious goal requires the construction of a complex apparatus in which the complexity of building two different systems does not add up trivially, since additional challenges must be tackled, e.g. making the two systems interact, i.e. superimposing atoms and ions.

During my Ph.D activity I pursued a number of different tasks that contributed to the construction of the setup for producing ultracold atom-ion mixtures. Among others, these tasks included the realization of the entire electric setup for the ion trap, the assembly of the Barium vacuum chamber, the realization of the ultra-high vacuum in the ion-side of the experimental setup, the design and part of the implementation of the Lithium optical setup.

At the time of writing of this thesis, we are currently attempting to trap the first Barium ions in the Paul trap, which would be the first trapped ions in Italy. To this end, we have optimized the trapping sequence in order to ensure that all the required steps – the oven heating, the photoionization phase and the radiofrequency trapping potential generation – work in synergy. In parallel, we are completing the Lithium optical system, while all the parts to assemble the Lithium vacuum chamber are already present in the laboratory and ready to be assembled.

When we will have trapped ions in the Paul trap, we will test and optimize the new electro-optical trapping scheme. The ions trapped with this potential will not experience micromotion and, when also the ultracold Lithium gases will be produced, the Lithium atoms could sympathetically cool the ions towards the so far unexplored ultracold regime. In order to activate the interaction also the Lithium optical transport will have to be set up and optimized.

Once completed, the Ba-Li apparatus will allow us to carry out fundamental experiments towards a deeper understanding of the atom-ion collisional physics. In the ultracold regime the atom-ion mixture will behave coherently and it will be possible to search for the predicted atom-ion Feshbach resonances [43]. The Feshbach resonances would constitute an exceptional tool to control the Ba-Li system by providing the possibility to tune atom-ion interactions. In this context, the single-particle state of an ion could be entangled with the many-body state of the neutral gas and the ion could act as a coherent impurity for the many-body system of ultracold atoms [177]. We could control the dynamics of the degenerate neutral gas by acting on the ion state, e.g. creating Schrödinger cat-like states for the atom-ion system [177]. In this

way it would be possible to investigate the role of the impurity, and, depending on the control we can exert through Feshbach resonances, access the physics of celebrated condensed matter models like the Anderson model [19] and the Kondo model [20].

Additionally, with a complete control over the atom-ion interactions, the neutral gas could be used as a buffer gas while we perform measurements on the ions state. For example, we could encode a qubit in one ion internal state and search for Feshbach resonances for which the atom-ion interactions are the same for both levels of the ion, i.e. for which the buffer gas does not reduce the ion qubit coherence time.

Finding the conditions for efficient sympathetic cooling of the ions could lead to protocols in which the computation can be performed on an ion-based quantum computer without interruptions for cooling the ion crystal.

Finally, we could perform metrological measurements by detecting possible collisional frequency shifts in high-precision spectroscopy of the $^2S_{1/2} \rightarrow ^2 D_{5/2}$ transition in $Ba^+$ in the presence of the Li buffer gas [81].

# Appendices

# Appendix A

# RF Drive Schematic

In this appendix is presented the complete schematic of the RF drive in Fig.s (A.2) and (A.3). The performance of the drive and its compactness are due in particular to the technique of making inductances and transformers. In presenting the schematic of such instrument I think it could be useful to give some details on how these inductors were realized. In order to make the drive compact it is essential to use ferromagnetic cores to enhance the inductance of each winding. Therefore the first step in building inducting components is to individuate the right ferrite material for cores. The working principle of the drive requires ferrite material with low dissipation factor at the desired resonance frequency, see Sec. [5.3].

Ferrite materials with low dissipation factor in the range of frequencies between 2 MHz and 20 MHz seems difficult to find in the market. We selected two different materials, nominally with similar dissipation factors: the Fericor DN5H material [178] and the Tomita 6B2 [179]. We test experimentally the performances of both materials and the Fericor's one results with lower dissipation factor than the other at about 3.5 MHz and we decide to use it in the drive prototype.

A copper wire with insulating enamel is then winded around the toroidal ferrite cores. We use wires with diameter of 0.2 mm. The inductance value $L_{\text{coil}}$ in function of the number of winding can be evaluated theoretically by supposing the winding as elliptical with axes equal to the dimensions of the toroid section (Fericor toroids have rectangular sections). However instead of solving a double elliptic integral it is possible to estimate experimentally the proportional factor $A_l$:

$$L_{\text{coil}} = A_l N_{\text{coil}}^2 \ . \tag{A.1}$$

Usually in the ferromagnetic core datasheet the $A_l$ values is given, but it is simple to evaluate by measuring the inductance values in function of the number of winding with a VNA. In Fig. A.1 it is showed an example of how $A_l$ was esteemed for (25×15×8) mm toroids.

The value $L_1 = L_2$ are chosen as $L_1 = L_{\text{eq}}/2$. Supposing the transformer as ideal (mutual induction coefficient $k = 1$) then $L_t = L_{\text{eq}}/4$. With a real mutual induction coefficient instead the transformer inductance is $L_t = L_{\text{eq}}/(2 + 2k)$: an esteem of the

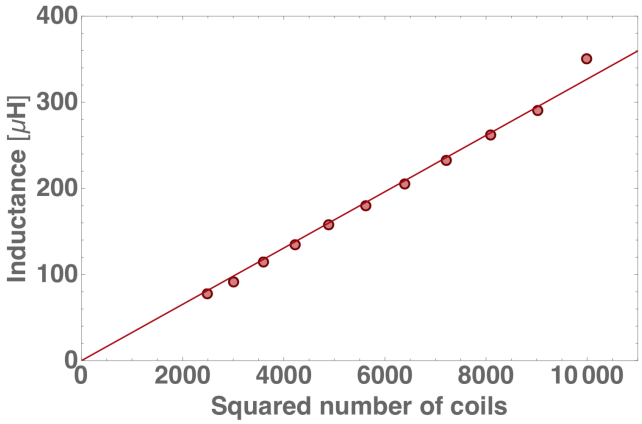


Figure A.1: Calibration of the $A_l$ parameter for handmade inductances. The measure is done using $(25 \times 15 \times 8)$ mm toroids made in Fericor DN5H ferrite and copper wire with 0.2 mm at 3.5 MHz frequency. The data are fitted with eq. (A.1) neglecting the offset constituted by the wire resistance. The estimated value is $A_l = 0.0327 \pm 0.0004$.

$k$ value can be given using a VNA. In order to enhance the $k$ as more as possible the transformer are winded with the method of *bifilar coils*.

Once realized, each inductance or transformer has to be characterized with a VNA. Then its value can be reported in a LTspice simulation [180] of the entire schematic where the resonance frequency is accurately predicted.

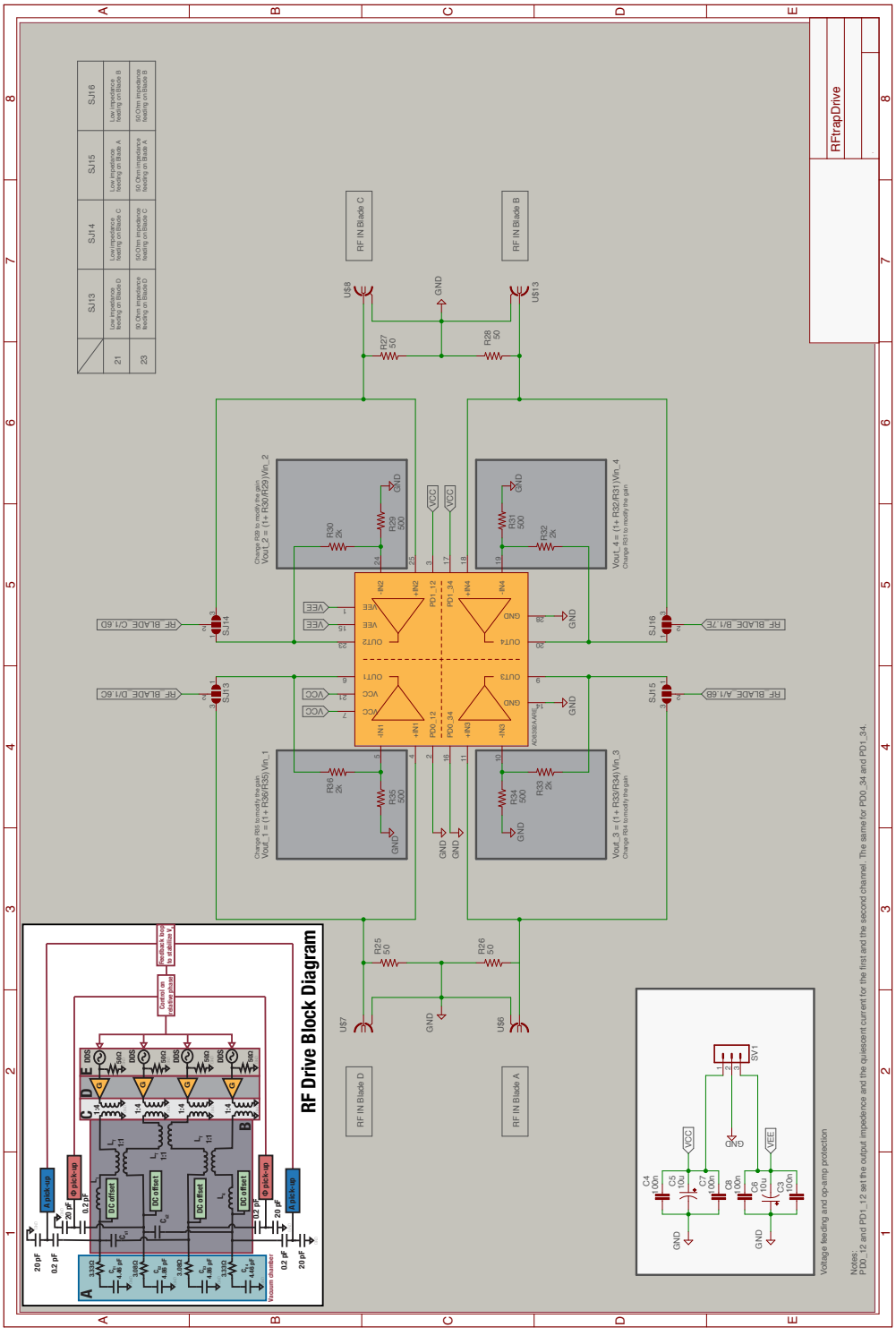


Figure A.2: First table of the RF drive schematic. The colors refer to the coding used in the block diagram in Fig. (5.5). In white the dual power supply circuit for the Analog Devices AD8392 op-amp. The jumpers SJ13, SJ14, SJ15, SJ16 allow to by-pass the pre-amplification and connect directly the DDSs output to the four interdependent resonant circuits.

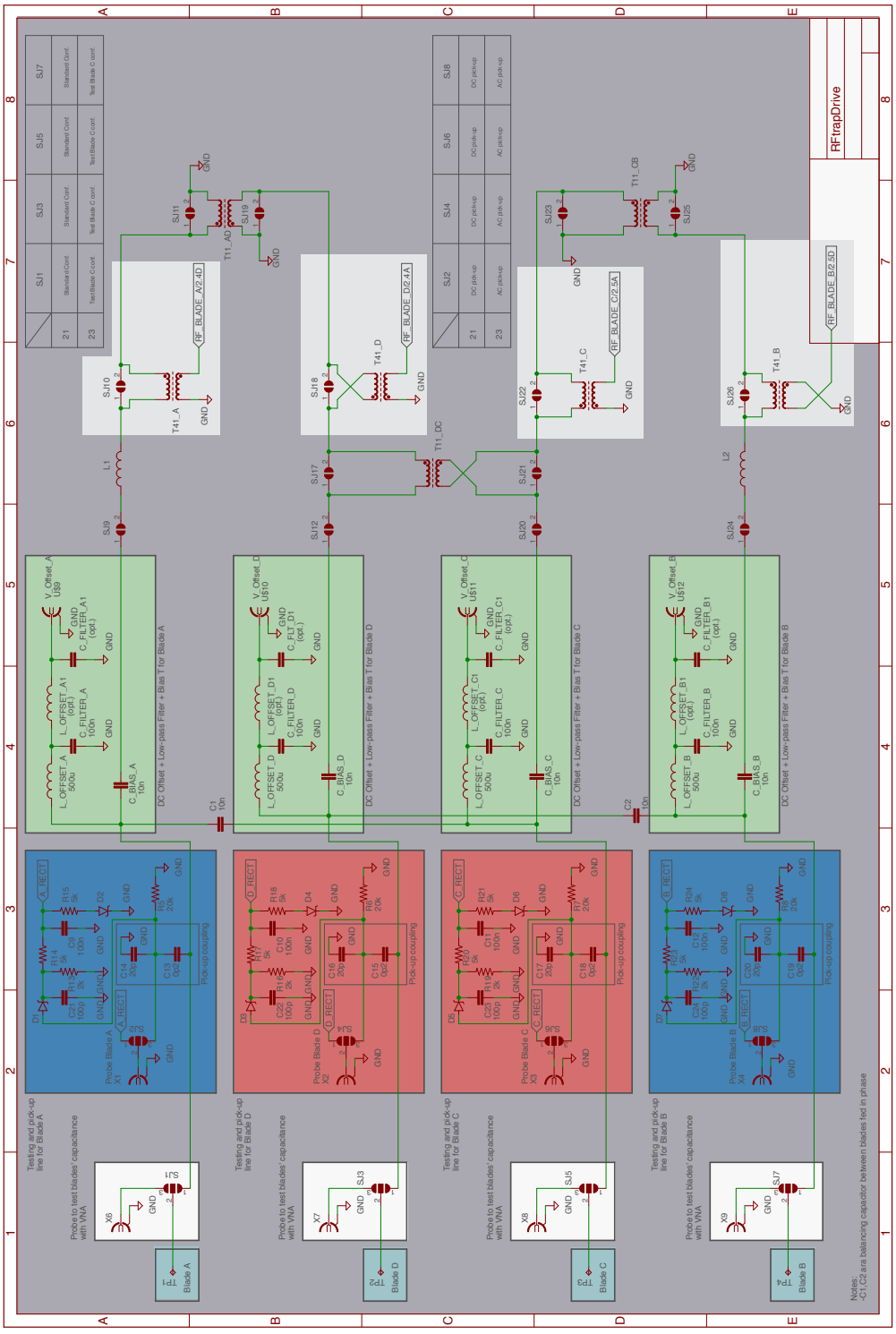


Figure A.3: Second table of the RF drive schematic. The colors refer to the coding used in the block diagram in Fig. (5.5): here are showed the block **B**, **C** and the four pick-ups. The pick-up electronics is the same in each pick-up: a dedicated jumper allows to configure the pick-up as amplitude or phase pick-up. In white there are some jumpers that connect directly the RF electrodes to four SMA output in the RF drive box panel: the board can be exploited to connect the trap terminals to a VNA for experimentally measure the trap load, see Sec. [4.7].

# Bibliography


[1] M. Lewenstein et al. "Ultracold atomic gases in optical lattices: mimicking condensed matter physics and beyond". In: *Advances in Physics* 56.2 (2007), pp. 243–379. DOI: 10.1080/00018730701223200.

[2] M. Greiner et al. "Quantum phase transition from a superfluid to a Mott insulator in a gas of ultracold atoms". In: *Nature* 415 (6867 2002). DOI: https://doi.org/10.1038/415039a.

[3] C. Chin et al. "Feshbach resonances in ultracold gases". In: *Reviews of Modern Physics* 82.2 (2010), pp. 1225–1286. DOI: 10.1103/revmodphys.82.1225.

[4] M. Greiner, C. Regal, and D. Jin. "Emergence of a molecular Bose–Einstein condensate from a Fermi gas". In: *Nature* 426 (2003), pp. 537–540. DOI: https://doi.org/10.1038/nature02199.

[5] D. J. Wineland et al. "Experimental issues in coherent quantum-state manipulation of trapped atomic ions". In: *J.Res.Natl.Inst.Stand.Tech.* 103.259 (1998). DOI: arXiv:quant-ph/9710025.

[6] M. Drewsen. "Ion Coulomb crystals". In: *Physica B: Condensed Matter* 460 (2015), pp. 105 –113. DOI: https://doi.org/10.1016/j.physb.2014.11.050.

[7] D. Leibfried et al. "Quantum dynamics of single trapped ions". In: *Rev. Mod. Phys.* 75 (1 2003), pp. 281–324. DOI: 10.1103/RevModPhys.75.281.

[8] H. Häffner, C.F. Roos, and R. Blatt. "Quantum computing with trapped ions". In: *Physics Reports* 469.4 (2008), pp. 155 –203. DOI: https://doi.org/10.1016/j.physrep.2008.09.003.

[9] R. Blatt and C. F. Roos. "Quantum simulations with trapped ions". In: *Nat. Phys.* 8 (4 2012), pp. 277–284. DOI: https://doi.org/10.1038/nphys2259.

[10] A. D. Ludlow et al. "Optical atomic clocks". In: *Rev. Mod. Phys.* 87 (2 2015), pp. 637–701. DOI: 10.1103/RevModPhys.87.637.

[11] G. Kurizki et al. "Quantum technologies with hybrid systems". In: *Proceedings of the National Academy of Sciences of the United States of America* 112 (13 2015). DOI: 10.1073/pnas.1419326112.

[12] G. R. Guthöhrlein et al. "A single ion as a nanoscopic probe of an optical field". In: *Nat.* 414 (6859 2001), pp. 49–51. DOI: 10.1038/35102129.

[13] S. Camerer et al. "Realization of an Optomechanical Interface Between Ultracold Atoms and a Membrane". In: *Phys. Rev. Lett.* 107 (22 2011), p. 223001. DOI: 10.1103/PhysRevLett.107.223001.

[14] C. Sias and M. Köhl. *Hybrid quantum systems of ions and atoms*. 2014. arXiv: 1401.3188 [cond-mat.quant-gas].

[15] U. Bissbort et al. "Emulating Solid-State Physics with a Hybrid System of Ultracold Ions and Atoms". In: *Phys. Rev. Lett.* 111 (8 2013), p. 080501. DOI: 10.1103/PhysRevLett.111.080501.

[16] R. Gerritsma et al. "Bosonic Josephson Junction Controlled by a Single Trapped Ion". In: *Phys. Rev. Lett.* 109 (8 2012), p. 080402. DOI: 10.1103/PhysRevLett.109.080402.

[17] R. Côté, V. Kharchenko, and M. D. Lukin. "Mesoscopic Molecular Ions in Bose-Einstein Condensates". In: *Phys. Rev. Lett.* 89 (9 2002), p. 093001. DOI: 10.1103/PhysRevLett.89.093001.

[18] L. Ratschbacher et al. "Controlling chemical reactions of a single particle". In: *Nat. Phys.* 8 (2012), 649–652. DOI: 10.1038/nphys2373.

[19] P. W. Anderson. "Localized Magnetic States in Metals". In: *Phys. Rev.* 124 (1 1961), pp. 41–53. DOI: 10.1103/PhysRev.124.41.

[20] J. Kondo. "Resistance Minimum in Dilute Magnetic Alloys". In: *Progress of Theoretical Physics* 32.1 (July 1964), pp. 37–49. DOI: 10.1143/PTP.32.37.

[21] C. Zipkes et al. "A trapped single ion inside a Bose–Einstein condensate". In: *Nature* 464 (7287 2010), pp. 388–391. DOI: 10.1038/nature08865.

[22] M. Tomza et al. "Cold hybrid ion-atom systems". In: *Rev. Mod. Phys.* 91 (3 2019), p. 035001. DOI: 10.1103/RevModPhys.91.035001.

[23] R. Schützhold et al. "Analogue of Cosmological Particle Creation in an Ion Trap". In: *Phys. Rev. Lett.* 99 (20 2007), p. 201301. DOI: 10.1103/PhysRevLett.99.201301.

[24] Z. Meir et al. "Dynamics of a Ground-State Cooled Ion Colliding with Ultracold Atoms". In: *Phys. Rev. Lett.* 117 (24 2016), p. 243401. DOI: 10.1103/PhysRevLett.117.243401.

[25] M. Cetina, A. T. Grier, and V. Vuletić. "Micromotion-Induced Limit to Atom-Ion Sympathetic Cooling in Paul Traps". In: *Phys. Rev. Lett.* 109 (25 2012), p. 253201. DOI: 10.1103/PhysRevLett.109.253201.

[26] H. S. W. Massey, C. B. O.Mohr, and J.E. Lennard-Jones. "Free paths and transport phenomena in gases and the quantum theory of collisions. II.The determination of the laws of force between atoms and molecules". In: *Proceedings of the Royal Society of London. Series A, Containing Papers of a Mathematical and Physical Character* 144.851 (1934), pp. 188–205. DOI: 10.1098/rspa.1934.0042.

[27] R. Grimm, M. Weidemüller, and Y. B. Ovchinnikov. "Optical Dipole Traps for Neutral Atoms". In: vol. 42. Advances In Atomic, Molecular, and Optical Physics. Academic Press, 2000, pp. 95 –170. DOI: https://doi.org/10.1016/S1049-250X(08)60186-X.

[28] B. H. Bransden, C. J. Joachain, and T. J. Plivier. *Physics of Atoms and Molecules*. Pearson Education, 2003.

[29] P. Schwerdtfeger and J. K. Nagle. "2018 Table of static dipole polarizabilities of the neutral elements in the periodic table". In: *Molecular Physics* 117.9-12 (2019), pp. 1200–1225. DOI: 10.1080/00268976.2018.1535143.

[30] E. Vogt and G. H. Wannier. "Scattering of Ions by Polarization Forces". In: *Phys. Rev.* 95 (5 1954), pp. 1190–1198. DOI: 10.1103/PhysRev.95.1190.

[31] M. P. Langevin. "Une formule fondamentale de théorie cinétique". In: *Ann. Chim. Phys.* 5 (1905).

[32] C. Zipkes et al. "Kinetics of a single trapped ion in an ultracold buffer gas". In: *New Journal of Physics* 13.5 (2011), p. 053020. DOI: 10.1088/1367-2630/13/5/053020.

[33] R. Shankar. *Principles of Quantum Mechanics*. Plenum Pub Corp, 2011.

[34] G. B. Arfken and H. J. Weber. *Mathematical Methods for Physicists*. Academic Press, 2005.

[35] E. Tiesinga et al. "A Spectroscopic Determination of Scattering Lengths for Sodium Atom Collisions". In: *J. Res. Natl. Inst. Stand. Technol.* 101 (4 1996), pp. 505–520. DOI: 10.6028/jres.101.051.

[36] R. Côté and A. Dalgarno. "Ultracold atom-ion collisions". In: *Phys. Rev. A* 62 (1 2000), p. 012709. DOI: 10.1103/PhysRevA.62.012709.

[37] W. Ketterle, D. S. Durfee, and D. M. Stamper-Kurn. *Making, probing and understanding Bose-Einstein condensates*. 1999. arXiv: cond-mat/9904034 [cond-mat].

[38] A. J. Moerdijk, B. J. Verhaar, and A. Axelsson. "Resonances in ultracold collisions of $^{6}$Li, $^{7}$Li, and $^{23}$Na". In: *Phys. Rev. A* 51 (6 1995), pp. 4852–4861. DOI: 10.1103/PhysRevA.51.4852.

[39] S. L. Cornish et al. "Stable $^{85}$Rb Bose-Einstein Condensates with Widely Tunable Interactions". In: *Phys. Rev. Lett.* 85 (9 2000), pp. 1795–1798. DOI: 10.1103/PhysRevLett.85.1795.

[40] T. Loftus et al. "Resonant Control of Elastic Collisions in an Optically Trapped Fermi Gas of Atoms". In: *Phys. Rev. Lett.* 88 (17 2002), p. 173201. DOI: 10.1103/PhysRevLett.88.173201.

[41] S. Jochim et al. "Magnetic Field Control of Elastic Scattering in a Cold Gas of Fermionic Lithium Atoms". In: *Phys. Rev. Lett.* 89 (27 2002), p. 273202. DOI: 10.1103/PhysRevLett.89.273202.

[42] K. M. O'Hara et al. "Observation of a Strongly Interacting Degenerate Fermi Gas of Atoms". In: *Science* 298.5601 (2002), pp. 2179–2182. DOI: 10.1126/science.1079107.

[43] Z. Idziaszek et al. "Quantum theory of ultracold atom-ion collisions". In: *Phys. Rev. A* 79 (1 2009), p. 010702. DOI: 10.1103/PhysRevA.79.010702.

[44] C. Zipkes et al. "Cold Heteronuclear Atom-Ion Collisions". In: *Phys. Rev. Lett.* 105 (13 2010), p. 133201. DOI: 10.1103/PhysRevLett.105.133201.

[45] T. Sikorsky et al. "Spin-controlled atom–ion chemistry". In: *Nat. Comm.* 9 (1 2018), p. 920. DOI: 10.1038/s41467-018-03373-y.

[46] Z. Meir et al. "Experimental apparatus for overlapping a ground-state cooled ion with ultracold atoms". In: *Journal of Modern Optics* 65.5-6 (2018), pp. 501–519. DOI: 10.1080/09500340.2017.1397217.

[47] S. Schmid, A. Härter, and J. H. Denschlag. "Dynamics of a Cold Trapped Ion in a Bose-Einstein Condensate". In: *Phys. Rev. Lett.* 105 (13 2010), p. 133202. DOI: 10.1103/PhysRevLett.105.133202.

[48] M. E. Gehm. "Preparation of an optically-trapped Degenerate Fermi Gas of 6Li: Finding the route to degeneracy". PhD Thesis. Duke University, 2003.

[49] G. Zürn et al. "Precise Characterization of $^6$Li Feshbach Resonances Using Trap-Sideband-Resolved RF Spectroscopy of Weakly Bound Molecules". In: *Phys. Rev. Lett.* 110 (13 2013), p. 135301. DOI: 10.1103/PhysRevLett.110.135301.

[50] A. Mazurenko et al. "A cold-atom Fermi–Hubbard antiferromagnet". In: *Nature* 545 (2017), pp. 462–466. DOI: 10.1038/nature22362.

[51] T. Bourdel et al. "Experimental Study of the BEC-BCS Crossover Region in Lithium 6". In: *Phys. Rev. Lett.* 93 (5 2004), p. 050401. DOI: 10.1103/PhysRevLett.93.050401.

[52] *Handbook of Basic Atomic Spectroscopic Data*. URL: https://www.nist.gov/pml/handbook-basic-atomic-spectroscopic-data.

[53] W. Neuhauser et al. "Visual observation and optical cooling of electrodynamically contained ions". In: *Appl. Phys.* 17 (123 1978). DOI: https://doi.org/10.1007/BF00885243.

[54] A. T. Grier et al. "Observation of Cold Collisions between Trapped Ions and Trapped Atoms". In: *Phys. Rev. Lett.* 102 (22 2009), p. 223201. DOI: 10.1103/PhysRevLett.102.223201.

[55] F. H. J. Hall et al. "Light-Assisted Ion-Neutral Reactive Processes in the Cold Regime: Radiative Molecule Formation versus Charge Exchange". In: *Phys. Rev. Lett.* 107 (24 2011), p. 243202. DOI: 10.1103/PhysRevLett.107.243202.

[56] A. Härter et al. "Single Ion as a Three-Body Reaction Center in an Ultracold Atomic Gas". In: *Phys. Rev. Lett.* 109 (12 2012), p. 123201. DOI: 10.1103/PhysRevLett.109.123201.

[57] M. Knoop, M. Vedel, and F. Vedel. "Lifetime, collisional-quenching, and j-mixing measurements of the metastable 3D levels of $Ca^+$". In: *Phys. Rev. A* 52 (5 1995), pp. 3763–3769. DOI: 10.1103/PhysRevA.52.3763.

[58] L. Ratschbacher et al. "Decoherence of a Single-Ion Qubit Immersed in a Spin-Polarized Atomic Bath". In: *Phys. Rev. Lett.* 110 (16 2013), p. 160402. DOI: 10.1103/PhysRevLett.110.160402.

[59] R. Ozeri, L. Khaykovich, and N. Davidson. "Long spin relaxation times in a single-beam blue-detuned optical trap". In: *Phys. Rev. A* 59 (3 1999), R1750–R1753. DOI: 10.1103/PhysRevA.59.R1750.

[60] T. Feldker et al. *Buffer gas cooling of a trapped ion to the quantum regime*. 2019. arXiv: 1907.10926 [quant-ph].

[61] K. Ravi et al. "Laser Deceleration of an Atomic Beam". In: *Nat. Comm.* 3 (1 2012), p. 1126. DOI: 10.1038/ncomms2131.

[62] W. G. Rellergert et al. "Evidence for sympathetic vibrational cooling of translationally cold molecules". In: *Nat.* 495 (490 2013). DOI: https://doi.org/10.1038/nature11937.

[63] H. Doerk, Z. Idziaszek, and T. Calarco. "Atom-ion quantum gate". In: *Phys. Rev. A* 81 (1 2010), p. 012708. DOI: 10.1103/PhysRevA.81.012708.

[64] R. Feynman. "Simulating physics with computers". In: *R.P. Int J Theor Phys* 21 (1982), p. 467. DOI: https://doi.org/10.1007/BF02650179.

[65] I. Bloch, J. Dalibard, and S. Nascimbéne. "Quantum simulations with ultracold quantum gases". In: *Nat. Phys.* 8 (4 2012), pp. 267–276. DOI: https://doi.org/10.1038/nphys2259.

[66] A. Negretti et al. "Generalized Kronig-Penney model for ultracold atomic quantum systems". In: *Phys. Rev. B* 90 (15 2014), p. 155426. DOI: 10.1103/PhysRevB.90.155426.

[67] M. Larsson, W. D. Geppert, and G. Nyman. "Ion chemistry in space". In: *Reports on Progress in Physics* 75.6 (2012), p. 066901. DOI: 10.1088/0034-4885/75/6/066901.

[68] S. Petrie and D. K. Bohme. "Ions in space". In: *Mass Spectrometry Reviews* 26.2 (2007), pp. 258–280. DOI: 10.1002/mas.20114.

[69] C. Monroe et al. "Demonstration of a Fundamental Quantum Logic Gate". In: *Phys. Rev. Lett.* 75 (25 1995), pp. 4714–4717. DOI: 10.1103/PhysRevLett.75.4714.

[70] J. I. Cirac and P. Zoller. "Quantum Computations with Cold Trapped Ions". In: *Phys. Rev. Lett.* 74 (20 1995), pp. 4091–4094. DOI: 10.1103/PhysRevLett.74.4091.

[71] G. K. Brennen et al. "Quantum Logic Gates in Optical Lattices". In: *Phys. Rev. Lett.* 82 (5 1999), pp. 1060–1063. DOI: 10.1103/PhysRevLett.82.1060.

[72] T. Calarco et al. "Quantum gates with neutral atoms: Controlling collisional interactions in time-dependent traps". In: *Phys. Rev. A* 61 (2 2000), p. 022304. DOI: 10.1103/PhysRevA.61.022304.

[73] M. A. Nielsen and I. L. Chuang. *Quantum Computation and Quantum Information*. Cambridge University Press, 2000.

[74] J. I. Cirac and P. Zoller. "A scalable quantum computer with ions in an array of microtraps". In: *Nature* 404 (6778 2000), pp. 579–581. DOI: 10.1038/35007021.

[75] C. Kollath, M. Köhl, and T. Giamarchi. "Scanning tunneling microscopy for ultracold atoms". In: *Phys. Rev. A* 76 (6 2007), p. 063602. DOI: 10.1103/PhysRevA.76.063602.

[76] T. Bothwell et al. "JILA SrI optical lattice clock with uncertainty of $2.0 \times 10^{-18}$". In: *Metrologia* 56.6 (2019), p. 065004. DOI: 10.1088/1681-7575/ab4089.

[77] T. Rosenband et al. "Frequency Ratio of $Al^+$ and $Hg^+$ Single-Ion Optical Clocks; Metrology at the 17th Decimal Place". In: *Science* 319.5871 (2008), pp. 1808–1812. DOI: 10.1126/science.1154622.

[78] A. D. Ludlow et al. "Sr Lattice Clock at $1 \times 10^{-16}$ Fractional Uncertainty by Remote Optical Evaluation with a Ca Clock". In: *Science* 319.5871 (2008), pp. 1805–1808. DOI: 10.1126/science.1153341.

[79] M. Takamoto et al. "An optical lattice clock". In: *Nature* 435 (7040 2005), pp. 321–324. DOI: 10.1038/nature03541.

[80] A. C. Vutha, T. Kirchner, and P. Dubé. "Collisional frequency shift of a trapped-ion optical clock". In: *Phys. Rev. A* 96 (2 2017), p. 022704. DOI: 10.1103/PhysRevA.96.022704.

[81] W. F. McGrew et al. "Atomic clock performance enabling geodesy below the centimetre level". In: *Nature* 564.7734 (2018), 87–90. DOI: 10.1038/s41586-018-0738-2.

[82] N. Huntemann et al. "Single-Ion Atomic Clock with $3 \times 10^{-18}$ Systematic Uncertainty". In: *Phys. Rev. Lett.* 116 (6 2016), p. 063001. DOI: 10.1103/PhysRevLett.116.063001.

[83] T. F. Gloger et al. "Ion-trajectory analysis for micromotion minimization and the measurement of small forces". In: *Phys. Rev. A* 92 (4 2015), p. 043421. DOI: 10.1103/PhysRevA.92.043421.

[84] H. J. Metcalf and P. van der Straten. *Laser Cooling and Trapping*. Springer, 1999.

[85] C. Cohen-Tannoudji and D. Guéry-Odelin. *Advances in Atomic Physics: An Overview*. World Scientific, 2011.

[86] W. D.Phillips and H. Metcalf. "Laser Deceleration of an Atomic Beam". In: *Phys. Rev. Lett.* 48 (9 1982), pp. 596–599. DOI: 10.1103/PhysRevLett.48.596.

[87] G. Valtolina. "Development of an experimental apparatus for the production and study of ultracold atomic gases of fermionic lithium". Master Thesis. Università degli Studi di Milano and Bicocca, 2011/2012.

[88] T.W. Hansch and A.L. Schalow. "Cooling of gases by laser radiation". In: *Optics Communications* 13 (1 1975), pp. 68–69. DOI: https://doi.org/10.1016/0030-4018(75)90159-5.

[89] J. Dalibard and C. Cohen-Tannoudji. "Laser cooling below the Doppler limit by polarization gradients: simple theoretical models". In: *J. Opt. Soc. Am. B* 6.11 (1989), pp. 2023–2045. DOI: 10.1364/JOSAB.6.002023.

[90] P. D. Lett et al. "Observation of Atoms Laser Cooled below the Doppler Limit". In: *Phys. Rev. Lett.* 61 (2 1988), pp. 169–172. DOI: 10.1103/PhysRevLett.61.169.

[91] E. L. Raab et al. "Trapping of Neutral Sodium Atoms with Radiation Pressure". In: *Phys. Rev. Lett.* 59 (23 1987), pp. 2631–2634. DOI: 10.1103/PhysRevLett.59.2631.

[92] M. Inguscio and L. Fallani. *Atomic Physics: Precise Measurements and Ultracold Matter*. Oxford University Press, 2013.

[93] G. Grynberg and J.-Y. Courtois. "Proposal for a Magneto-Optical Lattice for Trapping Atoms in Nearly-Dark States". In: *Europhysics Letters (EPL)* 27.1 (1994), pp. 41–46. DOI: 10.1209/0295-5075/27/1/008.

[94] M. Weidemüller et al. "A Novel Scheme for Efficient Cooling below the Photon Recoil Limit". In: 27.2 (1994), pp. 109–114. DOI: 10.1209/0295-5075/27/2/006.

[95] A. Burchianti et al. "Efficient all-optical production of large $^6$Li quantum gases using $D_1$ gray-molasses cooling". In: *Phys. Rev. A* 90 (4 2014), p. 043408. DOI: 10.1103/PhysRevA.90.043408.

[96] A. Aspect et al. "Laser Cooling below the One-Photon Recoil Energy by Velocity-Selective Coherent Population Trapping". In: *Phys. Rev. Lett.* 61 (7 1988), pp. 826–829. DOI: 10.1103/PhysRevLett.61.826.

[97] H. F. Hess et al. "Magnetic trapping of spin-polarized atomic hydrogen". In: *Phys. Rev. Lett.* 59 (6 1987), pp. 672–675. DOI: 10.1103/PhysRevLett.59.672.

[98] W. Ketterle and M. W. Zwierlein. *Making, probing and understanding ultracold Fermi gases*. 2008. DOI: 10.1393/ncr/i2008-10033-1.

[99] T. Hilker. "Laser Cooling of Bosonic and Fermionic Lithium". MA Thesis. Technischen Universität München, 2012.

[100] *Ion trappers worldwide*. URL: https://www.easymapmaker.com/map/ion_trappers.

[101] S. Earnshaw. "On the Nature of the Molecular Forces which Regulate the Constitution of the Luminiferous Ether". In: *Trans. Camb. Phil. Soc.* 7 (1842), 97–112.

[102] C. Zipkes. "A Trapped Single Ion Inside a Bose-Einstein Condensate". PhD Thesis. University of Cambridge, 2011.

[103] W. Paul. "Electromagnetic traps for charged and neutral particles". In: *Rev. Mod. Phys.* 62 (3 1990), pp. 531–540. DOI: 10.1103/RevModPhys.62.531.

[104] P. F. Herskind et al. "Positioning of the rf potential minimum line of a linear Paul trap with micrometer precision". In: 42.15 (2009), p. 154008. DOI: 10.1088/0953-4075/42/15/154008.

[105] D. J. Berkeland et al. "Minimization of ion micromotion in a Paul trap". In: *J. Appl. Phys.* **83**, 5025 (1998). URL: https://doi.org/10.1063/1.367318.

[106] M. Harlander et al. "Trapped-ion probing of light-induced charging effects on dielectrics". In: *New Journal of Physics* 12.9 (2010), p. 093035. DOI: 10.1088/1367-2630/12/9/093035.

[107] Y. Ibaraki, U. Tanaka, and S. Urabe. "Detection of parametric resonance of trapped ions for micromotion compensation". In: *Appl. Phys. B* 105 (219 2011). DOI: https://doi.org/10.1007/s00340-011-4463-x.

[108] A. Härter et al. "Minimization of ion micromotion using ultracold atomic probes". In: *Applied Physics Letters* 102.22 (2013), p. 221115. DOI: 10.1063/1.4809578.

[109] G. Modugno et al. "Bose-Einstein Condensation of Potassium Atoms by Sympathetic Cooling". In: *Science* 294.5545 (2001), pp. 1320–1322. DOI: 10.1126/science.1066687.

[110] F. G. Major and H. G. Dehmelt. "Exchange-Collision Technique for the rf Spectroscopy of Stored Ions". In: *Phys. Rev.* 170 (1 1968), pp. 91–107. DOI: 10.1103/PhysRev.170.91.

[111] K. Chen, S. T. Sullivan, and E. R. Hudson. "Neutral Gas Sympathetic Cooling of an Ion in a Paul Trap". In: *Phys. Rev. Lett.* 112 (14 2014), p. 143009. DOI: 10.1103/PhysRevLett.112.143009.

[112] R. G. DeVoe. "Power-Law Distributions for a Trapped Ion Interacting with a Classical Buffer Gas". In: *Phys. Rev. Lett.* 102 (6 2009), p. 063001. DOI: 10.1103/PhysRevLett.102.063001.

[113] M. Enderlein et al. "Single Ions Trapped in a One-Dimensional Optical Lattice". In: *Phys. Rev. Lett.* 109 (23 2012), p. 233004. DOI: 10.1103/PhysRevLett.109.233004.

[114] T. Huber et al. "A far-off-resonance optical trap for a $Ba^+$ ion". In: *Nat. Comm.* (5 2014), p. 5587. DOI: https://doi.org/10.1038/ncomms6587.

[115] A. Lambrecht et al. *Long lifetimes in optical ion traps*. 2016. arXiv: 1609.06429 [quant-ph].

[116] E. Perego. "A novel setup for trapping and cooling Barium ions for atom-ion experiments". PhD Thesis. Politecnico di Torino, 2019.

[117] B. E. A. Saleh and M. C. Teich. *Fundamental of Photonics*. Wiley-Interscience, 2007.

[118] J. Kaur et al. "Magic wavelengths in the alkaline-earth-metal ions". In: *Phys. Rev. A* 92 (3 2015), p. 031402. DOI: 10.1103/PhysRevA.92.031402.

[119] M. S. Safronova, U. I. Safronova, and C. W. Clark. "Magic wavelengths for optical cooling and trapping of lithium". In: *Phys. Rev. A* 86 (4 2012), p. 042505. DOI: 10.1103/PhysRevA.86.042505.

[120] C. E. Wieman and L. Hollberg. "Using diode lasers for atomic physics". In: *Rev. Sci. Instrum.* 62.1 (1991), pp. 1–20. DOI: 10.1063/1.1142305.

[121] X. Baillard et al. "Interference-filter-stabilized external-cavity diode lasers". In: *Opt. Comm.* 266.2 (2006), pp. 609–613. ISSN: 0030-4018. DOI: https://doi.org/10.1016/j.optcom.2006.05.011.

[122] L. Ricci et al. "A compact grating-stabilized diode laser system for atomic physics". In: *Opt. Comm.* 117.5 (1995), pp. 541–549. DOI: https://doi.org/10.1016/0030-4018(95)00146-Y.

[123] M. de Labachelerie and G. Passedat. "Mode-hop suppression of Littrow grating-tuned lasers". In: *Appl. Opt.* 32.3 (1993), pp. 269–274. DOI: 10.1364/AO.32.000269.

[124] P. McNicholl and H. J. Metcalf. "Synchronous cavity mode and feedback wavelength scanning in dye laser oscillators with gratings". In: *Appl. Opt.* 24.17 (1985), pp. 2757–2761. DOI: 10.1364/AO.24.002757.

[125] E. C. Cook et al. "High passive-stability diode-laser design for use in atomic-physics experiments". In: *Rev. Sci. Instrum.* 83.4 (2012), p. 043101. DOI: 10.1063/1.3698003.

[126] E. Kirilov et al. "Compact, robust, and spectrally pure diode-laser system with a filtered output and a tunable copy for absolute referencing". In: *Appl. Phys. B* 123.119 (2015). DOI: https://doi.org/10.1007/s00340-015-6049-5.

[127] S. D. Saliba et al. "Mode stability of external cavity diode lasers". In: *Appl. Opt.* 48.35 (2009), pp. 6692–6700. DOI: 10.1364/AO.48.006692.

[128] L. Duca et al. *Novel Littrow ECDL design with independent tuning of external cavity length and grating rotation, in preparation.*

[129] *Eagleyard photonics Gmbh website*. URL: https://www.eagleyard.com.

[130] *ppqSense QubeCL data-sheet*. URL: https://www.ppqsense.it/products/qubecl.

[131] *Eagleyard photonics Gmbh private communications.*

[132] A. Trenkwalder. *Private communication.*

[133] E. D. Black. "An introduction to Pound-Drever-Hall laser frequency stabilization". In: *American Journal of Physics* 69.1 (2001), pp. 79–87. DOI: 10.1119/1.1286663.

[134] U. Schünemann et al. "Simple scheme for tunable frequency offset locking of two lasers". In: *Rev. Scient. Instrum.* 70.1 (1999), pp. 242–243. DOI: 10.1063/1.1149573.

[135] J. S. Steinhart and S. R. Hart. "Calibration curves of thermistors". In: *Instruments and methods* 15 (1968), pp. 497–503.

[136] L. Duca. *Private communications.*

[137] M. Born and E. Wolf. *Principles of Optics: Electromagnetic Theory of Propagation, Interference and Diffraction of Light.* Cambridge University Press, 1970.

[138] M. Bass et al. *Handbook of Optics.* McGraw-Hill Education, 2009.

[139] A. Amico et al. "Time-Resolved Observation of Competing Attractive and Repulsive Short-Range Correlations in Strongly Interacting Fermi Gases". In: *Phys. Rev. Lett.* 121 (25 2018), p. 253602. DOI: 10.1103/PhysRevLett.121.253602.

[140] T. Lompe. "Efimov Physics in a three-component Fermi gas". MA Thesis. Ruperto-Carola University of Heidelberg, 2011.

[141] F. Berto and C. Sias. *Prospects for single photon sideband cooling in fermionic Lithium, in print.*

[142] W. Setiawan. "Fermi Gas Microscope". PhD Thesis. Harvard University, 2012.

[143] F. G. Huber. "Site-Resolved Imaging with the Fermi Gas Microscope". PhD Thesis. Harvard University, 2014.

[144] C. Gross, H. C. J. Gan, and K. Dieckmann. "All-optical production and transport of a large $^6$Li quantum gas in a crossed optical dipole trap". In: *Phys. Rev. A* 93 (5 2016), p. 053424. DOI: 10.1103/PhysRevA.93.053424.

[145] D. Griffiths. *Introduction to Quantum Mechanics.* Addison-Wesley, 2004.

[146] R. Franzosi et al. "Coherent transport of cold atoms in angle-tuned optical lattices". In: *Phys. Rev. A* 74 (1 2006), p. 013403. DOI: 10.1103/PhysRevA.74.013403.

[147] D. Rotter. "Quantum feedback and quantum correlation measurements with a single Barium ion". PhD Thesis. Leopold-Franzens-Universität Innsbruck, 2008.

[148] *Shapal Hi-M Soft.* URL: http://www.ceramic-substrates.co.uk/machinable-ceramics/shapal-m/?gclid=CjOKCQjwoqDtBRD-ARIsAL4pviDtSU_t0Zyp_jMNotkngAK4Qo6jjD2qCEvTyNz94g93lj2JOULu8nwaAte9EALw_wcB.

[149] D. S. Naik et al. "Bose–Einstein condensate array in a malleable optical trap formed in a traveling wave cavity". In: *Quantum Science and Technology* 3.4 (2018). DOI: 10.1088/2058-9565/aad48e.

[150] M. Keller et al. "A calcium ion in a cavity as a controlled single-photon source". In: *New Journal of Physics* 6 (2004), p. 95. DOI: 10.1088/1367-2630/6/1/095.

[151] M. Steiner et al. "Single Ion Coupled to an Optical Fiber Cavity". In: *Phys. Rev. Lett.* 110 (4 2013), p. 043003. DOI: 10.1103/PhysRevLett.110.043003.

[152] A. Stute et al. "Tunable ion–photon entanglement in an optical cavity". In: *Nat.* 485 (7399 2012), pp. 482–485. DOI: 10.1038/nature11120.

[153] S. T. Gulder. "Experimental Realization of Quantum Gates and the Deutsch-Jozsa Algorithm with Trapped $^{40}Ca^{+}$ Ions". PhD Thesis. Leopold-Franzens-Universität Innsbruck, 2003.

[154] N. Kjærgaard et al. "Isotope selective loading of an ion trap using resonance-enhanced two-photon ionization". In: *Appl. Phys. B* 71 (207 2000). DOI: https://doi.org/10.1007/s003400000296.

[155] S. De, U. Dammalapati, and L. Willmann. "Lifetime determination of the $5d^2\ ^3F_2$ state in barium using trapped atoms". In: *Phys. Rev. A* 91 (3 2015), p. 032517. DOI: 10.1103/PhysRevA.91.032517.

[156] G. Leschhorn, T. Hasegawa, and T. Schaetz. "Efficient photo-ionization for barium ion trapping using a dipole-allowed resonant two-photon transition". In: *Applied Physics B* 108.1 (2012), pp. 159–165. DOI: 10.1007/s00340-012-5101-y.

[157] B. Srivathsan et al. *Measuring the temperature and heating rate of a single ion by imaging*. 2019. arXiv: 1905.09011 [quant-ph].

[158] A. Omran et al. "Microscopic Observation of Pauli Blocking in Degenerate Fermionic Lattice Gases". In: *Phys. Rev. Lett.* 115 (26 2015), p. 263001. DOI: 10.1103/PhysRevLett.115.263001.

[159] L. Slodička et al. "Electromagnetically Induced Transparency from a Single Atom in Free Space". In: *Phys. Rev. Lett.* 105 (15 2010), p. 153604. DOI: 10.1103/PhysRevLett.105.153604.

[160] A. Detti. "Design and simulation of an optical objective for the imaging of Lithium atoms and Barium ions". MA Thesis. University of Florence, 2016.

[161] J. Brady. "A simple technique for making very fine, durable dissecting needles by sharpening tungsten wire electrolytically". In: *Bulletin of the World Health Organization* 32 (1 1965), pp. 143–144. URL: https://www.ncbi.nlm.nih.gov/pmc/articles/PMC2555190/.

[162] P. A. Kyaw. "Constructing an Ultra-High Vacuum Chamber and a Radio Frequency Helical Resonator for Trapping Ions". Bachelor's degree. Amherst College, 2014.

[163] R. L. Johnston et al. *Stress-corrosion cracking of Ti-bA1-4V alloy in methanol*. 1967.

[164] E. Perego et al. "A scalable hardware and software control apparatus for experiments with hybrid quantum systems". In: *Rev. Sci. Instrum.* **89**, 113116 (2018). URL: https://doi.org/10.1063/1.5049120.

[165] M. E. Gehm et al. "Dynamics of noise-induced heating in atom traps". In: *Phys. Rev. A* **61**, 029902 (1998). URL: https://doi.org/10.1103/PhysRevA.61.029902.

[166] Q. A. Turchette et al. "Heating of trapped ions from the quantum ground state". In: *Phys. Rev. A* **61**, 063418 (2000). URL: https://doi.org/10.1103/PhysRevA.61.063418.

[167] K. G. Johnson et al. "Active stabilization of ion trap radiofrequency potentials". In: *Rev. Sci. Instrum.* **87**, 053110 (2016). URL: https://doi.org/10.1063/1.4948734.

[168] J. D. Siverns et al. "On the application of radio frequency voltages to ion traps via helical resonators". In: *App. Phys. B* Siverns (2000). URL: https://doi.org/10.1007/s00340-011-4837-0.

[169] A. Reza et al. "Development of a Helical Resonator for ion trap application". In: Dec. 2015. DOI: 10.1109/AEMC.2015.7509206.

[170] W. W. Macalpine and R. O. Schildknecht. "Coaxial Resonators with Helical Inner Conductor". In: July 1959. URL: https://ieeexplore.ieee.org/stamp/stamp.jsp?arnumber=4065638.

[171] K. Deng et al. "A modified model of helical resonator with predictable loaded resonant frequency and $Q$-factor". In: *Rev. Sci. Instrum.* **85**, 104706 (2014). URL: https://doi.org/10.1063/1.4897478.

[172] J.R. Noriega et al. "Low power RF amplifier circuit for ion trap applications". In: *Rev. Sci. Instrum.* **87**, 094704 (2016). URL: https://doi.org/10.1063/1.4962707.

[173] D. Gandolfi et al. "Compact RF resonator for cryogenic ion traps". In: *Rev. Sci. Instrum.* **83**, 084705 (2012). URL: https://doi.org/10.1063/1.4737889.

[174] Y.-Y. Jau et al. "Low power high-performance radio frequency oscillator for driving ion traps". In: *Rev. Sci. Instrum.* **82**, 023118 (2011). URL: https://doi.org/10.1063/1.3558569.

[175] J. Keller et al. "Precise determination of micromotion for trapped-ion optical clocks". In: *J. Appl. Phys.* **118**, 104501 (2015). URL: https://doi.org/10.1063/1.4930037.

[176] A. Detti et al. "A compact radiofrequency drive based on interdependent resonant circuits for precise control of ion traps". In: *Rev. Sci. Instrum.* **90**, 023201 (2019). URL: https://doi.org/10.1063/1.5063305.

[177] M. Knap et al. "Time-Dependent Impurity in Ultracold Fermions: Orthogonality Catastrophe and Beyond". In: *Phys. Rev. X* 2 (4 2012), p. 041020. DOI: 10.1103/PhysRevX.2.041020.

[178] *Fericor D. O. O. website*. URL: https://fericor.com.

[179] *Tomita electric co. website for ferrites*. URL: https://www.tomita-electric.com/en/itemcat/ferrite/.

[180] *LTspice website*. URL: https://www.analog.com/en/design-center/design-tools-and-calculators/ltspice-simulator.html#.